Molecular Gas in Nearby Active Galactic Nuclei

Thesis by

Andrew Jordan Baker

In Partial Fulfillment of the Requirements

for the Degree of

Doctor of Philosophy

California Institute of Technology

Pasadena, California

2000

(Submitted January 5, 2000)

Acknowledgments

The aspect of working on this thesis which I've enjoyed the most has been the opportunity to interact with a great many fine astronomers. I've been extremely fortunate to have had Nick Scoville as my adviser; his intuition, back-of-the-envelope skill, and relentless focus on the big picture have had a major impact on this work and (I hope) on me. I also take great pleasure in thanking Anneila Sargent for her tireless efforts on behalf of the Caltech millimeter group, and for her unwavering support of my work in particular. I remain grateful to Wal Sargent for reasons including (but not limited to) his donation of a computer, his underwriting of trips to Palomar and Keck (even for peregrinations in the infrared!), and his expertise on football and Grace Brothers, Ltd. Support from Nick, Anneila, and Wal accounts for the fact that I will be gainfully employed upon leaving Caltech; "Schönen Dank" to all three on this score as well.

Of the other colleagues with whom I've had scientific interactions, I am especially grateful to two people. Luis Ho gave the 1996 colloquium which inspired this project, and has offered much stimulating conversation in the intervening years. Kazushi Sakamoto influenced the direction of my thesis with the scientific conclusions of *his* thesis, and has generously shared a number of key insights on data reduction and gas dynamics. I'd also like to thank the members of my thesis committee– Gerry Neugebauer, Sterl Phinney, and Chuck Steidel (along with Wal and Nick)– for their penetrating comments at my candidacy exam and my defense (and for their patience in waiting for the latter). I've had useful discussions of relevant astrophysical issues with Susanne Aalto, Roger Blandford, John Carpenter, Eugene Chiang, Andreas Eckart, Eiichi Egami, Peter Erwin, Paul Eskridge, Aaron Evans, Laura Ferrarese, David Frayer, Jack Gallimore, Reinhard Genzel, Peter Goldreich, Tamara Helfer, Shardha Jogee, Seppo Laine, Yoram Lithwick, Crystal Martin, Tom Murphy, Patrick Ogle, Rick Pogge, Alice Quillen, Mike Regan, Eva Schinnerer, Kartik Sheth, Patrick Shopbell, Linda Tacconi, Jean Turner, Jim Ulvestad, Min Yun, and no doubt several others to whom I apologize for omitting their names.

The data presented in these pages were obtained with the Owens Valley Radio Observatory millimeter array. I am therefore indebted to the past and present engineering and

technical staff at the observatory: David Woody, Steve Scott, James Lamb, Steve Padin, David Hawkins, Hemant Shukla, Ray Finch, Ron Lawrence, Curt Giovanine, and Colin Hall (many of whom were extremely patient with late-night phone calls). Fellow millimeter group members in the observing rotation have all helped in the acquisition (and in some cases, reduction) of my data: Susanne Aalto, Rachel Akeson, Geoff Blake, Peter Bryant, John Carlstrom, John Carpenter, Aaron Evans, Shardha Jogee, David Frayer, David Koerner, Oliver Lay, Vince Mannings, Kevin Marvel, Charlie Qi, Kazushi Sakamoto, Leonardo Testi, and Min Yun. I am especially grateful to former postdoc Debra Shepherd for her friendship and dedication. Money to operate the array (and to pay my salary) has come from American taxpayers through the National Science Foundation, and from the K. T. & E. L. Norris Foundation.

Supplementary infrared observations, which will figure more prominently in published papers than they do in these pages, were obtained at the Palomar Observatory. James Larkin, Rob Knop, and Keith Matthews built the "Has No Acronym" NIR spectrograph; Tom Hayward and collaborators at Cornell built the SpectroCam-10 MIR camera. Data were taken with the assistance of night assistants Rick Burruss, Karl Dunscombe, Jean Mueller, Kevin Rykoski, and Skip Staples, and of fellow students Marc Kuchner and Tom Murphy. I attribute the smoothness of my Palomar observing runs to the hard work of the observatory's administrative and technical staff.

Many members of the Caltech astronomy department with whom I have *not* discussed Lindblad resonances or millimeter flux calibration have nonetheless contributed to my thesis and my graduate school experience in important ways. Chris Fassnacht and Shri Kulkarni were especially instrumental in persuading me to come to Caltech in the first place. Cheryl Southard and Martin Shepherd have saved me from a number of computing disasters, not all of which were self-inflicted. Helen Knudsen, Joy Painter, Caroline Smith, and Anne Snyder have helped me track down vital but obscure references in the library; I am also grateful to Gina Armas, Nanci Candelin, Diane Fujitani, Sandy Lester, Candi Lewis, Judith Mack, and Gita Patel for shielding me from five and a half years' worth of paperwork. Among my fellow graduate students, I'd especially like to thank Rachel Akeson, Rebecca Bernstein, Chris Fassnacht, Laura Grego, and Todd Small for sharing their accumulated wisdom; Brad Behr, Roy Gal, Brian Kern, Marc Kuchner, and Ben Oppenheimer for trading ideas on our first-year problem sets; and Mindy Kellogg, Patrick Ogle, Mike Pahre, Alice

Shapley, and Pat Udomprasert for having made Robinson 3 a quiet place to work. Whatever level of fitness I retain is owed to exertions on tennis courts opposite Josh Bloom (and Peter Goldreich, an honorary student in this context), and on soccer fields with my fellow Cataclysmic Variables.

In my life outside of work, I've been sustained by friends outside of Caltech– notably Won, Dan, Scott, Arthur, Khoi, Gary, Rebecca, Anoop, Tony, and Tim. Above all, I am indebted to the members of my family, some of whom witnessed the inception of this work but not its completion. For all the reasons which are far too important to entrust to University Microfilms, I affectionately dedicate this thesis to them.

TO EPJ, MCJ, MFJ, CCB, & CLB
FROM AJB
CHRISTMAS 1999

Abstract

This thesis describes the distributions, physical conditions, and kinematics of the molecular gas in eight nearby galaxies whose Seyfert and LINER nuclei display broad Hα emission. We have mapped these systems at a linear resolution of $\sim 100\,\mathrm{pc}$ in the CO(2–1) rotational transition, as well as at lower resolution in the CO(1–0) line, using the Owens Valley Radio Observatory millimeter array. Subsequent kinematical modelling allows us to improve on this angular resolution by exploiting our high effective velocity resolution; we simultaneously determine the radial emissivity profile of each line and the velocity field which the gas traces. Analysis of the molecular emission from individual objects reveals (1) massive concentrations of molecular gas ($\sim 10^9\,\mathrm{M}_\odot$) at small galactocentric radii ($r \leq 500\,\mathrm{pc}$); (2) a pattern of high excitation at small radius, implied by variation in the ratio of CO(2–1) to CO(1–0) integrated intensities, which we attribute in part to the external heating of molecular clouds by energetic photons; (3) a high occurrence of nonaxisymmetric structures within 500 pc of the nucleus, including four gas bars; (4) evidence for episodic mass inflow along stellar bars outside 500 pc; and (5) apparent redirection of radio jets and ionizing photons from the nucleus by the molecular gas which they encounter. Our most striking discoveries are a dynamically decoupled secondary bar in the nucleus of NGC 7479, a mean integrated intensity ratio ≥ 1.85 in the nucleus of NGC 2681, and a warped molecular disk in the nucleus of NGC 1068.

Contents

List of Figures

List of Tables

Chapter 1 Introduction

This thesis describes the distributions, physical conditions, and kinematics of the molecular gas in eight nearby active galaxies. The original stimulus for the project was the lack of observational evidence for or against various theoretical pictures of how active galactic nuclei (AGN) are fuelled on scales of $\sim 100\,\mathrm{pc}$. This particular scale was chosen partly for convenience: in nearby ($d \leq 20\,\mathrm{Mpc}$) galaxies, it matches the resolution which can be obtained by millimeter interferometers at the limits of their current capabilities. Nevertheless, it still exceeds the Schwarzshild radius by many orders of magnitude, making it difficult to relate conclusions about large-scale fuelling mechanisms to the details of small-scale accretion physics. In this introduction, we briefly discuss the prospects for bridging this gap and their relationship to the data we will present in subsequent chapters.

1.1 Active and quiescent nuclei

In recent years, observers of stellar kinematics, gas dynamics, and emission line variability have measured the masses of black holes in the nuclei of ~ 20 nearby galaxies (van der Marel 1998). Somewhat surprisingly, many of these galaxies manifest none of the optical lines or compact radio cores which define *active* galactic nuclei (AGN). To pose the question of why some galaxies are active and others are not, however, presumes that we know *which* galaxies are active and which are not– an issue which remains decidedly unsettled. After careful removal of stellar absorption spectra, Ho et al. (1997a) find an unexpectedly high 10% of nearby galaxies displaying Seyfert emission features, as well as a further 33% showing Low-Ionization Nuclear Emission-line Region (LINER) spectra. The latter include several LINERs with broad nuclear Hα emission, unambiguous evidence that at least some members of this class are accretion-powered (Ho et al. 1997c), and suggestive that the detected systems may represent just the tip of the AGN iceberg. The prevalence of low-luminosity (and no-luminosity) galactic nuclei supports the proposition that all nearby galaxies with substantial bulges host massive central black holes (Wandel 1999), but that the rates of accretion onto these black holes range smoothly from high (a few $\mathrm{M_\odot\,yr^{-1}}$) to undetectable.

Various factors can explain weak or absent optical signatures of accretion in systems with massive bulges. First, broad or high-excitation emission lines can be extinguished by dust or washed out by competing emission from nuclear H II regions. Second, these lines may have low intrinsic luminosity if a black hole accretes through a radiatively inefficient advection-dominated accretion flow (ADAF). Third, a black hole may not be accreting at all because it lacks fuel. In practice, the first two of these explanations will be coupled to the third. A nucleus with a very low fuelling rate is likely to select an ADAF over the more radiatively efficient α-disk solution of the accretion equations. If the fuelling rate increases, the accretion flow will resemble an ADAF inside some transition radius r_{tr} and an α-disk at $r > r_{tr}$; for a high enough fuelling rate, r_{tr} is forced to vanishingly small radius, and the ADAF is suppressed (Narayan et al. 1998). Too high a fuelling rate, however, will tend to trigger inconvenient star formation. Sakamoto et al. (1999b) find evidence for this effect in a CO(1–0) survey of twenty spirals, which shows anti-correlation of M_{gas}/M_{dyn} with detection of nuclear activity.

In order to understand why only certain galaxies appear active, we must be able to determine their nuclear fuelling rates. Before we can estimate fuelling rates, however, we must identify their fuelling *mechanisms*. On scales of 100 pc, proposed scenarios include cloud-cloud collisions in flat (Lin et al. 1988) or warped (Sanders et al. 1989) disks, self-gravitational instabilities (Wada & Habe 1995) which may produce nested bars (Shlosman et al. 1989; Heller & Shlosman 1994), dissipative infall of satellite galaxies (Hernquist 1989), and shocks in nuclear spiral dust lanes (Martini & Pogge 1999). On larger scales, radial streaming in a barlike potential can probably drive gas to within 500 pc of the nucleus: Sakamoto et al. (1999b) find that gas is more centrally concentrated in barred than in unbarred galaxies. However, reports on the possible correlation of large-scale bars with nuclear activity are conflicting (Ho et al. 1997b; Mulchaey & Regan 1997; Knapen et al. 1999; Maiolino et al. 1999), in part due to the subtleties of determining which active galaxies are barred and which barred galaxies are active. The probable dissolution of bars by the mass they accumulate in the nucleus (Norman et al. 1996), and the possibility that nuclear activity tends to follow bar-driven nuclear star formation (Norman & Scoville 1988), emphasize that the *current* presence or absence of a large-scale bar may have very little to do with a galaxy's current activity level.

A final obstacle to establishing a relation between fuelling and nuclear activity is posed

Galaxy	R.A. (1950)	Dec. (1950)	Distance (Mpc)	Host type	Nuclear type	Alias(es)
(1)	(2)	(3)	(4)	(5)	(6)	(7)
NGC 1068	02:40:07	-00:13:30	14.4	(R)SA(rs)b	S1.9 (P)	M77 UGC 2188 Arp 37
NGC 2681	08:49:58	+51:30:18	13.3	(R′)SAB(rs)0a	L1.9 (D)	UGC 4645
NGC 3227	10:20:47	+20:07:06	20.6	SAB(s)a Pec	S1.5 (D)	UGC 5620 Arp 94 VV 209a
NGC 4051	12:00:37	+44:48:42	17.0	SAB(rs)bc	S1.2 (D)	UGC 7030
NGC 4438	12:25:14	+13:17:06	16.8	SA(s)0a Pec	L1.9 (P)	UGC 7574 Arp 120 VV 188
NGC 5005	13:08:37	+37:19:24	21.3	SAB(rs)bc	L1.9 (D)	UGC 8256
NGC 5033	13:11:08	+36:51:48	18.7	SA(s)c	S1.5 (D)	UGC 8307
NGC 7479	23:02:26	+12:03:00	32.4	SB(s)c	S1.9 (D)	UGC 12343

Table 1.1: Sample galaxies. The columns are (1) galaxy (2) right ascension (B1950) (3) declination (B1950) (4) distance in Mpc, from Tully (1988) (4) host galaxy type, from de Vaucouleurs et al. (1991) (5) class of nuclear optical spectrum, from Ho et al. (1997a), along with an assessment of whether the detection of a broad Hα component is **D**efinite or only **P**robable (Ho et al. 1997c) (6) common alias(es).

by the unknown rate of nuclear star formation, which UV observations of LINERs and Seyferts (Maoz 1998; Heckman 1999) and infrared spectroscopy of the Galactic center (Krabbe et al. 1995) suggest can efficiently dispose of inflowing material. If we cannot constrain what fraction of the material moving inward at $r \sim 100\,\mathrm{pc}$ ever reaches the Schwarzschild radius, any attempt to link the two scales is likely to fail. Our best hope may be a negative test. If we select a sample of galaxies according to their unusually high level of nuclear activity, we would (on average) expect their activity level to be lower in the future than at present. If we succeed in estimating their fuelling rates at 100 pc, only to discover that current rates of consumption at 1 pc are far exceeded by the current rates of inflow at 100 pc (i.e., by the *future* rates of inflow at 1 pc), we would be forced to concede that fuelling on large scales is substantially irrelevant to activity level.

1.2 Sample selection

In order to discriminate between the various proposed scenarios for mass transfer on 100-pc scales, it is desirable to study galaxies which have (a) a range of nuclear luminosities, so that we will be sensitive to correlations with parameters of the large-scale fuelling; (b) clear evidence of being accretion-powered; and (c) sufficient molecular gas to be easily mapped. Criterion (a) argues not only for the inclusion of Seyfert 1 and 2 nuclei, but also for the inclusion of LINERs, whose lower-ionization spectra are likely due to some intrinsic property rather than to an orientation effect. Including LINERs, however, risks adding sources whose nuclear lumniosity is *not* powered by accretion. To satisfy criterion (b), therefore, we drew the thesis sample from the 46 objects in the Ho et al. (1997a) survey showing broad Hα emission. To satisfy criterion (c), we identified the 15 of these 46 objects which had showed the strongest detections of CO(1–0) in previous single-dish observations. These 15 sources were mapped at 4″ resolution in the CO(1–0) line, and the eight nuclei showing the strongest molecular emission (i.e., the most promising for additional array observations, due to strength and minimal flux recovery problems) were chosen as the final thesis sample for 1″-resolution CO(2–1) observations. We list these eight objects in Table 1.1.

1.3 Organization of the thesis

The three chapters following this introduction are case studies of individual galaxies, which lay out our approaches to the analysis of gas kinematics and excitation. In Chapter 2, we show that an analytical approach can reproduce the observed gas kinematics in the strongly barred galaxy NGC 7479. In Chapter 3, we consider possible models for the high molecular excitation observed in the center of a galaxy with rather regular kinematics, NGC 2681. In Chapter 4, we apply the analytical tools developed in the two preceding chapters to the molecular gas structure in the nucleus of NGC 1068, concluding that its unusual kinematics are best described by a disk which is *warped*. We discuss our results for the five remaining galaxies in Chapter 5. Chapter 6 then summarizes the conclusions we draw from the sample as a whole. In Appendix A, we provide a primer on the practice of millimeter interferometry, while Appendix B presents detailed derivations of some of the formulas used in the main body of the text.

Chapter 2 Bar-driven inflow in NGC 7479

2.1 Introduction

Prior observations of the CO(1–0) line in a sample of 20 gas-rich spirals have suggested that streaming motions in barred galaxies can build up substantial molecular gas concentrations within 500 pc of their nuclei (Sakamoto et al. 1999a). These results are intriguing but raise new questions: we still wish to know the ultimate fate of the gas within 500 pc, and to determine the rates of inflow (steady or episodic) on all scales. In this paper, the first in a series of articles reporting high-resolution observations of the molecular gas in nearby active galaxies, we generate an analytical model to describe the gas dynamics in the strongly barred spiral NGC 7479 ($d = 32.4$ Mpc: Tully 1988). Using the model velocity field to improve on our angular resolution of $1''$ in the CO(2–1) transition, we conclude that inflow on ~ 100 pc scales is driven by torques from a secondary bar in the hitherto unresolved nuclear disk.

2.2 Observations

We observed the CO(2–1) transition in NGC 7479 with the Owens Valley Radio Observatory (OVRO) millimeter array (Padin et al. 1991; Scott & Finch 1992) during the 1998-99 season. Other investigators (Hüttemeister et al. 2000) shared complementary CO(1–0) observations from OVRO, obtained in 1996 with the same pointing center and central velocity. Table 2.1 summarizes both sets of observations. The array includes six 10.4 m diameter antennae (Leighton 1978) with half-power beamwidths of $61''$ and $30.5''$ at 115 GHz and 230 GHz, respectively. Data were obtained for full source transits (i.e., *tracks*) when the array was in three configurations, denoted L (**L**ow resolution), H (**H**igh resolution), and E (with improved *uv* sampling for sources near the celestial **E**quator). Two separate correlators processed continuum and spectral line data. An analog correlator recorded continuum bandwidths of 1 GHz centered at ± 1.5 GHz (the upper and lower sidebands) relative to the reference oscillator frequency. A digital correlator (Padin et al. 1993) provided multiple frequency channels in four modules of flexible bandwidth, whose positions within the 1 GHz

Date	Line	Array	Longest baseline	Passband calibrators	Flux cal	Gain calibrator	Strength
(1)	(2)	(3)	(4)	(5)	(6)	(7)	(8)
28 Feb 96	CO(1–0)	E	119 m	P1+P3	2	3C454.3	5.0 Jy
23 Apr 96	CO(1–0)	L	115 m	P1+P2+P3	1	3C454.3	4.6 Jy
14 Nov 98	CO(2–1)	L	103 m	P1+P2+P3	1	3C454.3	4.2 Jy
7 Dec 98	CO(2–1)	E	119 m	P1+P2	1	3C454.3	4.6 Jy
9 Jan 99	CO(2–1)	H	242 m	P1+P2	1	3C454.3	3.7 Jy
13 Mar 99	CO(2–1)	H	242 m	P1+P2	2	3C454.3	4.4 Jy

Table 2.1: OVRO observation log for NGC 7479. The columns are (1) date (2) CO transition (3) array configuration (4) maximum baseline used in mapping (5) passband calibrators, where P1 = 3C454.3, P2 = 3C345, and P3 = 3C84 (6) type of flux calibration, where 1 denotes use of Uranus and/or Neptune and 2 denotes bootstrapping from archived data (7) gain calibrator (8) flux density adopted for gain calibrator.

continuum bands could be set independently. For this work, we configured the modules to have the greatest possible contiguous bandwidth: taken together, 112 channels each Hanning-smoothed to 4 MHz resolution. We further smoothed the CO(2–1) data to 8 MHz resolution, giving both CO(1–0) and CO(2–1) channels the same 10.4 km s^{-1} velocity width.

We calibrated the data within the OVRO millimeter array database using the MMA package (Scoville et al. 1993). Four of the six tracks included observations of Uranus and/or Neptune; we used these to determine the flux density of 3C454.3 at these epochs, assuming the planets to be uniform disks (appropriately coupled to each projected baseline) matching standard brightness temperature models (Muhleman & Berge 1991; Orton et al. 1986). For the two tracks lacking observations of planets, we determined the flux scale by measuring the flux density of 3C454.3– from Uranus and/or Neptune– in the archived data for unrelated projects obtained close in time to ours. In either case, we only compared observations of planets to observations of 3C454.3 if both were obtained with similar elevations and coherences, in order to avoid systematic differences in atmospheric decorrelation. We estimate that the uncertainties in our flux scale are $\sim$ 10% for the CO(1–0) data and $\sim$ 15% for the CO(2–1) data. Each track included paired observations of 3C454.3, interleaved with observations of NGC 7479 every 30-40 minutes. We used these to remove the effects of instrumental and atmospheric variations on phase and amplitude gains. Observations of

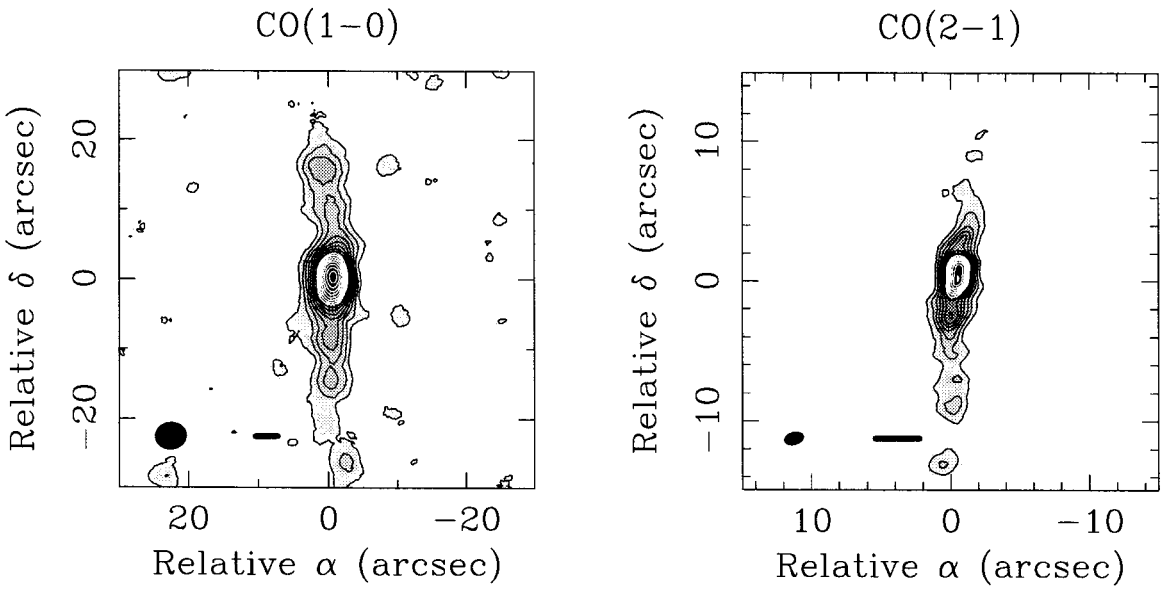

Figure 2.1: Zeroth moment maps of NGC 7479. Pixels with values less than $+1\sigma_{ch}$ were blanked before integrating, and contours are multiples of $2\,\sigma_{ch}\,\Delta v_{ch}\,\sqrt{n_{ch}}$ (4.5 and 5.9 Jy bm^{-1} km s^{-1}). The ellipses in the lower left corners show the synthesized beams; the bars nearby indicate 500 pc at $d = 32.4$ Mpc. Spatial offsets are relative to our phase center coordinates (see Table 2.5).

3C454.3 were also used for passband calibration, in conjunction with observations of 3C84 and/or 3C345.

After editing the visibilities in the DIFMAP package (Shepherd 1997), our final CO(1–0) dataset included 5.4 hours of integration and 28 distinct baselines; our final CO(2–1) dataset included 11.4 hours of integration and 32 distinct baselines. We mapped the data using the IMAGR task in the NRAO AIPS package, cleaning a single large region down to $+1\sigma_{ch}$ in each velocity channel. Maps of the 1 GHz continuum channel in the line-free sideband showed no evidence for emission at either 115 GHz or 230 GHz, so subtraction of continuum from the spectral line data was unnecessary. Moderately robust weighting produced synthesized beams of $4.48'' \times 3.92''$ at $-82.7°$ for the CO(1–0) map and $1.42'' \times 0.91''$ at $-72.7°$ for the CO(2–1) map. The price of this resolution was a slight increase in the per-channel rms noise, to $\sigma_{ch} = 33$ mJy bm^{-1} for the CO(1–0) map (12% larger than for natural weighting) and to $\sigma_{ch} = 43$ mJy bm^{-1} for the CO(2–1) map (25% larger than for natural weighting).

2.3 Results

2.3.1 CO(1–0)

Figure 2.1 shows the zeroth velocity moment of the CO(1–0) line in NGC 7479, integrated over $n_{ch} = 43$ velocity channels from 2117.2 to 2564.4 km s^{-1} LSR. Our calibration and imaging of the original *uv* data differ slightly from those of Hüttemeister et al. (2000), but apart from our nondetection of a feature at $+30''$ north of the nucleus the resulting maps are in good overall agreement. Emission is confined to a linear feature running from $-30''$ south to $+20''$ north of the nucleus, whose position angle slightly leads that of the stellar bar. The same structure also appears in Hα emission and $J-K$ and $H-K$ color maps (Quillen et al. 1995). After subtracting an estimate of the positive bias introduced to the moment map by blanking low-valued data cube pixels, we multiply by the reciprocal of the primary beam response and measure the structure's total CO(1–0) flux to be 222 ± 15 Jy km s^{-1}. This value is actually the average of separate measurements made for moment maps blanked at $\pm\sigma_{ch}$; our quoted uncertainty is half of the difference between measurements (see Appendix A.4 for details). Our detected flux corresponds to a total gas mass of $M_{gas} = 3.7 \pm 0.3 \times 10^9$ M$_\odot$, assuming a Galactic conversion factor $X = 3 \times 10^{20}$ cm^{-2} (K km s^{-1})$^{-1}$ (Young & Scoville 1991) and an extra factor of 1.36 to account for helium.

Since interferometric data are insensitive to emission with low surface brightness and/or a smooth distribution, we wish to estimate the fraction of the total line flux our map recovers. We have therefore corrected the entire data cube for the primary beam response, convolved it to half-power beamwidths of $45''$ and $23''$, and measured the integrated intensities of our convolved data at the pointing centers used for published single-dish observations. We find we have recovered $\sim 60\%$ of the total CO(1–0) emission seen by Young et al. (1995) in their $45''$ beam, and estimate from Figure 6a of Sempere et al. (1995) that we have recovered $\sim 62\%$ of the emission in their $23''$ beam. We make no attempt to correct for the undetected flux in what follows.

Within the linear molecular structure, the strongest emission arises in a central concentration which has dimensions $\sim 8.4'' \times 4.7''$ and an elongation at position angle $\sim 176°$. We measure the CO(1–0) flux from this structure to be 136 ± 5 Jy km s^{-1}, implying a gas mass $M_{gas} \simeq 2.3 \times 10^9$ M$_\odot$. The peak intensity in the nucleus is 387 ± 12 K km s^{-1} (corresponding to a peak $N_{H_2} = 11.6 \pm 0.4 \times 10^{22}$ cm^{-2}), and the peak brightness temperature seen

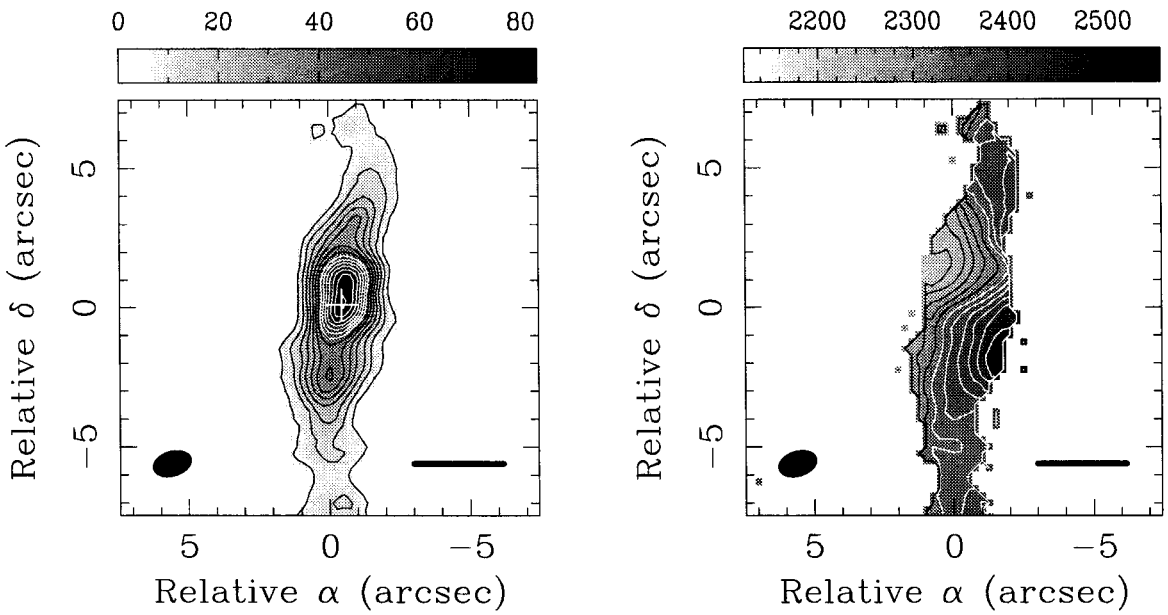

Figure 2.2: CO(2–1) moment maps of NGC 7479. Zeroth moment map shows the nuclear region of Figure 2.1, contoured at the same multiples of 5.9 Jy bm^{-1} km s^{-1}; a cross marks the position of the 20 cm continuum peak (see Table 2.5). First moment map was integrated with blanking of pixels $< +1\sigma_{ch}$, and is plotted here only where the zeroth moment map rises above its lowest contour. Isovelocity contours run from 2225 to 2475 km s^{-1} (LSR) in steps of 25 km s^{-1}.

above the cosmic background is 1.9 ± 0.2 K. Our estimates of the global and nuclear line parameters are broadly consistent with the results of Quillen et al. (1995) and Laine et al. (1999) derived from independent, multiple-pointing datasets also obtained at OVRO.

2.3.2 CO(2–1)

Figure 2.1 shows the zeroth velocity moment of the CO(2–1) line in NGC 7479, which we also present at greater magnification in Figure 2.2. Because of the smaller field of view (and perhaps a radial gradient in molecular excitation), we detect emission only from $-14''$ south to $+11''$ north of the nucleus. The total CO(2–1) flux in this region is 938 ± 99 Jy km s^{-1}. Comparison of our data with those of Sempere et al. (1995) (the latter convolved to half the original resolution) indicates that we have recovered $\sim 87\%$ of the total CO(2–1) emission within $23''$ of the nucleus. The large central concentration in the CO(1–0) map is now resolved into a still more concentrated peak of dimensions $\sim 4'' \times 3''$, with extensions to the north and south which appear to be trailing in the clockwise sense of the galactic

rotation. The brightest central peak has a CO(2–1) flux of $309 \pm 8\,\mathrm{Jy\,km\,s^{-1}}$; adding the emission from its northern and southern extensions brings the total to $525 \pm 15\,\mathrm{Jy\,km\,s^{-1}}$. We observe a peak intensity in the nucleus of $1527 \pm 53\,\mathrm{K\,km\,s^{-1}}$, and a peak brightness temperature above background of $10.0 \pm 0.8\,\mathrm{K}$.

Figure 2.2 also shows the first velocity moment of the CO(2–1) line in NGC 7479. Here we have blanked all pixels $\leq +1\,\sigma_{ch}$ before integrating in velocity, and have only plotted isovelocity contours where the zeroth moment map reaches its lowest contour level. As previously noted by Laine et al. (1999), the predominant velocity gradient in the central region runs roughly parallel to the kinematic major axis determined on large scales. In contrast, the material to the north and south of the nucleus exhibits velocity gradients which are perpendicular to its elongation. The latter pattern can in general appear if gas motions are (a) coplanar and noncircular, or (b) noncoplanar and circular. In view of the large-scale gas morphology seen in Figure 2.1 and the detection of a stellar bar by Quillen et al. (1995), the former scenario is clearly applicable here.

2.3.3 Integrated intensity ratio

The ratio of the integrated intensities of the CO(2–1) and CO(1–0) lines can be a useful probe of physical conditions: if both transitions trace the same material and the CO level populations are in LTE, the intensity ratio is a brightness temperature ratio constraining a combination of excitation temperature and opacity (see Section 3.5). An accurate measurement of the ratio $R = I_{\mathrm{CO(2-1)}}/I_{\mathrm{CO(1-0)}}$ requires that the two line maps should (a) resolve out structures on identical scales, and (b) have identical spatial resolution, in order that the effects of beam dilution on brightness temperature be the same. To enforce condition (a), we created new "truncated" sets of visibilities for each dataset, differing from the originals by their lack of any sampling at uv radii $r_{uv} \leq 10\,\mathrm{k}\lambda$. This threshold is slightly larger than the uv radius reached for the CO(2–1) line at the limit of antenna shadowing. Figure 2.3 illustrates the effects of truncation: we discarded only a small fraction ($\sim 0.5\%$) of the original CO(2–1) visibilities, but a larger fraction ($\sim 6\%$) of the original CO(1–0) visibilities. The map of the truncated CO(1–0) dataset had slightly higher noise ($34\,\mathrm{mJy\,bm^{-1}}$) and smaller synthesized beam ($4.37'' \times 3.81''$ at $-83.1°$) than the original; the map of the truncated CO(2–1) dataset was nearly unchanged.

After creating the two new maps and correcting them for the primary beam response, we

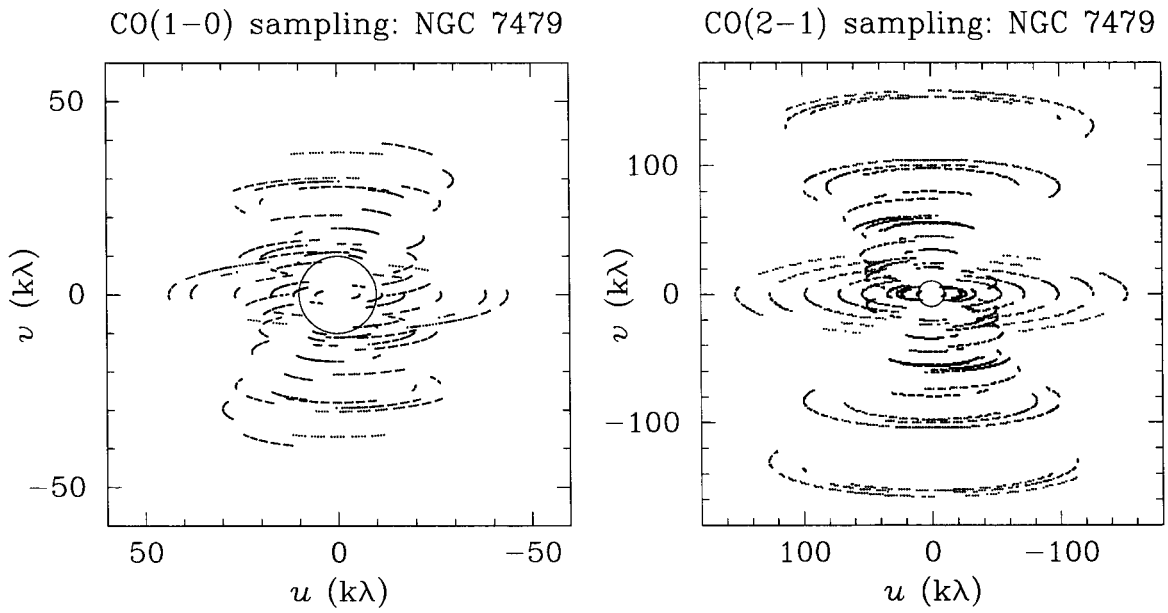

Figure 2.3: Truncated datasets for measuring R. The sampling of the Fourier plane is shown for the CO(1–0) and CO(2–1) datasets for NGC 7479 (note the different scales). The extent of CO(2–1) sampling to higher uv-radius permits a higher map resolution. The integrated intensity ratio R was measured from remapped datasets from which all points at less than $10\,\mathrm{k}\lambda$ radius had been excluded. A circle indicates this truncation radius on each plot; the cut removes more visibilities from the dataset (and extended flux from the map) for the CO(1–0) line than for the CO(2–1) line.

adopted two strategies to enforce condition (b) above. We first convolved both maps to $23''$ resolution and measured the integrated intensities at the pointing center of Sempere et al. (1995). Table 2.2 shows the result: our truncated datasets recover so much larger a fraction of the CO(2–1) emission than of the CO(1–0) emission that we infer the emission missed by the interferometer must have an extremely low intensity ratio ~ 0.16. This particular value is unlikely to be accurate outside $23''$, since Sempere et al. (1995) propose an average ratio of $R \simeq 0.6 > 0.45$ for the emission they map over a larger area. However, the fact that the emission we detect in our OVRO maps has a generally higher intensity ratio than the emission we miss does not seem in doubt. At least some of the emission in column (4) of Table 2.2 is undetected due to its smoothness rather than its low surface brightness, since we lose $14.6\,\mathrm{K\,km\,s^{-1}}$ of the CO(1–0) intensity and $2.5\,\mathrm{K\,km\,s^{-1}}$ of the CO(2–1) intensity in the course of truncating the original datasets.

In addition to estimating a global intensity ratio, we have measured local variations

Quantity (1)	IRAM detects (2)	OVRO detects (3)	OVRO misses (4)
uv sampling	$r_{uv} \geq 0$	$r_{uv} > 10\,\mathrm{k}\lambda$	$r_{uv} \leq 10\,\mathrm{k}\lambda$
$I_{\mathrm{CO(2-1)}}$	$20.4\,\mathrm{K\,km\,s^{-1}}$	$15.3\,\mathrm{K\,km\,s^{-1}}$	$5.1\,\mathrm{K\,km\,s^{-1}}$
$I_{\mathrm{CO(1-0)}}$	$45.1\,\mathrm{K\,km\,s^{-1}}$	$13.3\,\mathrm{K\,km\,s^{-1}}$	$31.8\,\mathrm{K\,km\,s^{-1}}$
R	0.45	1.15	0.16

Table 2.2: Global intensities and their ratios in NGC 7479. We compare the integrated intensities and intensity ratios within the inner $23''$ for (2) single-dish measurements estimated from Figure 6a of Sempere et al. (1995); (3) interferometer measurements determined from the truncated OVRO datasets; and (4) the flux missed by the interferometer due to low surface brightness and/or a smooth spatial distribution.

in R by convolving the data cube made from the truncated CO(2–1) data to the resolution of the cube made from the truncated CO(1–0) data, and integrating both cubes over four velocity windows (roughly symmetric with respect to systemic velocity) spanning the line. Calculating R separately for such partial moment maps allows us to see the apparent variation of the ratio with position and velocity, which may be due to real variations in physical conditions or to measurement uncertainties. Table 2.3 shows the ratios we observe in NGC 7479 over the four windows and the full width of the line. Each spatial box we used to measure R in a ratio map matched the location of an emission peak in one or both of the corresponding (partial) moment maps. We have also tabulated the peak brightness temperatures above background which we observe in these same boxes, since we can only use R and T_b to constrain physical conditions if both are measured in the same subsets of the data. While we do see some suggestions that the intensity ratio varies– notably in the window just redwards of systemic velocity, where the CO(1–0) and CO(2–1) peaks are not spatially aligned– most of our measurements in the nucleus fall in the rather narrow range of $0.9 \leq R \leq 1.2$.

2.4 Kinematic models

In modelling the motions of the molecular gas in NGC 7479, we must simultaneously determine both the potential in which the gas moves and the [emissivity] distribution of the gas in the potential. Decoupling the potential and the gas distribution can pose a challenge:

Velocities ($km\,s^{-1}$) (1)	Spatial feature (2)	$T_{b(2-1)}$ (K) (3)	$T_{b(1-0)}$ (K) (4)	R (5)
2117.2 - 2231.6	nucleus	1.28	1.63	0.86 ± 0.09
2231.6 - 2346.0	nucleus	1.92	1.78	1.22 ± 0.03
	southern extension	1.47	1.67	0.94 ± 0.10
2346.0 - 2450.0	nucleus: CO(1–0) peak	1.57	1.33	0.92 ± 0.18
	nucleus: CO(2–1) peak	1.56	1.60	1.46 ± 0.17
2450.0 - 2564.4	nucleus	1.23	1.56	0.72 ± 0.13
2117.2 - 2564.4	nucleus	1.92	1.80	1.06 ± 0.10

Table 2.3: Local intensity ratios in NGC 7479. Column (1) identifies four LSR velocity windows and the full linewidth over which we measured R, in spatial boxes centered on features which are described in column (2). The remaining columns give (3) the peak CO(1–0) brightness temperature (± 0.19 K), (4) the peak CO(2–1) brightness temperature (± 0.78 K), and (5) the average intensity ratio within the measurement box. The uncertainties in R are the formal dispersions over each box.

absence of high-velocity emission at small radii, for example, is consistent with either high gas density near a low central mass or low gas density near a high central mass. The next sections discuss our strategy for resolving such ambiguities. We review the salient properties of gas motions in a barred galaxy, describe the parameters and general approach of our model for NGC 7479, and present our results.

2.4.1 Orbits in barred potentials

The study of gas dynamics in barred galaxies has a vast literature to its credit, and is closely related to the study of *stellar* dynamics in barred systems (Sellwood & Wilkinson 1993). The most important stellar orbits permitted by a barred potential satisfy three criteria: they are stable, periodic (or nearly so) in a frame which rotates with the bar, and shaped in such a way that stars on the orbits can build up the bar potential itself. Periodicity is especially important: periodic orbits are the parents of the (possibly more numerous) chaotic orbits in a bar, and if nonintersecting are the preferred (i.e., long-lived) orbits for gas clouds. Models suggest the key periodic orbits in barred potentials belong to various "direct" families which revert to circular in the axisymmetric limit, and which tend to appear, disappear, or change their appearances at resonance radii. For an axisymmetric

potential augmented by a nonaxisymmetric perturbation, i.e., $\Phi \sim \Phi_0(r) + \Phi_1(r,\phi)$, the most important resonances are defined in terms of the circular frequency $\Omega(r)$ and epicyclic frequency $\kappa(r)$:

$$\Omega^2(r) = \frac{1}{r}\frac{d\Phi_0}{dr} \tag{2.1}$$

$$\kappa^2(r) = r\frac{d\Omega^2}{dr} + 4\Omega^2 \tag{2.2}$$

For a bar rotating with angular pattern speed Ω_p, the corotation resonance occurs where $\Omega(r) = \Omega_p$, and the inner/outer m:1 Lindblad resonances occur where $m(\Omega(r) - \Omega_p) = \pm\kappa(r)$. The latter resonances become important if the perturbing term Φ_1 includes a term proportional to $\cos(m\phi)$. Realistic barred potentials require a strong $m = 2$ term, giving rise to two preeminent families of orbits. Between corotation and an inner 2:1 Lindblad resonance (should one exist), the x_1 family of orbits (parallel to the bar) dominates. Inside an inner 2:1 Lindblad resonance, the x_2 family of orbits (perpendicular to the bar) dominates, although the existence of such a resonance does not guarantee there exists an x_2 family for all choices of bar potential (Bureau & Athanassoula 1999).

Hydrodynamic models of gas clouds in strongly barred potentials (Athanassoula 1992; Piner et al. 1995) predict that gas clouds will follow stellar orbits to a limited extent. Gas will move radially inward at the leading edge of a bar on orbits in the x_1 family. At an inner 2:1 Lindblad resonance or an analogous "contact point" in the absence of a resonance (Piner et al. 1995), much of the gas will shift onto more confined orbits in the x_2 family. The remainder will continue past the resonance/contact point until it collides in a shock with material on x_1 orbits flowing inward at the bar's opposite leading edge. Twin peaks of molecular gas (Kenney et al. 1992) and straight or curved dust lanes may appear where gas clouds moving in different directions collide. Depending on the orientation of the bar major axis with respect to a galaxy's rotation axis and our line of sight, the two orbit families may appear as distinct features in a position-velocity diagram (Handa et al. 1990; Binney et al. 1991; García-Burillo & Guélin 1995; García-Burillo et al. 1998; Laine et al. 1999; Hüttemeister et al. 1999). Because x_1 and x_2 orbits have perpendicular elongations, they will together define a "tilted X" or "figure of eight" pattern (Kuijken & Merrifield 1995; Athanassoula & Bureau 1999). Mundell & Shone (1999) demonstrate the agreement of this model with observations of H I in the barred galaxy NGC 4151. Regan et al. (1999)

demonstrate that the kinematics of molecular gas in seven barred galaxies also match the predictions of the model– notably large linewidths in dust lanes, which are not generated in most simulations treating gas clouds as ballistic particles.

We argue here that it is possible to describe gas motions in a barred potential without resorting to a full hydrodynamical simulation, simply by modifying the equations for epicyclic stellar motion to include dissipation terms. This approach was originally proposed by Sanders & Huntley (1976); subsequent work by other authors (Lindblad & Lindblad 1994; Wada 1994) demonstrated that the first moment map generated by such an analytical model can agree well with the first moment map predicted by a numerical one. Our observations of NGC 7479 permit an interesting application of the analytical approach, since (a) we can compare the model to an entire data cube, rather than to one of its moments; and (b) we can quantitatively compare our proposed pattern speed Ω_p and mass inflow rate to those deduced from detailed numerical models of the same system (Quillen et al. 1995; Laine et al. 1998). Moreover, if an analytical model successfully describes the gas motions in this strongly barred galaxy, we can confidently apply it to more weakly barred systems in which the "nearly circular" assumption of the epicyclic approximation is better justified.

In Appendix B.1, we build on the results of Sakamoto et al. (1999a) in deriving a fully general description of gas orbits in a barred potential. We model the dissipative behavior of the gas by introducing terms to damp epicyclic oscillations in both radius and azimuth, proportional to the radial and azimuthal velocities and to dissipation rates λ and μ respectively. For stellar orbits, $\lambda = \mu = 0$: the density response is in phase with the perturbing potential, and motions are singular at the corotation and 2:1 Lindblad resonances. For $\{\lambda, \mu\} \neq 0$, the density response either leads or lags the perturbing potential, and only the singularity at the corotation resonance persists. Admittedly, the dependence of radial and azimuthal perturbations on quantities calculated for the axisymmetric part of the potential means our identification of resonance radii is not entirely self-consistent. Resonances in real barred potentials are not restricted to particular radii; instead, epicyclic motions are driven to large amplitudes within extended annuli. Phinney (1994) pictures the width of such an annulus as the range in radius over which particles are trapped in libration in a frame rotating with the bar. For dissipative particles (i.e., gas clouds), a resonance annulus may witness enhanced rates of cloud collision, gas compression, and star formation (Buta & Combes 1996).

2.4.2 Model parameters: the potential

In Appendix B.2, we define a convention for coordinate transformations between sky and galaxy reference frames; within this framework, we we also derive an expression for the line-of-sight velocity as a function of sky position. Six parameters describe the geometry of a barred galaxy in the sky reference frame:

- The sky coordinates of the galaxy's dynamical center, $\hat{x}_0$ and $\hat{y}_0$.
- The systemic velocity of the galaxy, $\hat{v}_0$.
- The galaxy's inclination i, and the position angle of its ascending node α.
- The angle in azimuth ϕ_0 by which the bar's major axis leads the ascending node, as measured in the galaxy plane.

For NGC 7479, we initially assigned values to these parameters based on a fit to the first moment map of the H I line by Laine & Gottesman (1998), who propose $\hat{x}_0 = 23{:}02{:}26.52$ and $\hat{y} = +12{:}03{:}07.9$ (both B1950), $\hat{v}_0 = 2371\,\mathrm{km\,s^{-1}}$ (heliocentric), $i = 51°$, and $\alpha = 22°$. For our convention, $i = 139°$ is in fact the appropriate choice if the spiral arms are trailing, as hydrodynamical models suggest they are (Laine et al. 1998). Laine et al. (1999) estimate that the bar major axis differs from the ascending node by 25° in the plane of the galaxy; in our convention for clockwise circulation on the sky, this means $\phi_0 \simeq 165°$.

In specifying a shape for the potential, we assume that the perturbing term takes the form $\Phi_1(r,\phi) = \Phi_b(r)\cos(2\phi)$. In this case, three parameters can describe both the axisymmetric and the nonaxisymmetric contributions to the potential:

- A characteristic length scale, r_p.
- A characteristic velocity scale, v_p.
- A constant ε to describe the strength of the nonaxisymmetric perturbation.

We adopt here a logarithmic form for the potential, which gives

$$\Phi_0(r) = \frac{1}{2}v_p^2 \ln\left(1 + (r/r_p)^2\right) \tag{2.3}$$

$$\Phi_b(r) = \varepsilon\,\Phi_0(r) \tag{2.4}$$

with $\varepsilon < 0$ to align zero phase along the bar major axis. A potential of this form has been used by Binney et al. (1991) for a qualitative analysis of gas motions in the Galactic center. Although a simple (spherically symmetric) choice for $\Phi_0(r)$ will not accurately describe an entire galaxy, more complicated expressions are not warranted. Our observations do not extend to the typical scale lengths of conventional "bulge" or "disk" (much less "halo") mass components, and thus are even less likely than optical rotation curves to discriminate between specific potentials with broadly similar shapes. The conclusions we can draw from our data are further limited by the fact that we are only probing the motions of gas distributed in a flat, thin disk (see Section 2.4.3). An alternative strategy for obtaining a potential would be the derivation of both Φ_0 and Φ_1 from deep infrared imaging, under the assumption of constant M/L_J or M/L_K. Quillen et al. (1995) apply this technique to NGC 7479; unfortunately, the scale on which they smooth their image makes their derived potential inaccurate within $\sim 8''$ of the nucleus and unsuitable for use here. In general, high extinction and strong point sources imply that surface brightness will not be a secure proxy for stellar mass in the nuclear regions of active galaxies.

Finally, we require three model parameters to describe the characteristic angular velocities in a barred galaxy:

- The pattern speed of the bar, Ω_p. We assume this is independent of radius, although Friedli & Martinet (1993) and Sellwood & Wilkinson (1993) suggest that different features in a galaxy can have different pattern speeds.
- The rate of dissipation of radial oscillations, λ.
- The rate of dissipation of azimuthal oscillations, μ.

Note that these rates all depend inversely on the assumed distance to the source. Our initial guess for Ω_p was $27\,\mathrm{km\,s^{-1}\,kpc^{-1}}$, the value deduced from hydrodynamical simulations by Laine et al. (1998); λ and μ have no obvious counterparts in the numerical results. In total, then, we require $6 + 3 + 3 = 12$ parameters to describe the shape and geometry of a barred galaxy's potential.

2.4.3 Model parameters: the gas distribution

We assume that the molecular gas in NGC 7479 is distributed in an infinitesimally thin disk, thereby eliminating the gas scale height as a model parameter. In practice, the effects

of nonzero thickness cannot be clearly distinguished from those of spatial and velocity convolution. We also have some physical justification for our assumption: molecular gas is extremely dissipative, and unlikely to remain molecular if it undergoes extensive shocking. For these reasons we also adopt a constant line-of-sight velocity dispersion for the gas at all radii, σ_v, instead of specifying increased turbulence near the nucleus like that seen in some ionized gas disks (van der Marel & van den Bosch 1998). We can thus obtain an emissivity distribution whose surface density depends only on radius, as

$$\sigma(r) = \bar{\sigma}_{em} \left[1 + \eta \exp\left(- \frac{r - r_{in}}{r_{gas}} \right) \right] \tag{2.5}$$

over the range $r_{in} \leq r \leq r_{out}$ and zero elsewhere. This radial profile includes two components: one has constant surface density $\bar{\sigma}_{em}$, while the other declines exponentially from a peak of $\eta\,\bar{\sigma}_{em}$ at the inner radius of the disk. The second component allows for the existence of diffuse molecular gas near the nucleus whose excitation temperature and/or areal filling factor are higher than those seen in the rest of the disk. Because the excitation temperatures of the two CO transitions may be different from each other in *either* gas component, we allow $\bar{\sigma}_{em}$ and η to take on different values for the two lines. We also consider the possibility that the effective r_{out} may be different for the two lines. The CO(2–1) emission might appear to terminate at a smaller r_{out} than the CO(1–0) emission, either due to the different primary beams (for which we do not correct here), or because different uv sampling (for the two non-truncated datasets) means the CO(2–1) maps are less sensitive to smooth, extended structure. To describe the gas distribution for either transition singly, then, we require six model parameters: σ_v, r_{gas}, r_{in}, r_{out}, $\bar{\sigma}_{em}$, and η. To describe the gas distribution for both transitions simultaneously, we require nine model parameters: the first three in the above list, plus two each for r_{out}, $\bar{\sigma}_{em}$, and η which are appropriate for the two transitions.

We have constructed our model so that emissivity has natural units of integrated intensity, $\mathrm{K\,km\,s^{-1}}$ (see Section A.4). The CO luminosity from a small projected area in a rotating (r', ϕ') reference frame will now be $\sim \sigma(r')\, r' \Delta r' \Delta\phi'$ in units of $\mathrm{K\,km\,s^{-1}\,pc^2}$. We assign this luminosity to whichever pixel in the data cube shares the area's sky position and line-of-sight velocity. After distributing the emission in this way over the full projected area of the model, we convolve the resulting distribution to the resolutions of our assumed

velocity dispersion and our observed synthesized beam. We are left with the CO luminosity $L'_{\mathrm{CO(pix)}}$ predicted to emerge from each $(\Delta\theta_x, \Delta\theta_y, \Delta v_{ch})$ pixel in the data cube. Since the real data have brightness units of $I_\nu \sim \mathrm{Jy\,bm^{-1}}$, we can test our model after rescaling as follows:

$$\begin{aligned} I_{\nu(\mathrm{pix})} &= L'_{\mathrm{CO(pix)}} \times (d^2 \Delta\theta_x \Delta\theta_y \Delta v_{ch})^{-1} \times 10^{23}\, \frac{2k\Delta\Omega_b}{\lambda^2}\ \mathrm{Jy\,bm^{-1}} \qquad (2.6) \\ &= 4.62 \times 10^{-4} (J+1)^2 \left(\frac{L'_{\mathrm{CO(pix)}}}{\mathrm{K\,km\,s^{-1}\,pc^2}}\right)\left(\frac{d}{\mathrm{Mpc}}\right)^{-2}\left(\frac{\Delta v_{ch}}{\mathrm{km\,s^{-1}}}\right)^{-1}\left(\frac{\Delta\theta_a \Delta\theta_b}{\Delta\theta_x \Delta\theta_y}\right)\mathrm{Jy\,bm^{-1}} \end{aligned}$$

if $\Delta\theta_a$ and $\Delta\theta_b$ are the half-power widths of the synthesized beam and we are considering the CO$(J+1 \rightarrow J)$ transition. We make two final comments regarding our parametrization of $\sigma(r)$. First, our use of integrated intensity units for emissivity has the advantage that the intensity ratio as a function of galactocentric radius is trivially calculated from our model results. Second, a smoothly varying emissivity does not necessarily provide a good description of an intrinsically clumpy medium (see Section 3.5.1); our model thus remains valid only insofar as emission from a population of discrete clouds *does* look smooth when convolved to the resolution of the synthesized beam.

2.4.4 Approach to model fitting

Having specified a model potential and gas distribution for NGC 7479, we must choose some projection or subset of our data as the foundation for intuition and the reference for fitting. Many authors use only the zeroth and first velocity moments of a data cube:

$$M_0(\hat{x}, \hat{y}) = \int S_\nu(\hat{x}, \hat{y}, \hat{v}_z)\, d\hat{v}_z \qquad (2.7)$$

$$M_1(\hat{x}, \hat{y}) = \int \hat{v}_z S_\nu(\hat{x}, \hat{y}, \hat{v}_z)\, d\hat{v}_z \qquad (2.8)$$

with the latter conventionally normalized to the former. Unfortunately, M_0 maps can (at certain inclinations) be similar for many different gas structures, not all of which can be distinguished on the basis of their M_1 maps alone. While a well-ordered velocity field (with parallel isophotal and kinematic major axes) may indicate that gas orbits are circular and coplanar, twisted isovelocity contours do not by themselves distinguish between gas on noncircular orbits, gas on noncoplanar orbits, and gas flowing radially inward or outward.

Moreover, the M_1 map hides valuable information about the potential even when gas motions are regular: a spatial pixel whose spectrum peaks at velocities v_1 and v_2 will take the same value of M_1 as it would for a single peak at velocity $(v_1 + v_2)/2$ produced by a quite different potential. As an alternative to using the velocity moments of a data cube for modelling, we might consider using one or more position-velocity cuts *through* the cube. In this case, however, choosing the orientation and spatial center for a cut involves implicit assumptions about a galaxy's dynamical center and kinematic major axis which may not be well-founded. To avoid such biases, we fit our model for NGC 7479 to the full, three-dimensional data cube which (on the sky and in velocity) includes all molecular emission in the vicinity of the nucleus.

To obtain the maximum likelihood estimates of the model parameters, we must minimize the chi-square statistic

$$\chi^2 = \sum_{i,j,k} \left(\frac{D(\hat{x}_i, \hat{y}_j, \hat{v}_k) - M(\hat{x}_i, \hat{y}_j, \hat{v}_k)}{\sigma_{ijk}} \right)^2 \tag{2.9}$$

where $\hat{v}_k$ is the line-of-sight velocity in the kth velocity channel and we sum over every pixel with a value $\geq +1\sigma_{ch}$ in either the data (D) or the model (M) cube. To find a global minimum in χ^2 using a downhill simplex algorithm (Press et al. 1992), we must be able to differentiate χ^2 with respect to each of the model parameters. An analytical approach is nearly impossible given the form of $M_{ijk} = M(\hat{x}_i, \hat{y}_j, \hat{v}_k)$: using Gaussians $\hat{B}(\Delta\hat{x}, \Delta\hat{y})$ to denote the synthesized beam and $\hat{G}_v(\Delta\hat{v})$ to represent a velocity dispersion of σ_v, we write

$$M_{ijk} = \int\int d\hat{x}\, d\hat{y}\, \hat{B}(\hat{x} - \hat{x}_i, \hat{y} - \hat{y}_j) \int d\hat{v}_r\, \hat{G}_v(\hat{v}_r - \hat{v}_k)\, \delta\Big(\hat{v}_r - \hat{v}_0 + \hat{v}_z(\hat{x}, \hat{y})\Big)\, \sigma(\hat{x}, \hat{y}) \tag{2.10}$$

Since $\hat{v}_z$ and $\bar{\sigma}_{gas}$ depend on $(\hat{x}, \hat{y})$ through functions $r(\hat{x}, \hat{y})$ and $\phi(\hat{x}, \hat{y})$ in the *galaxy's* reference frame, we cannot write down derivatives for most of the model parameters unless we can uniquely deproject the sky coordinates $(\hat{x}, \hat{y})$ into the galaxy. Such deprojection is impossible for our description of orbits in a barred potential (see Appendix B.2), so we search for a χ^2 minimum indirectly by calculating the statistic over a grid of reasonable parameter values.

We estimate the goodness of a fit for any particular model from the reduced chi-square

$$\chi^2_\nu = \frac{\chi^2}{\nu} = \frac{\chi^2}{n_d - n_p} \tag{2.11}$$

where n_p is the number of model parameters (18 for either transition singly, 21 for both transitions simultaneously) and n_d is the number of independent data points. Note that n_d is *not* the number of pixels $n_x\, n_y\, n_v$ in the data cube being fitted: for pixel dimensions $\Delta\theta_x$ and $\Delta\theta_y$ and synthesized beam half-power widths $\Delta\theta_a$ and $\Delta\theta_b$, we have

$$n_d = \frac{4 \ln 2}{\pi} \frac{\Delta\theta_x \Delta\theta_y}{\Delta\theta_a \Delta\theta_b} n_x\, n_y\, n_v \tag{2.12}$$

If $\chi^2_\nu > 1$, we have a poor fit or have underestimated the uncertainty σ_{ijk} associated with each data point. Our *a priori* estimate of the latter is simply $\sigma_{ijk} = \sigma_{ch}$ (the per-channel rms noise); however, our actual uncertainties are likely to be much higher because real galaxies do not have precisely axisymmetric gas distributions.

2.4.5 Model results

We have applied our modelling technique to the CO(1–0) data alone, to the CO(2–1) data alone, and to both datasets simultaneously; our results for all three fits are listed in Table 2.4. The simultaneous minimization of χ^2_ν for both datasets in Model 3 does degrade the statistic for either dataset separately, to 315.9 for CO(1–0) (vs. 264.5 for Model 1) and to 74.6 for CO(2–1) (vs. 70.1 for Model 2). Model 3 is generally closer to Model 2 than to Model 1, due to the higher signal-to-noise ratio and larger number of independent data points in the CO(2–1) data. Judging from the agreement between the models, we seem to have determined many parameter values to good precision– notably the coordinates of the dynamical center $(\hat{x}_0, \hat{y}_0)$, systemic velocity $\hat{v}_0$, inclination i, length and velocity scales for the potential r_p and v_p, and pattern speed Ω_p. The sensitivity of our model results to parameter changes smaller than our synthesized beamwidths reflects our high velocity resolution (effectively $\sigma_v > \Delta v_{ch}$) in conjunction with a steeply rising rotation curve. Of the remaining parameters, λ and μ can have such similar effects on a model (see Figure B.1 for an illustration) that they are not easily distinguished, while r_{gas} is only constrained by the CO(2–1) data since the CO(1–0) emission requires no centrally peaked emissivity

Parameter	Units	Model 1	Model 2	Model 3
(1)	(2)	(3)	(4)	(5)
$\hat{x}_0$	RA (B1950)	23:02:26.36	23:02:26.37	23:02:26.37
$\hat{y}_0$	Dec (B1950)	+12:03:10.6	+12:03:10.7	+12:03:10.6
$\hat{v}_0$	$\mathrm{km\,s^{-1}}$ [LSR]	2344	2336	2336
i	$^\circ$	151	151	151
α	$^\circ$	28	21	27
ϕ_0	$^\circ$	176	164	170
r_p	pc	69	67	67
v_p	$\mathrm{km\,s^{-1}}$	298	298	298
ε	-	-0.074	-0.049	-0.058
Ω_p	$\mathrm{km\,s^{-1}\,pc^{-1}}$	0.26	0.28	0.29
λ	$\mathrm{km\,s^{-1}\,pc^{-1}}$	0.07	0.12	0.09
μ	$\mathrm{km\,s^{-1}\,pc^{-1}}$	0.06	0.02	0.05
σ_v	$\mathrm{km\,s^{-1}}$	37	72	68
r_{gas}	pc	-	5	4
r_{in}	pc	100	19	19
$r_{out(1-0)}$	pc	405	-	350
$\bar{\sigma}_{em(1-0)}$	$\mathrm{K\,km\,s^{-1}}$	888	-	988
$\eta_{(1-0)}$	-	0	-	0
$r_{out(2-1)}$	pc	-	356	350
$\bar{\sigma}_{em(2-1)}$	$\mathrm{K\,km\,s^{-1}}$	-	977	945
$\eta_{(2-1)}$	-	-	2	11
χ^2_ν	-	264.5	70.1	123.9

Table 2.4: Kinematic model results for NGC 7479. The columns are (1) parameter (2) units (3)–(5) values for best-fit models. M1 = bar model for CO(1–0), M2 = bar model for CO(2–1), M3 = bar model for CO(1–0) and CO(2–1).

component. We suspect that the relative amplitude of the bar perturbation (ε) is inferred to be larger in Model 1 than in Model 2 because CO(1–0) emission extends farther from the nucleus ($r_{out(1-0)} \geq r_{out(2-1)}$) towards the corotation resonance, where the bar's effects on gas motions are especially strong. One important pair of parameters, α and ϕ_0, specify the position angle α_B of the stellar bar on the sky according to

$$\alpha_B = \alpha + \mathrm{Arctan}\,(\tan\phi_0 \cos i) \tag{2.13}$$

From Models 1, 2, and 3, we thus predict that the stellar bar should appear at position angles 31.5°, 35.1°, and 35.8° east of north– values in better agreement with each other

Feature	Right ascension (B1950)	Declination (B1950)
(1)	(2)	(3)
OVRO pointing center	23:02:26.40	+12:03:10.6
20 cm continuum peak	23:02:26.37	+12:03:10.7
Peak CO(1–0) intensity	23:02:26.38	+12:03:10.6
Peak CO(2–1) intensity	23:02:26.40	+12:03:10.2
Dynamical center (Model 1)	23:02:26.36	+12:03:10.6
Dynamical center (Model 2)	23:02:26.37	+12:03:10.7
Dynamical center (Model 3)	23:02:26.37	+12:03:10.6

Table 2.5: Coordinates of features in the nucleus of NGC 7479. The 20 cm continuum position is from 1.5″-resolution VLA observations by Condon et al. (1990). The dynamical center positions are those predicted by the models described in Table 2.4.

than we obtain for ϕ_0 and α separately.

The parameters our models constrain most poorly are the inner radius of the gas disk (r_{in}) and the velocity dispersion of the gas (σ_v). We suspect that the inconsistencies here are related to each other, and that they stem from our description of the second emissivity component as an [unrealistically peaked] exponential. If the molecular gas in the nucleus actually has a top-hat profile in CO(2–1) emissivity and an inverted top-hat profile in CO(1–0) emissivity, then we would *expect* our parametrization of $\sigma(r)$ to lead to (a) a large r_{in} and small $\bar{\sigma}_{em(1-0)}$ in Model 1, so as to suppress CO(1–0) emission from the nucleus; (b) a small velocity dispersion in Model 1, so as to normalize the small $\bar{\sigma}_{em(1-0)}$ correctly; and (c) a suspiciously high intensity ratio R at the inner edge of the disk in Model 3. Effects (a) and (b) are precisely those seen in Table 2.4; we will return to effect (c) shortly.

For the remainder of this chapter, we will largely confine our discussion to the parameter estimates of Model 3. In Figures 2.4 through 2.6, we plot the CO(2–1) emission predicted by this model over the emission observed in each velocity channel. Since the corresponding channel maps for the CO(1–0) transition have higher noise and lower resolution, they are not sufficiently informative for us to show them here. Figures 2.7 through 2.9 show position-velocity cuts through the CO(2–1) data and model cubes at the position angles of the kinematic major axis (i.e., the line of nodes), the kinematic minor axis, and the bar major axis. Figure 2.10 shows equivalent zeroth moments of the CO(2–1) line in the data and

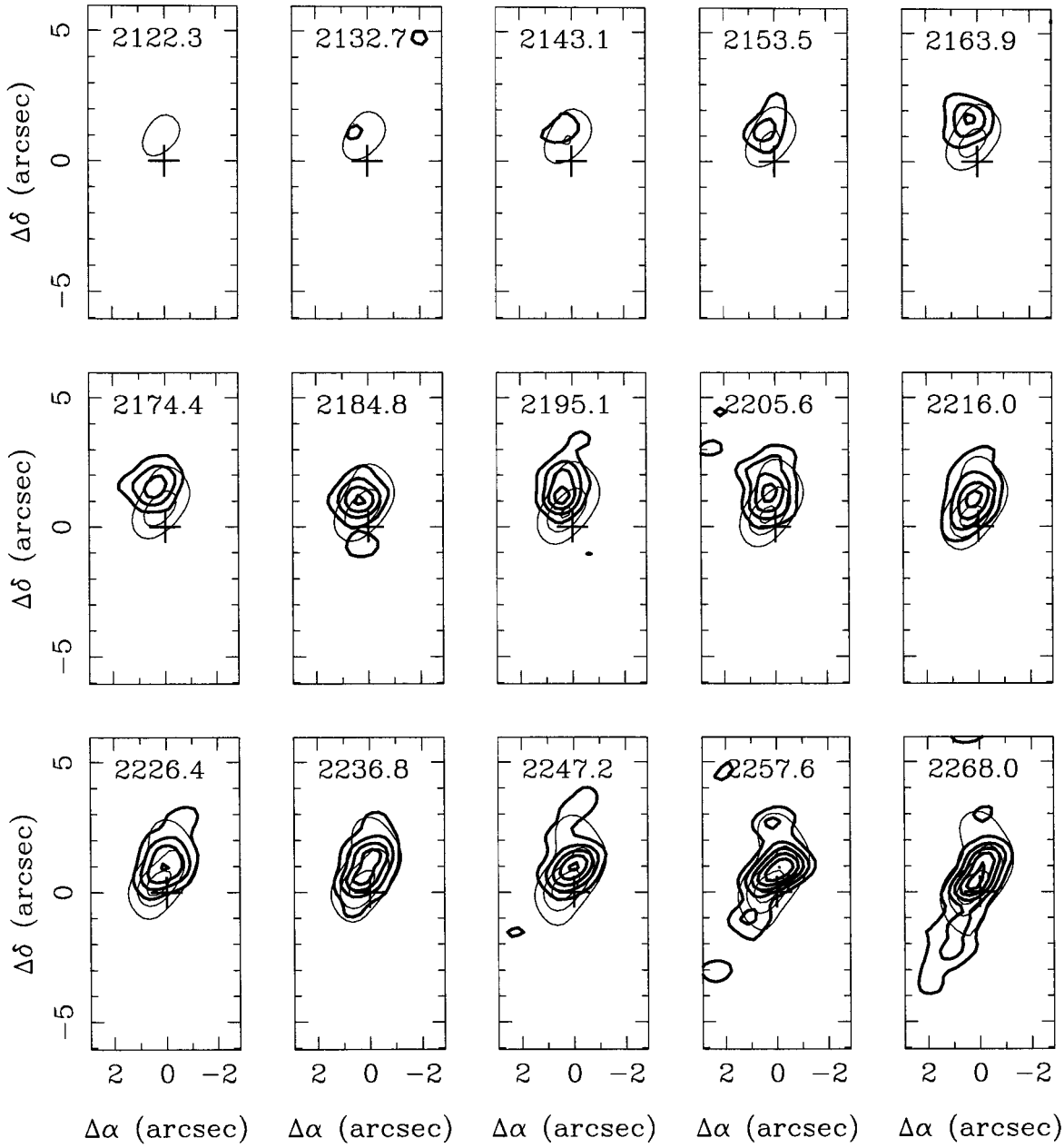

Figure 2.4: Blueshifted CO(2–1) velocity channels in NGC 7479. Light model contours are plotted over dark data contours; both are multiples of 92 mJy bm^{-1}. Spatial offsets are relative to the dynamical center of Model 3, which is also marked with a cross. Channel velocities are labelled in km s^{-1}.

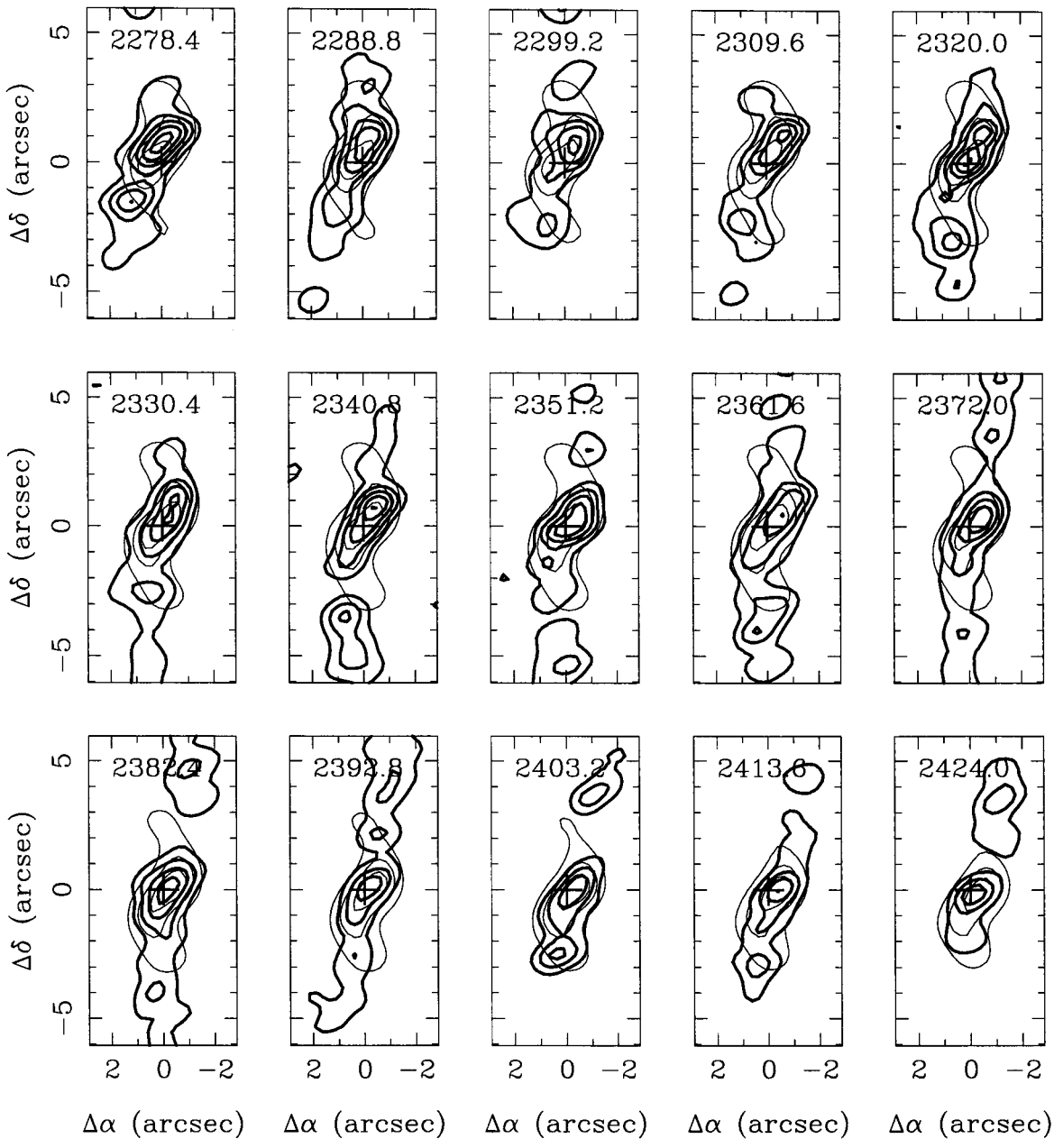

Figure 2.5: Systemic CO(2–1) velocity channels in NGC 7479. Notation is as in Figure 2.4.

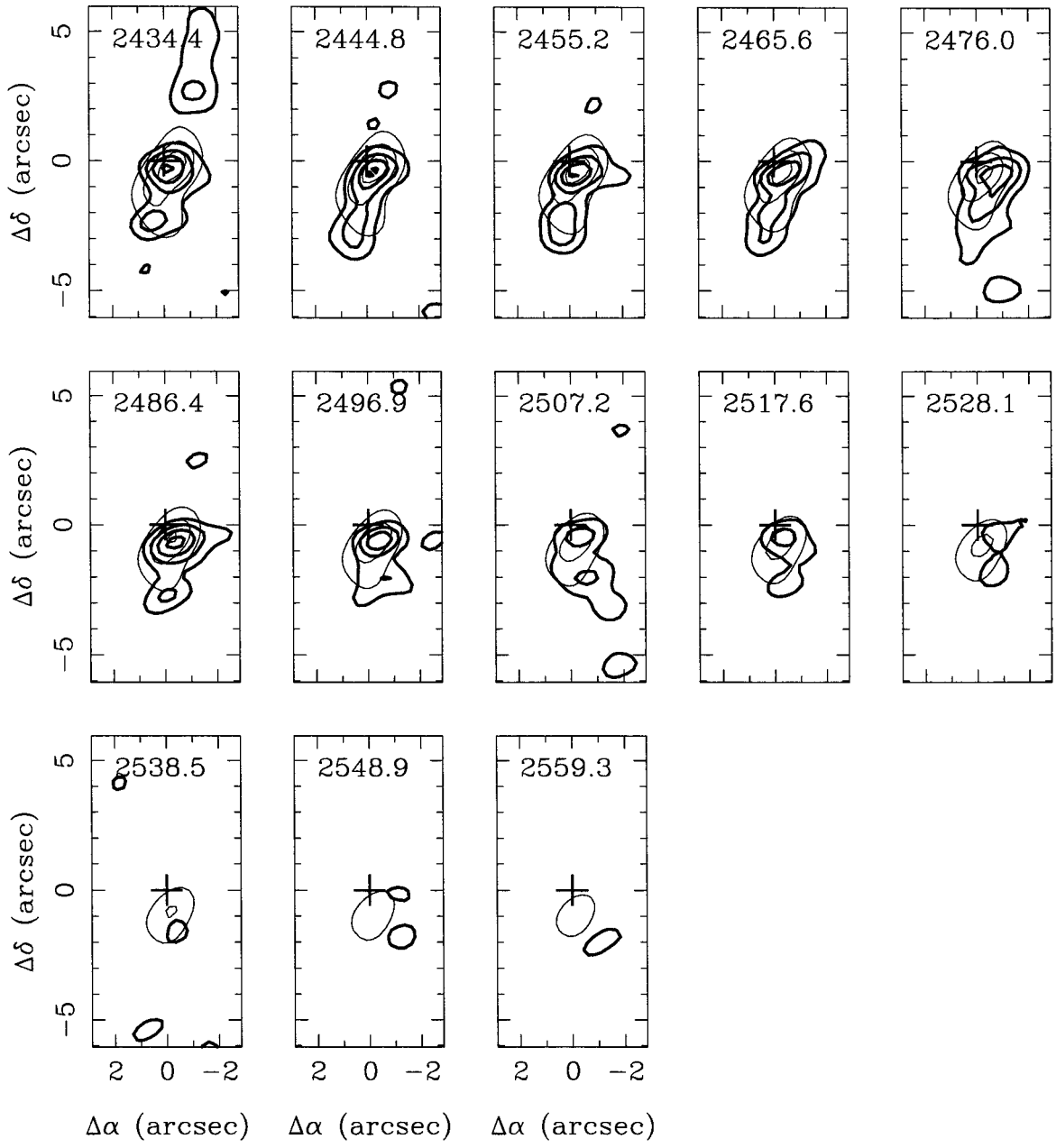

Figure 2.6: Redshifted CO(2–1) velocity channels in NGC 7479. Notation is as in Figure 2.4.

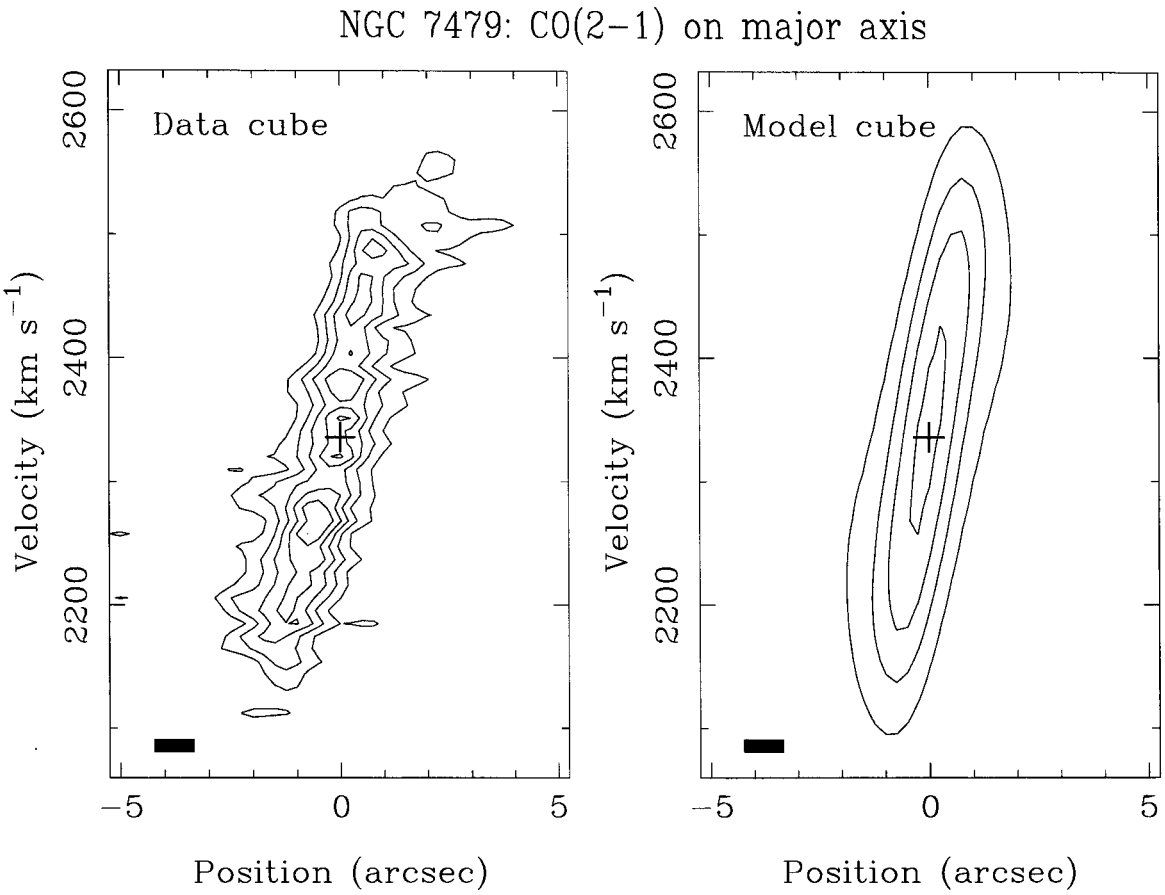

Figure 2.7: Major-axis position-velocity diagram for the CO(2–1) line in NGC 7479. A 1″-wide cut was taken along the kinematic major axis (at 27° east of north). The cross marks the galaxy's spatial and velocity center; offsets along the spatial scale are relative to this position. The rectangle indicates the spatial and velocity resolutions. Contours are multiples of 57 mJy bm^{-1}.

model cubes. The agreement of our model with the data is generally quite good. In each of the velocity channel maps, we successfully reproduce not only the emission from the strongest central peak, but also much of the structure extending to the north and/or south. The presence of a slight velocity gradient along the kinematic minor axis (see Figure 2.8) and the hints of two velocity components along the bar major axis (see Figure 2.9) also match the predictions of our model. The zeroth moment maps of Figure 2.10 do indicate that our model does not give a proper description– or at sufficiently large radii, *any* description, since r_{out} is too small– of the emission outside the innermost ±2.5″. The analytical description of motion in a bar potential we describe in Section 2.4.2 probably fails on these scales because

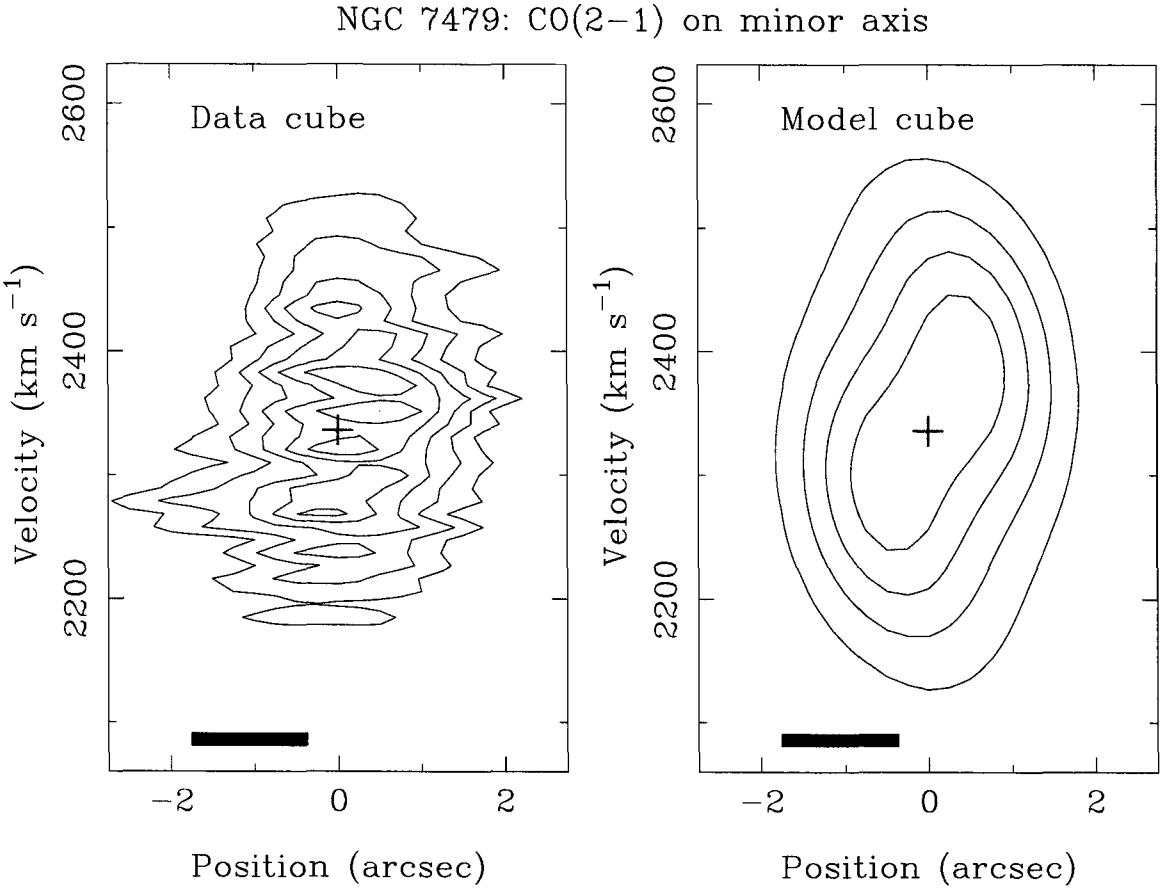

Figure 2.8: Minor-axis position-velocity diagram for the CO(2–1) line in NGC 7479. Notation is as for Figure 2.7, but the cut has been taken at 117° east of north.

the gas kinematics here are affected by mechanisms (e.g., self-gravity and shock focusing) which require a full hydrodynamical treatment.

One implication of our model is evident from Table 2.5: the position of the dynamical center we infer agrees almost perfectly with the position of the radio continuum peak, and in fact slightly better than it does with the position of the CO(2–1) intensity peak. We conclude that while the molecular emission may be asymmetrically distributed with respect to the active nucleus, the overall mass distribution is not. Since our model emissivity distribution (in particular, our inclusion of a centrally peaked component) would tend to bias our "dynamical center" towards the gas peak, we believe our conclusion is robust.

To illustrate further implications of our kinematic model, we show in Figure 2.11 the radial variation of various quantities calculated from our derived parameters. The top

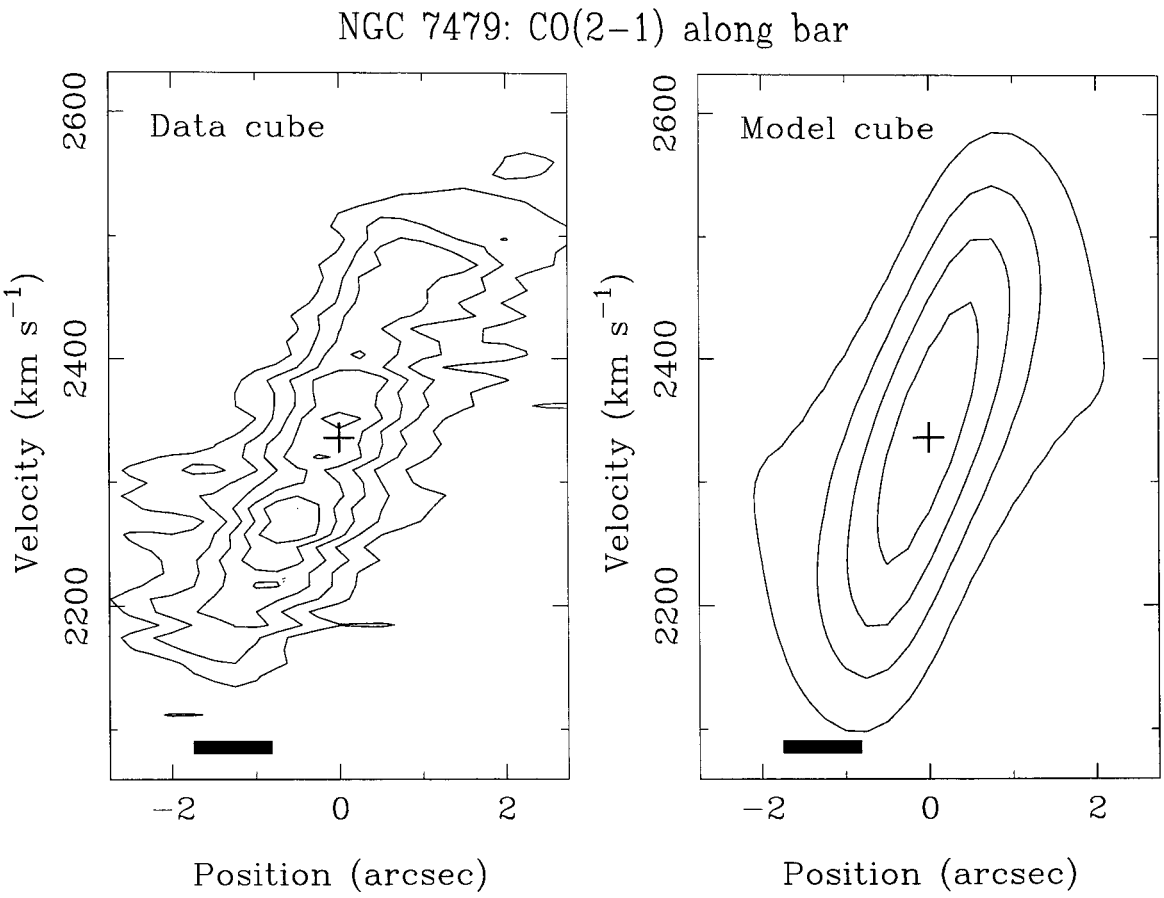

Figure 2.9: Bar-axis position-velocity diagram for the CO(2–1) line in NGC 7479. Notation is as for Figure 2.7, but the cut here has spatial width 3″ and lies along the position angle of the bar (35.8° east of north) inferred from Model 3 using Equation 2.13.

left panel shows the mass surface densities due to the logarithmic potential Φ_0 (spherical shells are here projected into planar annuli) and to the molecular gas itself, assuming a Galactic conversion factor $X = 3 \times 10^{20}\,\mathrm{cm^{-2}\,(K\,km\,s^{-1})^{-1}}$. Our decision not to include M_{gas} explicitly in our budget for enclosed mass is justified *post facto* by the fact that $M_{gas} \leq M_{dyn}$ at all radii. However, the apparent rise of the gas mass fraction to $\sim 66\%$ at $r_{out} = 350\,\mathrm{pc}$ is probably not real: NGC 7479 certainly includes additional stellar mass components with scale lengths $\gg r_p$. The top right panel of Figure 2.11 confirms this point. While the circular velocity curve generated by our potential will flatten at $v_p \sin i \simeq 144\,\mathrm{km\,s^{-1}}$, the H I rotation curve derived by Laine & Gottesman (1998) flattens at $v \sin i \simeq 170\,\mathrm{km\,s^{-1}}$ outside 90″ ($\sim 14.1\,\mathrm{kpc}$). We are not overly concerned by the discrepancy between the latter authors' estimate of $i \simeq 139°$ and our model's estimate of $i \simeq 151°$, particularly since

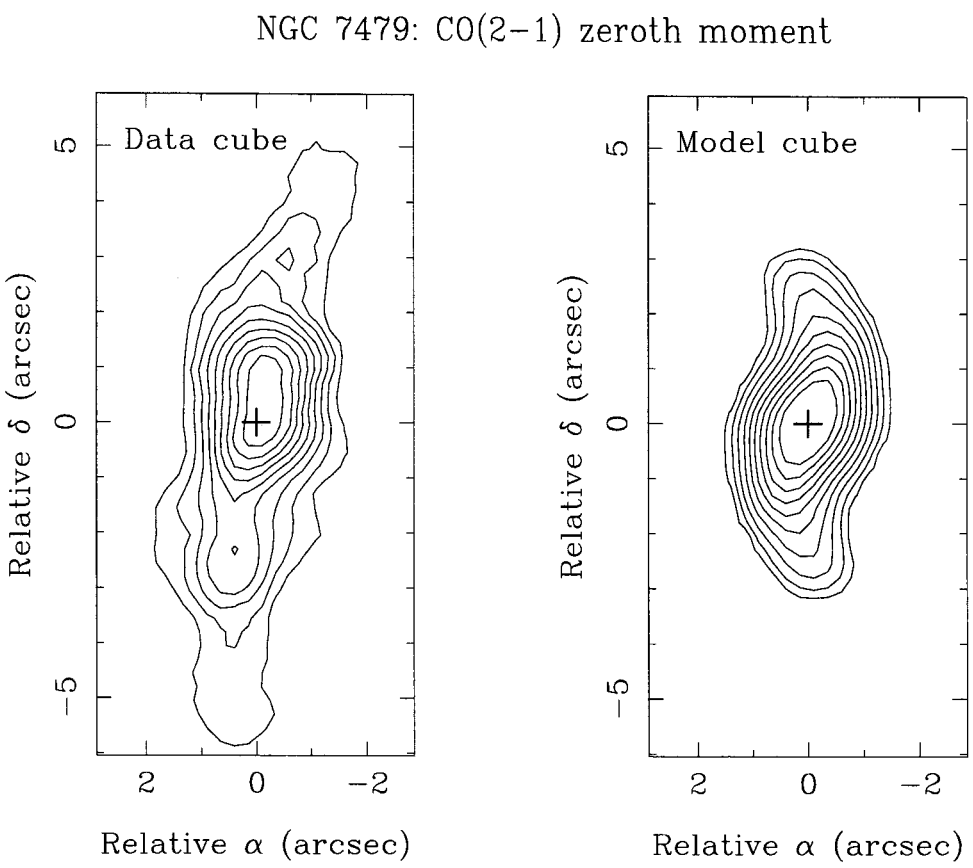

Figure 2.10: Zeroth moment map for the CO(2–1) line in NGC 7479. Both data and model cubes have been blanked at $+2\,\sigma_{ch}$; contours are multiples of $8.0\,\mathrm{Jy\,bm^{-1}\,km\,s^{-1}}$. Spatial offsets are relative to the dynamical center of Model 3, which is also marked with a cross.

the H I rotation curve is only derived at radii outside 40″.

The bottom left panel of Figure 2.11 illustrates the different emissivity variations of the two CO transitions: while we infer the CO(1–0) emission in NGC 7479 to have constant surface density, the CO(2–1) emission rises to a peak in the nucleus. We can use these dependences to infer the radial variation of the intensity ratio R, plotted in the bottom right panel of Figure 2.11. At the outer edge of the molecular disk, R will approach $\bar{\sigma}_{em(2-1)}/\bar{\sigma}_{em(1-0)} = 0.96$, a value consistent with optically thick emission from gas in LTE (see Section 3.5). In contrast, at r_{in} our model predicts

$$R_{max} = \frac{\bar{\sigma}_{em(2-1)}}{\bar{\sigma}_{em(1-0)}} \times \frac{1+\eta_{(2-1)}}{1+\eta_{(1-0)}} = 11.5 \tag{2.14}$$

Since $R > 4.0$ cannot be generated by a single zone of gas in LTE, we suspect (as discussed

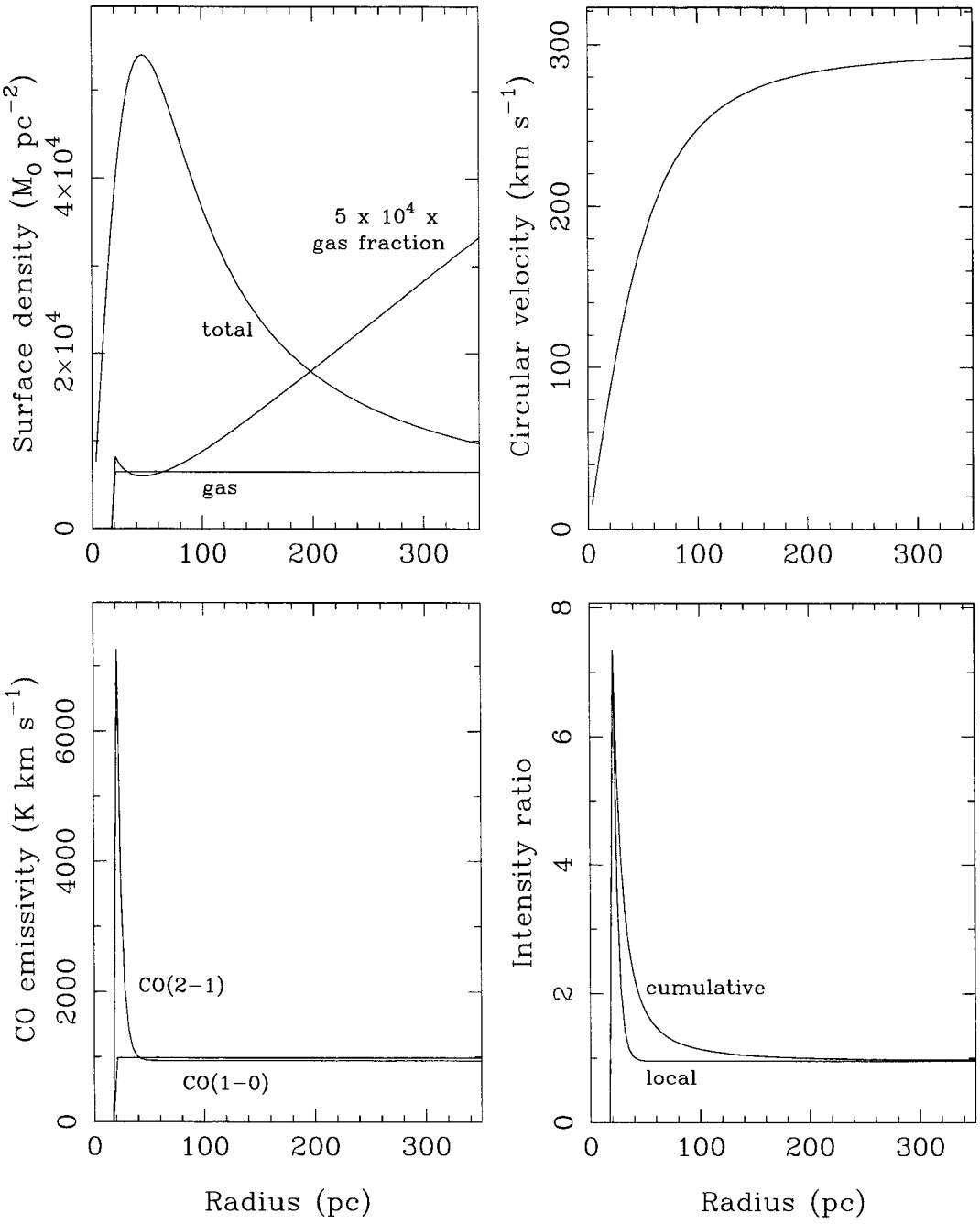

Figure 2.11: Radial plots from the kinematic model of NGC 7479. Top left: axisymmetric surface densities of gas and total dynamical mass, projected into the disk. The gas mass fraction is also plotted. Top right: circular velocity. Bottom left: emissivities of the two CO lines. The CO(1–0) emissivity corresponds to the constant surface density of 6460 $M_\odot$ pc^{-2} plotted at top left. Bottom right: intensity ratio. The lower curve is the [local] ratio of emissivities at each radius. Because the sharpness of the central peak likely results from our choice of parametrization, we have also plotted the [cumulative] ratio of enclosed CO luminosities at each radius, as a less model-dependent estimator of R.

above) that the high value of R_{max} we infer is partly an artifact of our parametrization of $\sigma(r)$. Our suspicion is amplified by the fact that Model 2 (fit to the CO(2–1) line only) selects a much lower value of $\eta_{(2-1)}$ than Model 3 (2 vs. 11). For a more robust estimate of R in the nucleus of NGC 7479, we have therefore calculated the ratio of CO *luminosities* predicted by our model. For

$$\begin{aligned} L'_{\rm CO} &= \int_0^{2\pi}\int_{r_1}^{r_2} \sigma(r)\; r\, dr\, d\phi \\ &= \bar{\sigma}_{em}\left[\pi r^2 - 2\pi\eta\, r_{gas}\,(r + r_{gas})\exp\Big(-\frac{r - r_{in}}{r_{gas}}\Big)\right]_{r_1}^{r_2} \end{aligned} \tag{2.15}$$

integrated from $r_1 = r_{in}$ to $r_2 = 100\,$pc, we derive $R \simeq 1.14$. In Section 3.5.3, we will find that intensity ratios in this range can be produced by optically thick emission from externally heated molecular clouds. Since an optically thick CO(1–0) line is a requirement if we are to relate $I_{\rm CO}$ to $N_{\rm H_2}$ using the Galactic conversion factor (see Section 3.5.1), we are satisfied that the estimates of molecular gas masses which we make throughout this chapter are reasonable.

2.5 Discussion

2.5.1 Physical conditions in the molecular gas

For NGC 7479, we have measured a mean value ($R = 1.06$) of the intensity ratio from the truncated datasets, as well as estimated values from our model of the full datasets which are representative of conditions at large ($R = 0.96$) and small ($R = 1.14$) galactocentric radius. We can now use these values to characterize the physical conditions in the molecular gas; we will only present highlights here, deferring a detailed justification of our argument to Section 3.5. We begin by estimating the kinetic temperature for the gas. IRAS flux densities give a global $60/100\,\mu$m color temperature for NGC 7479 of 38 K (Soifer et al. 1989). For the Planck-averaged grain emissivity of Draine & Lee (1984), this temperature implies a global dust mass of $M_{dust} \simeq 2.3 \times 10^6\,{\rm M}_\odot$– well below what we would expect for our global $M_{gas} = 3.7 \times 10^9\,{\rm M}_\odot$ (see Section 2.3.1) and a canonical gas-to-dust ratio of 100. We explain this inconsistency by positing the existence of a substantial dust mass at $T_d < 38\,$K; this leads us to adopt $T_{kin} \simeq 20\,$K for the molecular gas as well. A standard radiative transfer model for gas at this temperature (Goldsmith et al. 1983) allows us to convert our intensity

R	$\tau_{v(1-0)}$	$\tau_{v(2-1)}$
(1)	(2)	(3)
0.96	2.68	7.14
1.06	1.81	4.84
1.14	1.46	3.91

Table 2.6: CO optical depths in NGC 7479, calculated assuming (a) LTE at $T_{kin} = 20\,\mathrm{K}$; (b) constant dv/ds; and (c) a negligible rate of photon trapping. Columns are (1) measured or estimated intensity ratio (2) CO(1–0) optical depth, and (3) CO(2–1) optical depth.

ratios to lower limits on the gas number density: $R = 0.96$ implies $n_{\mathrm{H_2}} \geq 2820\,\mathrm{cm^{-3}}$, $R = 1.06$ implies $n_{\mathrm{H_2}} \geq 3470\,\mathrm{cm^{-3}}$, and $R = 1.14$ implies $n_{\mathrm{H_2}} \geq 3980\,\mathrm{cm^{-3}}$. By comparison, the critical densities of the two CO transitions at $T_{kin} = 20\,\mathrm{K}$ are $n_{crit(1-0)} \simeq 1850\,\mathrm{cm^{-3}}$ and $n_{crit(2-1)} \simeq 7090\,\mathrm{cm^{-3}}$. We can conclude that the CO(1–0) emission in NGC 7479 will be collisionally thermalized (i.e., satisfy $T_{ex(1-0)} = T_{kin}$) everywhere, but that the CO(2–1) excitation temperature may require some degree of photon trapping to reach T_{kin}.

Our confidence that the CO(1–0) line is thermalized allows us to constrain the optical depth and filling factor of the emission we detect. Using Equation 3.13 and our model parameters, we calculate the brightness temperature at the peak of the velocity profile to be 5.8 K. For our assumed $T_{kin} = 20\,\mathrm{K}$, this result requires that the areal filling factor at line center be $f_a(v) \geq 0.35$, and that the optical depth at line center be $\tau_v \geq 0.43$. We can proceed further if we momentarily assume that the CO(2–1) transition is also thermalized. In this case, if we make the additional assumptions that line profiles are flat (i.e., dv/ds is constant) and that radiative trapping is negligible, we can uniquely map the combination (R, T_{kin}) to the optical depths of both CO lines (see Figure 3.11). Table 2.6 lists the results of our calculations. Photon trapping in CO(2–1) lines of these optical depths will be sufficient to thermalize the transition (see Equation 3.31), consistent with our assumption of LTE above; however, our reliance on an NLTE mechanism to ensure that $T_{ex(2-1)} = T_{kin}$ implies that the subsequent LTE analysis of the intensity ratio is not entirely self-consistent.

2.5.2 Evidence for a secondary bar

We have already noted in Section 2.4.5 that the bar pattern speed ($\Omega_p \simeq 0.29\,\mathrm{km\,s^{-1}\,pc^{-1}}$) is a parameter whose value is remarkably consistent in all our kinematic models. Somewhat

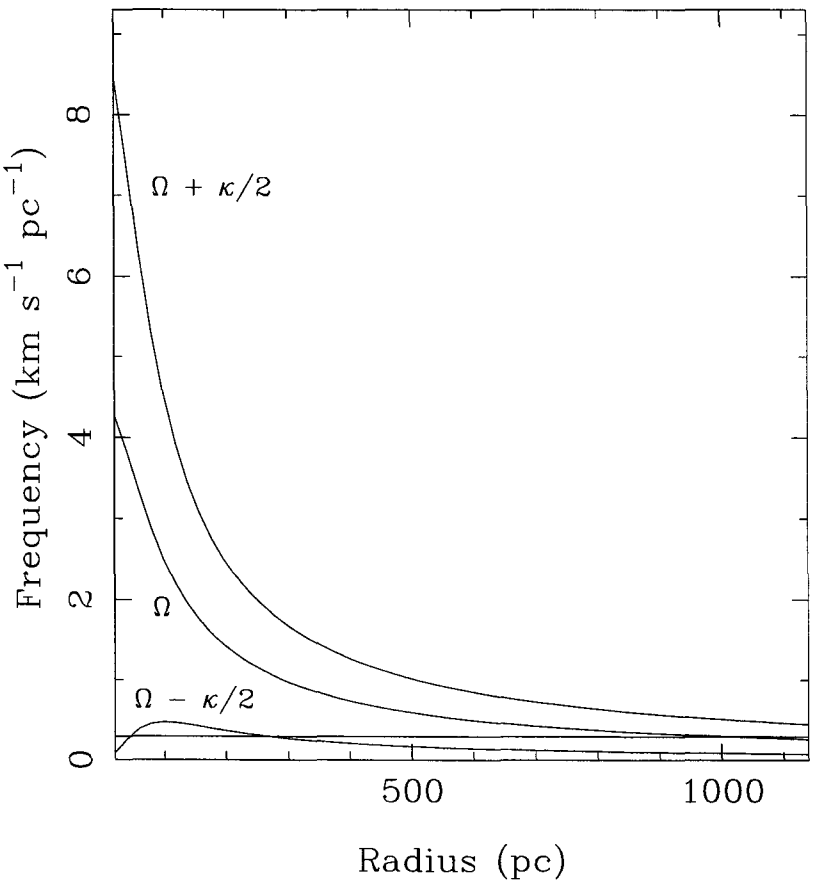

Figure 2.12: Angular frequencies in NGC 7479. We plot the runs of $\Omega(r)$ and $\Omega(r) \pm \kappa(r)/2$ which are determined by $v_p = 298\,\mathrm{km\,s^{-1}}$ and $r_p = 67\,\mathrm{pc}$ (i.e., by our Model 3). The horizontal line is drawn at $\Omega_p = 0.29\,\mathrm{km\,s^{-1}\,pc^{-1}}$. Inner 2:1 Lindblad resonances fall at 43 pc and 272 pc, while corotation occurs at 1.02 kpc; the outer 2:1 Lindblad resonance lies outside the plot at 1.75 kpc. Note that our frequency units of $\mathrm{km\,s^{-1}\,pc^{-1}} \simeq \mathrm{Myr^{-1}}$.

surprisingly, our Ω_p is completely *inconsistent* with the large-scale pattern speeds of 30 and $27\,\mathrm{km\,s^{-1}\,kpc^{-1}}$ (i.e., 0.030 and $0.027\,\mathrm{km\,s^{-1}\,pc^{-1}}$) deduced for NGC 7479 from hydrodynamical simulations (Sempere et al. 1995; Laine et al. 1998). This order-of-magnitude discrepancy is rather large to be due to an error in our analytical (or their numerical) modelling. In Figure 2.12, we plot the key angular frequencies derived from the axisymmetric term of our adopted potential, along with our estimate of Ω_p. Molecular gas in our model is largely confined to the range of radii $19\,\mathrm{pc} \leq r \leq 350\,\mathrm{pc}$, most of which also lies between the two inner 2:1 Lindblad resonances ($43\,\mathrm{pc} \leq r \leq 272\,\mathrm{pc}$). The [continuously] changing orientations of gas orbits near these resonances are precisely what allows our model to match the observed kinematics. Figure 2.12 tells us that if we were to lower our model's pattern

speed by an order of magnitude, *all* of the molecular emission would lie well inside the outer inner 2:1 Lindblad resonance, and we would expect less dramatic signatures of noncircular motions in our data.

We conclude that the discrepancy in pattern speeds on large and small scales is real, and that our model has identified an inner, secondary bar which is rotating ten times faster than the outer, primary bar. No existing observational results are inconsistent with this proposal. The hydrodynamical models of Sempere et al. (1995) and Laine et al. (1998) assume potentials which are generated from R and K-band images of NGC 7479, respectively. Nonstellar emission from the nucleus and the need to smooth the image before deriving Φ_R or Φ_K conspire against an accurate determination of the potential on the scales our CO observations trace; Laine et al. (1998) explicitly warn against trusting their potential within $8''$ of the nucleus. Prior nondetection of a secondary bar thus would not be surprising. The K-band-derived potential does locate an (outer) inner 2:1 Lindblad resonance at $\sim 800 - 900$ pc; given the uncertainties of their potential and our mass profile at these scales, we consider the inner 2:1 Lindblad resonance of the primary bar to be essentially coincident with the corotation resonance of the secondary bar at $r_{CR} \simeq 1.02$ kpc. Since the semimajor axis a of the secondary bar must be at least as large as the radius to which our model fits molecular gas motions, we derive an upper limit on the ratio r_{CR}/a of 2.9– easily consistent with the implication of hydrodynamical models that $r_{CR}/a \simeq 1.2$ (Athanassoula 1992).

Studies of other multiply-barred galaxies are also consistent with the secondary bar we propose for NGC 7479. Friedli & Martinet (1993) review observations of doubly-barred galaxies and find no preferred value for the relative orientation of the primary and secondary bar ($\Delta\alpha$), even after accounting for inclination. Erwin & Sparke (1999) find similar misalignments in three triply-barred systems. Since stellar orbits on opposite sides of a resonance in a [singly] barred galaxy (e.g., from the x_1 and x_2 families) will always have perpendicular elongations, the prevalence of $\Delta\alpha \neq 90^\circ$ suggests that most primary and secondary bars are dynamically decoupled. Numerical descriptions of periodic stellar orbits (Maciejewski & Sparke 1997, 1999) and N-body/SPH simulations of stellar and gas motions (Friedli & Martinet 1993; Combes 1994) indicate that the most likely configuration features a secondary bar which rotates in the same direction but faster than the primary bar. Such an arrangement is more likely to be stable against chaotic behavior if the corotation reso-

nance of the secondary bar coincides with an inner 2:1 Lindblad resonance of the primary bar– an alignment which proves generally useful in models of AGN fuelling (Shlosman et al. 1989; Heller & Shlosman 1994). In NGC 7479, we predict an $\alpha_B \simeq 35.8°$ which differs from the position angle of the [stellar] primary bar in NGC 7479, i.e., 41° (Laine et al. 1999), by 15° in the plane of the galaxy. We also see the higher secondary pattern speed and (roughly) the coincidence of resonances predicted by theory.

A few caveats concerning the putative secondary bar are in order at this point. First, we might expect the presence of a large central mass in NGC 7479 to destroy its secondary (if not also its primary) bar. While we can certainly avoid this fate if the core mass does not exceed $\sim 5\%$ of the total mass of disk and bulge (Norman et al. 1996), a more appealing explanation for both bars' stability is the likelihood of ongoing tidal torques by the remnant of a recently absorbed satellite galaxy (Laine & Heller 1999). Second, the ratio of bar pattern speeds in NGC 7479 substantially exceeds the values of 2-3 which emerge from more general models (Combes 1994; Maciejewski & Sparke 1999). Since ours is only the first observational test of these models, however, we set this objection aside for now. Finally, the rather close position angle agreement of the putative secondary with the primary bar invites speculation that we have given two names to a single structure. Isophote fitting to a high-resolution NICMOS image would test our prediction for the shape of the nuclear potential. However, the strong nonstellar emission, the near alignment of the bar and kinematic major axes in NGC 7479, and the expectation of only a $\sim 5 - 7\%$ level of nonaxisymmetry do not augur well for a robust result. Perhaps the most promising strategy to confirm the results of our model would be use of the [model-independent] method for measuring pattern speeds proposed by Tremaine & Weinberg (1984). Since the apparent ~ 3.4 Myr rotation period of the secondary bar is marginally shorter than the ~ 10 Myr timescale we expect for a burst of star formation (Heller & Shlosman 1994), CO emission may be able to satisfy this technique's requirement that the velocity field tracer obey equations of continuity.

2.5.3 Mass inflow

Our inclusion of damping terms in the equations of motion for gas clouds in a barred potential means that our model for NGC 7479 is intrinsically dissipative. However, because the system's phase space volume contracts to a limit cycle (i.e., to the orbital solutions of Appendix B.1) rather than to a point, we cannot self-consistently derive a rate of mass

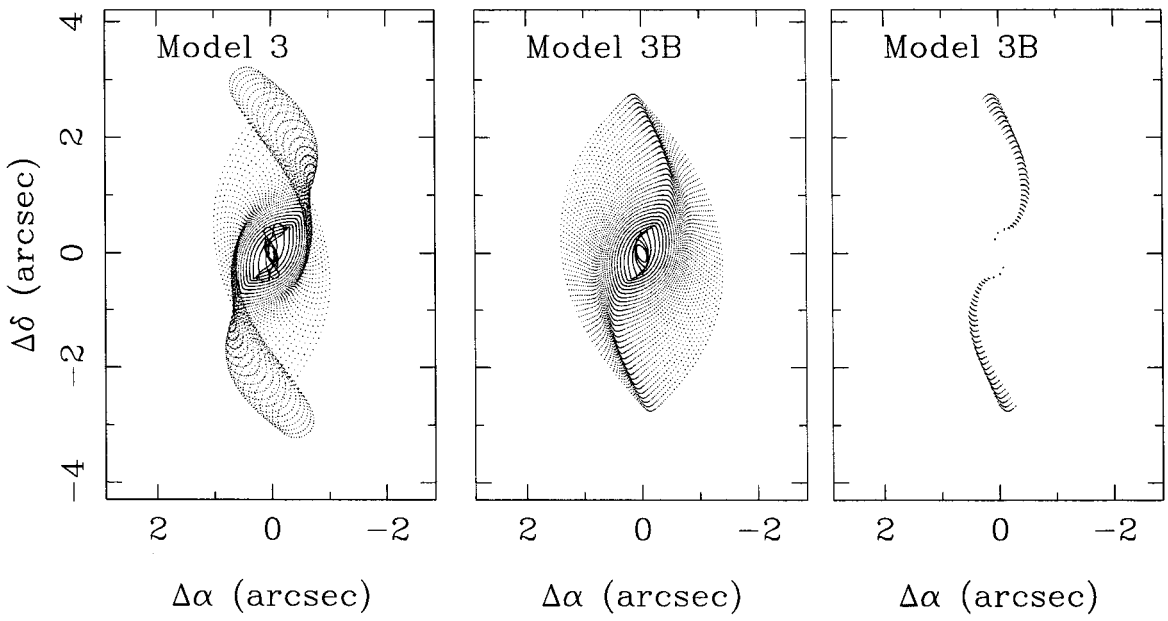

Figure 2.13: Orbit shapes in NGC 7479. The left panel plots points where Model 3 predicts nonzero emission (our actual sampling in azimuth is twice as fine as depicted here). The center panel shows Model 3B, identical to Model 3 apart from our adoption of $\lambda = \mu = 0.12$ to minimize self-intersection of orbits. The right panel plots only those points for Model 3B at which the local mass surface density is at least twice as large as the mean. Coordinates are relative to the dynamical center, as in Figures 2.4 through 2.10.

inflow from our model parameters. The motion of a pendulum is analogous: for certain driving forces and damping strengths, an ideal system will remain in motion indefinitely. Since NGC 7479 is not an ideal system, we expect it will undergo some degree of nuclear fuelling. On large scales, Quillen et al. (1995) estimate that the torque of the [primary] stellar bar will drive molecular gas inwards at $4 \pm 2\,\mathrm{M}_\odot\,\mathrm{yr}^{-1}$; Laine et al. (1999) estimate that only $\sim 0.5\,\mathrm{M}_\odot\,\mathrm{yr}^{-1}$ of this total will form stars before it reaches the nucleus. Our kinematic model for the nucleus can at least tell us *where* subsequent dissipation is likely to occur. In the left panel of Figure 2.13, we plot the shapes of the orbits (projected to the sky plane) which are predicted by our Model 3. The preference of χ^2_ν for a model which violates the assumption of nonintersecting orbits serves notice that our strictly analytical treatment of gas motions has its limitations. To reduce self-intersection of orbits in our model, we must decrease the bar strength (i.e., the absolute value of ε) or increase the rate of damping (i.e., λ and/or μ). We have taken the latter option, setting $\lambda = \mu = 0.12$, in order to obtain a more acceptable version of Model 3. The resulting orbits are plotted in

the middle panel of Figure 2.13 as Model 3B; the higher damping rates now drive χ^2_ν to 353.9, 77.3, and 134.4 for the CO(1–0), CO(2–1), and joint fits, respectively.

To ascertain where the rate of angular momentum loss is greatest in Model 3B, we consider the local variation of mass surface density along its orbits. We expect the proximal cause of dissipation to be collisions between discrete molecular clouds; these will naturally occur at higher rates where orbital crowding increases the space density of clouds. In the right panel of Figure 2.13, we have replotted only those points from the middle panel for which the surface density exceeds $y = 2$ times its value in the axisymmetric limit. We determine whether a point falls in this category by considering its linear distance d_ϕ from the next point to be plotted in azimuth: if the plotting interval in azimuth angle would be $\Delta\phi$ in the axisymmetric limit, the condition

$$d_\phi \leq \frac{r\,\Delta\,\phi}{y} \tag{2.16}$$

implies that clouds at radius r experience crowding. The regions plotted in the right panel of Figure 2.13 are nearly linear and lie along the leading edges of the bar, nicely matching the locations of the dissipative shocks predicted by hydrodynamical models.

2.6 Conclusions

From our models of the CO(1–0) and CO(2–1) emission in the nucleus of NGC 7479, we can draw the following conclusions:

- Molecular emission in NGC 7479 is distributed along the length of a linear feature, whose position angle leads that of the primary stellar bar. However, the molecular gas is highly centrally concentrated: $\sim 61\%$ of our detected CO(1–0) emission and $\sim 56\%$ of our detected CO(2–1) emission originate within $\sim 4.5''$ of the nucleus.

- The massive central disk has kinematics consistent with our expectations for gas in an inner, secondary bar, whose pattern speed is an order of magnitude larger than that of the primary bar. Consistent with models of doubly-barred galaxies, the corotation resonance of the secondary bar probably coincides with an inner 2:1 Lindblad resonance of the primary bar. Our result constitutes the first *measurement*

of the pattern speed of a secondary gas bar, and confronts theoretical predictions that the ratio of secondary:primary pattern speeds should be 2–3:1.

- Mass inflow on $\sim 100\,\mathrm{pc}$ scales will be triggered by cloud-cloud collisions in regions of orbital crowding– specifically, in linear features running along the leading edges of the bar.

- Variation of the integrated intensity ratio R implies that the temperature and/or density of the molecular gas is lower in the outskirts of the disk than in the nucleus, and is lower still in the material which the interferometer fails to detect. The particular value $R > 1$ we observe in the nucleus can be attained by optically thick emission from molecular clouds which are externally heated.

2.7 Acknowledgments

We thank Susanne Hüttemeister, Susanne Aalto, and collaborators for the use of their CO(1–0) data, Kazushi Sakamoto for an extensive correspondence on gas dynamics in barred galaxies, Sterl Phinney for suggestions on confirming the existence of a distinct secondary bar, and Seppo Laine for supplying the coefficients for a K-band-generated potential.

Chapter 3 Warm molecular gas in NGC 2681

3.1 Introduction

NGC 2681 is a nearby ($d \simeq 13.3\,\mathrm{Mpc}$), nearly face-on ($\imath \simeq 20°$), early-type (S0a) spiral galaxy. Infrared imaging by Erwin & Sparke (1999) indicates the existence of [misaligned] stellar bars on three length scales– $50 - 60'' \sim 3.2 - 3.9\,\mathrm{kpc}$, $15 - 20'' \sim 0.9 - 1.3\,\mathrm{kpc}$, and $1.8 - 4.0'' \sim 116 - 258\,\mathrm{pc}$. The nucleus of the galaxy hosts a Low-Ionization Nuclear Emission-line Region (LINER). Ho et al. (1997c) ["definitely"] detect a $1550\,\mathrm{km\,s^{-1}}$ FWHM component in the Hα line after subtraction of the stellar absorption spectrum, persuasive evidence that the nuclear luminosity is generated by accretion. No hard X-ray observations (as yet) exist to confirm this suggestion. In this work, the second in a series of papers discussing the molecular gas distributions seen in nearby active galaxies, we present high-resolution CO observations of NGC 2681 which imply that its nucleus contains both a large central mass and a substantial flux of high-energy photons capable of heating the interstellar medium.

3.2 Observations

We observed the CO(1–0) transition in NGC 2681 at OVRO in 1997, and the CO(2–1) transition during the 1998-99 season; Table 3.1 summarizes both sets of observations. Continuum and spectral line data were obtained simultaneously, as described in Section 2.2; the CO(1–0) and CO(2–1) datasets include 112 and 56 velocity channels, respectively, each with width $10.4\,\mathrm{km\,s^{-1}}$. Data were calibrated and imaged as described in Section 2.2. The flux scale for each track was determined by measuring the flux density of our gain calibrator, 0923+392, either by direct comparison to Uranus and Neptune, or by bootstrapping from archived observations of the planets (and bright, frequently-observed quasars). We estimate that the uncertainties in our flux scale are $\sim 10\%$ for the CO(1–0) data and $\sim 15\%$ for the CO(2–1) data. For passband calibration of each track we used 3C273, in one case augmented by 3C111 and 0923+392 itself.

Date	Line	Array	Longest baseline	Passband calibrator(s)	Flux cal	Gain calibrator	Strength
(1)	(2)	(3)	(4)	(5)	(6)	(7)	(8)
1 May 97	CO(1–0)	L	115 m	P1	2	0923+392	3.6 Jy
17 Oct 98	CO(2–1)	L	115 m	P1	2	0923+392	2.6 Jy
21 Nov 98	CO(2–1)	L	103 m	P1	2	0923+392	3.0 Jy
16 Dec 98	CO(2–1)	H	242 m	P1+P2+P3	2	0923+392	3.3 Jy
02 Feb 99	CO(2–1)	L	115 m	P1	1	0923+392	2.3 Jy

Table 3.1: OVRO observation log for NGC 2681. The columns are (1) date (2) CO transition (3) array configuration (4) maximum baseline used in mapping (5) passband calibrator(s), where P1 = 3C273, P2 = 3C111, and P3 = 0923+392 (6) type of flux calibration, where 1 denotes use of Uranus and Neptune and 2 denotes bootstrapping from archived data (7) gain calibrator (8) flux density adopted for gain calibrator.

After editing the visibilities in the DIFMAP package (Shepherd 1997), our final CO(1–0) dataset included 3.5 hours of integration and 10 distinct baselines; our final CO(2–1) dataset included 13.6 hours of integration and 30 distinct baselines. We mapped the data using the IMAGR task in the NRAO AIPS package, cleaning a single large region down to $+1\sigma$ in each velocity channel. Maps of the 1 GHz continuum channel in the line-free sideband showed no evidence for emission at either 115 GHz or 230 GHz, so subtraction of continuum from the spectral line data was unnecessary. Moderately robust weighting produced synthesized beams of $4.18'' \times 3.38''$ at $-20.5°$ for the CO(1–0) map and $1.27'' \times 1.16''$ at $-71.6°$ for the CO(2–1) map. The price of this resolution was an increase in the per-channel rms noise, to 30 mJy bm^{-1} for the CO(1–0) map (10% larger than for natural weighting) and to 49 mJy bm^{-1} for the CO(2–1) map (153% larger than for natural weighting). The seemingly drastic cost in sensitivity of our weighting scheme for the CO(2–1) data is not excessive: it reflects the exceptional quality of the (more numerous) visibilities from L configuration tracks, rather than any problems with the H configuration data.

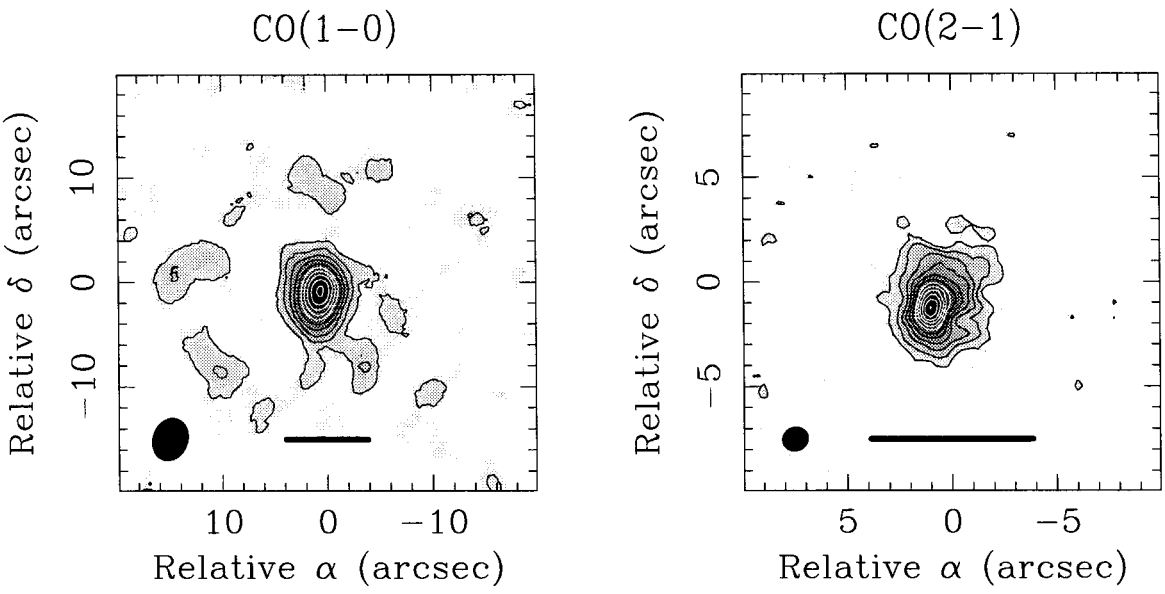

Figure 3.1: Zeroth moment maps of NGC 2681. Pixels with values less than $+1\sigma_{ch}$ were blanked before integrating, and contours are multiples of $2\,\sigma_{ch}\,\Delta v_{ch}\,\sqrt{n_{ch}}$ (2.6 and 4.3 Jy bm^{-1} km s^{-1}). The ellipses in the lower left corners show the synthesized beams; the bars nearby indicate 500 pc at $d = 13.3$ Mpc.

3.3 Results

3.3.1 CO(1–0)

Figure 3.1 shows the zeroth velocity moment of the CO(1–0) line in NGC 2681, integrated over $n_{ch} = 18$ velocity channels from 599.8 to 787.0 km s^{-1} heliocentric. Most of the molecular emission comes from a moderately resolved concentration in the nucleus with dimensions $5.6'' \times 3.9''$ and an elongation at position angle $\sim 178°$. Following the protocol in Section 2.3, we measure the total line flux in this structure to be 39.0 ± 7.2 Jy km s^{-1} (adopting the *a priori* uncertainty from Appendix A.4, since the empirical uncertainty estimate is only ± 0.01 Jy km s^{-1}). For a Galactic conversion factor of $X = 3 \times 10^{20}$ cm^{-2} (K km s^{-1})$^{-1}$ (Young & Scoville 1991) and an extra factor of 1.36 to account for helium, this flux corresponds to a total gas mass of $M_{gas} = 1.1 \pm 0.2 \times 10^8\,M_\odot$. The CO(1–0) emission in the nucleus has a peak brightness temperature of 2.6 ± 0.2 K above background, and a peak intensity of 171 ± 9 K km s^{-1}.

Outside the nucleus, we also see some hints of more extended low-level emission, perhaps arranged in a spiral arm pattern; our suspicion is bolstered by the fact that the features do

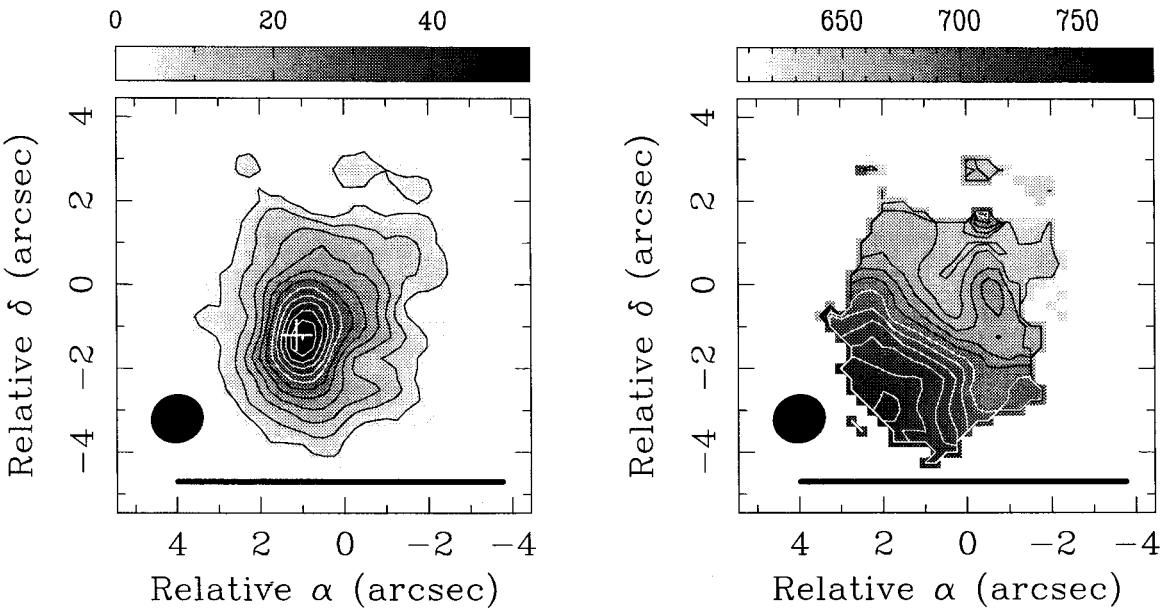

Figure 3.2: CO(2–1) moment maps of NGC 2681. Zeroth moment map shows the nuclear region of Figure 3.1, contoured at the same multiples of 4.3 Jy bm^{-1} km s^{-1}; a cross marks the position of the 20 cm continuum peak (see Table 3.5). First moment map was integrated with blanking of pixels $< +1\sigma_{ch}$, and is plotted here only where the zeroth moment map rises above its lowest contour. Isovelocity contours run from 640 to 740 km s^{-1} in steps of 10 km s^{-1}.

not appear at the locations of the central source's sidelobes in the undeconvolved (dirty) map. If indeed real, they contribute an additional ~ 24 Jy km s^{-1} to the CO(1–0) flux in the map, i.e., an additional $\sim 0.7 \times 10^8$ M$_\odot$ to the total gas mass. Indirect evidence for still more distributed molecular material comes from comparison with single-dish observations: our map recovers only $\sim 37\%$ of the emission detected by Young et al. (1995) in the inner 45″ (half-power beamwidth), and only $\sim 36\%$ of the emission detected by Braine et al. (1993) in the inner 23″ (cf. Section 3.3.3). We considered the possibility that the weighting scheme we adopted in imaging caused us to resolve out substantial emission. However, upon remapping the data using natural weighting (at $4.98'' \times 3.70''$ resolution), our nominal flux recovery shrank to $\sim 31\%$ for both convolving beams due to higher negative striping near the nucleus.

3.3.2 CO(2–1)

Figure 3.1 shows the zeroth velocity moment of the CO(2–1) line in NGC 2681, which we also present at greater magnification in Figure 3.2. Here we only detect emission in the nucleus, in a fairly axisymmetric distribution whose dimensions are $\sim 6'' \times 5''$. We observe a peak brightness temperature of $9.4 \pm 0.8\,\mathrm{K}$, a peak intensity of $822 \pm 34\,\mathrm{K\,km\,s^{-1}}$, and a total line flux of $252 \pm 11\,\mathrm{Jy\,km\,s^{-1}}$ in this molecular structure. Convolution to the $23''$ resolution of single-dish observations by Braine et al. (1993) implies that our map recovers most ($\sim 94\%$) of the total CO(2–1) emission in this galaxy.

Figure 3.2 also shows the first velocity moment of the CO(2–1) data cube. The velocity field in the nucleus of NGC 2681 appears to be regular at the smallest galactocentric radii, but farther out (especially to the northwest) we see disturbed isovelocity contours. There are reasons to suspect that noncircular motions along a bar could contribute to the kinematic pattern which we see. First, the disk's isophotal major axis is not precisely parallel to its kinematic major axis, an effect we see most clearly upon examining the highest contours in the zeroth moment map. Second, we *know* from the work of Erwin & Sparke (1999) that NGC 2681 contains a bar of total length $2a = 3.6 - 8''$ (at a position angle of 20°)– in good agreement with the size of the disk itself. While we are confident that this tertiary bar and our molecular disk are related at some level, however, we cannot easily associate the details of the first moment map with the influence of the bar. The morphology of the ends of the bar (in an unsharp masked NICMOS image) suggests that it circulates in a counter-clockwise sense on the sky, and therefore that the stellar bar must *lead* the gas response; this situation is counter to our expectations. Furthermore, we would expect streaming gas at the perigalacticon of a noncircular orbit to be blueshifted (redshifted) when it is at the east (west) end of the bar's minor axis. Such a pattern is (perhaps) present to the northwest of the nucleus, but is violated to the southwest and the northeast. These contradictions may become less severe if we assume a different position angle and/or sense of circulation for the tertiary bar, or if we attribute some of the isovelocity contour twisting to streaming in spiral arms, but our own data do not justify major drives to model these possibilities.

3.3.3 Integrated intensity ratio

In order to characterize the CO(2–1) to CO(1–0) intensity ratio in NGC 2681, we remapped both datasets after truncating their *uv* sampling at $r_{uv} \leq 10\,\mathrm{k}\lambda$ (see Section 2.3.3). The map of the truncated CO(1–0) dataset had slightly higher noise ($33\,\mathrm{mJy\,bm^{-1}}$) and smaller synthesized beam ($3.92'' \times 3.19''$ at $-21.5°$) than the original; the map of the truncated CO(2–1) dataset was nearly unchanged. To estimate a global value for R, we convolved these new maps to $23''$ resolution and remeasured what fractions we recovered of the single-dish intensities detected by Braine et al. (1993). Table 3.2 shows the result: even more dramatically than for NGC 7479 (see Section 2.3.3), the intensity ratio of the emission we detect with the interferometer is higher than the intensity ratio of the emission we miss. We have interpreted the OVRO data conservatively in reaching this conclusion. Convolution to $23''$ particularly overwhelms source emission with noisy off-source pixels in our CO(1–0) map of the truncated data; we nominally recover only $2.7\,\mathrm{K\,km\,s^{-1}}$ of the single-dish detection, which would imply a global intensity ratio of 2.92 for the emission detected in the truncated maps. The actual value of this ratio (see below) is roughly 1.85, which we use in Table 3.2 to predict the CO(1–0) intensity we *should* have recovered in a $23''$ beam. Even after taking this step, we deduce an almost unphysically low intensity ratio for the undetected (smooth and/or low surface brightness) emission of 0.041. Allen & Lequeux (1993) have inferred the presence of cold, probably subthermally excited emission in the disk of M 31, but still measure intensity ratios ≥ 0.2. We suspect in fact that the Braine et al. (1993) CO(1–0) detection in NGC 2681 may be erroneous, a possibility the authors themselves concede after noting that their global intensity ratio of 0.30 is "surprisingly low." Even if we assume that the true total CO(1–0) intensity is a factor of three lower, however, we still derive a value for R in the undetected emission (0.19) far lower than 1.85. This is the general pattern we would expect for a galaxy whose nuclear regions have higher temperature and density than its outskirts.

In addition to considering the global intensity ratio in NGC 2681, we have measured local variations in R by comparing partial moment maps of the data cubes for both truncated datasets (after convolving the CO(2–1) maps to the resolution of the CO(1–0) maps). Table 3.3 lists the results, for four velocity windows (roughly symmetric with respect to systemic velocity) and the full linewidth; we also list the peak brightness temperatures

Quantity (1)	IRAM detects (2)	OVRO detects (3)	OVRO misses (4)
uv sampling	$r_{uv} \geq 0$	$r_{uv} > 10\,\mathrm{k}\lambda$	$r_{uv} \leq 10\,\mathrm{k}\lambda$
$I_{\mathrm{CO}(2-1)}$	$9.0\,\mathrm{K\,km\,s^{-1}}$	$7.9\,\mathrm{K\,km\,s^{-1}}$	$1.1\,\mathrm{K\,km\,s^{-1}}$
$I_{\mathrm{CO}(1-0)}$	$30.0\,\mathrm{K\,km\,s^{-1}}$	$4.3\,\mathrm{K\,km\,s^{-1}}$	$25.7\,\mathrm{K\,km\,s^{-1}}$
R	0.30	1.85	0.041

Table 3.2: Global intensities and their ratios in NGC 2681. We compare the integrated intensities and intensity ratios within the inner 23″ for (2) single-dish measurements by Braine et al. (1993); (3) interferometer measurements determined from the truncated OVRO datasets; and (4) the flux missed by the interferometer due to low surface brightness and/or a smooth spatial distribution. Note that in column (3), we *adopt* the ratio of 1.85 for the full line from Table 3.3 and use this to predict $I_{\mathrm{CO}(1-0)}$, since the convolved version of the map made from the truncated CO(1–0) data is extremely noisy and yields an even lower value.

observed in the spatial boxes used to make the ratio measurements. All four (independent) measurements of R across the velocity width of the line produce values well in excess of unity; even careful deployment of the 10% and 15% uncertainties in our flux scales at 115 GHz and 230 GHz can only reduce the average R for the full linewidth from 1.85 to 1.43. These intensity ratios are unusually high– Braine et al. (1993) find an average ratio of 0.89 ± 0.06 on 23″ in their survey of 81 galaxies– and cannot be explained by optically thick emission from clouds which are similar to those in the Galactic disk. We will examine possible explanations for this result in Section 3.5, after using a kinematic model to constrain the behavior of the intensity ratio on scales smaller than the nominal resolution of our ratio maps.

3.4 Kinematic models

3.4.1 Model description

Our strategy for modelling the gas kinematics in NGC 2681 is similar to the one we adopt in Section 2.4 to fit our observations of NGC 7479. Since the rotation curve in NGC 2681 appears to turn over within the radius of the gas disk, we have here adopted a Plummer

Velocities ($\mathrm{km\,s^{-1}}$) (1)	Spatial feature (2)	$T_{b(2-1)}$ (K) (3)	$T_{b(1-0)}$ (K) (4)	R (5)
599.8 - 651.8	nucleus	2.38	2.65	1.55 ± 0.12
651.8 - 693.4	nucleus	2.41	1.42	2.34 ± 0.16
693.4 - 735.0	nucleus	2.33	2.05	1.58 ± 0.13
735.0 - 787.0	nucleus	2.16	1.65	1.73 ± 0.21
599.8 - 787.0	nucleus	2.63	2.59	1.85 ± 0.05

Table 3.3: Local intensity ratios in NGC 2681. Column (1) identifies four velocity windows and the full linewidth over which we measured R, in spatial boxes centered on features which are described in column (2). The remaining columns give (3) the peak CO(1–0) brightness temperature ($\pm 0.24\,\mathrm{K}$), (4) the peak CO(2–1) brightness temperature ($\pm 0.78\,\mathrm{K}$), and (5) the average intensity ratio within the measurement box. The uncertainties in R are the formal dispersions over each box.

model to describe the nuclear potential:

$$\Phi_0(r) = -v_p^2 \left(1 + (r/r_p)^2\right)^{-\frac{1}{2}} = -GM_p \left(r_p^2 + r^2\right)^{-\frac{1}{2}} \tag{3.1}$$

$$\Phi_b(r) = \varepsilon\left(r_p r^2\right)\left(r^2 + r_p^2\right)^{-\frac{3}{2}} \Phi_0(r) \tag{3.2}$$

where $v_p = \sqrt{GM_p}/r_p$. As $r_p \to 0$ we recover the Keplerian potential due to a point mass M_p; since v_p is not meaningful in this limit, we adopt M_p and r_p as parameters. A Plummer potential has been used to model bulge and/or halo distributions by Norman et al. (1996) and Kaufmann & Contopoulos (1996), and is also the $z = 0$ limit of the Kuzmin-Toomre and Miyamoto-Nagai potentials used to model disks (Friedli & Benz 1993; Norman et al. 1996; Heller & Shlosman 1996). Our choice of $\Phi_b(r)$ follows that of Sanders (1977) and Wada (1994); we [would] use $\varepsilon > 0$ to align $\phi = 0$ with the bar major axis.

In fact, we have elected not to introduce a bar perturbation to our model for NGC 2681. While the existence of the (tertiary) stellar bar at the radius of the molecular gas disk suggests that noncircular motions might be present, the weak and asymmetric twisting of the first moment map contours does not clearly motivate fitting to a barred potential. We would in any case be hampered by a limitation of our simple bar model. Flat-disk fits to the CO(1–0) and CO(2–1) data cubes separately (Models 1 and 2 in Table 3.4) reveal an inconsistency: at large radii, there is more molecular mass in a given annulus in the disk

Parameter	Units	Model 1	Model 2	Model 3
(1)	(2)	(3)	(4)	(5)
$\hat{x}_0$	RA (B1950)	08:49:57.68	08:49:57.69	08:49:57.69
$\hat{y}_0$	Dec (B1950)	+51:30:12.0	+51:30:11.9	+51:30:11.8
$\hat{v}_0$	$\mathrm{km\,s^{-1}}$	680.0	678.8	679.5
i	$^\circ$	29.2	27.4	24.0
α	$^\circ$	-26.7	-31.5	-30.3
r_p	pc	6	17	18
M_p	$10^8\,\mathrm{M_\odot}$	2.9	2.85	3.54
σ_v	$\mathrm{km\,s^{-1}}$	15.5	26	21
r_{gas}	pc	12	18	6
r_{in}	pc	8	12	18
$r_{out(1-0)}$	pc	145	-	145
$\bar{\sigma}_{em(1-0)}$	$\mathrm{K\,km\,s^{-1}}$	294	-	306
$\eta_{(1-0)}$	-	9	-	0
$r_{out(2-1)}$	pc	-	176	157
$\bar{\sigma}_{em(2-1)}$	$\mathrm{K\,km\,s^{-1}}$	-	258	294
$\eta_{(2-1)}$	-	-	9	25
χ^2_ν	-	133.8	58.0	75.9

Table 3.4: Kinematic model results for NGC 2681. The columns are (1) parameter (2) units (3)–(5) values for best-fit models. M1 = flat disk model for CO(1–0), M2 = flat disk model for CO(2–1), M3 = flat disk model for CO(1–0) and CO(2–1), with self-consistent treatment of the contribution made by the molecular gas to the potential (see Section 3.4.1). Parameters are those described in Section 2.4.

(calculated from the CO(1–0) emission using the Galactic conversion factor) than there is total dynamical mass in the corresponding spherical shell. To enforce the realistic condition $M_{gas} \leq M_{dyn}$ at all radii, we have therefore added a term in quadrature to $\Omega(r)$ which corresponds to the molecular mass:

$$\Omega^2(r) \sim 1.36 \times 4.808 \times \pi G \bar{\sigma}_{em(1-0)} \frac{r^2 - r_{in}^2}{r^3} \tag{3.3}$$

where the variables are defined as in Section 2.4 and the first two constants are motivated in Appendix A.4. This term is only proportional to the constant-surface-density component of our model's CO(1–0) emissivity, since the exponentially peaked nuclear component may come from diffuse, unbound material which does not trace mass. The new term (and corresponding adjustments to $\kappa(r)$) would severely complicate self-consistent fits to a barred

potential– another reason we assume strictly circular motions here.

Our preferred model (Model 3 in Table 3.4) fits the CO(1–0) and CO(2–1) data cubes simultaneously and does incorporate the contribution of the molecular gas mass to the potential. Apart from the coordinates of the radio continuum peak (see Table 3.5), the existing literature was of little use in providing initial guesses for model parameters. The optical isophotes are nearly circular and yield estimates of the inclination from 0° (Tully 1988) to $22° \pm 10°$ (de Vaucouleurs et al. 1991). The morphology of the tertiary bar in the image of Erwin & Sparke (1999) is suggestive of counter-clockwise rotation on the sky.

3.4.2 Model results

We present the results of our models in Table 3.4. Since Models 1 and 2 predict $M_{gas} \geq M_{dyn}$ at large radii, they are useful only insofar as a comparison reveals the typical uncertainty in parameters which they both (independently) estimate. Their agreement is good overall, with only the scale length of the Plummer potential (r_p) and the velocity dispersion of the gas (σ_v) appearing poorly constrained. Model 3 satisfies $M_{gas} \leq M_{dyn}$ at all radii and provides the parameter estimates which we will use in the remainder of this work. Note that our simultaneous minimization of χ^2_ν for both datasets slightly degrades the statistic for either dataset separately, to 140.9 for CO(1–0) (vs. 133.8 for Model 1) and to 62.0 for CO(2–1) (vs. 58.0 for Model 2). Two encouraging coincidences in our parameter estimates are worthy of note. First, the outer radius of the gas disk has nearly the same value derived from the CO(1–0) data ($r_{out(1-0)} = 145\,\mathrm{pc}$) as from the CO(2–1) data ($r_{out(2-1)} = 157\,\mathrm{pc}$). This agreement suggests that the different uv sampling of the two (untruncated) datasets has not resulted in drastically different sensitivities to smooth, extended structure in our maps of the two lines. Second, our model locates the dynamical center less than a beamwidth away from the peaks in the integrated CO intensities, and closer still to the peak 20 cm continuum (Figure 3.5). The model's use of a centrally peaked emissivity distribution could in principle have biased our estimated dynamical center towards the location of the gas peak. The dynamical center's superior agreement with the continuum peak (and by implication the active nucleus) thus argues strongly against the presence of an $m = 1$ perturbation to the galaxy's mass distribution at small radius.

In Figures 3.3 through 3.6, we plot the emission predicted by Model 3 over the emission observed in each velocity channel. The agreement of our model with both datasets is visually

Feature	Right ascension (B1950)	Declination (B1950)
(1)	(2)	(3)
OVRO pointing center	08:49:57.60	+51:30:13.0
20 cm continuum peak	08:49:57.72	+51:30:11.8
Peak CO(1–0) intensity	08:49:57.70	+51:30:11.5
Peak CO(2–1) intensity	08:49:57.76	+51:30:11.2
Dynamical center (Model 1)	08:49:57.68	+51:30:12.0
Dynamical center (Model 2)	08:49:57.69	+51:30:11.9
Dynamical center (Model 3)	08:49:57.69	+51:30:11.8

Table 3.5: Coordinates of features in the nucleus of NGC 2681. The 20 cm continuum position is from a 5.4″-resolution FIRST map (White et al. 1997). The dynamical center positions are those predicted by the models described in Table 3.4.

quite good. The only possible suggestions of noncircular motions appear in the 688.2 and 698.6 $\mathrm{km\,s^{-1}}$ velocity channels of the CO(2–1) data, where the observed emission is not reflection-symmetric about the kinematic major axis. Figures 3.7 and 3.8 show position-velocity cuts through the data and model cubes along the kinematic major axis. The latter figure clearly shows the decline in the rotation curve (outside ~ 26 pc in our model) which motivated our use of a Plummer rather than a logarithmic potential.

In Figure 3.9, we present the radial variation of various quantities calculated from our model parameters. The top left panel shows the mass surface densities due to the Plummer potential (spherical shells are here projected into planar annuli) and to the molecular gas itself. As noted in Section 3.4.1, we have treated these as separate contributions in order to guarantee that the total mass projected into the disk exceeds M_{gas} at all radii. Our approach implies that the Plummer potential should correspond strictly to the distributions of stellar and dark mass (at these radii we expect the mass contributed by atomic gas to be relatively small). Within 150 pc, we thus infer an enclosed stellar plus dark mass of

$$M(r) = M_p\, r^3 \left(r^2 + r_p^2\right)^{-\frac{3}{2}} = 0.98\, M_p = 3.5 \times 10^8\, \mathrm{M}_\odot \tag{3.4}$$

By comparison, the total molecular gas mass within the same radius is approximately

$$M_{gas}(r) = 1.36 \times 4.808 \times \pi \bar{\sigma}_{em(1-0)}\, (r^2 - r_{in}^2) = 1.4 \times 10^8\, \mathrm{M}_\odot \tag{3.5}$$

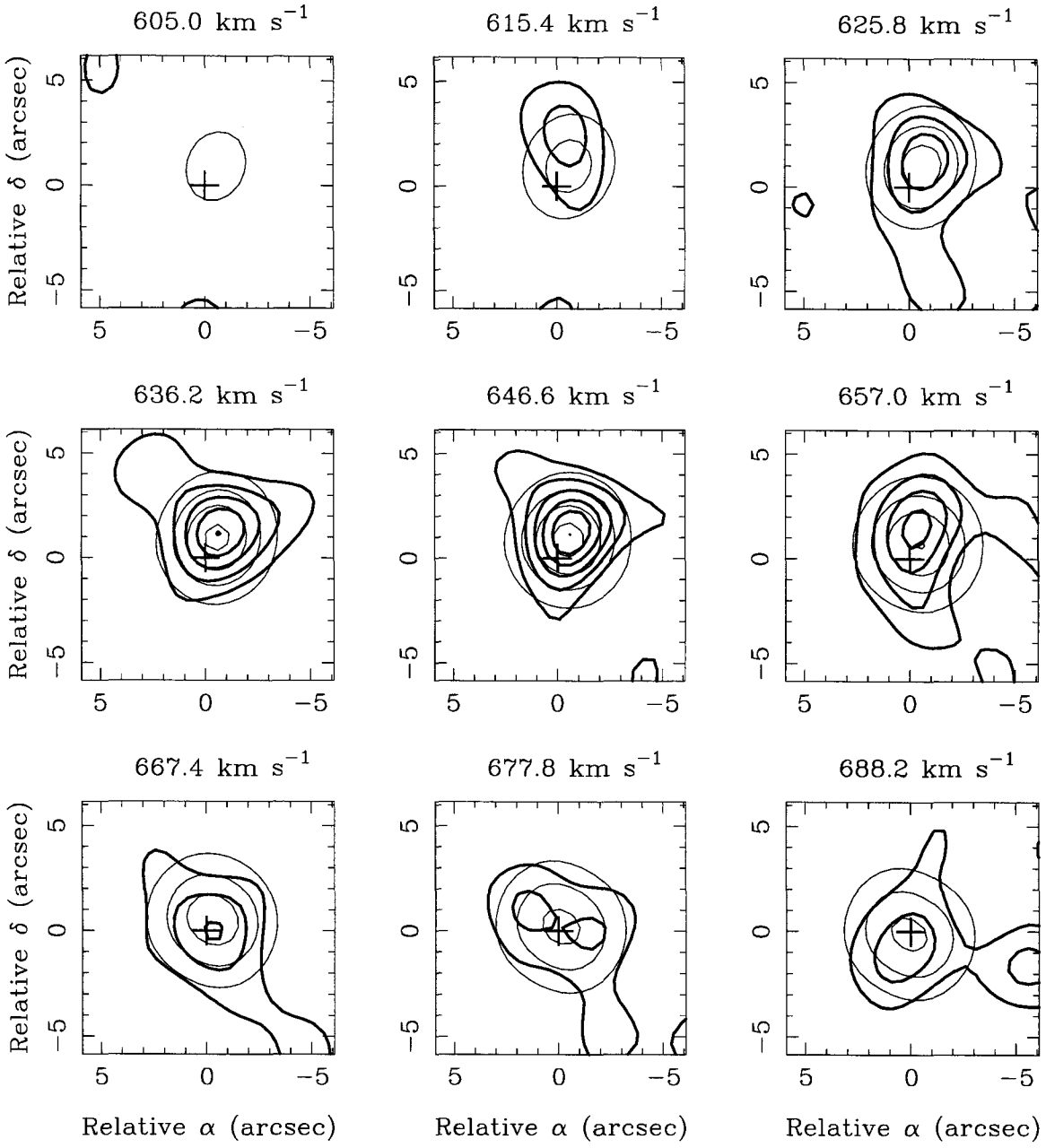

Figure 3.3: Blueshifted CO(1–0) velocity channels in NGC 2861. Light model contours are plotted over dark data contours; both are multiples of 99 mJy bm^{-1}. Spatial offsets are relative to the dynamical center of Model 3, which is also marked with a cross.

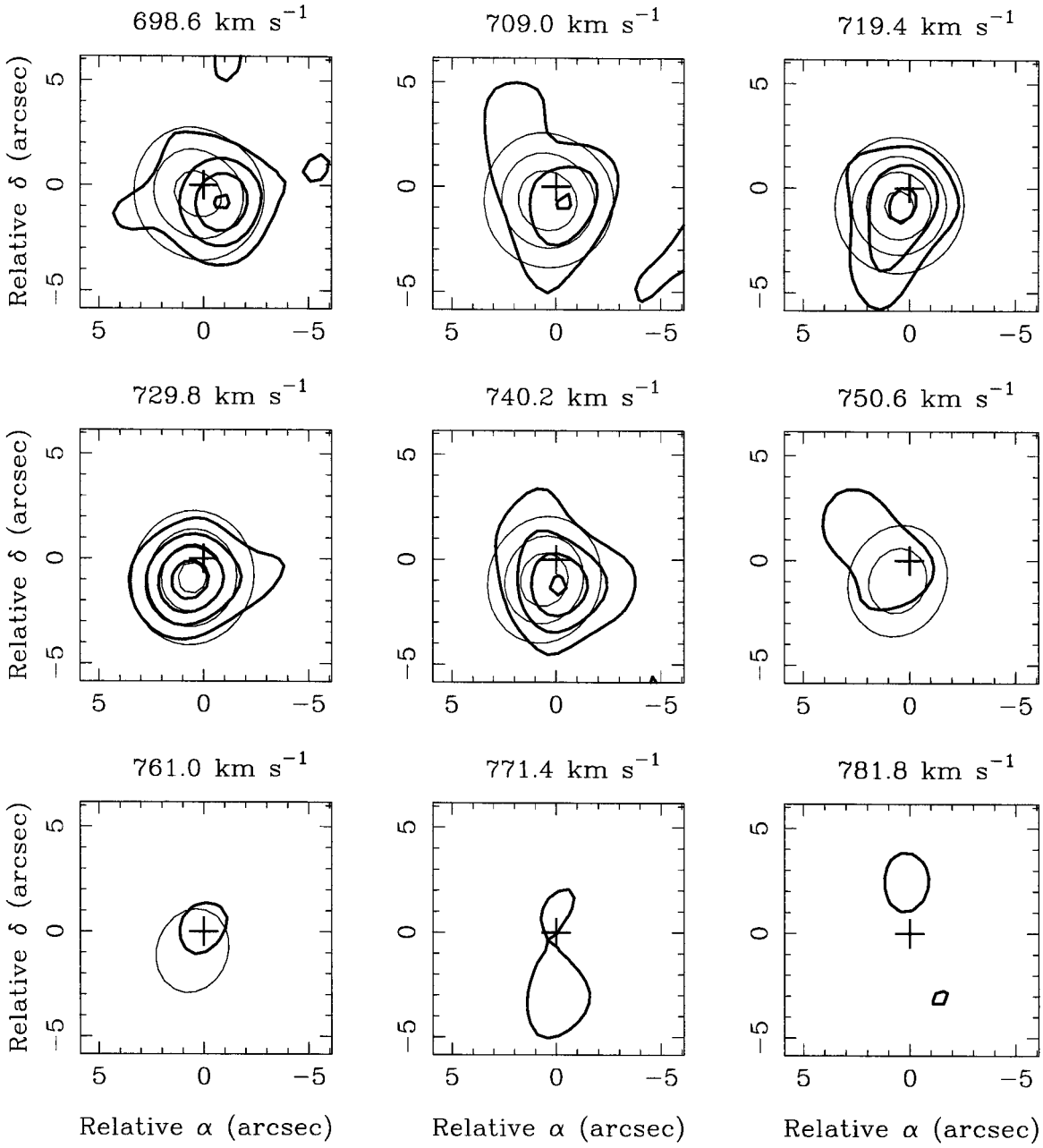

Figure 3.4: Redshifted CO(1–0) velocity channels in NGC 2861. Notation is as in Figure 3.3.

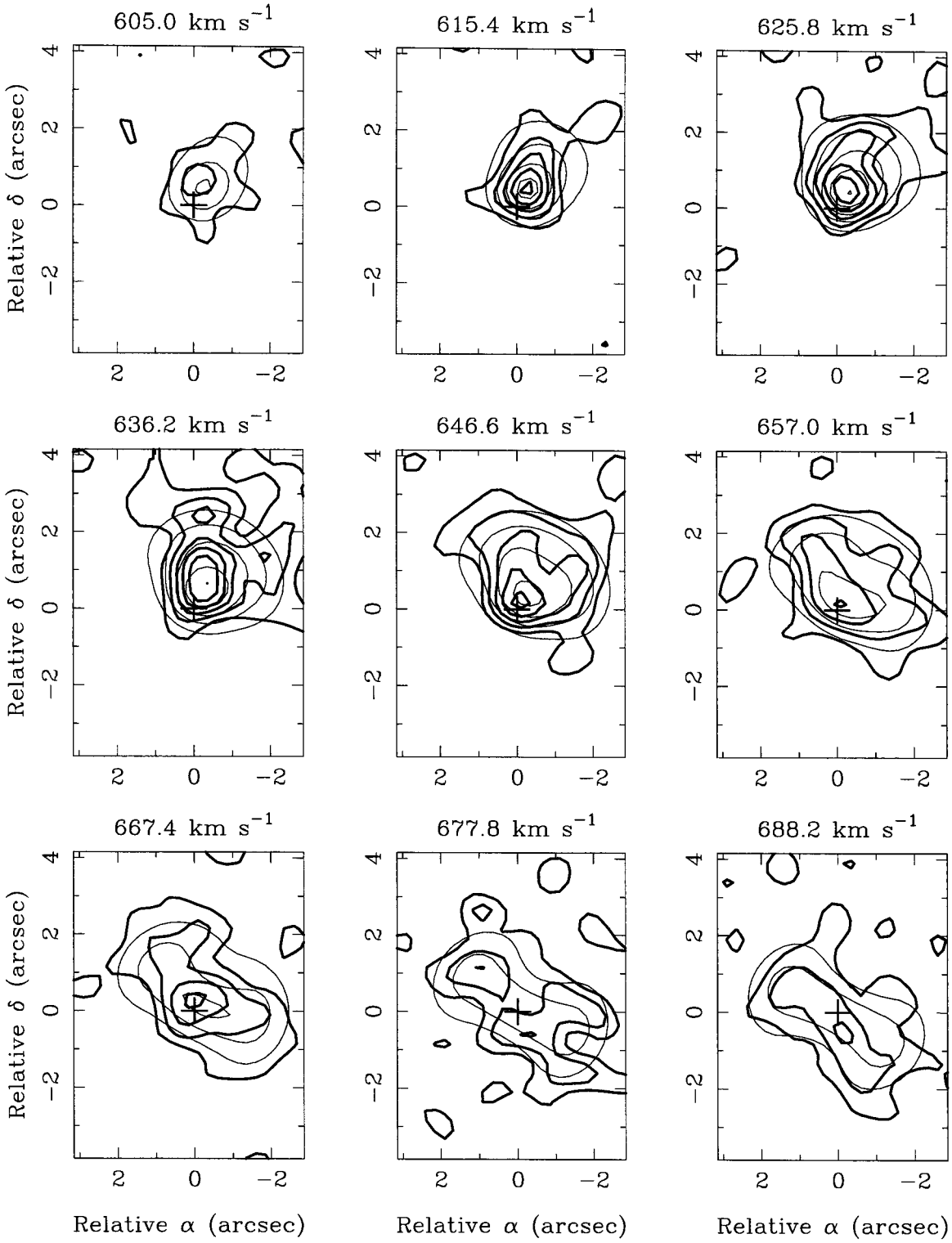

Figure 3.5: Blueshifted CO(2–1) velocity channels in NGC 2861. Light model contours are plotted over dark data contours; both are multiples of 59 mJy bm^{-1}. Spatial offsets are relative to the dynamical center of Model 3, which is also marked with a cross.

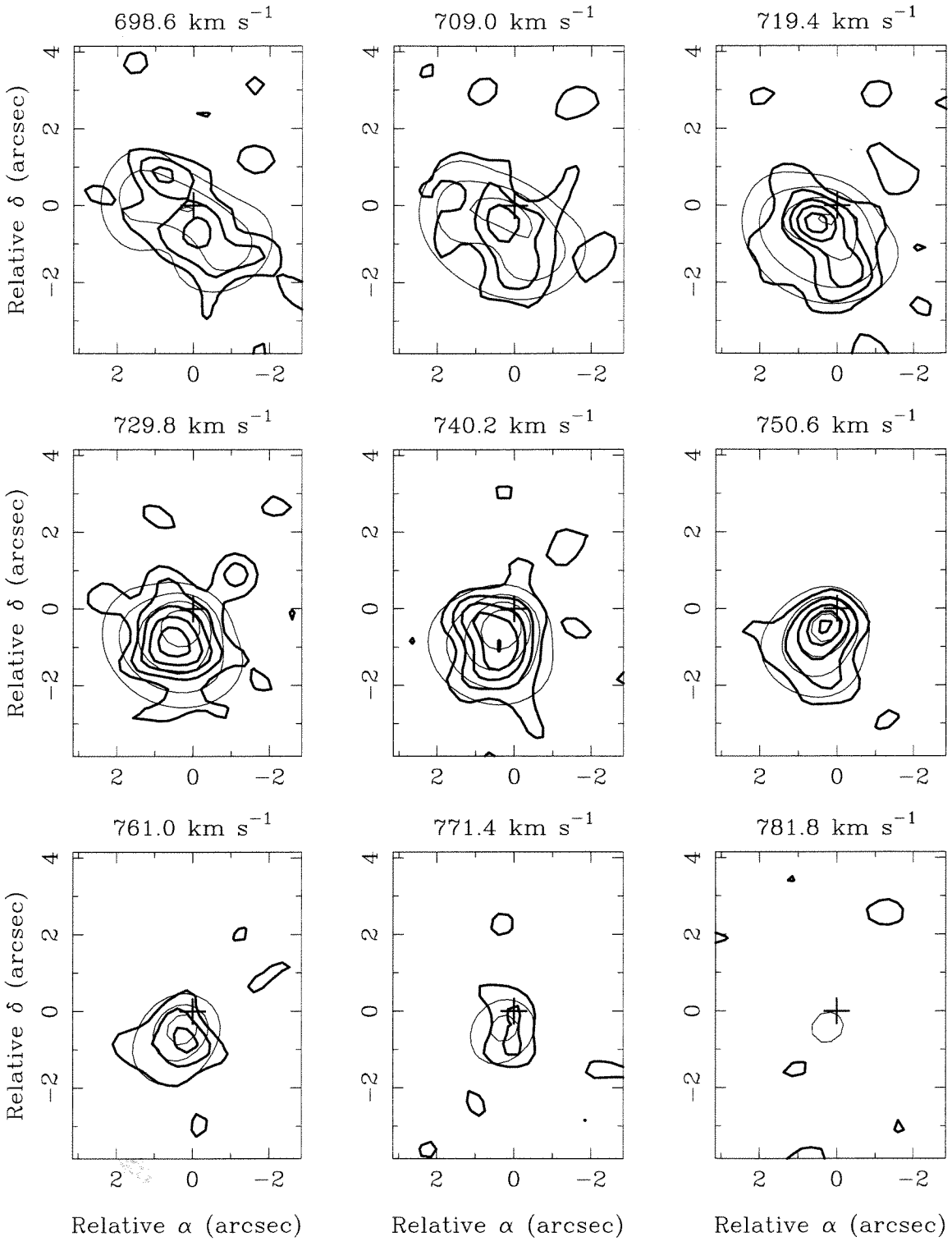

Figure 3.6: Redshifted CO(2–1) velocity channels in NGC 2861. Notation is as in Figure 3.5.

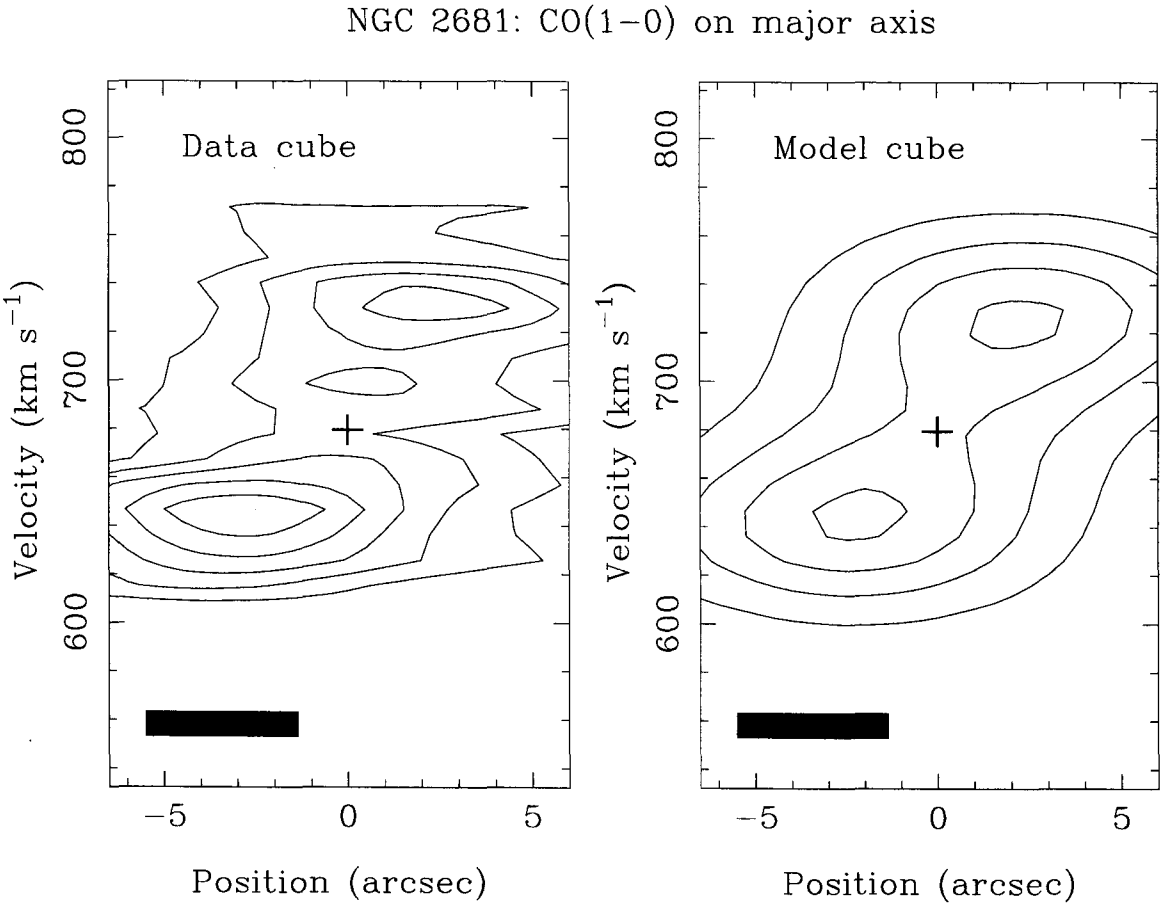

Figure 3.7: Position-velocity diagram for the CO(1–0) line in NGC 2861. A 2″-wide cut was taken at the position angle of the ascending node (−30.3° E of N). The cross marks the galaxy's spatial and velocity center; offsets along the spatial scale are relative to this position. The rectangle indicates the spatial and velocity resolutions. Contours are multiples of 56 mJy bm^{-1}.

where the flat CO(1–0) emissivity translates directly to a constant mass surface density of $1.36 \times 4.808 \times \bar{\sigma}_{em(1-0)} = 2001\,\mathrm{M}_\odot\,\mathrm{pc}^{-2}$. We conclude $\sim 29\%$ of the mass in the inner 150 pc of NGC 2681 is in molecular form. The local gas mass fraction (also plotted in the top left panel of Figure 3.9) varies substantially from this average, exceeding 50% for all radii ≥ 70 pc. The extreme values of this fraction near the edge of the disk ($\rightarrow 94\%$ at 150 pc) are probably untrustworthy: a model more realistic than ours would include additional stellar mass components with scale lengths $\gg r_p$. It is therefore not clear how seriously we err by ignoring self-gravity of the molecular disk in our model. We are more confident about our description of the mass distribution at small radii. Evaluating $M(r)$ at the peak of the

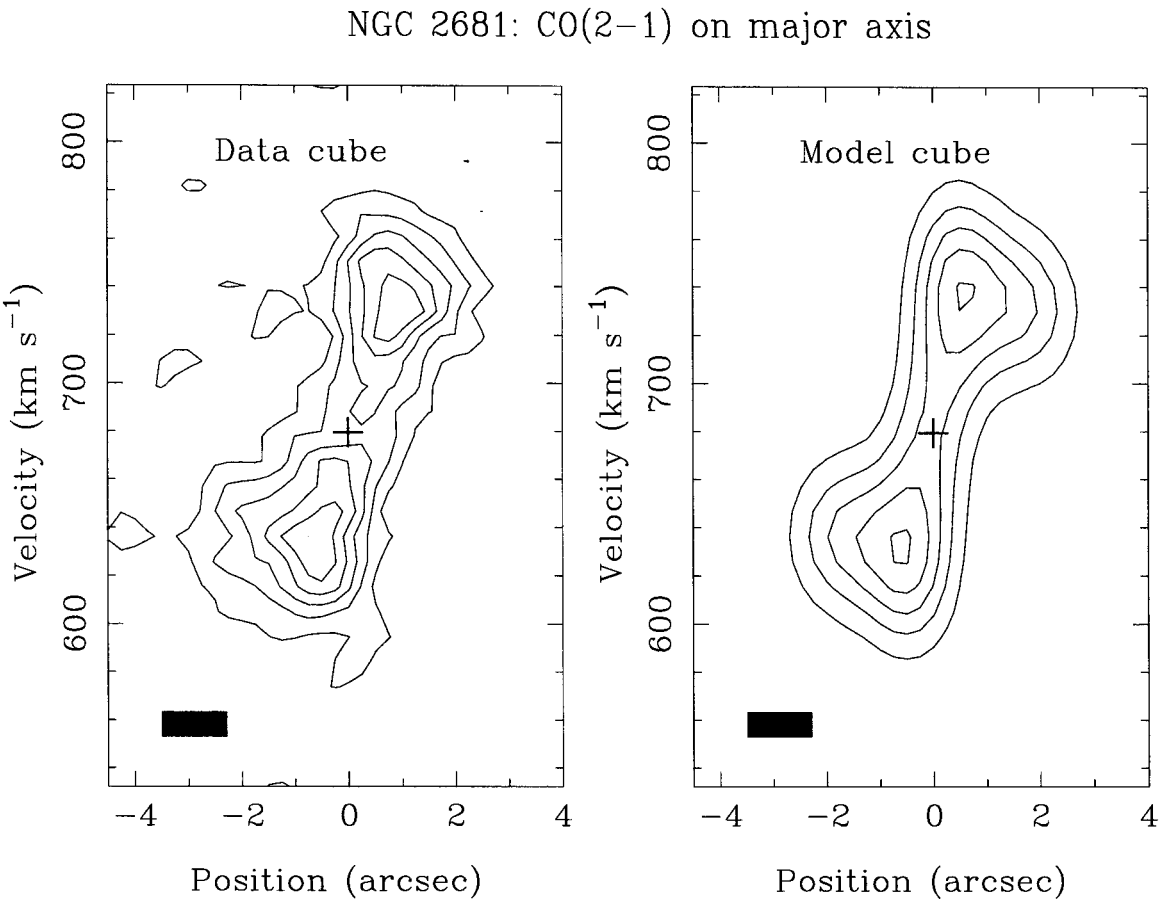

Figure 3.8: Position-velocity diagram for the CO(2–1) line in NGC 2861. Notation is as for Figure 3.7, but the spatial width of the cut is now 1″. Contours are multiples of 86 mJy bm^{-1}.

rotation curve (shown in the top right panel of Figure 3.9) implies that NGC 2681 contains 2.0×10^8 M$_\odot$ within 26 pc of its nucleus, and gives us an upper limit on the mass of a central black hole.

Perhaps the most striking implication of our model is illustrated in the bottom left panel of Figure 3.9: the CO(1–0) emission in NGC 2681 has constant surface density, while the CO(2–1) emission peaks strongly at the nucleus. This discrepancy is *not* an artifact of the different angular resolutions of our two datasets, since our approach to kinematic modelling constitutes an implicit deconvolution. The difference is also not a consequence of the difference in *uv* sampling. If a smoothly distributed component had been resolved out of our CO(2–1) maps, our model *could* have been fooled into fitting an unrealistically strong central CO(2–1) peak. Our apparent recovery of $\sim 94\%$ of the total CO(2–1) emission

(Braine et al. 1993) and the agreement of our model's outer gas radii inferred independently from the CO(1–0) and CO(2–1) data exclude this possibility.

The bottom right panel of Figure 3.9 shows the predicted radial variation of the intensity ratio R; since the CO(1–0) emissivity is flat, the ratio shows the same central cusp seen in the CO(2–1) emissivity. At large radius, R will generally approach $\bar{\sigma}_{em(2-1)}/\bar{\sigma}_{em(1-0)} = 0.96$. This value is consistent with optically thick emission from gas in LTE, suggesting that the molecular emission outside the nucleus of NGC 2681 comes from a rather ordinary population of molecular clouds (see Section 3.5.1 below). In contrast, Equation 2.14 implies that the value of R at the inner edge of the gas disk is nominally $R_{max} = 25.0$. Such a high ratio (in fact, *any* $R > 4.0$) cannot arise if both CO transitions trace the same material (see Section 3.5.2). The particular value $R_{max} = 25.0$ is likely to be an overestimate, since Model 3 does not discriminate strongly against the presence of a weak central peak in the CO(1–0) emissivity. Changing $\eta_{(1-0)}$ from 0 to 5.24 in Model 3 would only increase the total χ^2_ν from 75.9 to 76.4 (and the χ^2_ν for the CO(1–0) fit alone from 140.9 to 142.9), while reducing R_{max} to 4.0 at $r = r_{in}$. We also suspect that our parametrization of the second emissivity component as an exponential is producing an artificially sharp peak. To render our estimate of R in the nucleus of NGC 2681 less dependent on such biases of our model, we have calculated the ratio of the CO luminosities (CO emissivities integrated over projected area) enclosed at each radius. This "cumulative" intensity ratio is also plotted in the bottom right panel of Figure 3.9; we will adopt the value of 2.76 at 65 pc (1″) radius as representative of molecular emission in the nucleus.

Our model's inference of a high intensity ratio at small radius is validated by two considerations. First, since $R \simeq 2.76$ results from the different *shapes* of the CO(1–0) and CO(2–1) emissivity distributions, rather than from different normalizations, we cannot ascribe a high ratio to uncertainty in flux calibration (e.g., of our single CO(1–0) track). Second, the four independent values of R measured from the truncated datasets (tabulated in Table 3.3) average to 1.80, clearly greater than 1. For comparison, we calculate the cumulative intensity ratio at the outer edge(s) of the molecular disk in our model to be 1.46. The shortfall in our model is due to the difference between integration over, and convolution in, solid angle, and to the fact that the truncation described in Section 3.3.3 affects the CO(1–0) dataset more severely than the CO(2–1) dataset.

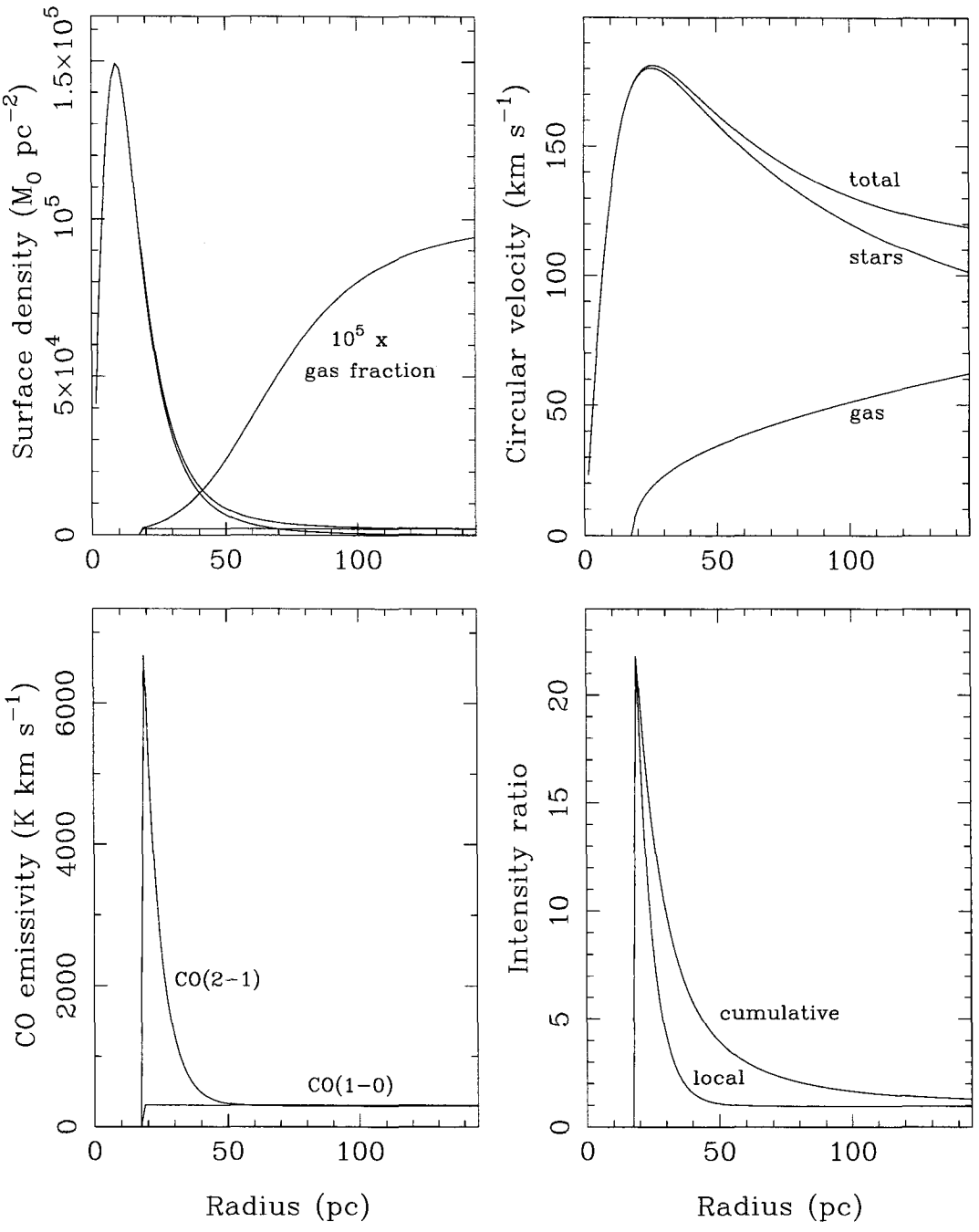

Figure 3.9: Radial plots from the kinematic model of NGC 2681. Top left: stellar, gas, and total mass surface densities projected into the disk. The gas mass fraction is also plotted. Top right: circular velocities due to the stellar, gas, and total enclosed masses. Bottom left: emissivities of the two CO lines. The CO(1–0) emissivity corresponds to the constant surface density of 2001 $M_\odot$ pc^{-2} plotted at top left. Bottom right: intensity ratio. The lower curve is the [local] ratio of emissivities at each radius. Because the sharpness of the central peak likely results from our choice of parametrization, we have also plotted the [cumulative] ratio of enclosed CO luminosities at each radius, as a less model-dependent estimator of R.

3.5 Excitation models

Given CO(1–0) and CO(2–1) observations of any object, we can only connect the line intensities and their ratio to actual physical conditions if we understand both the excitation of the CO rotational ladder and the radiative transfer of the line emission. These two issues are coupled by photon trapping if CO lines become optically thick: absorption and stimulated emission will generally cause the rotational level populations to approach local thermodynamic equilibrium (LTE) even if the number density of colliders n_{H_2} is nominally too low to thermalize them. An additional complication arises in studies of external galaxies, where the molecular gas fills some unknown fraction $f_a(v) \leq 1$ of the synthesized beam at each velocity v. Before pursuing a detailed analysis of the molecular emission from NGC 2681, we will therefore review in Section 3.5.1 the standard picture of how molecular gas is distributed in external galaxies, as well as the (related) standard approach to deriving molecular mass from CO(1–0) luminosity. We continue with the development of a fairly standard, one-zone model for the gas in NGC 2681 (Section 3.5.2), and of more exotic models depending on external heating of the galaxy's molecular clouds (Section 3.5.3).

3.5.1 Molecular gas in galaxies: the standard paradigm

Molecular emission lines in external galaxies show (1) lower peak brightness temperatures than those seen for Galactic molecular clouds, and (2) smooth velocity profiles. These properties imply that a galaxy's molecular gas is typically distributed in a population of discrete clouds whose areal filling factor $f_a(v)$ is small but smoothly varying with velocity (Dickman et al. 1986). Conveniently, the characteristic filling factor may be small enough (so long as the galactic disk is not viewed edge-on) that the clouds in each velocity interval do not shadow each other along the line of sight. The overall velocity profile for a particular synthesized beam will thus depend on the brightness temperatures, areas, and numbers of clouds whose velocities fall in each interval. Line profiles in external galaxies are broader than those of individual Galactic molecular clouds, thanks to the line-of-sight velocity dispersion of clouds with a common systematic (e.g., orbital) motion, and to gradients in the systematic motion across the spatial width of the beam. Kinematic modelling (see Section 3.4) can separate these two contributions to the linewidth.

The standard determination of molecular mass from CO(1–0) luminosity is related to

the above picture of multiple, non-overlapping clouds lying in each synthesized beam. Appendix A.4 derives the constants of proportionality relating the gas mass in molecular clouds M_{gas} to the flux and luminosity in the CO(1–0) line, in terms of a standard (Galactic) conversion factor $X = N_{\rm H_2}/I_{\rm CO}$. This ratio between molecular hydrogen column density and the integrated intensity of the CO(1–0) line has been estimated using three different approaches:

1. Bloemen et al. (1986) compare the CO luminosity and the gamma ray flux (due to cosmic ray interactions with hydrogen nuclei) in the inner Galaxy; they infer $X = 2.2 \times 10^{20}\,{\rm cm^{-2}\,(K\,km\,s^{-1})^{-1}}$. This method is in principle independent of assumptions about the distribution of the molecular gas, although it does require a careful census of each phase of the interstellar medium (and assumes that the cosmic ray flux is constant across the Galaxy).

2. A number of authors compare the visual extinction and the integrated intensity of the ^{13}CO(1–0) line along the same lines of sight through dark clouds. Extinction is easily related to $N_{\rm H_2}$ for a constant dust/gas ratio. If optically thin, the ^{13}CO(1–0) line will also be proportional to $N_{\rm H_2}$ for a constant $^{13}{\rm CO/H_2}$ abundance ratio. An estimate of X then requires a relation between the integrated intensities of the ^{12}CO(1–0) and ^{13}CO(1–0) lines. Sanders et al. (1984) argue against using poorly justified assumptions of LTE, preferring an empirical approach which yields $X = 3.9 \times 10^{20}\,{\rm cm^{-2}\,(K\,km\,s^{-1})^{-1}}$ for two sets of dark cloud measurements.

3. If the CO brightness temperature along a line of sight depends more on the *number* of clouds intercepted than on their surface brightness temperatures (i.e., T_b is roughly constant), and if each of these clouds is virialized (i.e., its velocity width depends on its mass and radius), then the integral

$$I_{\rm CO} = \int T_b\,dv \simeq T_b \sum \Delta v \propto T_b \sum \left(\frac{M}{r}\right)^{\frac{1}{2}} \propto T_b \sum n_{\rm H_2}^{\frac{1}{2}}\, r \propto \left[T_b\, n_{\rm H_2}^{-\frac{1}{2}}\right] N_{\rm H_2} \qquad (3.6)$$

predicts a proportionality with $X \propto n_{\rm H_2}^{\frac{1}{2}}\, T_b^{-1}$. Galactic molecular clouds generally show brightness temperatures $\sim 10\,{\rm K}$ in an optically thick CO(1–0) line, making constant T_b a reasonable assumption. Virialization is implied by the *agreement* of this method with the two described above (Solomon & Barrett 1991). Sanders et al.

(1985) derive $X = 4.6 \times 10^{20}\,\mathrm{cm^{-2}\,(K\,km\,s^{-1})^{-1}}$ from a sample of 80 clouds in the inner Galaxy, while Solomon et al. (1987) estimate $X = 2.5 - 4.1 \times 10^{20}\,\mathrm{cm^{-2}\,(K\,km\,s^{-1})^{-1}}$ for Galactic clouds ranging in mass from 10^6 to $10^5\,\mathrm{M_\odot}$.

The last of these three methods is the most robust and has received the most attention in the context of extragalactic observations. Dickman et al. (1986) derive the exact forms of X for clouds which have (a) fixed density and arbitrary sizes, or (b) arbitrary densities and a fixed size distribution. Bryant & Scoville (1996) derive X for a fixed size distribution and a power-law dependence of mean density on cloud size, but with additional corrections for external pressure and magnetic support. Combining their expressions with a Galactic conversion factor is only legitimate, however, insofar as each synthesized beam on an external galaxy really does intercept many discrete, virialized clouds. In ultraluminous infrared galaxies, molecular gas may comprise a single, continuous structure (Downes et al. 1993; Solomon et al. 1997; Scoville et al. 1997; Downes & Solomon 1998); in this case, the velocity linewidth will be due to the total [stellar and interstellar] mass, leading a Galactic conversion factor to overestimate M_{gas}. Such an overestimate is also possible if CO(1–0) emission originates in diffuse gas whose linewidth is non-gravitational, as may be the case in some starburst galaxies (Aalto et al. 1994). A separate source of uncertainty in use of the Galactic conversion factor is the dependence of X on the combination $n_{\mathrm{H_2}}^{\frac{1}{2}}\,T_b^{-1}$ in the virial-mass derivation. Fortunately, variations in the true value of $N_{\mathrm{H_2}}/I_{\mathrm{CO}}$ are unlikely to be as large as claimed by Maloney & Black (1988), who consider only independent variations of cloud temperature and density. In this work, we will generally assume the standard paradigm for molecular gas in galaxies, and follow Young & Scoville (1991) in using $X = 3 \times 10^{20}\,\mathrm{cm^{-2}\,(K\,km\,s^{-1})^{-1}}$ as a "standard" Galactic conversion factor.

3.5.2 One-zone models

Our primary objective in modelling the molecular emission from NGC 2681 is to reproduce the intensity ratios and peak brightness temperatures tabulated in Table 3.3. We also wish to account for the distinct intensity ratios of 0.96 (at $\sim 150\,\mathrm{pc}$) and ~ 2.76 (in the nucleus) estimated from our kinematic model in Section 3.4.2. Our initial excitation model will assume that the two CO lines trace the same ["one zone" of] material at each radius. For this approach, our first task is to estimate the kinetic temperature of the gas, which we

assume to be identical for clouds at a given galactocentric radius. Since the filling factor $f_a(v) \leq 1$ of the gas is unknown, our own observations can only suggest that in the nucleus, $T_{kin} \geq 9.4\,\mathrm{K}$ (the peak brightness temperature observed in the CO(2–1) line). Consideration of dust temperatures will provide a more helpful constraint on T_{kin}.

The ratio of IRAS flux densities $S_\nu(25\,\mu\mathrm{m})/S_\nu(60\,\mu\mathrm{m}) = 0.08$ places NGC 2681 in the regime of "cold" galaxies showing little emission from warm dust. The ratio $S_\nu(60\,\mu\mathrm{m})/S_\nu(100\,\mu\mathrm{m}) = 0.60$ implies a global mass-weighted grain temperature of $T_d = 38\,\mathrm{K}$ for a dust emissivity $\propto \nu$ (Soifer et al. 1989). We can use this temperature to compare total dust and molecular gas masses. Following Helou et al. (1985) and Soifer et al. (1986), we write the galaxy's far-infrared flux as

$$F_{\mathrm{FIR}} \simeq 1.5 \times 1.26 \times 10^{-11} \Big(2.58\, S_\nu(60\,\mu\mathrm{m}) + S_\nu(100\,\mu\mathrm{m})\Big)\ \mathrm{erg\,cm^{-2}\,s^{-1}} \tag{3.7}$$

for flux densities in Jy. The corresponding dust mass is then

$$\begin{aligned} M_{dust} &= \frac{4a\rho\, d^2\, F_{\mathrm{FIR}}}{< Q > \sigma\, T_d^4} \\ &= 7.65 \times 10^7\,\mathrm{M_\odot} \left(\frac{d}{\mathrm{Mpc}}\right)^2 \left(\frac{T_d}{\mathrm{K}}\right)^{-4} \Big(2.58\, S_\nu(60\,\mu\mathrm{m}) + S_\nu(100\,\mu\mathrm{m})\Big) \end{aligned} \tag{3.8}$$

if we adopt a Planck-averaged emissivity of $< Q >= 2.51 \times 10^{-3}$ for 38 K, a grain radius $a = 0.1\,\mu\mathrm{m}$, and a grain density $\rho = 3\,\mathrm{g\,cm^{-3}}$ (Draine & Lee 1984). Evaluating this expression for NGC 2681, we find $M_{dust} = 2.0 \times 10^5\,\mathrm{M_\odot}$ and (upon comparison with the molecular gas mass calculated in Section 3.3.1) derive an apparent gas-to-dust ratio of 900. This value is surprisingly high, especially given that our CO(1–0) map has a smaller field of view than the IRAS observations and is probably resolving out some of the molecular emission to boot. A more reasonable gas-to-dust ratio (~ 100) is still possible, however, if much of the dust in NGC 2681 is too cold to be detected by IRAS at $60\,\mu\mathrm{m}$.

The implication that much of the dust in NGC 2681 is colder than 38 K raises the question of whether we should also adopt $T_{kin} < 38\,\mathrm{K}$ in our excitation model. Indeed, a survey of Galactic molecular clouds by Scoville & Good (1989) shows the clouds' average $60/100\,\mu\mathrm{m}$ color temperatures exceeding their peak CO(1–0) brightness temperatures by a factor of three on average. This discrepancy could result from inefficient dust-gas collisional coupling (although it might merely be indicating that the gas has a lower areal filling

factor than the dust). Even if $T_{kin} < T_d$ in every region, however, we would expect at least some of the gas in NGC 2681 to have $T_{kin} \geq 38/3 = 12.7\,\mathrm{K}$. The beam-averaged dust temperature in NGC 2681 exceeds the dust temperatures ($\leq 25 - 30\,\mathrm{K}$) inferred from $40 - 250\,\mu\mathrm{m}$ observations of the Galactic center (Odenwald & Fazio 1984), suggesting that in some fraction of the IRAS beam interstellar meterial is more strongly heated by star formation or the active nucleus. We will therefore assume henceforth that $T_{kin} \sim 20\,\mathrm{K}$ in the disk and $\sim 40\,\mathrm{K}$ in the nucleus of NGC 2681.

The calculation of emergent line intensities and intensity ratios for molecular gas with a given kinetic temperature, number density, and CO abundance permits a number of competing strategies. In its simplest form, we would expect the line brightness temperature above background at velocity v to be

$$T_b(v) = f_a(v)\,\frac{\lambda^2}{2k}\,(1 - \exp(-\tau_v))\left(B_\nu(T_{ex}) - B_\nu(T_{cmb})\right) \tag{3.9}$$

for optical depth τ_v. Observations of molecular gas near Galactic H II regions reveal that this expression is *too* simple: clouds with temperature gradients show similar velocity profiles when mapped in transitions with different optical depths (e.g., CO(1–0) and its isotopomeric cousins). Such agreement implies that optically thick lines are somehow tracing material throughout a cloud, not just at its surface. The general explanation for this paradox is that a cloud's superthermal linewidth translates to a large mean free path for any photon escaping a local volume in radiative contact. The details of this explanation are linked to the origin of superthermal cloud linewidths, for which three scenarios have been proposed:

1. Clouds may be microturbulent: their full linewidths may be represented in *any* local volume (Leung & Liszt 1976). This scenario is probably ruled out by the absence of the widespread saturated and self-absorbed line profiles which it predicts.

2. Cloud linewidths may be due to large velocity gradient (LVG) bulk motions (Goldreich & Kwan 1974; Scoville & Solomon 1974). The version of this scenario which attributes all bulk motions to collapse is excluded because it predicts implausibly high star formation rates and low cloud lifetimes; however, the key assumption of constant dv/dr may remain valid for other configurations.

3. Clouds may consist of many narrow-linewidth clumps whose filling factor is low and

velocity dispersion is high (Martin et al. 1984; Kwan & Sanders 1986). In the simplest formulations of this scenario, clumps are assigned a fixed excitation temperature and do not couple radiatively. More realistic Monte Carlo simulations by Park & Hong (1995) fix only the clump *kinetic* temperature (thus allowing excitation to vary) and include radiative interactions between clumps. Extensions of the latter work (Park et al. 1996; Park & Hong 1998) suggest that the filling factor of any inter-clump medium is likely to be low, and that LVG models may correctly estimate a cloud's density although not its abundance.

For studies of external galaxies, the low filling factor of the gas severely complicates calculation of line intensities. Mathematically, we can adapt the predictions of an LVG model for a cloud perfectly coupled to the beam by introducing an *ad hoc* factor $f_a(v)$ as above. Clumpy-cloud models are more naturally extended to extragalactic observations. Martin et al. (1984) and Kwan & Sanders (1986) derive analytical expressions for an "effective" optical depth τ_v', defined by the average

$$1 - \exp(-\tau_v') = < f_a(v)\,(1 - \exp(-\tau_v)) > \tag{3.10}$$

over the solid angle of the beam, from various *a priori* clump velocity distributions. For extragalactic sources, observations can in principle constrain the clump velocity distribution: a kinematic model will specify the velocity dispersion and rotational motion of the clouds which contain the clumps. In this spirit, Eckart et al. (1990) develop a hybrid of the LVG and clumpy-cloud models to describe the molecular gas in IC 342. While commendably realistic, however, even this approach rests on untestable assumptions about the spatial and velocity scales of the "clumps" within clouds for which the local excitation is derived.

Fortunately, the intensity *ratio* of the two CO lines can (at least for certain conditions in a one-zone model) be independent both of the areal filling factor and of our strategy for describing it. We therefore make use of the published LVG models of Goldsmith et al. (1983), which predict the intensity ratio R (and emergent CO(1–0) brightness temperature) for a spherical cloud with unit filling factor. Figure 3.10 shows their results for gas kinetic temperatures of 20 K and 40 K. In the left-hand panel, we see that an intensity ratio of ~ 0.96 from gas at 20 K requires a number density $n_{\mathrm{H_2}} \geq 2800\,\mathrm{cm}^{-3}$. The right-hand panel shows that an intensity ratio of 2.76 from gas at 40 K requires $n_{\mathrm{H_2}} \geq 14500\,\mathrm{cm}^{-3}$.

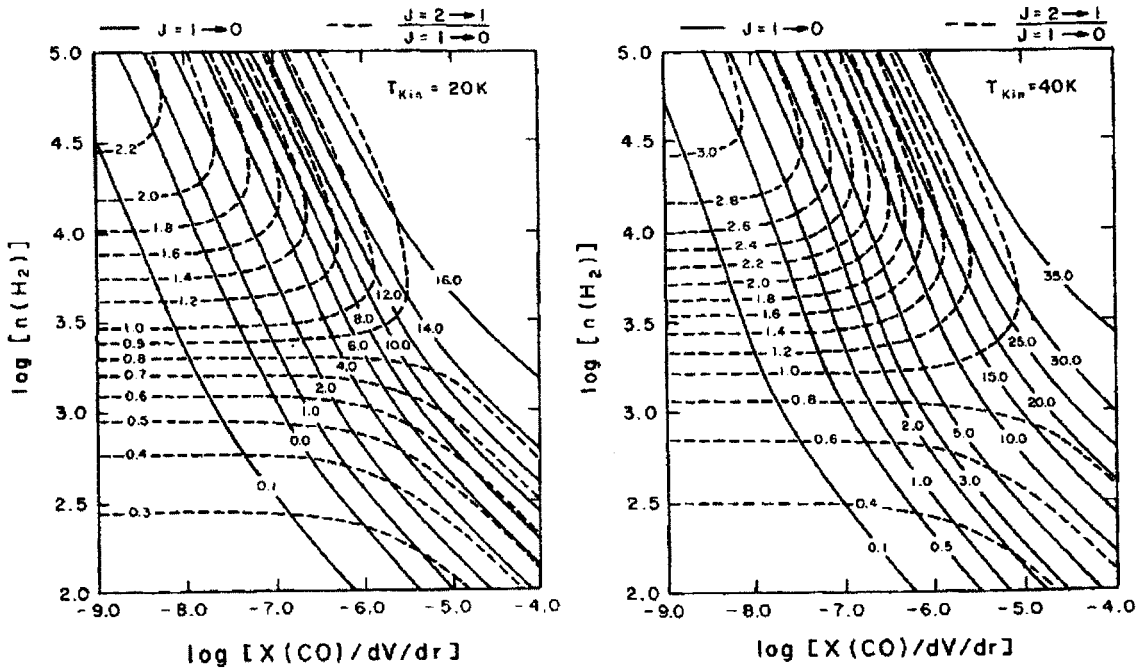

Figure 3.10: LVG models at 20 K and 40 K, reproduced from Goldsmith et al. (1983). We can use a measured intensity ratio to infer a lower limit on n_{H_2}.

Note that we can only poorly constrain the quantity $X_{\rm CO}/(dv/dr)$ using these figures, since the LVG model's predicted brightness temperatures are related to the observed brightness temperatures by the unknown factor $f_a(v)$. Our number density estimates can be compared to the critical densities of the two lines at 20 and 40 K, which we calculate using the He–CO collisional rate coefficients q_{ul} of Green & Chapman (1978) rescaled for H_2 collisions by a factor of 1.5. Defining

$$n_{crit(1-0)} = \frac{A_{10}}{q_{10}} \tag{3.11}$$

$$n_{crit(2-1)} = \frac{A_{21}}{q_{21} + q_{20}} \tag{3.12}$$

we obtain for 20 K $n_{crit(1-0)} \simeq 1850\,{\rm cm}^{-3}$ and $n_{crit(2-1)} \simeq 7090\,{\rm cm}^{-3}$; at 40 K, we find $n_{crit(1-0)} \simeq 2090\,{\rm cm}^{-3}$ and $n_{crit(2-1)} = 7680\,{\rm cm}^{-3}$.

In the outer regions of the molecular disk (where we infer $R = 0.96$ and assume $T_{kin} = 20\,{\rm K}$), n_{H_2} exceeds the critical density for CO(1–0) but not for CO(2–1). In general, $n_{H_2} > n_{crit}$ implies that a transition will be thermalized ($T_{ex} \rightarrow T_{kin}$) by collisions alone, regardless

of the amount of photon trapping. We can then solve Equation 3.9 for the product $f_a(v)\,(1-\exp(-\tau_v))$ once we are given some brightness temperature $T_b(v)$. From our kinematic model, we estimate that the CO(1–0) brightness temperature at the local mean velocity anywhere in the disk (i.e., at the peak of the Gaussian velocity profile) will be

$$T_{b(1-0)}(v_{pk}) = \frac{\bar{\sigma}_{em(1-0)}}{\sqrt{2\pi}\sigma_v} = \frac{306\,\mathrm{K\,km\,s^{-1}}}{\sqrt{2\pi}\times 21\,\mathrm{km\,s^{-1}}} = 5.8\,\mathrm{K} \tag{3.13}$$

Since

$$\frac{\lambda^2}{2k}\left(B_\nu(20) - B_\nu(2.736)\right) = 16.5\,\mathrm{K} \tag{3.14}$$

at 115 GHz, we conclude that $f_a(v)\,(1-\exp(-\tau_v)) = 0.35$. We can now place limits on $f_a(v)$ and τ_v separately: $f_a(v) \geq 0.35$ (with equality for high optical depth) and $\tau_v \geq 0.43$ (with equality for unit filling factor). Note that these limits are only valid at the local mean velocity; less stringent limits will apply in the line wings. We also cannot easily constrain the CO(2–1) optical depth, since $n_{\mathrm{H_2}} < n_{crit(2-1)}$ and it is not obvious that radiative trapping is sufficient to thermalize the transition.

In contrast, $n_{\mathrm{H_2}} > n_{crit}$ in the nucleus of NGC 2681 for *both* transitions, allowing us to assume $T_{ex(1-0)} = T_{ex(2-1)} = T_{kin}$ and to ignore photon trapping altogether. We can estimate a CO(2–1) brightness temperature for the nucleus by calculating the mean $\bar{\sigma}_{em(2-1)}$ over $r \leq 65\,pc$ (the same region used to estimate $R \simeq 2.76$) and dividing by $\sqrt{2\pi}\sigma_v$; the result is 16.0 K. Our assumption of $T_{kin} = 40\,\mathrm{K}$ now implies that $f_a(v)\,(1-\exp(-\tau_v)) = 16.0/34.5 = 0.46$, and thus that $f_a(v) \geq 0.46$ and $\tau_v \geq 0.62$ at the line peak. If we use the peak observed $T_{b(2-1)}(v) = 9.4\,\mathrm{K}$ in this analysis, we derive less stringent limits of $f_a(v) \geq 0.27$ and $\tau_v \geq 0.32$ at line peak. The still lower angular resolution of our CO(1–0) observations means that the observed peak $T_{b(1-0)}(v)$ is still less representative of gas conditions in the nucleus *per se*.

For gas in which both the CO(1–0) and CO(2–1) transitions are thermalized with $T_{ex} = T_{kin}$, it is possible to pursue a simultaneous analysis of the optical depths in both lines. In LTE, the optical depth at velocity v in the CO($J+1 \rightarrow J$) transition (derived in

Appendix B.3) becomes

$$\tau_v = \frac{8\pi^3 B_0 \mu_0^2}{3kT_{kin}} (J+1) \exp\Big[-\frac{(J+1)(J+2)}{Z}\Big] \Big(\exp\Big[\frac{2(J+1)}{Z}\Big] - 1\Big) \Theta(v) \tag{3.15}$$

where Z is a high-T_{kin} approximation for the partition function, and the integral

$$\Theta(v) = \int ds\, n_{\mathrm{H_2}} X_{\mathrm{CO}}\, \phi(v) \tag{3.16}$$

describes the fraction of the CO column density along the line of sight which lies in each velocity range. Evaluating Equation 3.15 for CO(1–0) and CO(2–1) yields

$$\tau_{v(2-1)} = \frac{16\pi^3 B_0 \mu_0^2}{3kT_{kin}} \exp\Big[-\frac{2}{Z}\Big] \Big(1 - \exp\Big[-\frac{4}{Z}\Big]\Big) \Theta(v) \tag{3.17}$$

$$\tau_{v(1-0)} = \frac{8\pi^3 B_0 \mu_0^2}{3kT_{kin}} \Big(1 - \exp\Big[-\frac{2}{Z}\Big]\Big) \Theta(v) \tag{3.18}$$

Note that there is a unique temperature T_{crit} at which $\tau_{v(2-1)} = \tau_{v(1-0)}$ for all values of $\Theta(v)$. Defining $y = \exp(-2/Z)$, equal optical depths imply $2y(1-y^2) = 1-y$ and

$$T_{crit} = \frac{2hB_0}{k \ln(\sqrt{3}+1)} = 5.56\,\mathrm{K} \tag{3.19}$$

For $T_{kin} < T_{crit}$, $\tau_{v(2-1)} < \tau_{v(1-0)}$; for $T_{kin} > T_{crit}$, $\tau_{v(2-1)} > \tau_{v(1-0)}$. We can combine these results with Equation 3.9 to evaluate the integrated intensity ratio for some velocity range:

$$\begin{aligned} R &= \frac{I_{\mathrm{CO}(2-1)}}{I_{\mathrm{CO}(1-0)}} = \frac{\int T_{b(2-1)}(v)\, dv}{\int T_{b(1-0)}(v)\, dv} \\ &= \frac{1}{4}\Big[\frac{B_{\nu_{2-1}}(T_{kin}) - B_{\nu_{2-1}}(T_{cmb})}{B_{\nu_{1-0}}(T_{kin}) - B_{\nu_{1-0}}(T_{cmb})}\Big] \frac{\int dv\, f_a(v)\,(1 - \exp(-\tau_{v(2-1)}))}{\int dv\, f_a(v)\,(1 - \exp(-\tau_{v(1-0)}))} \end{aligned} \tag{3.20}$$

For $T_{kin} = T_{crit}$, we obtain the same intensity ratio for any dependence of $f_a(v)$, namely $R = R_{crit} \simeq 0.644$. In the limit of high optical depths,

$$\begin{aligned} R &\rightarrow \frac{1}{4}\Big[\frac{B_{\nu_{2-1}}(T_{kin}) - B_{\nu_{2-1}}(T_{cmb})}{B_{\nu_{1-0}}(T_{kin}) - B_{\nu_{1-0}}(T_{cmb})}\Big] \frac{\int dv\, f_a(v)}{\int dv\, f_a(v)} \\ &= \frac{1}{4}\Big[\frac{B_{\nu_{2-1}}(T_{kin}) - B_{\nu_{2-1}}(T_{cmb})}{B_{\nu_{1-0}}(T_{kin}) - B_{\nu_{1-0}}(T_{cmb})}\Big] \end{aligned} \tag{3.21}$$

since $f_a(v)$ is identical for two lines tracing the same material. In the limit of low optical

depths and high T_{kin}, we obtain an upper bound on R (for a one-zone model) of

$$\begin{aligned} R &\rightarrow \frac{1}{4}\left[\frac{B_{\nu_{2-1}}(T_{kin}) - B_{\nu_{2-1}}(T_{cmb})}{B_{\nu_{1-0}}(T_{kin}) - B_{\nu_{1-0}}(T_{cmb})}\right] \frac{\int dv\, f_a(v)\, \tau_{v(2-1)}}{\int dv\, f_a(v)\, \tau_{v(1-0)}} \\ &\rightarrow \frac{1}{2}\left[\frac{B_{\nu_{2-1}}(T_{kin}) - B_{\nu_{2-1}}(T_{cmb})}{B_{\nu_{1-0}}(T_{kin}) - B_{\nu_{1-0}}(T_{cmb})}\right] \frac{\exp(-2/Z)\,(1 - \exp(-4/Z))}{1 - \exp(-2/Z)} \frac{\int f_a(v)\,\Theta(v)\,dv}{\int f_a(v)\,\Theta(v)\,dv} \\ &\rightarrow \frac{1}{2}\left[\frac{\nu_{2-1}^2}{\nu_{1-0}^2}\right]\frac{4}{2} = 4 \end{aligned} \tag{3.22}$$

since the product $f_a(v)\,\Theta(v)$ will also be the same for both lines. For moderate optical depths, R will in general depend on our specifications for $\Theta(v)$ and $f_a(v)$, e.g., on our adoption of a clumpy-cloud or LVG model for radiative transfer. Making the assumption of constant dv/ds allows us to simplify R for *any* optical depths, since τ_v becomes independent of v (see Equation B.61) and passes through the integrals:

$$\begin{aligned} R &\rightarrow \frac{1}{4}\left[\frac{B_{\nu_{2-1}}(T_{kin}) - B_{\nu_{2-1}}(T_{cmb})}{B_{\nu_{1-0}}(T_{kin}) - B_{\nu_{1-0}}(T_{cmb})}\right] \frac{(1 - \exp(-\tau_{v(2-1)}))}{(1 - \exp(-\tau_{v(1-0)}))} \frac{\int dv\, f_a(v)}{\int dv\, f_a(v)} \\ &= \frac{1}{4}\left[\frac{B_{\nu_{2-1}}(T_{kin}) - B_{\nu_{2-1}}(T_{cmb})}{B_{\nu_{1-0}}(T_{kin}) - B_{\nu_{1-0}}(T_{cmb})}\right] \frac{(1 - \exp(-\tau_{v(2-1)}))}{(1 - \exp(-\tau_{v(1-0)}))} \\ &= \frac{T_{b(2-1)}}{T_{b(1-0)}} = R_T \end{aligned} \tag{3.23}$$

The integrated intensity ratio R thus collapses to a brightness temperature ratio R_T.

We wish now to estimate the optical depths of the CO(2–1) and CO(1–0) lines in the nucleus of NGC 2681. Figure 3.11 shows the ratio of brightness temperatures $R_T = T_{b(2-1)}/T_{b(1-0)}$ as a function of $\Theta(v)$ and T_{kin}, where we now assign $\Theta(v)$ conventional units of $\mathrm{cm}^{-2}\,(\mathrm{km\,s}^{-1})^{-1}$. We plot curves of constant R_T, ranging from 0.444 to 3.344 in steps of 0.1. Along each curve, $\tau_{v(1-0)}$ and $\tau_{v(2-1)}$ increase from left to right; thick lines in the figure correspond to optically thick CO(1–0) emission, which is confined to curves for $R_T < 1$. The curve for $R_T = R_{crit}$ is the flat line at $T_{kin} = T_{crit}$. At high $\Theta(v)$, all curves for $R_T < 1$ approach an upper or a lower limit to T_{kin}; no such limits apply to the curves for $R_T > 1$. To use this figure to advance our analysis, we *must* assume constant dv/ds so that we can set $R = R_T$ as in Equation 3.23. For the nucleus of NGC 2681, our measurement of $R = 2.76$ and assumption of $T_{kin} = 40\,\mathrm{K}$ imply that $\Theta(v) \simeq 7.6 \times 10^{15}\,\mathrm{cm}^{-2}\,(\mathrm{km\,s}^{-1})^{-1}$ and (after substitution into Equation 3.15) that $\tau_{v(1-0)} = 0.10$ and $\tau_{v(2-1)} = 0.33$. The latter result is reasonably consistent with our earlier estimate that $\tau_{v(2-1)} \geq 0.32 - 0.62$ at the mean local

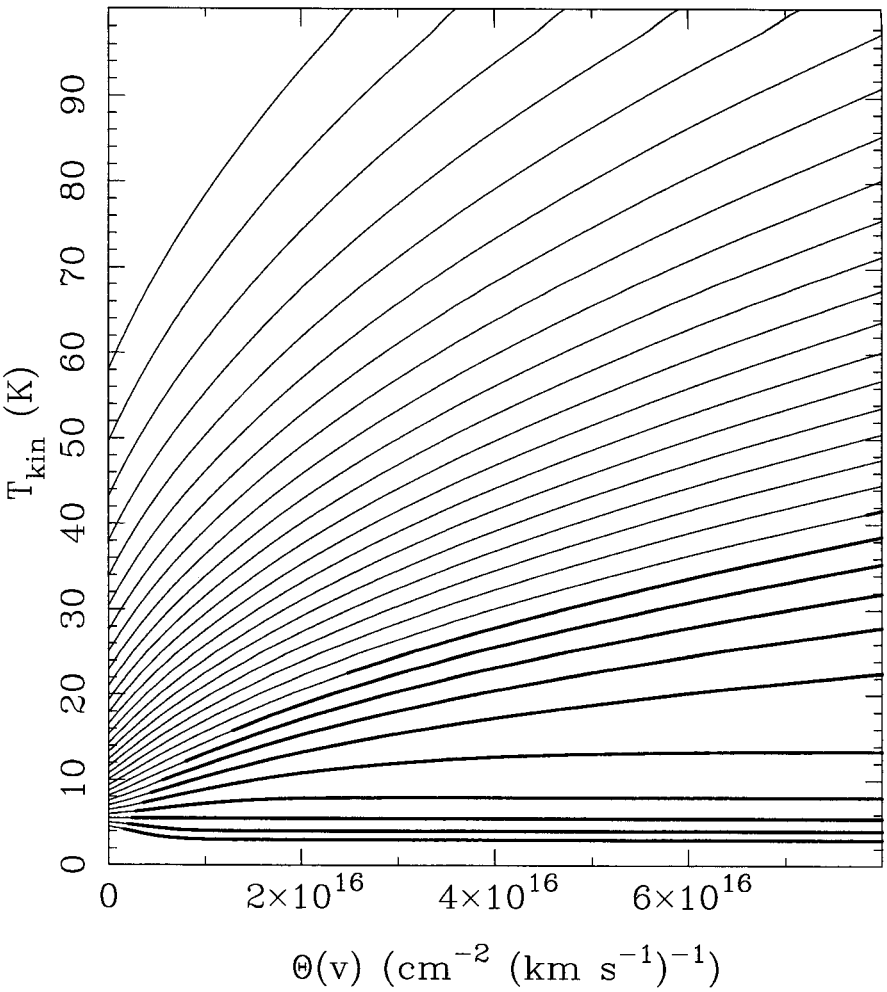

Figure 3.11: One-zone LTE model: curves in the $(\Theta(v), T_{kin})$ plane for constant brightness temperature ratio $R_T = T_{b(2-1)}/T_{b(1-0)}$. Curves are plotted for R_T ranging from 0.444 (at bottom) to 3.344 (at top) in steps of 0.1, and are boldfaced where $\tau_{v(1-0)} \geq 1$.

velocity.

One consequence of assuming constant dv/ds is our ability to write

$$\Theta(v) = \bar{n}_{\mathrm{H_2}} \frac{X_{\mathrm{CO}}}{dv/ds} = \bar{n}_{\mathrm{H_2}} \frac{X_{\mathrm{CO}}}{\Delta v/\Delta s} \tag{3.24}$$

We can further simplify $\Theta(v)$ by using an approximate relation between Δv and Δs for an ensemble of virialized clouds– a configuration motivated by the discussion in Section 3.5.1.

A spherical cloud with radius r_{cl} will have mass

$$M_{cl} \simeq 1.36 \times \frac{4\pi}{3} r_{cl}^3 \times 2 m_{\rm H}\, f_v\, n_{\rm H_2} \simeq \frac{r_{cl}\,(\Delta v)^2}{G} \tag{3.25}$$

if it consists of clumps whose internal number density is $n_{\rm H_2}$ and volume filling factor is f_v (i.e., $\bar{n}_{\rm H_2} = f_v\, n_{\rm H_2}$). The mean path length through such a cloud will be

$$\Delta s \simeq \frac{4}{3}\, r_{cl} \tag{3.26}$$

Combining Equations 3.25 and 3.26, we can eliminate r_{cl} to obtain

$$\begin{aligned} \frac{\Delta v}{\Delta s} &\simeq \left(1.36 \times \frac{3\pi}{2} \times m_{\rm H} G\right)^{\frac{1}{2}} \left(f_v\, n_{\rm H_2}\right)^{\frac{1}{2}} \\ &= 8.45 \times 10^{-21} \left(\frac{f_v\, n_{\rm H_2}}{\rm cm^{-3}}\right)^{\frac{1}{2}} {\rm km\,s^{-1}\,cm^{-1}} \end{aligned} \tag{3.27}$$

This approximation is true both for a single virialized cloud and for an ensemble thereof. Substituting into Equation 3.24, we find

$$n_{\rm H_2} = 0.714\, f_v^{-1} \left(\frac{X_{\rm CO}}{10^{-4}}\right)^{-2} \left(\frac{\Theta(v)}{10^{16}\,{\rm cm^{-2}\,(km\,s^{-1})^{-2}}}\right)^2 {\rm cm^{-3}} \tag{3.28}$$

where we have normalized $X_{\rm CO}$ to a fairly standard abundance. Our estimate of $\Theta(v)$ now implies that in the nucleus of NGC 2681,

$$n_{\rm H_2} \simeq 0.412\, f_v^{-1} \left(\frac{X_{\rm CO}}{10^{-4}}\right)^{-2} {\rm cm^{-3}} \tag{3.29}$$

In view of our previous determination from Figure 3.10 that $n_{\rm H_2} \geq 14500\,{\rm cm^{-3}}$, this result is rather perplexing. Each of several scenarios might account for part of the factor $14500/0.412 \simeq 3.52 \times 10^4$ by which the coefficient in Equation 3.29 falls short:

1. The CO abundance is unusually low. For this to be the sole contributing factor, however, we would require a smaller $X_{\rm CO} = 5.3 \times 10^{-7}$ than is observed in any Galactic molecular clouds.

2. The filling factor is unusually low. Here we would nominally require $f_v \simeq 2.8 \times 10^{-5}$ to explain the full shortfall in $n_{\rm H_2}$– a rather glaring contradiction of our earlier estimate that $f_a(v) \geq 0.27 - 0.46$ for the CO(2–1) emission at its local mean velocity, since we

expect typically $f_a(v) \leq f_v^{2/3}$.

3. The molecular gas in the nucleus of NGC 2681 is not virialized. For a predominantly non-gravitational linewidth, $\Delta v/\Delta s$ would be larger than we have indicated in Equation 3.27, and $\Theta(v)$ would in turn be smaller. Seeing such an effect in an active nucleus would not be surprising; however, too large a linewidth would conflict with our kinematic model's rather low estimate of $\sigma_v = 21\,\mathrm{km\,s^{-1}}$ for the velocity dispersion. We would also expect any shocks or outflow in the molecular gas to be accompanied by one of the two [possibly more important] scenarios we mention next.

4. Our assumption of a single zone of molecular gas is bad. Recalling that $\tau_{v(2-1)} > \tau_{v(1-0)}$ for $T_{kin} > T_{crit}$, we can imagine that for a cloud whose surface is hotter than its interior, the CO(2–1) line will reach $\tau_{v(2-1)} \sim 1$ in gas with higher T_{kin} than characterizes the material where $\tau_{v(1-0)} \sim 1$. In this situation, the two transitions will *not* trace the same material. Among other consequences, LVG radiative transfer calculations would be incorrect and $R > 1$ would no longer be a sure sign of optically thin CO(1–0) emission. We will examine this possibility more closely in Section 3.5.3.

5. The kinetic temperature in the nucleus of NGC 2681 exceeds 40 K. If we repeat the steps of our analysis for $T_{kin} = 60\,\mathrm{K}$, we find that (a) $n_{crit(1-0)}$ and $n_{crit(2-1)}$ increase to $\simeq 2290\,\mathrm{cm^{-3}}$ and $\simeq 8080\,\mathrm{cm^{-3}}$, respectively; (b) our lower limit on $n_{\mathrm{H_2}}$ from the LVG models of Goldsmith et al. (1983) is relaxed to $\simeq 6310\,\mathrm{cm^{-3}}$; (c) our lower limits on the optical depth and areal filling factor of the CO(2–1) line at the local mean velocity are relaxed to $f_a(v) \geq 0.17 - 0.29$ and $\tau_{v(2-1)} \geq 0.19 - 0.35$; and (d) our constant-$dv/ds$ interpretation of Figure 3.11 increases $\tau_{v(2-1)}$ to 0.59 and $\Theta(v)$ to $2.8 \times 20^{16}\,\mathrm{cm^{-2}\,(km\,s^{-1})^{-1}}$. Equation 3.29 now becomes

$$n_{\mathrm{H_2}} \simeq 5.47\, f_v^{-1} \left(\frac{X_{\mathrm{CO}}}{10^{-4}}\right)^{-2} \mathrm{cm^{-3}} \tag{3.30}$$

This experiment has generally positive results: the apparent shortfall in $n_{\mathrm{H_2}}$ is reduced to a more manageable $6310/5.47 \simeq 1150$, and the estimates of CO(2–1) optical depth based on the intensity ratio and on the peak $T_{b(2-1)}$ are in good agreement. Unfortunately, we have also reduced our confidence in the claim that $T_{ex} = T_{kin}$ for the CO(2–1) line. Photon trapping for an optical depth of $\tau_{v(2-1)} = 0.59$ will lower

the effective critical density by roughly the escape probability for a spherical cloud:

$$\beta(\tau_{v(2-1)}) = \frac{1 - \exp\left(-\tau_{v(2-1)}\right)}{\tau_{v(2-1)}} = 0.76 \tag{3.31}$$

This effect conveniently reduces $n_{crit(2-1)}$ to $\simeq 6100$, just below our lower bound on n_{H_2} at 60 K. However, our reliance on an NLTE mechanism to ensure thermalization of the CO(2–1) line suggests that our subsequent LTE analysis of the intensity ratio may be too simplistic. A fully self-consistent NLTE version of Figure 3.11 would become essential if we were to consider additional models with $T_{kin} > 60$ K.

The success of a one-zone treatment of the gas in the nucleus of NGC 2681 is decidedly mixed. Although we have not demonstrated a perfectly self-consistent model, our calculations consistently imply that (a) at least some of the molecular gas at $r \leq 65$ pc is warm, with T_{kin} probably ≥ 60 K, and (b) the optical depth of the emission from this gas is rather low for both CO lines. The persistence of low-τ_v material in the vicinity of an active nucleus, where we would naively expect the destruction rate of weakly self-shielding CO molecules to be enhanced, is a somewhat unexpected result. In the following section, we explore the possibility that this may be an *erroneous* result which originates in an incorrect assumption that both of the transitions we have mapped truly trace the same material.

3.5.3 External heating models

A fairly standard alternative to a one-zone model of a galaxy's molecular gas locates much of its CO emission in a second, diffuse component– cloud "envelopes" or an unbound inter-cloud medium– which has LTE conditions distinct from those of cloud "cores." The existence of such material has been deduced from CO isotopomer observations in starburst nuclei (Turner et al. 1990; Wall et al. 1993; Aalto et al. 1994, 1995) and the Galaxy (Polk et al. 1988); the diffuse gas accounts for ^{12}CO emission in excess of what can emerge from cold, dense cores seen in optically thick ^{13}CO emission. The presence of this second "zone" of material does not necessarily correlate with an elevated ^{12}CO intensity ratio ($R > 1$), however. Turner et al. (1990) do estimate $R \simeq 1.8$ in the inner 22″ of M 82, while Wall et al. (1993) find $R \simeq 1.1 - 1.3$ in the inner 20″ of five starburst nuclei and Aalto et al. (1994) measure $R \simeq 1.12$ in the inner 43″ of NGC 1808. However, the mean $\bar{R} = 0.93 \pm 0.22$ measured in the sample of 19 infrared-bright (i.e., star-forming) galaxies of Aalto et al.

(1995) agrees well with the mean $\bar{R} = 0.89 \pm 0.06$ determined by Braine et al. (1993) for their survey of spirals. In the absence of ^{13}CO observations of NGC 2681, we thus lack the specific evidence (and the requisite number of observational constraints) to justify a two-zone model like those of the cited authors. There are in any case grounds to suspect that most two-zone models may be somewhat unrealistic– lack of radiative coupling between the two zones, discretization of physical conditions which are likely to be continuous, and vague specification for how the diffuse component is heated to a higher kinetic temperature.

A distinct approach to modelling molecular line emission entails describing both (outside-in) heating and (inside-out) radiative transfer within the same parcel of gas. This strategy eliminates some of the artificiality of the two-zone approach; it also discards the requirement that the two CO transitions trace the same material, giving us a helpful flexibility as we try to model intensity ratios $R > 1$. The details of such an external heating model are tightly meshed with our choice of mechanism for heating the gas. Our first candidate is ionization of H_2 by $\sim 2 - 10\,\mathrm{eV}$ cosmic rays, which constitutes the primary source of energy for Galactic cloud interiors at a rate $\zeta_0 \simeq 4 \times 10^{-17}\,\mathrm{s}^{-1}$ (Black 1987). Cosmic rays of comparable energies are probably present in active nuclei, accelerated either by SNR shocks or (as a low-energy tail of the observed $E \geq 10^{18}\,\mathrm{eV}$ distribution) by shocks or magnetic reconnection in accretion disks (Axford 1994). Unfortunately, acceleration in SNR need not produce specifically *external* heating of clouds, while acceleration in accretion disks remains doubtful without confirmation in QSO spectra of the expected spallation by $10^7 - 10^{12}\,\mathrm{eV}$ cosmic rays (Crosas & Weisheit 1996). We therefore do not consider cosmic ray heating a viable scenario at this time. A second possible mechanism for external heating of molecular clouds is the injection of mechanical energy from a radio jet. Since NGC 2681 shows no evidence for such a jet, we do not consider this possibility.

A third, more promising mechanism is photoelectric heating of dust grains by a strong UV continuum. Correlation of [CII] $158\,\mu$m with CO(1–0) emission in external galaxies suggests that the latter is enhanced where young stars heat PDR (photon-dominated region) cloud surfaces (Crawford et al. 1985). The possible connection between external heating of PDRs and a high intensity ratio R was originally suggested in a study of M 82 by Young & Scoville (1984). The particular value of the intensity ratio expected in this scenario can be estimated from the calculations of Tauber & Goldsmith (1990), who generate [clumpy-cloud] models for the CO emission from the Orion molecular cloud. For UV field

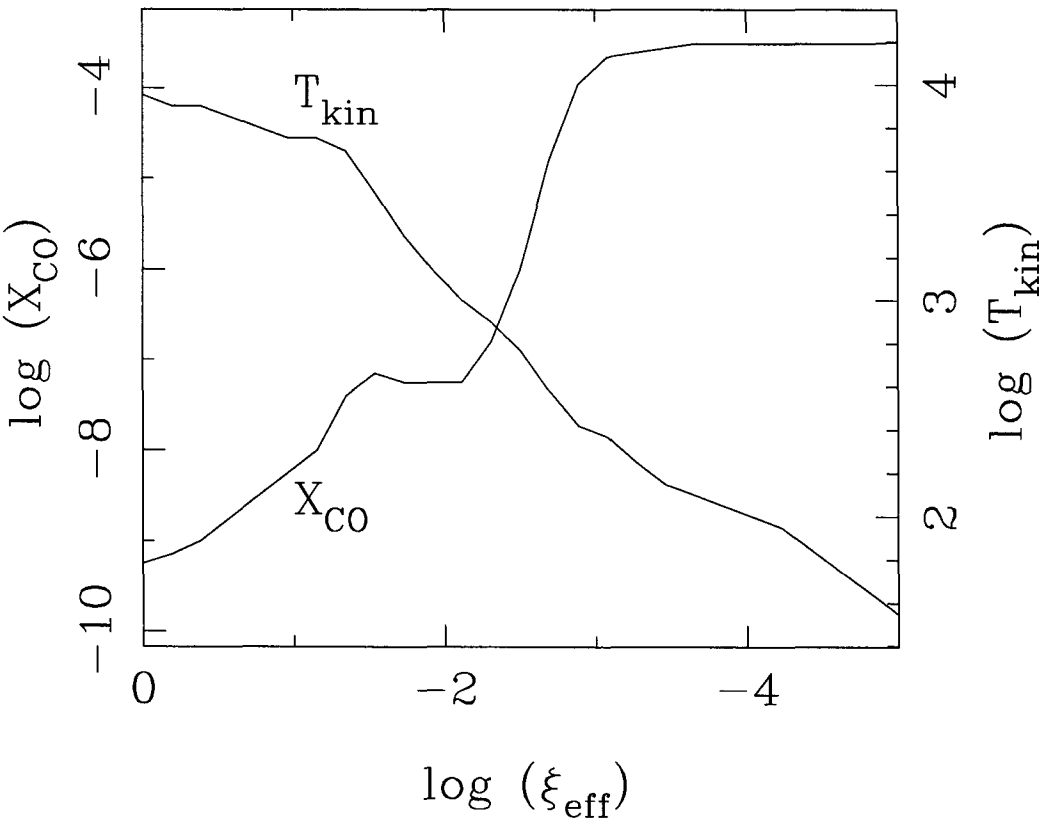

Figure 3.12: Heating in an XDR model, after Maloney et al. (1996). As specified in Equation 3.32, each choice for the incident flux F_X corresponds to a different mapping between the effective ionization parameter ξ_{eff} and the path length into the cloud $L = N_{tot}/n_{tot}$. For fixed F_X, L increases from left to right in this figure.

enhancements of $G_0 = 3 \times 10^2 - 3 \times 10^4$ above the average interstellar field, R (evaluated at line center) takes values $\simeq 1.42 - 1.54$; the upper end of this range is actually achieved at $G_0 = 3 \times 10^3$. We cannot constrain how badly we would overestimate M_{gas} using a standard conversion factor in this case, since the authors do not provide information on the optical depths of the CO lines. Although its predictions for R still fall below our measurement of 2.76 in the nucleus of NGC 2681, the Tauber & Goldsmith (1990) model might still permit higher intensity ratios for different assumed dependences of the volume filling factor f_v, internal number density n_{H_2}, core CO abundance X_{CO}, and velocity distribution of the clumps. In addition, we would expect any nonstellar contribution to the UV continuum to affect its penetration into the model cloud as a function of depth.

Our last possible explanation for external heating of molecular clouds is irradiation by

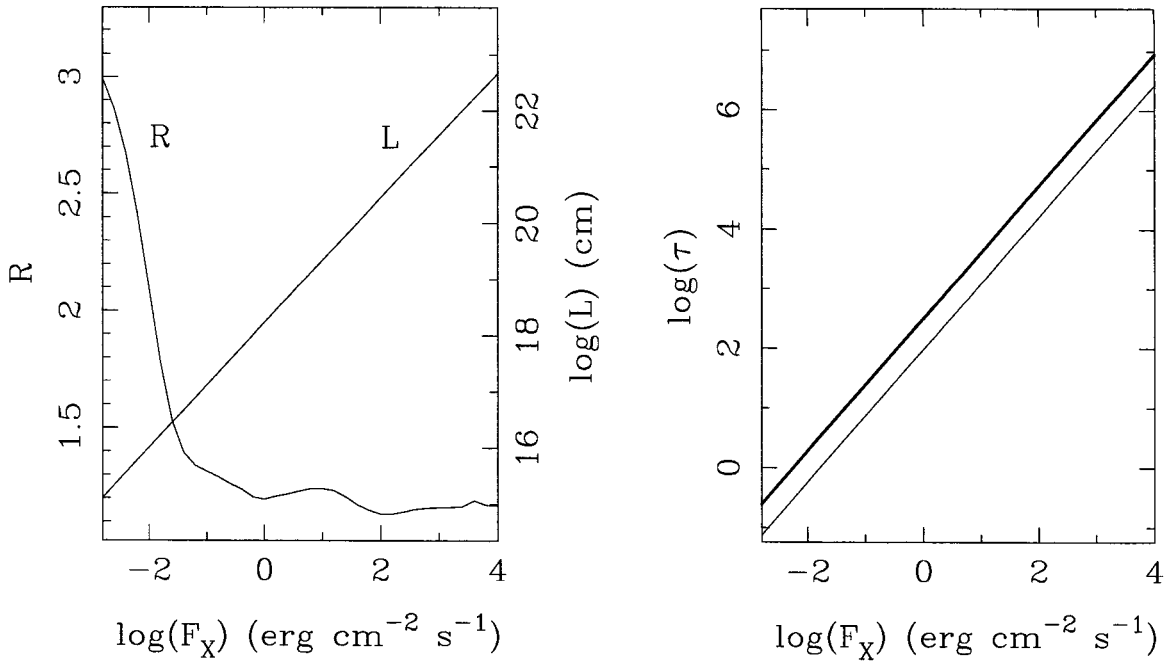

Figure 3.13: Intensity ratios and optical depths in an XDR model, after Maloney et al. (1996). Left panel shows R and total path length $L = s_{max} - s_{min}$ as a function of the incident X-ray flux F_X, where we have integrated emission over the range in s corresponding to the range in effective ionization parameter ξ_{eff} shown in Figure 3.12. Right panel shows the total optical depths $\tau_v(s_{max})$ for the CO(1–0) and [boldfaced] CO(2–1) transitions.

X-rays from the active nucleus. In principle, this mechanism has an important advantage over heating by UV photons when we try to explain high CO intensity ratios: higher-energy X-rays can penetrate to greater depths, where the gas they heat will have higher CO abundance. To explore this scenario in detail, we turn to the XDR ("X-ray Dissociation Region") model of Maloney et al. (1996), who consider a plane-parallel slab of gas illuminated by a power-law flux $F_X(E) \propto E^{-\alpha}$. UV photons are assumed to be attenuated by a $10^{21}\,\mathrm{cm}^{-2}$ column of atomic hydrogen, leaving photoelectric absorption (at $E \leq 10\,\mathrm{keV}$) and Compton scattering (at $E > 10\,\mathrm{keV}$) as the dominant mechanisms for heating within the slab. Kinetic temperature falls and fractional CO abundance rises at increasing depth into the slab, which is indexed here by an effective ionization parameter

$$\xi_{eff} = 1.26 \times 10^{-4} \left(\frac{F_X}{\mathrm{erg\,cm^{-2}\,s^{-1}}}\right) \left(\frac{n_{tot}}{10^5\,\mathrm{cm^{-3}}}\right)^{-1} \left(\frac{N_{tot}}{10^{22}\,\mathrm{cm^{-2}}}\right)^{-0.9} \qquad (3.32)$$

appropriate for $\alpha \simeq 0.7$, where $N_{tot} = N_{\mathrm{H}} + N_{\mathrm{H_2}}$ and $n_{tot} = n_{\mathrm{H}} + n_{\mathrm{H_2}}$. Strictly speaking,

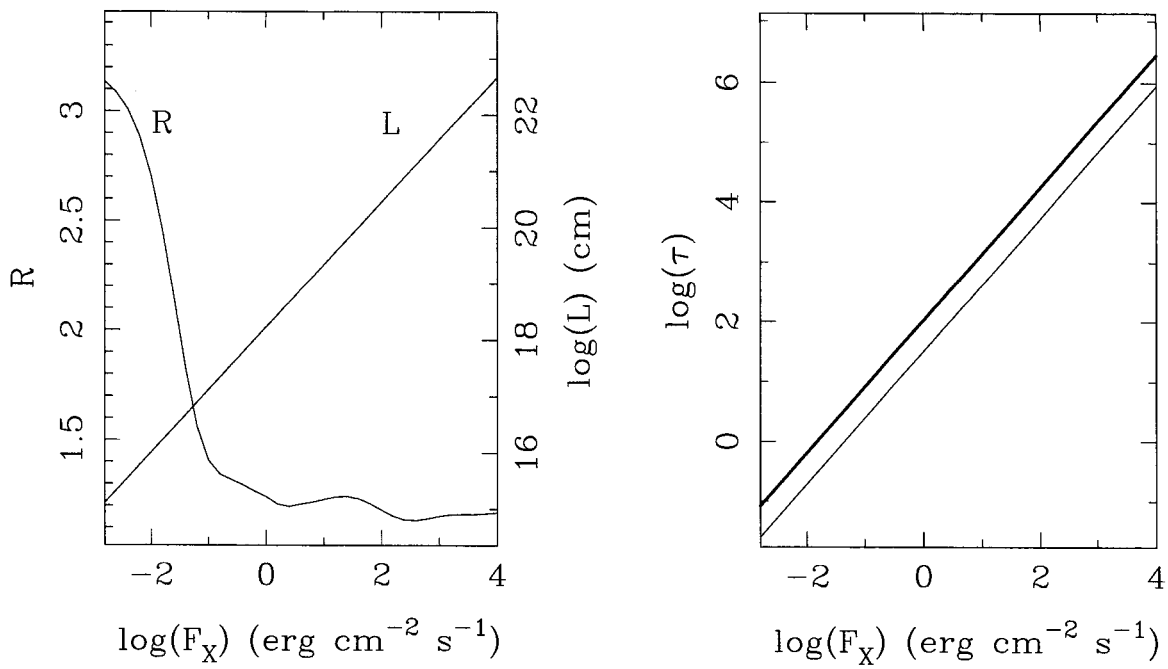

Figure 3.14: The effect of changing the local velocity width Δv in the XDR model of Maloney et al. (1996). The models whose results we plot here are identical to those which generated Figure 3.13, except for the use of $\Delta v = 15\,\mathrm{km\,s^{-1}}$ rather than $5\,\mathrm{km\,s^{-1}}$ in Equation 3.37.

Maloney et al. (1996) only present a single model with fixed

$$F_X \simeq 84 \left(\frac{L_X}{10^{44}\,\mathrm{erg\,s^{-1}}}\right)\left(\frac{r}{100\,\mathrm{pc}}\right)^{-2} \mathrm{erg\,cm^{-2}\,s^{-1}} \tag{3.33}$$

and ξ_{eff} varying within the slab as this flux is attenuated over the column density range $N_{tot} = 10^{21} - 10^{23}\,\mathrm{cm^{-2}}$. Most of their models instead assume a fixed N_{tot} and vary ξ_{eff} by varying F_X; these two approaches turn out to be largely equivalent, since the model results depend much more strongly on ξ_{eff} than on N_{tot} or n_{tot}.

To calculate the emergent CO line intensities in the XDR model, we have first interpolated T_{kin} and X_{CO} from the authors' fixed-F_X model for $-1.07 \geq \log(\xi_{eff}) \geq -2.87$ (their Figure 10), and from their fixed-N_{tot} model outside this range (their Figure 3a). Our Figure 3.12 shows the result; the combined model assumes $n_{tot} = 10^5\,\mathrm{cm^{-3}}$ and local velocity width $5\,\mathrm{km\,s^{-1}}$ everywhere within the slab. Next, we have determined that photon trapping is not likely to play an important role in the radiative transfer of CO emission out of the slab. Schinke et al. (1985) calculate the rate coefficients for the $J \rightarrow 0$ collisional

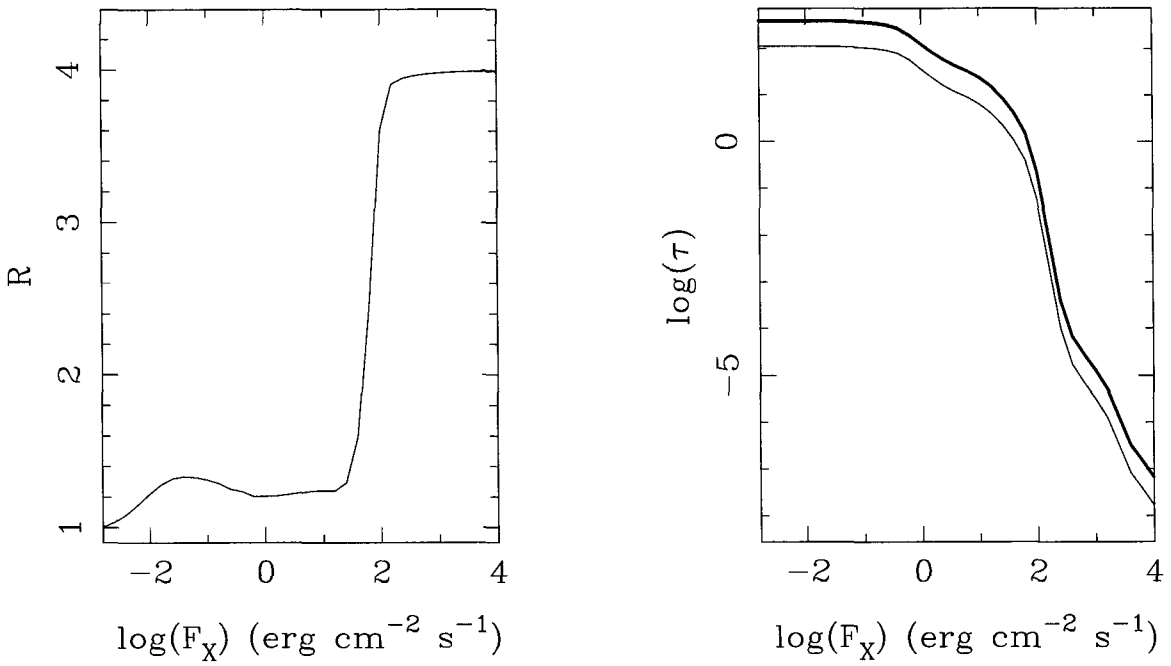

Figure 3.15: Values of R, L, and $\tau_v(s_{max})$ from the model of Figure 3.13, where s_{max} has now been fixed at 1×10^{18} cm, and we have assumed that gas at depths with $\log(\xi_{eff}) < -5$ has $T_{kin} = 35.5\,\mathrm{K}$ and $X_{\mathrm{CO}} = 3.3 \times 10^{-4}$. Values of F_X which yield $\tau_v(s_{max}) < 1$ should be ignored, since penetration of X-rays to s_{max} is inconsistent with the semi-infinite slab geometry assumed by Maloney et al. (1996).

transitions of CO at temperatures up to 2000 K (note that these strictly apply only to collisions with para-H_2, although here we will assume identical cross-sections for ortho-H_2). We recover the corresponding rates for collisional de-excitation by the detailed balance relation

$$q_{J0} = q_{0J}\,(2J+1)\exp\left(\frac{hB_0J(J+1)}{kT_{kin}}\right) \tag{3.34}$$

giving $q_{10} \simeq 2.35 \times 10^{-11}\,\mathrm{cm^3\,s^{-1}}$ and $q_{20} \simeq 7.04 \times 10^{-11}\,\mathrm{cm^3\,s^{-1}}$ at $T_{kin} = 2000\,\mathrm{K}$. At this temperature, we can conclude $n_{crit(1-0)} \simeq 3060\,\mathrm{cm^{-3}}$ and (altogether ignoring q_{21}, which requires evaluating a sum over Wigner $3j$-symbols) $n_{crit(2-1)} \leq 9820\,\mathrm{cm^{-3}}$. Since our assumed $n = 10^5\,\mathrm{cm^{-3}}$ exceeds both of these values, we can assume that both the CO(1–0) and CO(2–1) transitions are thermalized. This argument may be somewhat weakly justified near the surface of the cloud, where $T_{kin} > 2000\,\mathrm{K}$ and the collisional cross-sections q_{J0} should reflect the fact that not all of the hydrogen will be molecular; however, since the fractional CO abundance will also be quite low at this depth, we anticipate a relatively

small effect on the emergent CO emission and intensity ratio.

We can now proceed to solve the equation of radiative transfer for both transitions. If the surface of the slab is perpendicular to our line of sight (with the X-ray source interposed), we can write for each transition

$$\begin{aligned} \frac{2k}{\lambda^2} T_b(v) &= B_\nu(T_{cmb}) \left(1 - \exp\left(-\tau_v(s_{max})\right)\right) \\ &+ \int_{s_{min}}^{s_{max}} B_\nu(T_{kin}(s)) \frac{d\tau_v}{ds}\Big(T_{kin}(s), X_{\rm CO}(s)\Big) \exp\left(-\tau_v(s)\right) ds \end{aligned} \tag{3.35}$$

where s_{min} and s_{max} are the path lengths mapped to $\log(\xi_{eff}) = 0$ and $\log(\xi_{eff}) = -5$ by Equation 3.32 for some assumed F_X. The expression $\tau_v(s)$ denotes the integral

$$\tau_v(s) = \int_{s_{min}}^{s} \frac{d\tau_v}{ds}\Big(T_{kin}(s'), X_{\rm CO}(s')\Big) ds' \tag{3.36}$$

where we have adapted Equation 3.15 in deriving

$$\frac{d\tau_v}{ds} = \frac{8\pi^3 B_0 \mu_0^2}{3kT_{kin}(s)} (J+1) \exp\Big[-\frac{(J+1)(J+2)}{Z(s)}\Big] \Big(\exp\Big[\frac{2(J+1)}{Z(s)}\Big] - 1\Big) \frac{n_{tot} X_{\rm CO}(s)}{\Delta v} \tag{3.37}$$

In Equation 3.37 we have evaluated $\Theta(v)$ by assuming constant dv/ds; this assumption also permits us to evaluate $R \rightarrow T_{b(2-1)}/T_{b(1-0)}$ independent of the areal filling factor. Figure 3.13 shows the results of our calculations for a range of incident X-ray fluxes. The left panel plots both the derived R and the total path length $L = s_{max} - s_{min}$ which correspond to each value of F_X. For small F_X, $\log(\xi_{eff})$ changes from 0 to -5 over a rather short path length; as a result, optical depths $\sim \tau_v(s)$ are on the low side and we can obtain intensity ratios ≥ 2.5. For larger F_X, we require a longer path length for $\log(\xi_{eff})$ to reach -5; in this case, $\tau_v(s)$ will typically be $\gg 1$, as our plot of $\tau_v(s_{max})$ in the right panel of Figure 3.13 illustrates. In contrast to the one-zone model's prediction of $R \rightarrow 1$ at high optical depths, however, we find here that $R \rightarrow 1.1 - 1.2$: the CO(2–1) transition becomes optically thick closer to the surface of the slab, where the gas temperature is higher. Our result confirms that CO(1–0) emission can be optically thick for at least certain $R > 1$, and suggests that use of the Galactic conversion factor to calculate gas masses is defensible in nuclei whose intensity ratios are only moderately greater than unity.

Although the viability of X-ray heating as an explanation for such intensity ratios seems

robust, a particular observed R can correspond to many combinations of XDR model parameters. In Figure 3.14, we show the values of R, L, and $\tau_v(s_{max})$ which result if we replace $\Delta v = 5\,\mathrm{km\,s^{-1}}$ in Equation 3.37 with a larger $\Delta v = 15\,\mathrm{km\,s^{-1}}$. Although this modification is inconsistent with the Δv assumed by Maloney et al. (1996) in deriving the variations of T_{kin} and X_{CO} with path length, it is not unreasonable if some of the irradiated gas is diffuse and turbulent. Comparison with Figure 3.13 confirms the expected result: increasing the linewidth generally reduces optical depths and increases the intensity ratio observed at a given F_X and total path length L. In Figure 3.15, we show a different variation on the standard XDR model: we plot the intensity ratio and optical depths expected from a slab of constant thickness $\sim 0.3\,\mathrm{pc}$ for a range in F_X. Here we have made rather significant departures from the assumptions of Maloney et al. (1996). At high F_X, the penetration of a large fraction of F_X to s_{max} compromises the assumption of a semi-infinite slab geometry made by Maloney et al. (1996) in constructing their model; our inference of $R \gg 1$ in this regime is therefore essentially meaningless. At low F_X, we have assumed that the temperature and fractional CO abundance far from the illuminated surface of the slab are constant for $\log(\xi_{eff}) \leq -5$ (i.e., $T_{kin} = 35.5\,\mathrm{K}$ and $X_{\mathrm{CO}} = 3.3 \times 10^{-4}$). This is a plausible assumption which is broadly consistent with the standard XDR model; in fact, our prediction of R reaching $1.2 - 1.3$ at low F_X and high $\tau_v(s_{max})$ may be more realistic than the $R \gg 2$ seen in Figure 3.13. Besides the local velocity width and cloud thickness, clumpiness, oblique illumination, and different treatments of UV attenuation could easily change our predictions for R. Such aspects of the XDR model will change the dependences of $T_{kin}(s)$ and $X_{\mathrm{CO}}(s)$ from those we have used, and are thus beyond the scope of this thesis.

3.6 Conclusions

From our models of the CO(1–0) and CO(2–1) emission in the nucleus of NGC 2681, we can draw the following conclusions:

1. The mass distribution in NGC 2681 is strongly centrally concentrated, with approximately $2.0 \times 10^8\,\mathrm{M_\odot}$ contained within $r \leq 26\,\mathrm{pc}$.

2. Most of the galaxy's molecular emission is confined to an annulus with $18\,\mathrm{pc} \leq r \leq$

$145 - 157\,\mathrm{pc}$; the outer radius has a scale comparable to the semimajor axis of an apparent tertiary bar.

3. The integrated intensity ratio R is higher near the inner radius of the disk than near the outer radius, and is higher for the emission we detect with the interferometer than for the emission which we fail to detect. These trends provide qualitative evidence that density and/or kinetic temperature of the molecular gas rise as we move from the outskirts of the galaxy to its center.

4. Near the nucleus of the galaxy, we estimate R to be well in excess of unity (~ 1.85 using our data convolved to $4''$ resolution, and ~ 2.76 using our model results for the innermost $1''$). These intensity ratios are among the highest ever measured, and are best explained if the gas has high kinetic temperature ($T_{kin} \geq 60$) and rather low optical depths in the CO lines. The persistence of low-optical-depth molecular material in the vicinity of an active nucleus is more plausible if much of the emission we see arises on the surfaces of clouds which are illuminated by strong UV or X-ray fluxes.

Chapter 4 A warped molecular disk in NGC 1068

4.1 Introduction

At $d = 14.4\,\mathrm{Mpc}$ (Tully 1988), NGC 1068 is the nearest bright Seyfert galaxy. Extensively studied at all wavelengths, it has also been the sole subject of a recent conference, whose "Ringberg standards" for nomenclature and numerical values (Bland-Hawthorn et al. 1997a) we will adopt here unless our own data argue otherwise. Among active galaxies, NGC 1068 is notable for the infrared-bright starburst extending over its inner 1.4 kpc in radius. The same region is also rich in molecular gas, which a number of interferometric studies of the CO(1–0) line have resolved into a nearly continuous pair of spiral arms (Planesas et al. 1991; Kaneko et al. 1992; Helfer & Blitz 1995; Tacconi et al. 1997). Less prominent CO(1–0) emission is seen at the galaxy's nucleus by Helfer & Blitz (1995) and Tacconi et al. (1997), in a structure which is strongly detected in the dense gas tracers HCN(1–0) and CS(2–1) (Jackson et al. 1993; Tacconi et al. 1994; Helfer & Blitz 1995; Tacconi et al. 1997). Between the spiral arms and the nucleus, there are hints of molecular emission along the leading edge of a stellar bar (Helfer & Blitz 1995; Tacconi et al. 1997). In order to determine what happens to such gas *after* it flows into the nucleus, we have obtained new 1.5″-resolution observations of the CO(2–1) line in NGC 1068. Our data reveal that the molecular gas structure in the galaxy's nucleus exhibits asymmetric excitation and unusual kinematics; taken together, these results are best explained as signatures of gas motions in a warped molecular disk.

4.2 Observations

We observed the CO(1–0) transition in NGC 1068 in 1995, and the CO(2–1) transition between 1995 and 1997; Table 4.1 summarizes both sets of observations, which include a CO(1–0) track in a C (unusually **C**ompact) configuration of the array. Continuum and spectral line data were obtained simultaneously, as described in Section 2.2; the CO(1–0) and CO(2–1) datasets include 112 and 56 velocity channels, respectively, each with width

Date	Line	Array	Longest baseline	Passband calibrator(s)	Flux cal	Gain calibrator(s)	Strength
(1)	(2)	(3)	(4)	(5)	(6)	(7)	(8)
1 Apr 95	CO(1–0)	E	206 m	P1	2	0336-019	2.4 Jy
24 Apr 95	CO(1–0)	L	115 m	P1	1	0336-019	1.9 Jy
25 May 95	CO(1–0)	L	115 m	P2+P3	2	0336-019	1.6 Jy
25 Sep 95	CO(1–0)	C	68 m	P2+P3	1	0336-019	1.3 Jy
1 Dec 95	CO(2–1)	E	119 m	P1	1	0420-014	2.2 Jy
						0235+164	0.5 Jy
20 Dec 95	CO(2–1)	H	242 m	P2	1	0420-014	2.6 Jy
4 Feb 97	CO(2–1)	L	72 m	P1	1	0420-014	2.3 Jy
						0235+164	1.2 Jy

Table 4.1: OVRO observation log for NGC 1068. The columns are (1) date (2) CO transition (3) array configuration (4) maximum baseline used in mapping (5) passband calibrator(s), where P1 = 3C273, P2 = 3C454.3, and P3 = 0528+134 (6) type of flux calibration, where 1 denotes use of Uranus and/or Neptune and 2 denotes bootstrapping from archived data (7) gain calibrator(s) (8) flux density adopted for gain calibrator(s).

10.4 km s^{-1}. A passband instability in the four redmost channels of the CO(2–1) dataset reduced its usable bandwidth from 582.4 km s^{-1} to 540.8 km s^{-1}, but the affected channels contained no line emission and did not impair our ability to model the continuum (see below). The data were calibrated as described in Section 2.2. Because our gain calibrator for the (earlier) CO(1–0) observations, 0336-019, was not bright enough at 230 GHz to support calibration of CO(2–1) data, we adopted 0420-014 and (to a very limited extent) 0235+164 as gain calibators for the latter observations. We determined the flux scale for each track by measuring the phase calibrator flux density(ies), either by direct comparison to Uranus and Neptune, or by bootstrapping from archived observations of the planets (and bright, frequently-observed quasars). We estimate that the uncertainties in our flux scale are $\sim$ 10% for the CO(1–0) data and $\sim$ 15% for the CO(2–1) data. For passband calibration of each track we used one or more of 3C273, 3C454.3, and 0528+134.

After editing for quality in the DIFMAP package (Shepherd 1997), our final CO(1–0) dataset included 11.4 hours of integration and 40 distinct baselines; our final CO(2–1) dataset included 8.0 hours of integration and 35 distinct baselines. We mapped the data using the IMAGR task in the NRAO AIPS package. Moderately robust weighting produced

synthesized beams of $3.64'' \times 3.48''$ at 45.4° for the CO(1–0) map and $1.80'' \times 1.49''$ at 65.7° for the CO(2–1) map. The price of this resolution was a slight increase in the per-channel rms noise over what would have been achieved with natural weighting– by 31% for the CO(1–0) map and by 3% for the CO(2–1) map. Our deconvolution was complicated by four factors: (1) NGC 1068 contains a relatively strong nuclear continuum source; (2) its line emission dominates the contribution of the thermal background to the noise in our maps; (3) it lies almost exactly on the celestial equator; and (4) we obtained our data using different gain calibrators for the two different transitions. We discuss our responses to each of these challenges below.

4.2.1 Continuum subtraction

Continuum emission was detected in the line-free (lower) sideband of the 1 GHz continuum data at 112 GHz, but not in the line-free (upper) sideband of the 1 GHz continuum data at 230 GHz. At 112 GHz, emission is extended to the north and south of an unresolved nuclear source; the extensions correspond well with the northern and southern radio lobes observed in centimeter continuum by Gallimore et al. (1996). Our unresolved feature encompasses emission from all of the nuclear components identified by these authors, and agrees well in flux density with an extrapolation from their derived spectral indices. Because our editing of the data resulted in slightly different *uv* sampling for our upper and lower continuum sidebands, we elected to subtract a model of the continuum emission from our line data (a) in the *uv* plane (b) based on the line-free channels in our upper sideband data at 115 GHz. A map made from the sum of these channels showed a nuclear peak whose strength and position agreed with our [higher signal-to-noise] detection at 112 GHz. Following subtraction of this continuum model, we deconvolved the spectral-line visibilities as described below.

4.2.2 Noise determination

In our initial attempt to estimate the per-channel rms in our data cubes (i.e., the $+1\,\sigma$ level to which we would clean the maps), we created inverted but undeconvolved "dirty cubes," in which we measured the rms far from the source in each velocity channel. For a weak source, channels with line emission might on average have rms $\leq 10\%$ higher than channels without line emission; such an excess would be attributed to low-level sidelobes,

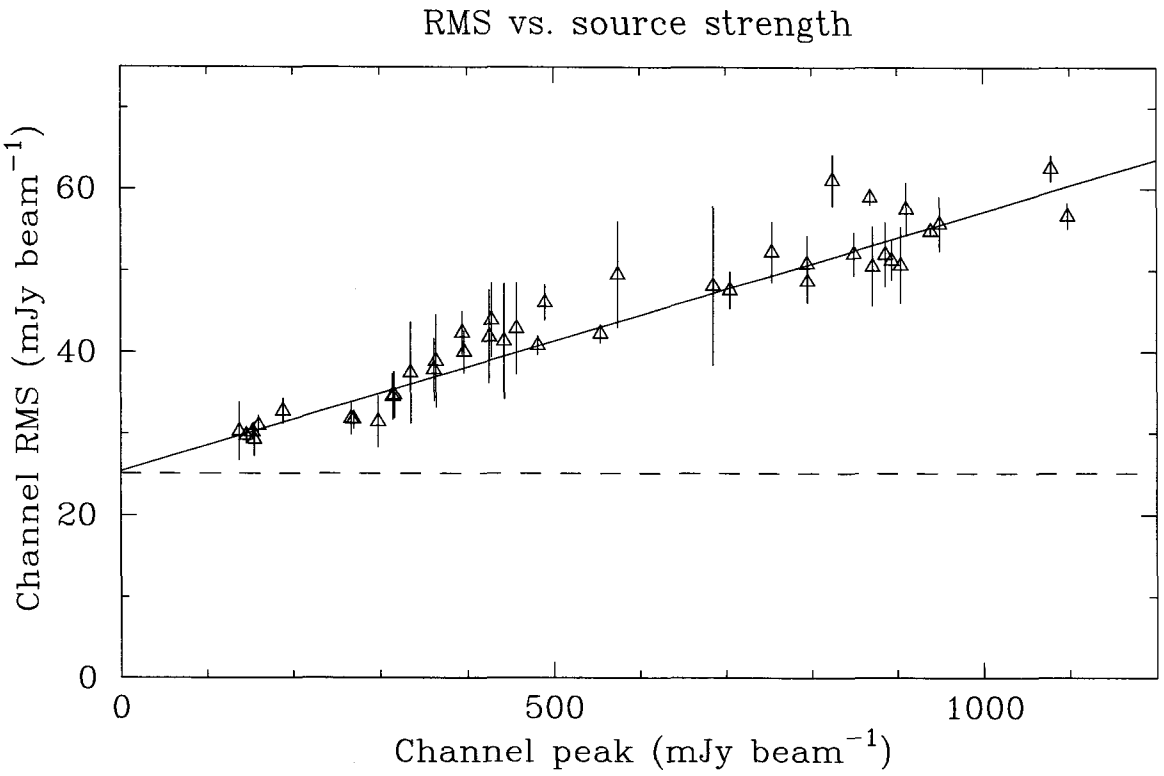

Figure 4.1: RMS vs. peak for a strong source. Each triangle indicates the peak flux density and the noise in a different uncleaned velocity channel of the NGC 1068 CO(2–1) dataset. The noise is estimated from the average of four separate off-source measurements in the channel, whose dispersion is indicated by an error bar. The solid line is a least-squares fit to the points, indicating a contribution to the noise in each channel of $\simeq 3.2\%$ of the source peak. The dashed line indicates the average noise in the line-free channels (none of which are plotted as triangles). The agreement between this value and the y-intercept of the least-squares fit implies that the noise budget has been fully reckoned.

and we would confidently clean all channels to the rms level of the line-free channels. Our NGC 1068 datasets, in contrast, have rms levels in the line channels which are not only substantially higher than those in the line-free channels, but are also well-correlated with the strengths of the source in the same channels. Figure 4.1 demonstrates this relation for our CO(2–1) data, which matches the expectation for strong sources mapped by arrays (Anantharamaiah et al. 1989). If much of the excess noise in the line channels is due to scattered flux which (as a result of calibration errors) cannot be removed by deconvolution, we would ultimately deconvolve ficticious "source" emission by naively cleaning to the rms level of the line-free channels. We avoided this pitfall by exploiting the location of NGC 1068 on the celestial equator, as we describe below.

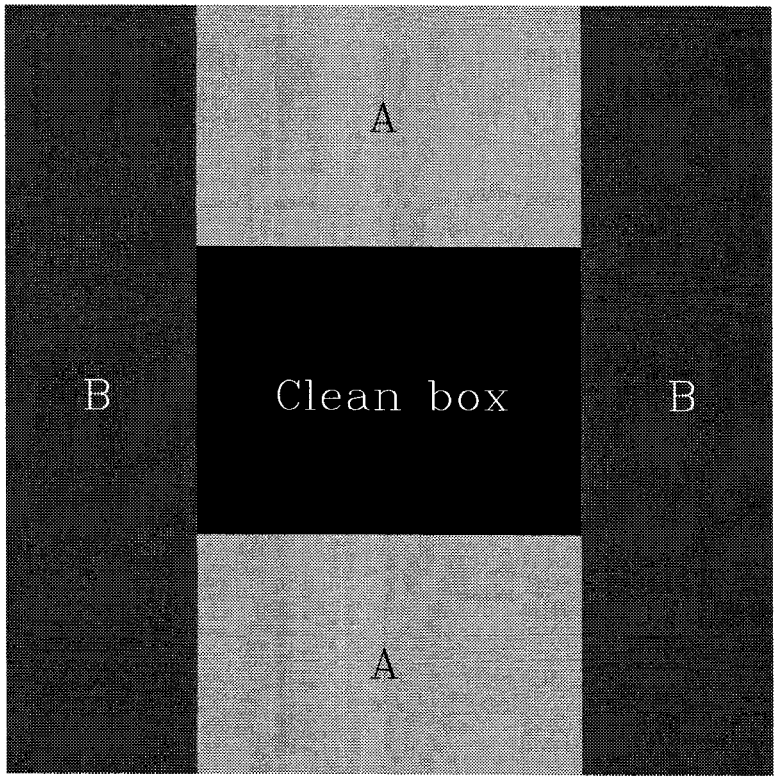

Figure 4.2: Schematic of our NGC 1068 deconvolution. If true source emission is restricted to the area of the clean box, then the strongest sidelobes will appear in the regions marked A. Deconvolution will shift sidelobe emission from regions A and B into the clean box. Overcleaning will shift noise from A into the clean box, leaving rms(A) < rms(B); undercleaning will not shift enough sidelobe emission from A into the clean box, leaving rms(A) > rms(B).

4.2.3 Deconvolution on the celestial equator

If a source has declination $\sim 0°$, a small array will poorly sample the uv plane in the v direction. The resulting lack of information about certain sets of Fourier components produces (in the image plane) high sidelobes to the north and south of every true emission source. Unfortunately, the characteristic separation between the main beam and its first, highest sidelobe for the uv sampling of our NGC 1068 datasets is very close to the north-south separation between the nucleus and the molecular spiral arms. To avoid subjective distinctions between source and sidelobe emission in assigning "clean boxes" to individual velocity channels, we therefore adopted a single clean box for all channels, which enclosed all of the emission in the zeroth moment map. As Figure 4.2 suggests, deconvolution tended to shift "sidelobe" emission from regions north and south of the clean box into the box,

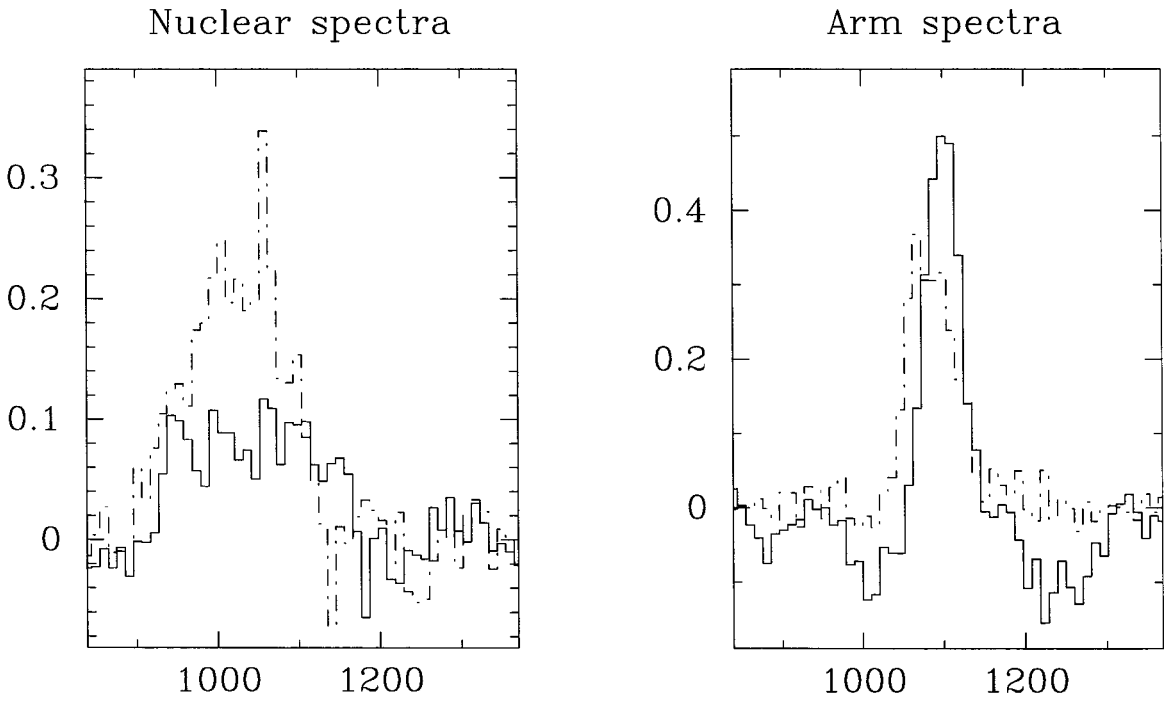

Figure 4.3: CO(1–0) and CO(2–1) spectra from the nucleus and the north spiral arm in NGC 1068. Solid lines are for CO(1–0); dotted lines are for CO(2–1).

while leaving regions to the east and west of the box essentially untouched. We determined effective $+1\,\sigma$ stopping points for our deconvolutions by noting that overcleaning would also shift *noise* from the north and south regions into the clean box, leaving the apparent rms to the north and south of the box *lower* than the rms to the east and west. Conversely, undercleaning would leave the rms to the north and south of the clean box *higher* than that to the east and west, since in this case not enough true sidelobe emission would have been deconvolved. We thus obtained a per-channel rms noise of $65\,\mathrm{mJy\,bm^{-1}}$ for the CO(1–0) map and $60\,\mathrm{mJy\,bm^{-1}}$ for the CO(2–1) map, since cleaning to these values gave post-deconvolution rms (far from the source) which was equal in regions to the north and south, and to the east and west, of the clean box.

The resulting maps look reasonable, but our CO(2–1) map has an emission feature in the north spiral arm which is disturbingly close to due north of a strong lobe in the nucleus. To confirm that neither of these features is a sidelobe of the other, we took spectra through both of them and through the corresponding positions in the CO(1–0) data cube (after re-registration of the datasets as described below). Figure 4.3 shows the result: the two

CO(2–1) features arise at velocities which are different from each other but identical to those of the corresponding features in the CO(1–0) data (whose *uv* sampling is more complete).

4.2.4 Gain calibration and registration

Our use of different gain calibrators for different transitions introduced the risk of a relative astrometric error between our maps in the two CO lines (beyond the astrometric uncertatinties inherent in the array's pointing model). To evaluate this possibility, we took two test tracks in the spring of 1998 which switched between 0336-019, 0420-014, and (as a third reference object) 3C84. After mapping 0336-019 and 0420-014 using 3C84 as a gain calibrator, we found that 0420-014 appeared to be displaced by approximately 0.75″ to the south relative to the other two quasars. Somewhat mysteriously, this offset exists in spite of the fact that our quasar coordinates agree with those in the VLA calibrator catalog. This has motivated us to shift our CO(2–1) map 0.75″ south; the resulting astrometry is good to approximately 0.25″ as deduced from the agreement between the 112 GHz continuum peak and centimeter continuum source S1 (the likely location of the black hole), and from the improved agreement between the CO(1–0) and CO(2–1) gas peaks.

4.3 Results

4.3.1 CO(1–0)

Figure 4.4 shows the zeroth velocity moment of the CO(1–0) line in NGC 1068, integrated over $n_{ch} = 41$ velocity channels from 896.2 to 1322.6 $\mathrm{km\,s^{-1}}$ LSR. Consistent with previous observations, the total emission is dominated by the two molecular arms, whose overall appearance matches the published maps of Planesas et al. (1991) and Tacconi et al. (1997), as well as new unpublished BIMA data (Helfer 1999). Integrating over the galaxy's full projected area, we derive a total line flux of $1717.2 \pm 173\,\mathrm{Jy\,km\,s^{-1}}$, corresponding to $57.1 \pm 5.7 \times 10^8\,\mathrm{M_\odot}$ for a Galactic conversion factor of $X = 3 \times 10^{20}\,\mathrm{cm^{-2}\,(K\,km\,s^{-1})^{-1}}$ (Young & Scoville 1991) and an extra factor of 1.36 to account for helium. Convolution of our map to the resolutions of single-dish observations by Young et al. (1995) and Planesas et al. (1989) leads us to conclude that we have recovered $\sim 36\%$ and $\sim 30\%$ of the emission these authors detect in half-power beamwidths of 45″ and 23″, respectively. Inside the spiral arms, we do not see unambiguous evidence of a molecular bar, although the arms

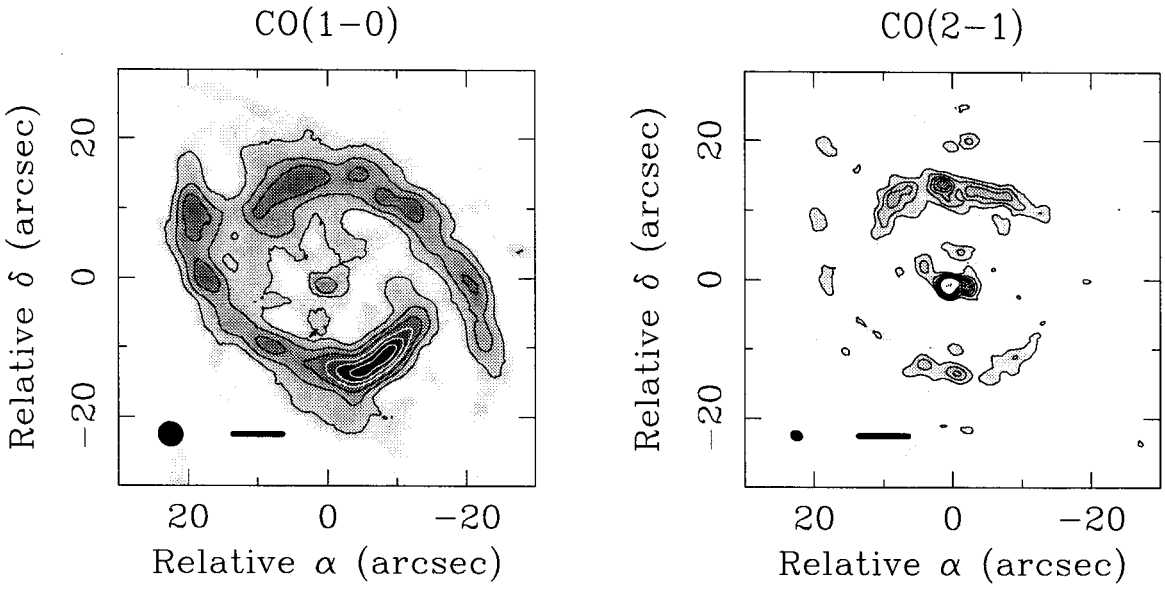

Figure 4.4: Zeroth moment maps of NGC 1068. Pixels with values less than $+1\sigma_{ch}$ were blanked before integrating, and contours are multiples of $2\,\sigma_{ch}\,\Delta v_{ch}\,\sqrt{n_{ch}}$ (8.6 and 8.0 Jy bm^{-1} km s^{-1}). The ellipses in the lower left corners show the synthesized beams; the bars nearby indicate 500 pc at $d = 14.4$ Mpc.

do begin to curl inward towards the nucleus at the correct position angle. In contrast, we have achieved a weak but unambiguous detection of CO(1–0) in the nucleus, with peak brightness temperature 1.6 ± 0.6 K, peak integrated intensity 188 ± 32 K km s^{-1}, and total line flux 31.5 ± 6.6 Jy km s^{-1} $\sim 1.0 \pm 0.2 \times 10^8$ M$_\odot$.

4.3.2 CO(2–1)

Figure 4.4 shows the zeroth velocity moment of the CO(2–1) line in NGC 1068, which we also present at greater magnification in Figure 4.5. Those portions of the spiral arms which lie nearly north and south of the nucleus are visible to a limited extent; to the east and west, primary beam attenuation renders the arms almost undetectably weak. Convolution to the 23″ resolution of single-dish observations by Planesas et al. (1989) implies that our map recovers only $\sim$ 11% of the total CO(2–1) emission seen at their pointing center. In the nucleus, our map shows quite strong emission from a double-lobed structure straddling the position of the 112 GHz continuum peak. The total CO(2–1) flux from this structure is 280.0 ± 12.9 Jy km s^{-1}, two-thirds of which comes from the lobe to the east of the continuum peak. The peak CO(2–1) brightness temperature (6.7 ± 0.5 K) and integrated intensity

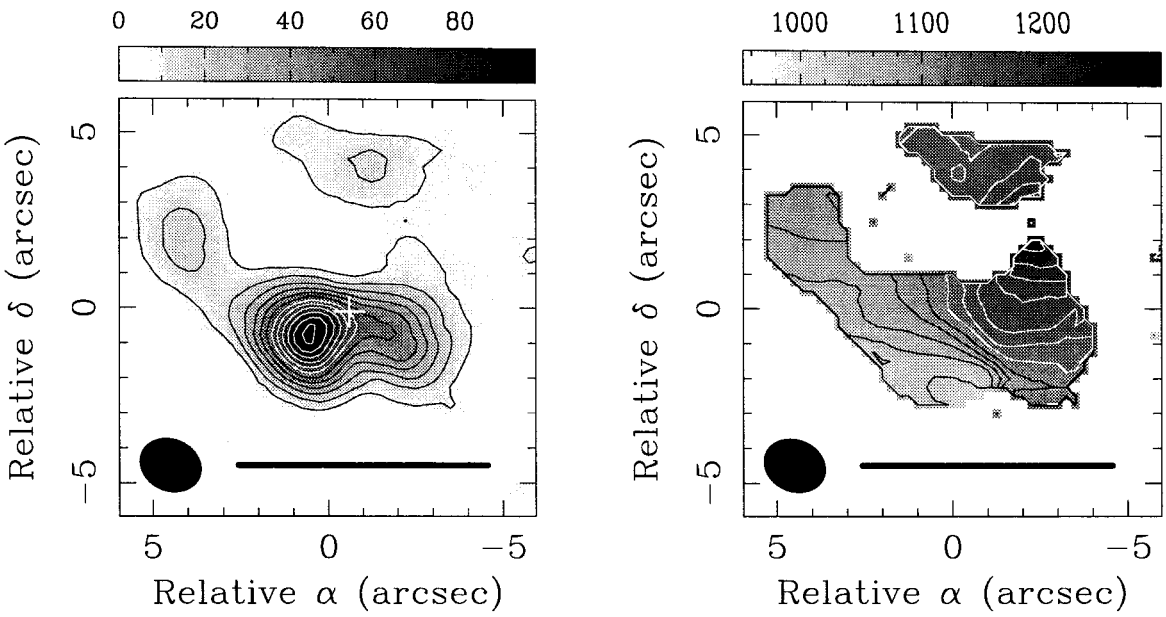

Figure 4.5: CO(2–1) moment maps of NGC 1068. Zeroth moment map shows the nuclear region of Figure 4.4, contoured at the same multiples of 8.0 Jy bm^{-1} km s^{-1}; a cross marks the position of the radio continuum peak (see Table 4.5). First moment map was integrated with blanking of pixels $< +1\sigma_{ch}$, and is plotted here only where the zeroth moment map rises above its lowest contour. Isovelocity contours run from 1020 to 1240 km s^{-1} in steps of 20 km s^{-1}.

(874.7 ± 34.6 K km s^{-1}) are also attained in the east lobe. Away from the brightest emission in the nucleus, we also see emission features to the north and northeast of the double lobes; these contribute 26.0 ± 6.0 and 30.8 ± 6.5 Jy km s^{-1} to the total line flux.

The right panel of Figure 4.5 shows the first velocity moment of the CO(2–1) data cube. Somewhat surprisingly, the kinematic major axis of the nuclear material does *not* match the east-west kinematic major axis seen on larger scales (or the east-west elongation of the nuclear gas itself). Instead, as previously detected in HCN(1–0) observations by Jackson et al. (1993) and Tacconi et al. (1994), the predominant velocity gradient has a position angle $\sim 135°$ at small radii, before twisting to smaller position angle on larger scales. The overall twisting of isovelocity contours requires that gas motions in this volume be noncircular and/or noncoplanar. Ordinarily, we would immediately opt for noncircularity, identifying the two lobes with the twin peaks seen in other barred galaxies where molecular gas is believed to build up at inner 2:1 Lindblad resonances (Kenney et al. 1992). However, the well-established presence of different symmetry axes in NGC 1068 (see Section 4.5.2),

Quantity (1)	IRAM detects (2)	OVRO detects (3)	OVRO misses (4)
uv sampling	$r_{uv} \geq 0$	$r_{uv} > 10\,\mathrm{k}\lambda$	$r_{uv} \leq 10\,\mathrm{k}\lambda$
$I_{\mathrm{CO(2-1)}}$	$240\,\mathrm{K\,km\,s^{-1}}$	$22\,\mathrm{K\,km\,s^{-1}}$	$218\,\mathrm{K\,km\,s^{-1}}$
$I_{\mathrm{CO(1-0)}}$	$218\,\mathrm{K\,km\,s^{-1}}$	$30\,\mathrm{K\,km\,s^{-1}}$	$188\,\mathrm{K\,km\,s^{-1}}$
R	1.10	0.73	1.16

Table 4.2: Global intensity ratios in NGC 1068. We compare the integrated intensities and intensity ratios within the inner 23″ for (2) single-dish measurements by Planesas et al. (1989) and Braine et al. (1993); (3) interferometer measurements determined from the truncated OVRO datasets; and (4) the flux missed by the interferometer due to low surface brightness and/or a smooth spatial distribution.

combined with the measurements of the intensity ratio R which we describe below, together imply that a noncoplanar configuration may be a more likely scenario. We note in passing that the feature northeast of the east lobe has a position and (blueshifted) velocity which match our expectations for material flowing into the nucleus at the leading edge of the stellar bar. Episodic inflow of such discrete gas concentrations offers a natural explanation for why star formation and accretion in galactic nuclei appear to take place with a duty cycle less than unity (Balzano 1983).

4.3.3 Integrated intensity ratio

In order to characterize the CO(2–1) to CO(1–0) intensity ratio in NGC 1068, we remapped both datasets after truncating their uv sampling at $r_{uv} \leq 10\,\mathrm{k}\lambda$ (see Section 2.3.3). The map of the truncated CO(1–0) dataset had slightly higher noise ($68\,\mathrm{mJy\,bm^{-1}}$) and smaller synthesized beam (3.34″ × 3.16″ at 57.0°) than the original; the map of the truncated CO(2–1) dataset was nearly unchanged. To estimate a global value for R, we convolved these new maps to 23″ resolution and remeasured what fractions we recovered of the single-dish intensities detected by Planesas et al. (1989). Table 4.2 shows the result: contrary to the pattern displayed by NGC 7479 (see Section 2.3.3) and NGC 2681 (see Section 3.3.3), the intensity ratio of the emission we detect is lower than the intensity ratio of the emission we miss. In most galaxies we would expect smoothly distributed material to have lower temperature and/or density than the emission our maps recover, leading to a lower intensity ratio; however, we speculate that the high star formation rate in NGC 1068 may give rise to

Velocities ($km\,s^{-1}$) (1)	Spatial feature (2)	$T_{b(2-1)}$ (K) (3)	$T_{b(1-0)}$ (K) (4)	R (5)
896.2 - 1010.6	nucleus	1.62	1.40	1.20 ± 0.09
1010.6 - 1114.6	E lobe	2.44	1.23	2.33 ± 0.13
	W lobe	1.61	1.33	0.90 ± 0.20
1114.6 - 1218.6	nucleus	1.75	1.62	1.51 ± 0.08
1218.6 - 1322.6	nucleus: CO(2–1) peak	0.99	1.32	1.33 ± 0.14
896.2 - 1322.6	E lobe: CO(2–1) peak	2.70	1.55	1.72 ± 0.11
	W lobe: CO(2–1) peak	1.75	1.62	1.42 ± 0.17
	E and W lobes	2.70	1.62	1.61 ± 0.22

Table 4.3: Local intensity ratios in NGC 1068. Column (1) identifies four LSR velocity windows and the full linewidth over which we measured R, in spatial boxes centered on features which are described in column (2). The remaining columns give (3) the peak CO(2–1) brightness temperature (± 0.52 K), (4) the peak CO(1–0) brightness temperature (± 0.60 K), and (5) the average intensity ratio within the measurement box. The uncertainties in R are the formal dispersions over each box. The fourth velocity window lacks any clear CO(1–0) peak, so we have located this measurement box squarely on the CO(2–1) peak.

a substantial mass of warm, diffuse molecular gas with higher optical depth in the CO(2–1) line than in the CO(1–0) line (see Section 3.5.2).

In addition to considering the global intensity ratio in NGC 1068, we have measured local variations in R by comparing partial moment maps of the data cubes for both truncated datasets (after convolving the CO(2–1) maps to the resolution of the CO(1–0) maps). Table 4.3 lists the results, for four velocity windows (roughly symmetric with respect to systemic velocity) and the full linewidth; we also list the peak brightness temperatures observed in the spatial boxes used to make the ratio measurements. All but one of our measurements of R yield values well above unity, similar to the result we obtained in Section 3.3.3 for NGC 2681. Unlike NGC 2681, however, NGC 1068 has a clear excitation *gradient*, with R increasing as we move from west to east. To account for $R > 1$, we require the CO emission lines to have low optical depths and suspect that at least some of the excess be due to external heating of molecular clouds (see Section 3.5.3). To account for the *asymmetry* in R, we must explain why gas in the east lobe has a lower optical depth and/or higher rate of external heating than gas in the west lobe. Neither option can be easily reconciled with the proposition that the molecular gas in the nucleus of NGC 1068 is distributed in a coplanar

structure. However, if we permit a noncoplanar geometry, we obtain a natural explanation for the gradient in R: to the east of the nucleus we see the directly illuminated surface of a warped disk, while to the west we see the *back* of the disk and a weaker signature of external heating. Our sudden ability to explain both the peculiar kinematics and the peculiar excitation in NGC 1068 is what motivates the kinematic model of a warped disk which we develop below.

4.4 Kinematic models

4.4.1 Model description

In a disk which is warped rather than flat, annuli of gas at different radii have different rotational axes. Standard nomenclature describes the variation of rotational axes in terms of "warps" and "twists": if we imagine a system of polar coordinates $(\bar{\theta}, \bar{\phi})$ aligned with the innermost annulus of gas, a change in the polar angle $\bar{\theta}$ of the rotational axis produces a pure warp, while a change in azimuth $\bar{\phi}$ defines a twist. We can specify rates of warping and twisting in such coordinates using arbitrary functions of radius:

$$\bar{\theta}(r) = \bar{\theta}_0 + f_1(r) \tag{4.1}$$

$$\bar{\phi}(r) = \bar{\phi}_0 + f_2(r) \tag{4.2}$$

The rather involved relation between these rates of warping and twisting in a disk reference frame and the variation of the rotation axis on the sky is derived by Christodoulou et al. (1993). From the point of view of generating a model cube, however, it is simpler to use the formalism of Herrnstein (1995), in which we directly describe the orientation of each gas ring in terms of its inclination on the sky and the position angle of its ascending node:

$$i(r) = i_0 + f_1(r)\Big(= i_0 + i_1 r\Big) \tag{4.3}$$

$$\alpha(r) = \alpha_0 + f_2(r)\Big(= \alpha_0 + \alpha_1 r\Big) \tag{4.4}$$

Herrnstein (1995) uses a linear dependence for $f_1(r)$ and a quadratic dependence for $f_2(r)$; we will use linear dependences for both, as indicated above.

Apart from the inclusion of the two new parameters i_1 and α_1, our approach to mod-

Parameter	Units	Value
(1)	(2)	(3)
$\hat{x}_0$	RA (B1950)	02:40:07.057
$\hat{y}_0$	Dec (B1950)	-00:13:30.78
$\hat{v}_0$	$\mathrm{km\,s^{-1}}$ [LSR]	1105
i_0	$^\circ$	89
i_1	$^\circ\,\mathrm{pc^{-1}}$	-0.37
α_0	$^\circ$	129
α_1	$^\circ\,\mathrm{pc^{-1}}$	-0.20
r_p	pc	31
v_p	$\mathrm{km\,s^{-1}}$	118
M_p	$10^7\,\mathrm{M_\odot}$	3.0
σ_v	$\mathrm{km\,s^{-1}}$	47
r_{gas}	pc	3
r_{in}	pc	32
$r_{out(1-0)}$	pc	163
$\bar{\sigma}_{em(1-0)}$	$\mathrm{K\,km\,s^{-1}}$	356
$\eta_{(1-0)}$	-	0
$r_{out(2-1)}$	pc	159
$\bar{\sigma}_{em(2-1)}$	$\mathrm{K\,km\,s^{-1}}$	535
$\eta_{(2-1)}$	-	2
χ^2_ν	-	126.3

Table 4.4: Kinematic model for NGC 1068. Columns are (1) parameter (2) units (3) best-fit values.

elling the gas kinematics in NGC 1068 is similar to the one we have adopted in previous chapters. As in Section 2.4, we adopt a logarithmic potential; as in Section 3.4, we do not introduce a bar perturbation. Because the signal-to-noise is considerably lower in our CO(1–0) observations than in our CO(2–1) observations of NGC 1068, we have chosen to derive our initial fit to the latter data cube only. After converging to a stable solution, we have then varied the three parameters which affect only our model CO(1–0) cube (i.e., $r_{out(1-0)}$, $\bar{\sigma}_{em(1-0)}$, and $\eta_{(1-0)}$) so as to minimize the joint χ^2_ν. One further adaption was necessary: since a logarithmic potential alone cannot reproduce the kink observed at systemic velocity in a position-velocity cut through the nucleus (see Figure 4.9), we have added a point-mass term to our model for the potential. This last adjustment gives our model a total of 19 independent parameters.

Feature	Right ascension (B1950)	Declination (B1950)
(1)	(2)	(3)
OVRO pointing center	02:40:07.076	-00:13:31.45
Radio continuum peak	02:40:07.036	-00:13:31.56
Peak CO(1–0) intensity	02:40:07.118	-00:13:29.82
Peak CO(2–1) intensity	02:40:07.142	-00:13:30.20
Dynamical center	02:40:07.057	-00:13:30.78

Table 4.5: Coordinates of features in the nucleus of NGC 1068. The continuum peak whose position we list is feature S1; we adopt its coordinates from Bland-Hawthorn et al. (1997a). The dynamical center position is obtained from the kinematic model described in Table 4.4.

4.4.2 Model results

We present the results of our model in Table 4.4. Our minimum value of χ^2_ν for the simultaneous fit of both transitions is obviously rather high (χ^2_ν for the two transitions separately is 61.5 for CO(1–0) and 143.3 for CO(2–1)), but this is an inevitable result of our adoption of axisymmetric emissivities to describe a clearly nonaxisymmetric structure. In Figures 4.6 through 4.8, we plot the CO(2–1) emission predicted by our model over the emission observed in each velocity channel. Since the CO(1–0) data have lower signal-to-noise and resolution, and were only considered at the last stage of the fit, we do not show them here. Figure 4.9 shows position-velocity cuts through the CO(2–1) data and model cubes along the kinematic major axis for $r = 0$ (note, however, that since $r_{in} > 0$ no emission in our model actually rotates about the corresponding symmetry axis). Figure 4.10 shows equivalent zeroth moments of the CO(2–1) line in the data and model cubes. Evidence that our model is an oversimplified version of reality is ubiquitous: we have not reproduced the full velocity width of the east lobe, the elongated morphologies in the channels to the red of systemic velocity, or anything like the peanut shape of the zeroth moment map. However, a fair number of the velocity channels on *both* sides of line center, as well as the position-velocity diagram, are at least reasonably well-matched.

One implication of the model is apparent from Table 4.5: the position of the dynamical center we infer agrees much more closely (especially in right ascension) with the position of the radio continuum peak than with either of the integrated intensity peaks. We conclude

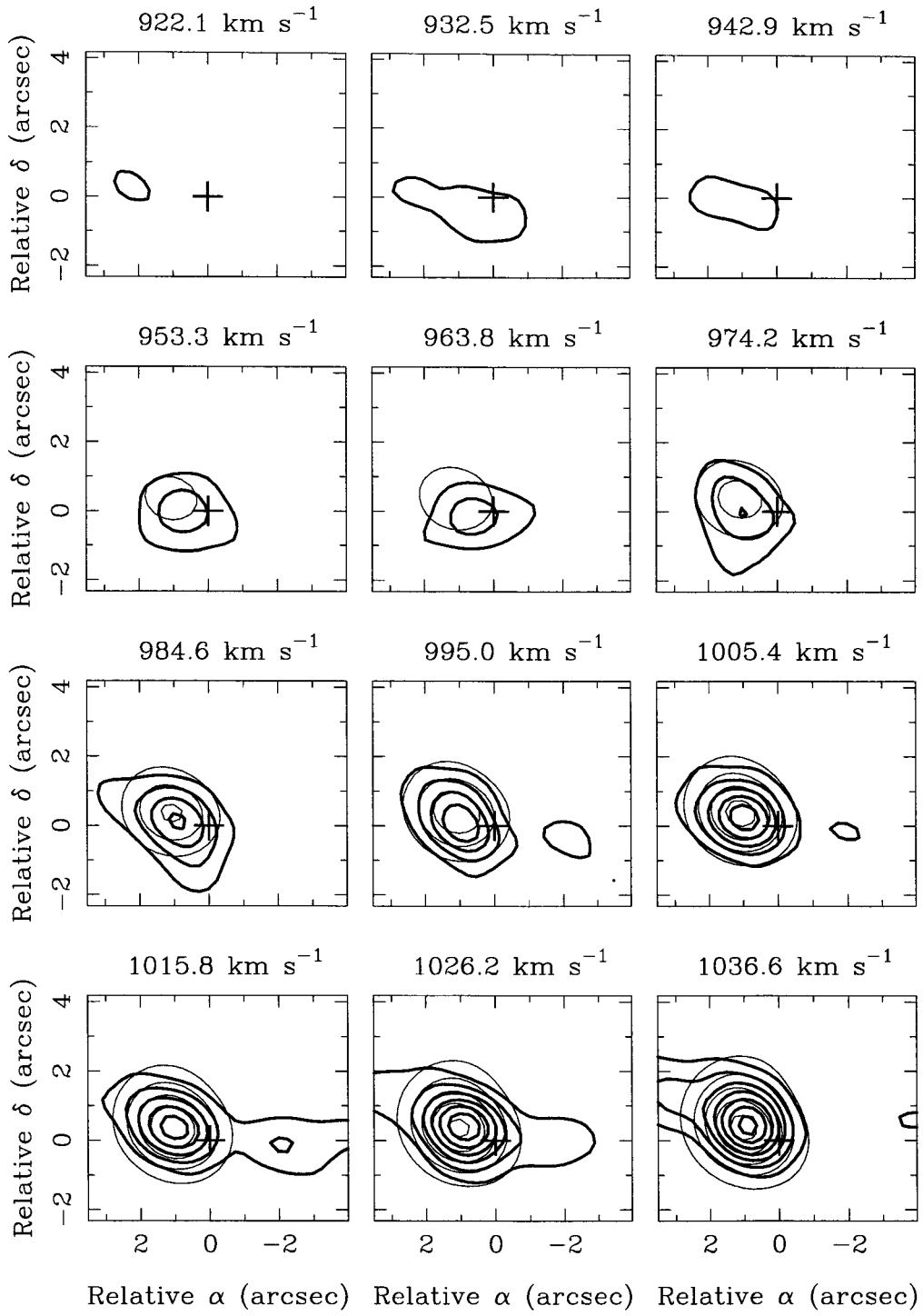

Figure 4.6: Blueshifted CO(2–1) velocity channels in NGC 1068. Light model contours are plotted over dark data contours; both are multiples of 97 mJy bm^{-1}. Spatial offsets are relative to the dynamical center, which is also marked with a cross.

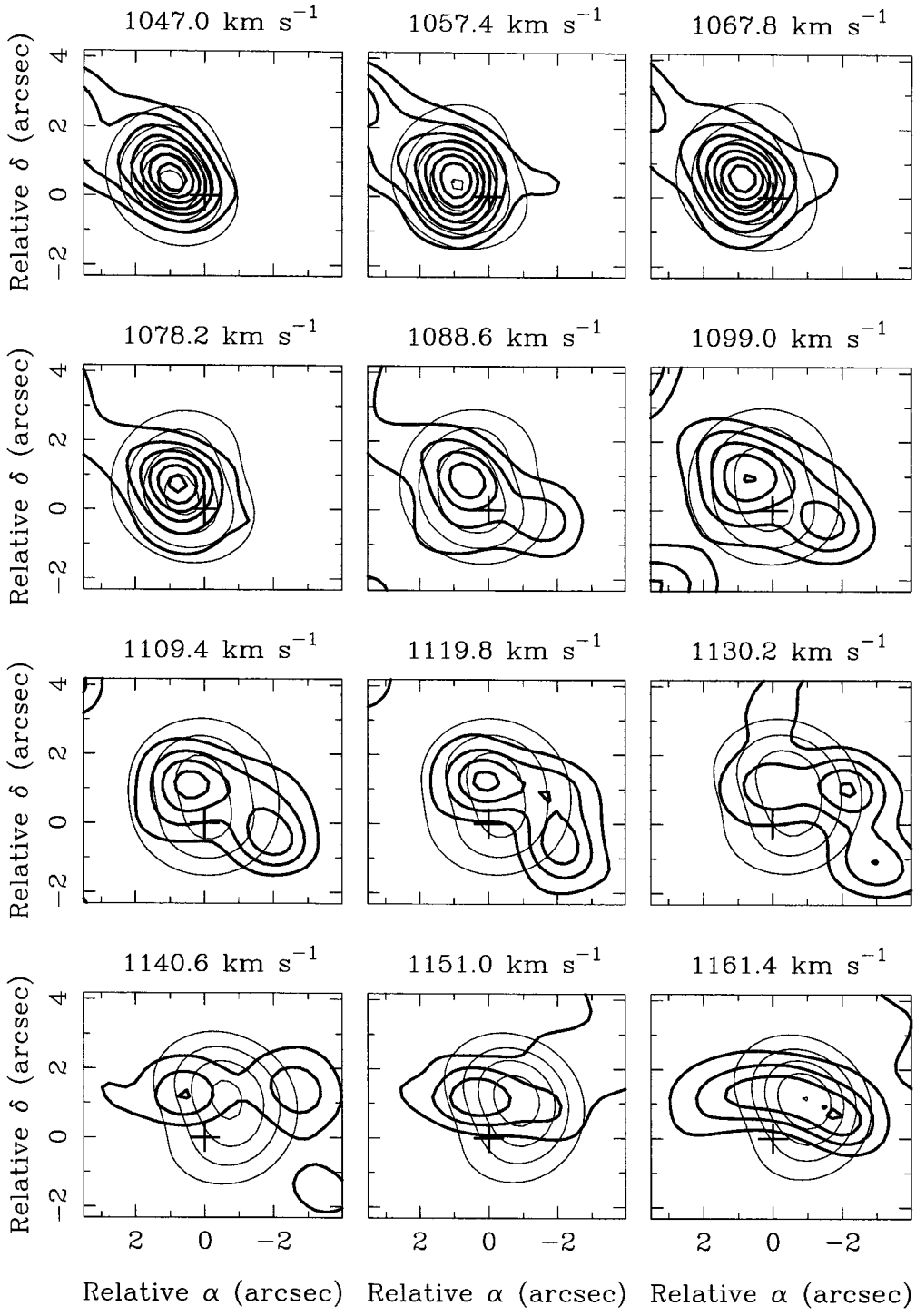

Figure 4.7: Systemic CO(2–1) velocity channels in NGC 1068. Notation is as in Figure 4.6.

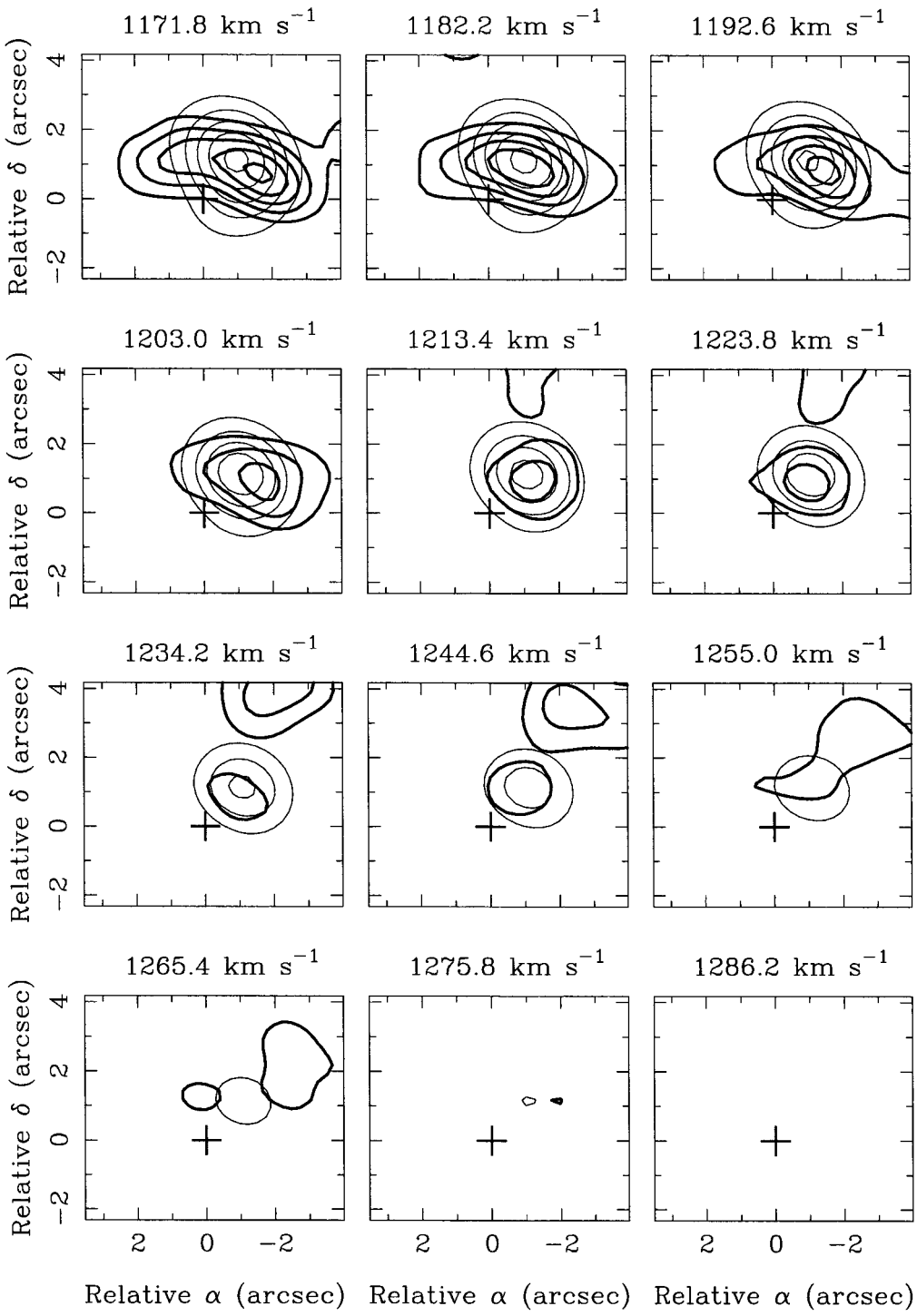

Figure 4.8: Redshifted CO(2–1) velocity channels in NGC 1068. Notation is as in Figure 4.6.

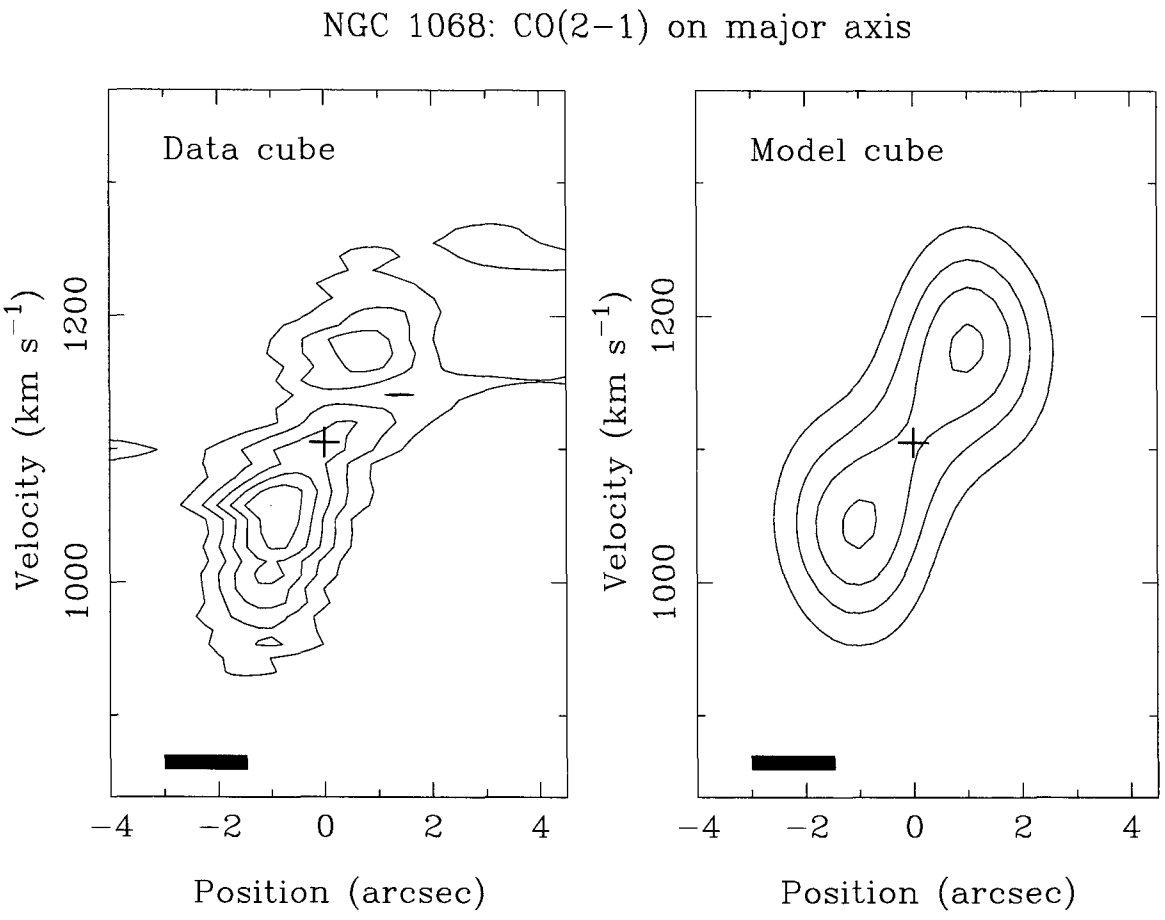

Figure 4.9: Position-velocity diagram for the CO(2–1) line in NGC 1068. A 1″-wide cut was taken along the kinematic major axis at $r = 0$ (at $\alpha_0 = 129°$ east of north). The cross marks the galaxy's spatial and velocity center; offsets along the spatial scale are relative to this position. The rectangle indicates the spatial and velocity resolutions. Contours are multiples of 111 mJy bm^{-1}.

that while the molecular emission may be asymmetrically distributed with respect to the active nucleus, the overall mass distribution is not. A second unambiguous result is our need for a point-mass contribution to the model potential corresponding to $M_p = 3.0 \times 10^7\,\mathrm{M}_\odot$. In the course of deriving our fit, we found that χ^2_ν discriminates *against* a nonzero scale length for this mass component. Any spherically symmetric mass distribution interior to our derived $r_{in} = 32\,\mathrm{pc}$ will make a contribution to M_p; since Greenhill & Gwinn (1997) estimate the mass of the black hole in NGC 1068 to be $\sim 1.5 \times 10^7\,\mathrm{M}_\odot$, we conclude that there is an equal mass in stars within $r \leq 32\,\mathrm{pc}$. A third prediction of our model concerns the integrated intensity ratio. As in NGC 7479 and NGC 2681, the CO(2–1) emissivity

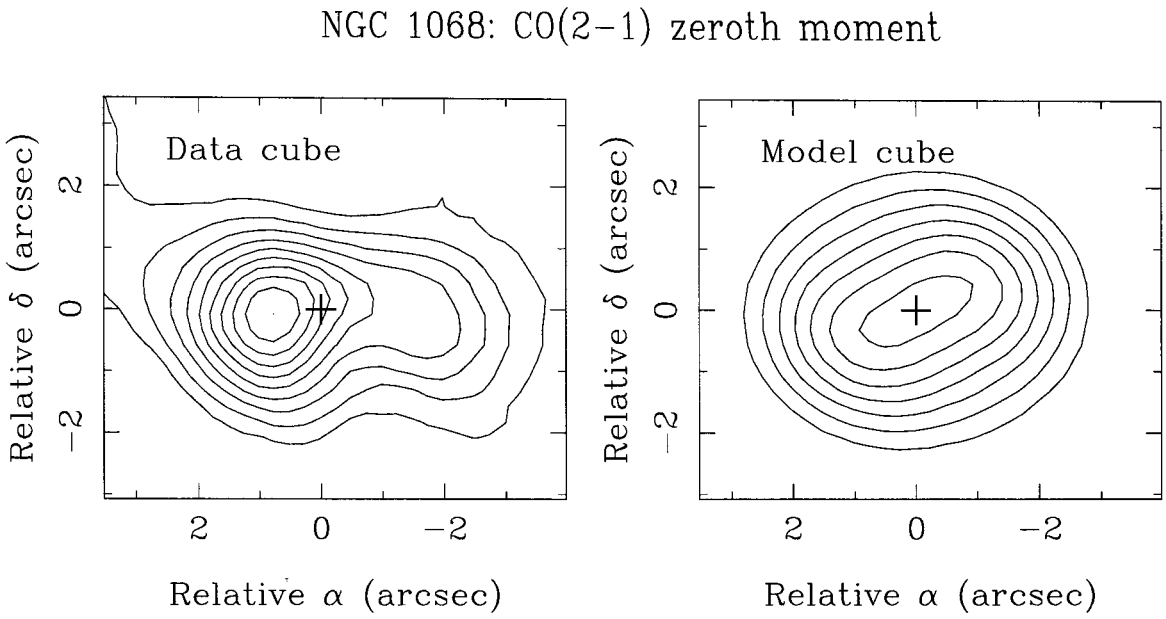

Figure 4.10: Zeroth moment map for the CO(2–1) line in NGC 1068. Both data and model cubes have been blanked at $+2\,\sigma_{ch}$; contours are multiples of $10.0\,\mathrm{Jy\,bm^{-1}\,km\,s^{-1}}$. Spatial offsets are relative to the dynamical center, which is also marked with a cross.

appears to rise at smaller radius while the CO(1–0) emissivity remains constant; however, the surface density of CO(2–1) emission is so large that we predict $R > 1$ at *all* radii in the nuclear disk. In view of the intense nuclear activity in NGC 1068 and the assumption of a high external heating rate which motivated our warped disk model, this situation is not unexpected. The most interesting implication of our model relates to the precise values it determines for the rates at which i and α change with radius. From Table 4.4, we estimate that (i, α) evolves from $\sim (77°, 123°)$ at $r = r_{in}$ to $\sim (30°, 97°)$ at $r = r_{out}$. The sense of this change is consistent with our assumption that the east lobe of the warped disk is directly illuminated by the active nucleus (i.e., that the surface we see is on the far side of the galaxy). More remarkably, these limiting values are *extremely* close to the orientations of the innermost maser disk, which has $i \geq 85°$ and $\alpha \simeq 135°$ (Greenhill & Gwinn 1997), and of the larger galactic disk, which has $i \simeq 40 \pm 3°$ and $\alpha \simeq 90 \pm 5°$ as determined from H I observations (Brinks et al. 1997). We appear to have identified a "missing link" of sorts between the symmetry axes of material on large and small scales.

4.5 Discussion

4.5.1 Physical conditions in the molecular gas

To help constrain the physical conditions in the nucleus of NGC 1068, we can apply the one-zone analysis we developed in Section 3.5 to the mean of the intensity ratio over both lobes, $\simeq 1.61$. From the IRAS $60/100\,\mu$m color temperature of 42 K (Soifer et al. 1989) and the grain emissivity law of Draine & Lee (1984), we infer a global dust mass of $\sim 3.1 \times 10^6\,\mathrm{M}_\odot \sim 5.4 \times 10^{-4} \times M_{gas}$ for the gas mass estimated in Section 4.3.1. We conclude (as before) that much of the dust in NGC 1068 is likely to be cold; however, since we are considering gas which we know to be warm and have low optical depth, we adopt $T_{kin} \simeq 40\,\mathrm{K}$ in the nucleus (as for the nucleus of NGC 2681) rather than the 20 K we have used elsewhere. We can now infer from Figure 3.10 that $n_{\mathrm{H}_2} \geq 3200$, i.e., that the CO(1–0) line can be thermalized without any need for photon trapping. The peak brightness temperature above the background which we can achieve for $T_{kin} = 40\,\mathrm{K}$ is 36.5 K; comparison to our peak observed CO(1–0) brightness temperature of 1.6 K places rather weak lower limits of $f_a(v) \geq 0.04$ and $\tau_v \geq 0.04$. Since we cannot self-consistently assume $T_{ex(2-1)} = T_{kin}$ for a strictly LTE analysis using Figure 3.11, we must put off any further modelling.

4.5.2 The nuclear geometry

We return now to consideration of the geometry which our kinematic model predicts for the warped molecular disk. Observations of NGC 1068 at a number of wavelengths paint a picture of a galaxy in which there are three characteristic symmetry axes. In terms of inclination, we know that the maser disk has $i \geq 85°$ (Greenhill & Gwinn 1997) and that the base of the ionization cone opens at $i \sim 75°$ (Cecil et al. 1990)– both considerably different from the $30° - 40°$ inclination of the galactic H I disk. Position angle variations are even better documented, and follow a pattern which we hope to suggest in our arrangement of Table 4.6. As molecular gas dissipates angular momentum and moves inward through the warped disk, its rotation axis will ultimately be projected to a position angle of 33° on the sky when it reaches $r = r_{in}$. If the warped structure persists to still smaller radii (i.e., its CO abundance has a sharp edge which the disk itself lacks), we predict $\alpha \rightarrow 39°$– in good agreement with the position angle of the maser disk. The *outflow* axis on small

Measurement	Radius ($''$)	PA ($^\circ$)	Reference
(1)	(2)	(3)	(4)
CO(2–1) disk	3.5	**33**	this work
maser disk	0.015	**45**	Greenhill & Gwinn (1997)
ionized disk	< 0.010	20	Gallimore et al. (1997)
radio jet	0.4	12	Gallimore et al. (1996)
NIR continum polarimetry	0.6	10	Packham et al. (1997)
optical spectropolarimetry	< 4.3	7	Antonucci et al. (1994)
radio jet	6	**33**	Wilson & Ulvestad (1982)
[OIII] NLR	40	**32**	Pogge (1988)

Table 4.6: Position angle alignments in NGC 1068. Columns are (1) feature with a defined rotation axis, or measurement of a scattering direction (2) length scale (3) position angle of axis (4) reference. Above the horizontal line, we list tracers which we assume to be moving inward; below the horizontal line we list tracers which are moving outward. Boldfaced entries in column (3) mark features which are associated with or redirected by the molecular gas.

scales appears to be altogether different– we estimate $\alpha \sim 7^\circ - 12^\circ$– and may be defined by the spin axis of the black hole. This axis is preserved out to roughly the scale length of our molecular disk, at which point it reverts to the same position angle we infer for the disk's inner edge. Such agreement suggests that the radio jet and the flux of ionizing photons are being redirected from their original path out of the nucleus, and is consistent with several studies of the NLR in NGC 1068 which invoke jet/cloud interactions (Capetti et al. 1997; Bock et al. 1998). We appear to have confirmed a prescient comment of Wilson & Tsvetanov (1994), who remark that "In NGC 1068, it is notable that the axes of both the radio ejecta and ionization cones change with increasing distance from the nucleus, while maintaining a close correpsondence with each other. This result suggests that both the radio plasmoid and ionizing photon trajectories are recollimated on the $\simeq 100\,$pc scale. Presumably this recollimation is effected by a gaseous torus, the plane of which warps by $\simeq 15^\circ$ between the $< 30\,$pc and $\simeq 100\,$pc scales."

Although we have assembled a coherent picture of the nuclear geometry in NGC 1068 in which a warped molecular disk fits naturally, it remains for us to explain why there is a warp at all. Misalignments between the spin axes of black holes and of their host galaxies' disks are thought to be common (Pringle et al. 1999), but here we appear to have a *third* axis on

scales of $\sim 100\,\mathrm{pc}$ to account for. Possible explanations include the recent accretion by the host galaxy of material with a different angular momentum vector, the tumbling of a triaxal halo about one of its principal axes, or the radiation-induced instability first identified by Pringle (1996)– all of which have been advanced as possible causes of the warping of ionized gas disks seen in NGC 4261 and NGC 6251 (Ferrarese et al. 1996; Ferrarese & Ford 1999). Whether any of these mechanisms can adequately account for the distortion of a massive *molecular* disk out to large radii is a question which is important but (regrettably) outside the scope of the present work.

4.6 Acknowledgments

We thank Peter Papadopoulos for sharing his CO(3–2) spectrum and Eva Schinnerer for several useful conversations.

Chapter 5 Molecular gas in five nearby active galaxies

5.1 Introduction

Previous chapters in this thesis have examined the complex gas dynamics and enhanced molecular excitation in the centers of three nearby active galaxies (NGC 7479, NGC 2681, and NGC 1068). We now extend our analysis to OVRO observations of five more AGN–the Seyfert nuclei NGC 3227, NGC 4051, and NGC 5033, and the low-ionization nuclear emission-line regions (LINERs) NGC 4438 and NGC 5005. At least some (and perhaps all) of these galaxies have been affected by interactions with companions. NGC 3227 is strongly interacting with NGC 3226 ($2' \simeq 12$ kpc away at 20.6 Mpc), while NGC 4438 has recently collided with NGC 4435 ($4.3' \simeq 21$ kpc away at 16.8 Mpc) in the Virgo cluster. Less dramatically, NGC 5005 and NGC 5033 may comprise a binary pair ($41' \simeq 255$ kpc apart at 21.3 Mpc), and NGC 4051 is suggested by Byrd et al. (1987) to be tidally influenced by NGC 4013 ($78' \simeq 386$ kpc away at 17.0 Mpc). Interactions will tend to promote bar formation and drive gas inflow; in this chapter, we will discuss the details of this process which are manifested in our molecular gas observations.

Each of the galaxies we have studied contains a massive gas structure at $r \leq 500$ pc from the nucleus, as well as gas with lower surface density seen farther out in the disk. In NGC 5005 and NGC 5033, the central structures themselves have kinematic features consistent with those expected to arise in nuclear bars. In NGC 3227, NGC 4051, and NGC 5005, larger-scale bars appear to supply molecular gas to the central concentrations in discrete fuelling episodes. The asymmetry of the molecular mass distribution with respect to the nucleus is also likely to impact the rate of fuelling in NGC 3227 and NGC 5033.

5.2 Observations

Table 5.1 summarizes our observations of the CO(1–0) and CO(2–1) transitions in the five galaxies, which we conducted over a two-year period between April 1997 and January 1999. We obtained continuum and spectral line data simultaneously, as described in Section 2.2;

the CO(1–0) and CO(2–1) datasets generally included 112 and 56 velocity channels, respectively, each with width $10.4\,\mathrm{km\,s^{-1}}$. The flux scale for each track was determined by measuring the flux density of the gain calibrator(s), either by direct comparison to Uranus and Neptune, or by bootstrapping from archived observations of the planets (and bright, frequently-observed quasars). We estimate that the uncertainties in our flux scales are $\sim 10\%$ for the CO(1–0) data and $\sim 15\%$ for the CO(2–1) data. For passband calibration of each track, we used 3C273 in all cases but one. After combining the data from different tracks and editing visibilities in the DIFMAP package (Shepherd 1997), we mapped each galaxy using the IMAGR task in the NRAO AIPS package. Test maps of the 1 GHz continuum channel in the line-free sideband showed no evidence for emission at either 115 GHz or 230 GHz in any of the sources, so subtraction of continuum from the spectral line data was unnecessary. For our line maps, we adopted moderately robust weighting and cleaned a single large region down to $+1\sigma_{ch}$ in each velocity channel. Table 5.2 lists various parameters of the visibility data and of the maps which we produced from them. Section 2.2 provides a more detailed account of our general approach to calibration and imaging. Our handling of particular datasets merits additional comments in a few cases.

5.2.1 NGC 3227

The continuum and spectral line data were centered at reference velocities which differed by $62.6\,\mathrm{km\,s^{-1}}$ for the CO(1–0) and CO(2–1) datasets. Since we still observed the full width of each line, and since $62.6\,\mathrm{km\,s^{-1}} \simeq 6 \times \Delta v_{ch}$, this discrepancy did not compromise our results.

5.2.2 NGC 4051

For the 4 March 1998 CO(1–0) track, we used 3C111 (rather than 3C273) as our passband calibrator. Because of an erroneous radio position listed in van der Hulst et al. (1981), all of our CO(1–0) observations were obtained at a pointing center with declination +44:48:39, approximately 5″ of the true nucleus. Our correction for the response of the primary beam is appropriate for this pointing center, but all other references (e.g., Figure 5.2 and Table 5.15) are to the corrected pointing center used for the CO(2–1) observations.

Galaxy	Date	Line	Array	Longest baseline	Flux cal	Gain calibrator(s)	Strength
(1)	(2)	(3)	(4)	(5)	(6)	(7)	(8)
NGC 3227	4 May 97	CO(1–0)	L	115 m	2	0923+392	4.9 Jy
	3 Mar 98	CO(1–0)	H	242 m	2	0923+392	5.0 Jy
	14 Oct 97	CO(2–1)	L	115 m	2	0923+392	2.6 Jy
	17 Dec 97	CO(2–1)	H	242 m	2	0923+392	2.6 Jy
	10 Feb 98	CO(2–1)	H	242 m	2	0923+392	3.3 Jy
NGC 4051	7 May 97	CO(1–0)	L	115 m	1	1308+326	1.1 Jy
	4 Mar 98	CO(1–0)	H	242 m	2	1308+326	1.4 Jy
						1150+497	0.9 Jy
	9 Mar 98	CO(1–0)	H	242 m	2	1308+326	1.3 Jy
	3 Nov 97	CO(2–1)	L	115 m	2	1308+326	0.8 Jy
	3 Dec 97	CO(2–1)	H	242 m	1	1308+326	1.0 Jy
	13 Dec 97	CO(2–1)	H	242 m	2	1308+326	1.0 Jy
						1150+497	0.5 Jy
NGC 4438	4 May 97	CO(1–0)	L	115 m	1	3C273	29.2 Jy
	8 May 97	CO(1–0)	L	115 m	2	3C273	29.2 Jy
	4 Nov 98	CO(2–1)	L	94 m	2	3C273	12.3 Jy
	25 Nov 98	CO(2–1)	E	119 m	1	3C273	9.6 Jy
	17 Dec 98	CO(2–1)	H	242 m	2	3C273	15.4 Jy
	6 Jan 99	CO(2–1)	H	242 m	2	3C273	15.1 Jy
NGC 5005	27 Apr 97	CO(1–0)	L	115 m	1	1308+326	1.0 Jy
	5 Feb 98	CO(1–0)	H	242 m	1	1308+326	1.6 Jy
	12 Feb 98	CO(1–0)	H	242 m	1	1308+326	1.6 Jy
	16 Feb 98	CO(1–0)	H	242 m	2	1308+326	1.6 Jy
	17 Mar 98	CO(1–0)	U	400 m	2	1308+326	1.5 Jy
	28 Apr 98	CO(1–0)	L	115 m	1	1308+326	1.3 Jy
	5 May 98	CO(1–0)	L	115 m	1	1308+326	1.3 Jy
	18 Oct 97	CO(2–1)	L	115 m	2	1308+326	0.8 Jy
	16 Dec 97	CO(2–1)	H	242 m	1	1308+326	1.0 Jy
NGC 5033	14 May 97	CO(1–0)	L	115 m	1	1308+326	1.0 Jy
	25 Jan 98	CO(2–1)	L	115 m	1	1308+326	0.9 Jy
	8 Mar 98	CO(2–1)	H	242 m	2	1308+326	1.1 Jy
	9 Mar 98	CO(2–1)	H	242 m	1	1308+326	1.1 Jy

Table 5.1: OVRO observations of five active galaxies. The columns are (1) galaxy (2) date (3) CO transition (4) array configuration (5) maximum baseline used in mapping (6) type of flux calibration, where 1 denotes use of Uranus and/or Neptune and 2 denotes bootstrapping from archived data (7) gain calibrator(s) (8) flux density adopted for gain calibrator(s).

Galaxy	Map	Time (hours)	Base-lines	Resolution (arcsec)	PA (degrees)	σ_{ch} (mJy bm^{-1})	σ_{ch}/σ_{nat}
(1)	(2)	(3)	(4)	(5)	(6)	(7)	(8)
NGC 3227	CO(2–1)	7.6	30	1.43×1.11	-41.6	29	1.09
	CO(1–0)	8.6	30	2.81×2.36	-28.5	27	1.08
				2.70×2.28	-29.5	28	
NGC 4051	CO(2–1)	9.5	30	1.33×1.01	-66.2	22	1.04
	CO(1–0)	8.3	30	3.02×2.60	-60.7	31	1.03
				2.90×2.48	-60.4	32	
NGC 4438	CO(2–1)	11.4	33	1.49×1.17	-61.6	51	1.26
	CO(1–0)	4.5	15	5.10×3.51	-23.9	45	1.16
				4.96×3.42	-24.2	47	
NGC 5005	CO(2–1)	5.3	25	1.17×0.90	-70.5	48	1.01
	CO(1–0)	29.9	42	1.45×1.27	87.5	25	2.18
				1.43×1.25	86.7	26	
NGC 5033	CO(2–1)	8.9	30	1.46×1.15	-52.8	27	1.14
	CO(1–0)	5.4	15	4.74×3.54	-31.6	34	1.09
				4.30×3.40	-32.3	36	

Table 5.2: OVRO maps of five active galaxies. The columns are (1) galaxy (2) transition (3) integration time, in hours (4) number of distinct baselines (5) synthesized beam, in arcseconds (6) position angle of synthesized beam, in degrees east of north (7) per-channel rms, in mJy bm^{-1} (8) factor by which the per-channel rms exceeds the value which would have been given by natural weighting. The third line for each galaxy describes the CO(1–0) map made from *uv* data truncated at 10 kλ (see Section 5.3).

5.2.3 NGC 5005

We obtained one CO(1–0) track in a new array configuration yielding "Ultrahigh" resolution (thanks to several $\sim$ 400 m baselines) of $\sim 1''$ at 115 GHz. During this track, a passband instability in one of the spectral-line correlator modules limited our usable bandwidth to 84 velocity channels; however, by re-centering the three remaining modules on the galaxy's systemic velocity we maintained coverage of its full linewidth ($\sim$ 707 km s^{-1} FWZI). We could *not* cover the entire CO(2–1) line with a single local oscillator setting, since our 56 velocity channels at 230 GHz only provided $\sim$ 582.4 km s^{-1} of total bandwidth. We therefore deployed the correlator modules across the line with gaps of 52.0, 20.8, and 52.0 km s^{-1} ($\sim$ 6, 2, and $6 \times \Delta v_{ch}$) between them. The four velocity windows for which we do have coverage are listed in Table 5.11.

Galaxy (1)	Quantity (2)	IRAM detects (3)	OVRO detects (4)	OVRO misses (5)
	uv sampling	$r_{uv} \geq 0$	$r_{uv} > 10\,\mathrm{k}\lambda$	$r_{uv} \leq 10\,\mathrm{k}\lambda$
NGC 3227	$I_{\mathrm{CO(2-1)}}$	$42.0\,\mathrm{K\,km\,s^{-1}}$	$14.9\,\mathrm{K\,km\,s^{-1}}$	$27.1\,\mathrm{K\,km\,s^{-1}}$
	$I_{\mathrm{CO(1-0)}}$	$54.0\,\mathrm{K\,km\,s^{-1}}$	$13.2\,\mathrm{K\,km\,s^{-1}}$	$40.8\,\mathrm{K\,km\,s^{-1}}$
	R	0.78	1.12	0.66
NGC 5033	$I_{\mathrm{CO(2-1)}}$	$33.0\,\mathrm{K\,km\,s^{-1}}$	$6.3\,\mathrm{K\,km\,s^{-1}}$	$26.7\,\mathrm{K\,km\,s^{-1}}$
	$I_{\mathrm{CO(1-0)}}$	$21.0\,\mathrm{K\,km\,s^{-1}}$	$2.5\,\mathrm{K\,km\,s^{-1}}$	$18.5\,\mathrm{K\,km\,s^{-1}}$
	R	1.57	2.54	1.44

Table 5.3: Global intensities and their ratios in NGC 3227 and NGC 5033. We compare the integrated intensities and intensity ratios within the inner 23″ for (3) single-dish measurements by Braine et al. (1993); (4) interferometer measurements determined from the truncated OVRO datasets; and (5) the flux missed by the interferometer due to low surface brightness and/or a smooth spatial distribution. Note that in column (4), the CO(2–1) intensity recovered in the truncated map is nominally higher than in the original map.

5.2.4 NGC 5033

The pointing center for our CO(1–0) observations was 0.04″ south of the pointing center for our CO(2–1) observations. Since this discrepancy is much less than the size of either synthesized beam, we have ignored it in what follows.

5.3 Results

Figures 5.1 through 5.7 show the zeroth and first velocity moments of the CO(1–0) and CO(2–1) transitions in each galaxy. As in Section 2.3, we have integrated over n_{ch} velocity channels while ignoring all pixels with values less than $+1\,\sigma_{ch}$ (see Table 5.2) to produce these maps. We have also examined the CO(2–1) to CO(1–0) intensity ratio in the five galaxies, first remapping all the datasets after truncating their uv sampling at $r_{uv} \leq 10\,\mathrm{k}\lambda$ (see Section 2.3.3). The maps of the truncated CO(1–0) datasets generally have higher noise and smaller synthesized beams than the originals; we have listed both sets of values in Table 5.2. Maps of the truncated CO(2–1) datasets are virtually unchanged. For NGC 3227 and NGC 5033, we estimate global values for R by convolving the new maps to 23″ resolution, and (re)measuring what fractions we recover of the single-dish intensities measured by Braine et al. (1993). Table 5.3 shows the results: in both cases, the intensity ratio of the

emission we detect with the interferometer is higher than the intensity ratio of the emission we miss. These results fit the pattern of NGC 7479 (see Section 2.3.3) and NGC 2681 (see Section 3.3.3), leaving NGC 1068 (see Section 4.3.3) as the exception to the rule.

In addition to considering global intensity ratios, we have examined local variations in R by comparing partial moment maps of the data cubes for both truncated datasets (after convolving the CO(2–1) maps to the resolution of the CO(1–0) maps). We measure R for prominent gas structures which appear in (a) one of four velocity windows, roughly symmetric with respect to systemic velocity, and/or (b) the integral over a galaxy's full linewidth. We also measure the peak (beam-diluted) brightness temperatures observed in the spatial boxes used to make the ratio measurements. Tables 5.4 through 5.13 present the parameters of both emission lines (measured from the full datasets) and the intensity ratio (measured from the truncated datasets) for each galaxy in turn. The listed values and uncertainties are obtained as described in Section 2.3.

5.3.1 NGC 3227

For NGC 3227, we have integrated over $n_{ch} = 50$ velocity channels from 865.7 to 1385.9 km s^{-1} to generate the maps in Figure 5.1. Convolution of the zeroth moment maps to a 23″ half-power beamwidth and comparison to the single-dish observations of Braine et al. (1993) implies that we are recovering only half as much of the total CO(2–1) emission ($\sim$ 31%) as we are of the total CO(1–0) emission ($\sim$ 62%). We suspect that much of the missing CO(2–1) flux is in fact associated with structures present in the map and is only barely resolved out due to our paucity of sampling at small uv radius, since the CO(1–0) flux recovery drops sharply from 62% to 24% when we apply the 10 kλ truncation described above. Other parameters of the emission in both lines are presented in Table 5.4.

Our molecular maps of both transitions are dominated by a strong, almost triangular distribution of dimensions $\sim 11'' \times 6''$. This structure's elongation and predominant velocity gradient are roughly parallel to the line of nodes determined from a model of the inner H I disk (Mundell et al. 1995b), as well as to a line connecting the centers of NGC 3227 and its nearby companion NGC 3226. Apart from this central disk, we see features to the northwest [$\sim (-8'', +4'')$] and southeast [$\sim (+12'', -10'')$] of the nucleus which are prominent in CO(1–0) and weakly visible in CO(2–1). These off-nuclear features are strikingly elongated, as is a third (NNW) structure seen at $(-10'', +12'')$ in the CO(1–0) map. We suggest that

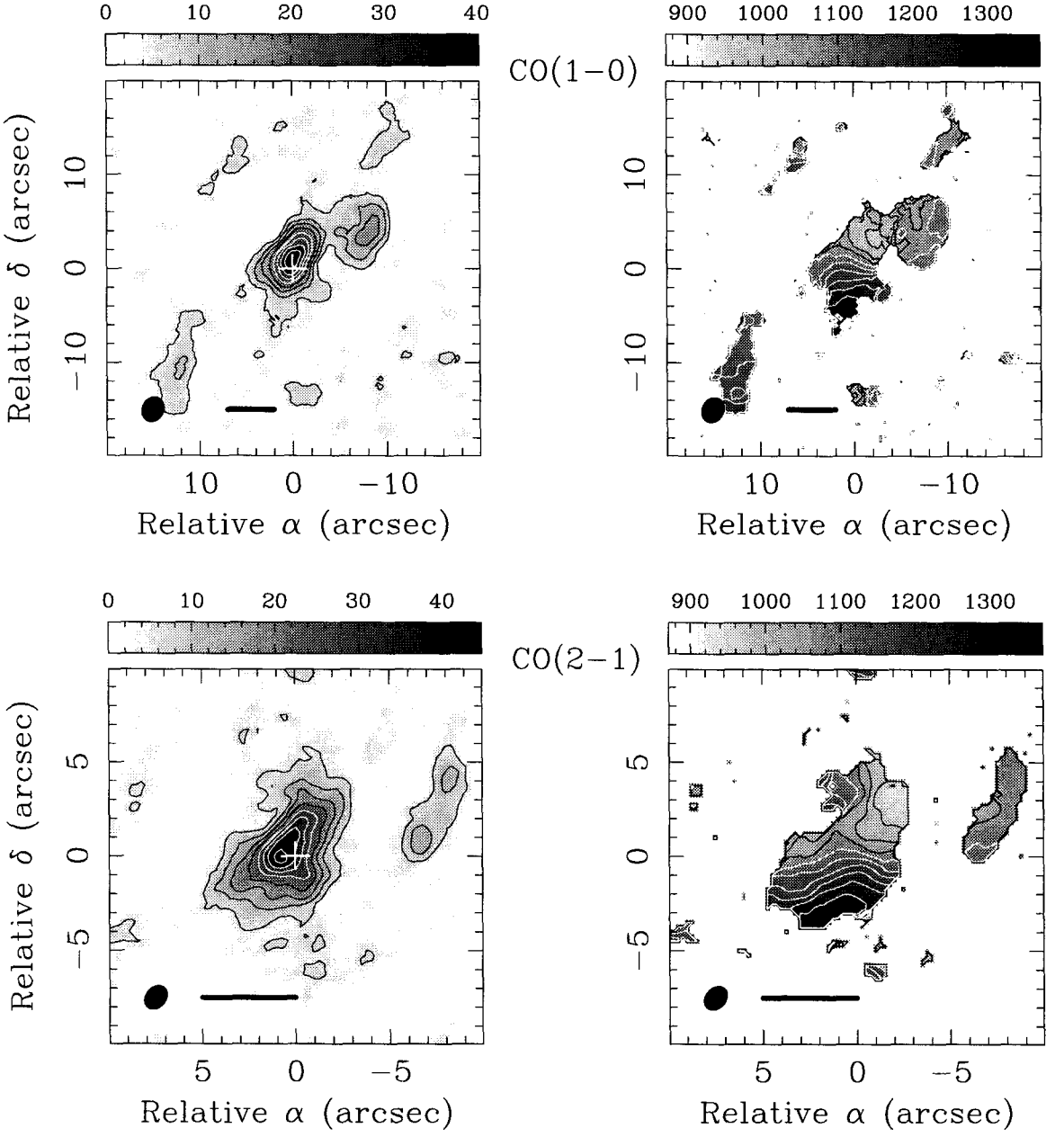

Figure 5.1: Moment maps of NGC 3227. The ellipses at lower left show the synthesized beams; the bars nearby indicate 500 pc at 20.6 Mpc; the crosses mark the position of the radio continuum peak (see Table 5.15). Contours in the zeroth moment maps are multiples of 4.5 Jy bm^{-1} km s^{-1} for CO(1–0) and 5.5 Jy bm^{-1} km s^{-1} for CO(2–1). Isovelocity contours in both first moment maps run from 940 to 1300 km s^{-1} (heliocentric) in steps of 40 km s^{-1}.

Feature (1)	Quantity (2)	CO(1–0) (3)	CO(2–1) (4)	Units (5)
Central disk	peak T_b	3.30 ± 0.42	4.91 ± 0.43	K
	peak $I_{\rm CO}$	542 ± 28	661 ± 31	$\rm K\,km\,s^{-1}$
	$F_{\rm CO}$	130 ± 8	412 ± 15	$\rm Jy\,km\,s^{-1}$
	M_{gas}	8.8 ± 0.5		$10^8\,\rm M_\odot$
SE clump	$F_{\rm CO}$	29 ± 6	66 ± 11	$\rm Jy\,km\,s^{-1}$
	M_{gas}	2.0 ± 0.4		$10^8\,\rm M_\odot$
NW clump	$F_{\rm CO}$	51 ± 6	48 ± 11	$\rm Jy\,km\,s^{-1}$
	M_{gas}	3.5 ± 0.4		$10^8\,\rm M_\odot$
NNW clump	$F_{\rm CO}$	17 ± 5	-	$\rm Jy\,km\,s^{-1}$
	M_{gas}	1.2 ± 0.3		$10^8\,\rm M_\odot$
Full galaxy	$F_{\rm CO}$	254 ± 23	502 ± 37	$\rm Jy\,km\,s^{-1}$
	M_{gas}	17.3 ± 1.6		$10^8\,\rm M_\odot$

Table 5.4: Parameters of emission in NGC 3227. All quantities are measured from maps made using the full (pre-truncation) *uv* datasets. The uncertainty listed for each measurement is the larger of the *a priori* and empirical prescriptions described in Appendix A.4. Molecular gas masses are inferred from CO(1–0) fluxes, assuming a Galactic conversion factor of $X = 3 \times 10^{20}\,\rm cm^{-2}\,(K\,km\,s^{-1})^{-1}$ (see Section 3.5).

they represent discrete concentrations of molecular gas at the leading edges of a bar. Such a scenario has already been suggested for NGC 3227 by Fernandez et al. (1999), although the molecular structures these authors attribute to a bar come from the CO(1–0) map of Meixner et al. (1990) which agrees rather poorly with ours. Arguments that NGC 3227 is in fact barred are made by Mulchaey et al. (1997), whose K_s image hints at a bar of length $> 80''(\sim 8\,\rm kpc)$ at position angle $\sim 150°$; by González Delgado & Pérez (1997), who infer a 4.3 kpc bar running roughly north-south from the residuals to isophote fitting of a λ5900 Å image; and by Mundell et al. (1995b) on the basis of their H I map. The difficulty of isolating an elongated structure in a highly inclined system means that these results must be considered rather tentative. However, González Delgado & Pérez (1997) also observe two chains of H II regions which would coincide with the leading edges of the putative bar if the galaxy's spiral arms trail, and which are *definitely* aligned with the off-nuclear molecular features.

Unfortunately, our attribution of the molecular structures in NGC 3227 to a central disk and bar (on the basis of the zeroth moment maps) appears less secure when we also

Velocities ($km\,s^{-1}$)	Feature	$T_{b(2-1)}$	$T_{b(1-0)}$	R
(1)	(2)	(3)	(4)	(5)
865.7 - 1000.9	nucleus	2.24	3.23	0.68 ± 0.12
1000.9 - 1125.8	nucleus: CO(1–0) peak	2.02	2.54	0.74 ± 0.24
	nucleus: CO(2–1) peak	2.02	2.53	0.93 ± 0.25
	NW clump	1.51	2.71	0.60 ± 0.04
1125.8 - 1250.6	nucleus	1.62	2.74	1.02 ± 0.35
	SE clump	1.15	3.46	0.53 ± 0.06
1250.6 - 1385.9	nucleus	2.18	2.85	0.85 ± 0.24
865.7 - 1385.9	nucleus	2.18	2.85	0.89 ± 0.12
	NW clump	1.51	2.68	0.37 ± 0.08
	SE clump	1.09	3.10	0.43 ± 0.09

Table 5.5: Local intensity ratios in NGC 3227. All quantities are measured from maps made using the truncated *uv* datasets. Column (1) identifies four velocity windows and the full linewidth over which we measured R, in spatial boxes centered on spatial features which are described in column (2). The remaining columns give (3) the peak CO(2–1) brightness temperature (± 0.43 K), (4) the peak CO(1–0) brightness temperature (± 0.42 K), and (5) the average intensity ratio within the measurement box. The uncertainties in R are the formal dispersions over each box.

consider the first moment maps. At the large galactocentric radii of the SE and NNW emission features, we lack sufficient information about the local velocity field to establish whether the gas is on circular or noncircular orbits. For the NW feature, the discontinuous isovelocity contours in the CO(1–0) first moment map clearly imply that the dominant motion is not circular. However, contrary to our expectation that material at the leading edge of a bar should be flowing inward with greater-than-circular velocity, we find that the NW clump is *redshifted* with respect to the local circular velocity! We must therefore conclude that this gas is moving outward in the plane of the disk, or (somewhat more plausibly) that it is not in the plane of the disk at all. Association of this peculiar motion with jet-driven outflow is not viable, since the symmetry axis of the radio emission and optical ionization cone on large scales has position angle $\sim 30^\circ$ (Mundell et al. 1995a). An alternative is that the gas is subject to tidal forces: Mundell et al. (1995b) isolate H I emission from a structure with anomalous (also redshifted) velocity to the northwest of the nucleus, which they suggest is debris from the interaction between NGC 3226 and NGC 3227, or in fact a third interaction partner.

In NGC 3227, R is clearly higher in the nucleus ($\sim 0.7-1.0$) than it is in the off-nuclear features ($\sim 0.4-0.6$); this is the pattern we would expect if the central structure has higher temperature and/or density. The existence of excitation gradients within the nucleus itself is implied by the variation of R with velocity window, and by the positional discrepancy between the peak line intensities in the single window just blueward of systemic velocity. We adopt $R \simeq 0.89$ as a representative value for use in our analysis in Section 5.5 below.

5.3.2 NGC 4051

For NGC 4051, we have integrated over $n_{ch} = 26$ velocity channels from 594.4 to 864.8 km s^{-1} to generate the maps in Figure 5.2. Convolution of the CO(1–0) zeroth moment map to a 45″ half-power beamwidth and comparison to the single-dish observations of Young et al. (1995) implies we are only detecting $\sim 35\%$ of the total CO(1–0) emission. While we may be failing to detect some low-surface-brightness material– as has been seen to the southeast of the nucleus in comparable observations by Kohno et al. (1999)– we are also likely to be resolving out emission from smoothly distributed gas.

The large-scale velocity field in NGC 4051 has been mapped in H I by Liszt & Dickey (1995) and in Hα by Kaneko et al. (1997). These observations (and the assumption of trailing spiral arms) imply that the galaxy's disk has an inclination of $\sim 40°$, with its ascending node at position angle $\sim 132°$. Inspection of Figure 5.2 shows that if molecular gas is confined to this disk plane, only one visible structure– the central peak in our CO(2–1) map– can be close to axisymmetric. A Gaussian fit to this peak yields dimensions of $\sim 4'' \times 3''$ (consistent with $i \sim 41°$) at a position angle of $\sim 113°$; note that our kinematic model (see Section 5.4.2 below) predicts $\alpha \sim 125°$, in better agreement with the H I observations.

Outside this central disk, emission in both zeroth moment maps is slightly elongated at a position angle of $\sim 11°$; a Gaussian fit to the CO(1–0) map gives dimensions of $\sim 7.4'' \times 5.9''$. If deprojected to the plane of the galaxy, this structure is neither circular nor aligned with a large-scale bar ($> 100''$ long at position angle 138°) possibly present in the K_s image of Mulchaey et al. (1997). We conclude that we are seeing an *inner* bar, in which streaming motions of the gas produce the highest line-of-sight velocities seen in our first moment maps. This scenario can account for the detection by Kaneko et al. (1997) of a steeper rotation curve in the inner 10″ of their Hα data, which the authors of that paper attribute to a change in the symmetry axis of the galaxy at small radius. The agreement in orientation

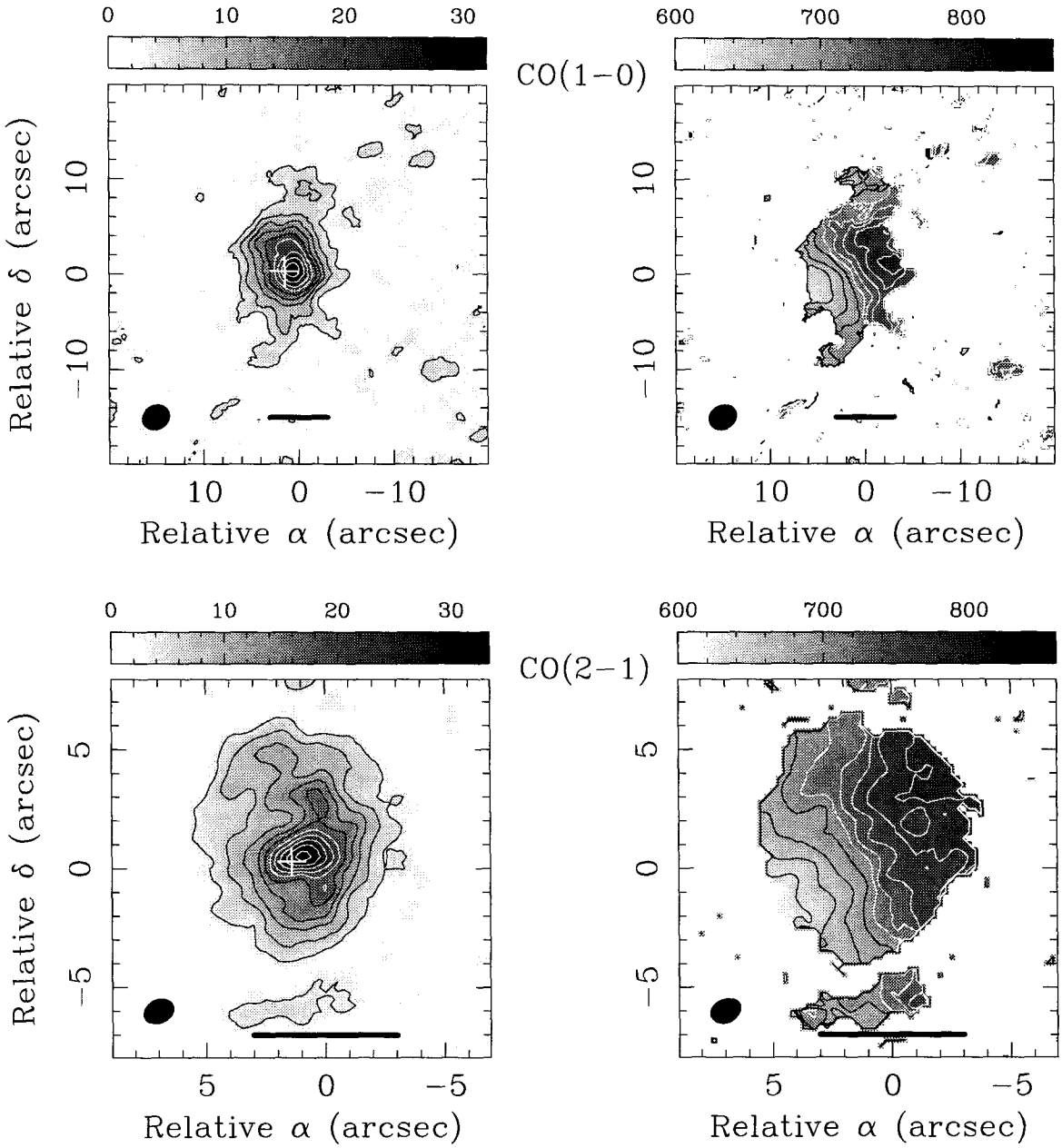

Figure 5.2: Moment maps of NGC 4051. Notation is as in Figure 5.1 (bars are 500 pc at 17.0 Mpc). Contours in the zeroth moment maps are multiples of 3.3 Jy bm^{-1} km s^{-1} for CO(1–0) and 3.2 Jy bm^{-1} km s^{-1} for CO(2–1). Isovelocity contours in both first moment maps run from 630 to 810 km s^{-1} (heliocentric) in steps of 20 km s^{-1}.

Feature (1)	Quantity (2)	CO(1–0) (3)	CO(2–1) (4)	Units (5)
Inner bar	peak T_b	3.87 ± 0.32	5.92 ± 0.22	K
	peak $I_{\rm CO}$	375 ± 19	570 ± 20	$\rm K\,km\,s^{-1}$
	$F_{\rm CO}$	132 ± 6	415 ± 10	$\rm Jy\,km\,s^{-1}$
	M_{gas}	6.1 ± 0.3		$10^8\,\rm M_\odot$
Central disk	$F_{\rm CO}$	-	141 ± 3	$\rm Jy\,km\,s^{-1}$
N clump	$F_{\rm CO}$	11 ± 3	-	$\rm Jy\,km\,s^{-1}$
	M_{gas}	0.5 ± 0.1		$10^8\,\rm M_\odot$
S clump	$F_{\rm CO}$	11 ± 3	-	$\rm Jy\,km\,s^{-1}$
	M_{gas}	0.5 ± 0.1		$10^8\,\rm M_\odot$
Full galaxy	$F_{\rm CO}$	167 ± 10	502 ± 37	$\rm Jy\,km\,s^{-1}$
	M_{gas}	7.7 ± 0.5		$10^8\,\rm M_\odot$

Table 5.6: Parameters of emission in NGC 4051. Notation is as for Table 5.4. The "inner bar" includes the central disk which is resolved (only) in the CO(2–1) map, but not the extensions to the north and south which are seen (only) in the CO(1–0) map.

of the central molecular disk and the H I and Hα disk argue against any such change in the symmetry axis.

In our CO(1–0) maps, we detect additional emission features to the north and south of the inner bar. We suggest that these features correspond to $\sim 5 \times 10^7\,\rm M_\odot$ concentrations of gas which are moving inward along the *outer* bar observed by Mulchaey et al. (1997). For the northern clump in particular we have good kinematic evidence to support this assertion: the mean velocity is blueshifted with respect to that of neighboring material in the inner bar, as we would expect for gas near perigalacticon on an elongated orbit. We only offer a qualitative description of the gas dynamics in NGC 4051 at this stage, however, because the orientation of the outer stellar bar is difficult to determine (given how closely it follows the line of nodes), while the orientation of an inner stellar bar is not known at all.

From the absence of CO(2–1) emission from the clumps north and south of the inner bar, we can infer that the excitation in this gas is lower than in the inner bar and nuclear disk. For these regions, we adopt the intensity ratio averaged over the full linewidth ($R \simeq 0.99$) as a representative value for our analysis in Section 5.5 below.

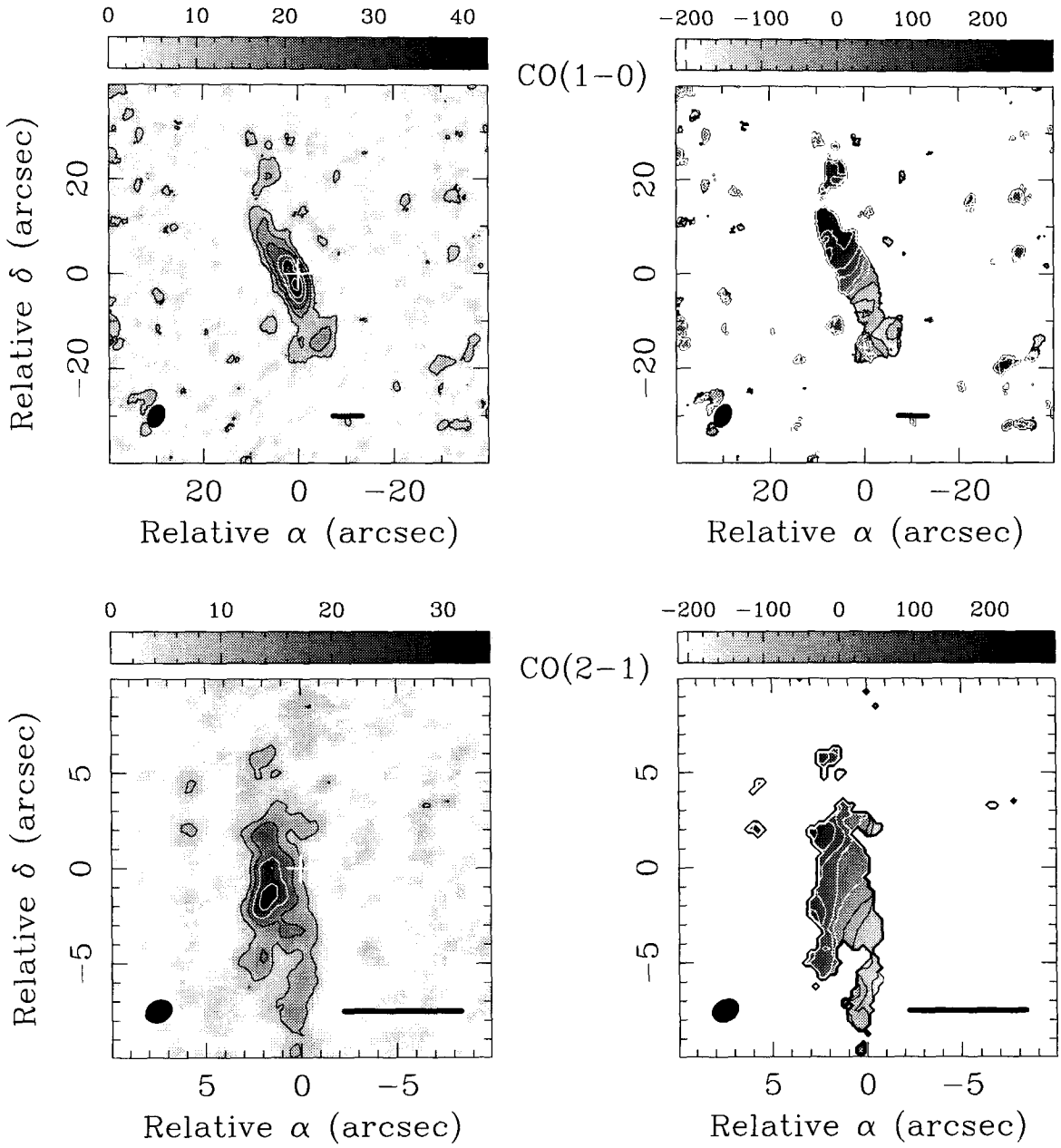

Figure 5.3: Moment maps of NGC 4438. Notation is as in Figure 5.1 (bars are 500 pc at 16.8 Mpc). Contours in the zeroth moment maps are multiples of 6.5 Jy bm^{-1} km s^{-1} for CO(1–0) and 7.4 Jy bm^{-1} km s^{-1} for CO(2–1). Isovelocity contours in both first moment maps run from -200 to 200 km s^{-1} (heliocentric) in steps of 50 km s^{-1}.

Velocities ($km\,s^{-1}$) (1)	Feature (2)	$T_{b(2-1)}$ (3)	$T_{b(1-0)}$ (4)	R (5)
594.4 - 667.2	nucleus	2.25	3.22	0.81 ± 0.12
667.2 - 729.6	nucleus: CO(1–0) peak	2.16	3.26	0.88 ± 0.14
	nucleus: CO(2–1) peak	2.21	2.12	1.01 ± 0.23
	northern extension	1.85	2.61	0.66 ± 0.17
729.6 - 792.0	nucleus	1.78	3.35	0.65 ± 0.04
	northern extension	1.86	2.92	0.87 ± 0.16
792.0 - 864.8	nucleus	2.11	3.67	0.77 ± 0.09
594.4 - 864.8	nucleus	2.33	3.88	0.99 ± 0.09

Table 5.7: Local intensity ratios in NGC 4051. Notation is as for Table 5.5. Uncertainties in peak brightness temperatures are ± 0.40 K for CO(2–1) and ± 0.41 K for CO(1–0). The "northern extension" in the two central velocity windows falls north of the nuclear peak but still within the inner bar.

5.3.3 NGC 4438

For NGC 4438, we have integrated over $n_{ch} = 49$ velocity channels from -219.3 to 290.5 $km\,s^{-1}$ to generate the maps in Figure 5.3. Convolution of the zeroth moment maps to lower resolution and comparison to single-dish observations gives somewhat perplexing results: our data nominally recover $\sim$ 143% of the CO(1–0) emission detected by Kenney & Young (1988) in a 45″ half-power beamwidth, $\sim$ 34% of the CO(1–0) emission detected by Combes et al. (1988) in a 23″ half-power beamwidth, and $\sim$ 98% of the CO(2–1) emission detected by Combes et al. (1988) in a 12″ half-power beamwidth. We suspect that pointing uncertainties in the single-dish observations probably account for much of the spread in these estimates. For an alternate gauge of our flux recovery, we compare the total CO(1–0) flux in our map, i.e., 223 ± 33 Jy $km\,s^{-1}$, to the $\sim$ 479 Jy $km\,s^{-1}$ estimated for the entire galaxy by Combes et al. (1988). The ratio of 47% is properly a lower limit on the fraction of the total emission detected by the interferometer, since our observations of only a single pointing limit our effective field of view.

Our CO(1–0) map is dominated by a structure with dimensions $\sim 25'' \times 8''$ at a position angle $\sim 30°$; the elongation of this structure is parallel both to its predominant velocity gradient and to the position angle of the galaxy's optical isophotes (de Vaucouleurs et al. 1991). The velocity field in this main [molecular] disk appears to be an irregular variation

Feature (1)	Quantity (2)	CO(1–0) (3)	CO(2–1) (4)	Units (5)
Main disk	peak T_b	1.95 ± 0.47	4.20 ± 0.51	K
	peak $I_{\rm CO}$	211 ± 17	458 ± 49	$\rm K\,km\,s^{-1}$
	$F_{\rm CO}$	148 ± 14	133 ± 11	$\rm Jy\,km\,s^{-1}$
	M_{gas}	6.7 ± 0.6		$10^8\,\rm M_\odot$
SW clump	$F_{\rm CO}$	46 ± 9	-	$\rm Jy\,km\,s^{-1}$
	M_{gas}	2.1 ± 0.4		$10^8\,\rm M_\odot$
NE clump	$F_{\rm CO}$	20 ± 6	-	$\rm Jy\,km\,s^{-1}$
	M_{gas}	0.9 ± 0.3		$10^8\,\rm M_\odot$
Full galaxy	$F_{\rm CO}$	223 ± 33	297 ± 35	$\rm Jy\,km\,s^{-1}$
	M_{gas}	10.1 ± 1.5		$10^8\,\rm M_\odot$

Table 5.8: Parameters of emission in NGC 4438. Notation is as for Table 5.4. Since the CO(2–1) emission appears quite different from the CO(1–0) emission, we take the "main disk" in the former case to include all the bright CO(2–1) emission visible in Figure 5.3, and the "full galaxy" to include various diffuse features elsewhere in the map.

on solid-body rotation, making it difficult for us to locate the dynamical center. The radio continuum peak falls within a beamwidth of the CO(1–0) intensity peak to the northwest. Besides the main disk, we see distinct molecular structures to the southwest and northeast which display somewhat more complicated kinematics. Previous OVRO observations of NGC 4438 by Kenney et al. (1995) detect emission from both the main disk and the southwest clump, albeit blended together due to slightly lower angular resolution. These authors' estimate of the total $F_{\rm CO(1-0)} = 216 \pm 33\,\rm Jy\,km\,s^{-1}$ agrees very well with ours.

Our CO(2–1) map of NGC 4438 looks rather irregular: there is no line emission (much less an emission peak) at the location of the radio continuum peak, the morphology of the emission does not match any structure in our CO(1–0) map in size, shape, or orientation, and the overall symmetry of the map is extremely low. The predominant velocity gradient in the CO(2–1) emission (i.e., southwest to northeast) does at least agree with what we see in the CO(1–0) data. While we must make some allowance for irregularity in this galaxy in view of its violent interaction with NGC 4435, we suspect noisy visibility data may be partly to blame. Our concerns are amplified by two additional points. First, the signal to noise at peak intensity is rather low compared to what we achieve in our other CO(2–1) maps. Second, our estimates of the intensity ratio R vary widely from window to window in

Velocities ($km\,s^{-1}$)	Feature	$T_{b(2-1)}$	$T_{b(1-0)}$	R
(1)	(2)	(3)	(4)	(5)
-219.3 - -94.4	nucleus	0.79	1.52	0.49 ± 0.10
	SW clump	0.81	1.42	0.62 ± 0.07
-94.4 - 30.4	nucleus: CO(1–0) peak	0.90	1.26	0.61 ± 0.20
	nucleus: CO(2–1) peak	0.92	1.26	0.97 ± 0.30
30.4 - 155.2	nucleus	0.96	1.95	0.58 ± 0.05
155.2 - 290.5	nucleus	0.63	1.24	0.50 ± 0.11
-219.3 - 290.5	nucleus: CO(1–0) peak	0.94	1.90	0.67 ± 0.26
	nucleus: CO(2–1) peak	0.96	1.95	0.88 ± 0.25

Table 5.9: Local intensity ratios in NGC 4438. Notation is as for Table 5.5. Uncertainties in peak brightness temperatures are ± 0.68 K for CO(2–1) and ± 0.26 K for CO(1–0).

velocity, have large uncertainties, and tend towards the low values which we would expect if our deconvolution were scattering much of the true flux away from the source. For the purposes of our analysis in Section 5.5, we estimate $R \simeq 0.77$ (i.e., the average of our two measurements over the full linewidth) but note that most of our other measurements give lower values.

5.3.4 NGC 5005

Because our CO(1–0) observations of NGC 5005 permit imaging at higher resolution *and* sensitivity than those of the other four galaxies, and because they have already been the subject of one collaborative paper (Sakamoto et al. 2000), we discuss them here in particular detail. Figure 5.4 shows a zeroth moment map of the CO(1–0) emission from the galaxy's entire disk, calibrated and imaged to take advantage of the dataset's sensitivity (although not precisely as described in Section 5.2). As discussed in Sakamoto et al. (2000), we can identify four components in the galaxy's molecular distribution. The most extended is a nearly-circular ring with radius ~ 3 kpc; this structure appears nearly continuous if mapped at lower resolution, and is unlikely to be a pair of tightly-wrapped spiral arms. At the nucleus, we see a central molecular disk with radius ~ 1 kpc. Adjacent to the nuclear disk (but inside the 3 kpc ring), we find a distinct gas condensation which we identify as the "northwest stream." The material in this structure has a velocity inconsistent with circular rotation; instead, it appears to be flowing inward at the leading edge of a bar which may be

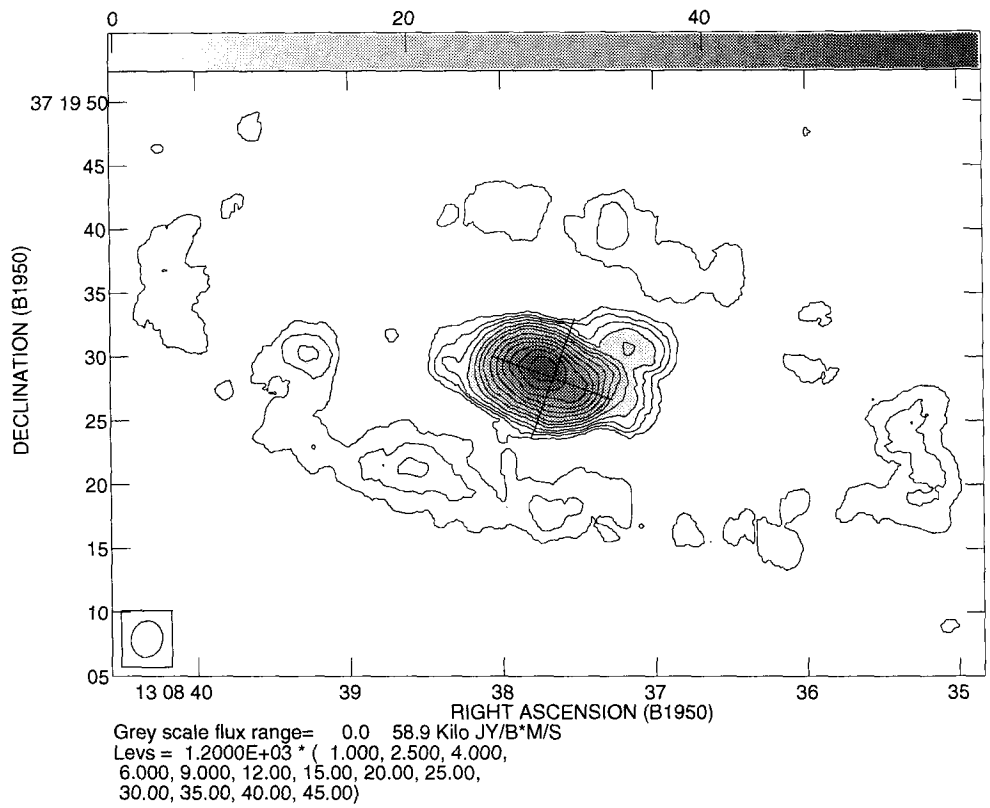

Figure 5.4: Zeroth moment map of CO(1–0) in the disk of NGC 5005, from Sakamoto et al. (2000). At lower resolution, the 3 kpc ring appears nearly continuous. The emission feature perched to the northwest of the nucleus is inferred to be streaming inward at the leading edge of a bar. The synthesized beam for this mapping of the data is $2.88'' \times 2.44''$ at $-18.9°$; the per-channel rms in the data cube is $14\,\mathrm{mJy\,bm^{-1}}$.

visible in the infrared (Eskridge 1999). The emission peak due east of the nuclear disk but slightly inside the 3 kpc ring is likely to be a counterpart "east stream" at the bar's other leading edge but slightly larger galactocentric radius.

In addition to the striking kinematic signatures seen in the northwest and east streams, we see evidence for noncircular motions in the 3 kpc ring itself. A position-velocity cut along the kinematic minor axis of the galaxy (at 155°) shows that the gas to the south of the nucleus has less than systemic velocity, while the gas to the north of the nucleus has greater than systemic velocity. This pattern is expected if the "nearly circular" ring is an ellipse elongated along a bar running roughly east-west. In such a configuration, gas on

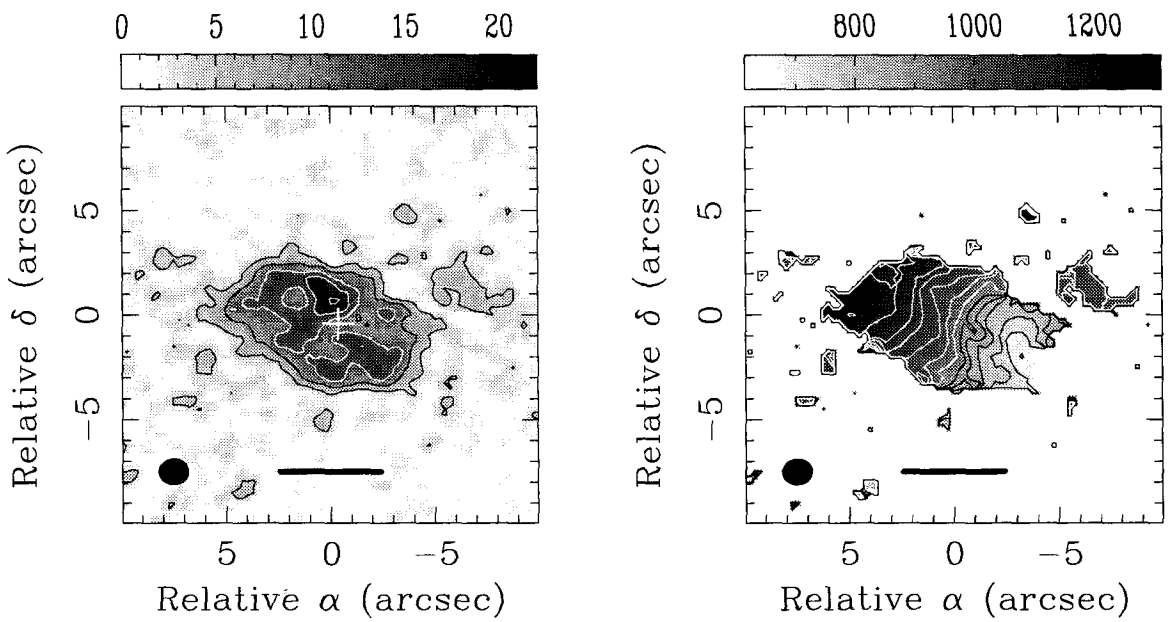

Figure 5.5: CO(1–0) moment maps of the nucleus of NGC 5005. Notation is as in Figure 5.1. Contours in the zeroth moment map are multiples of $4.3\,\mathrm{Jy\,bm^{-1}\,km\,s^{-1}}$. Isovelocity contours in the first moment map run from 700 to $1200\,\mathrm{km\,s^{-1}}$ (heliocentric) in steps of $50\,\mathrm{km\,s^{-1}}$.

an elongated orbit will be on its way from apogalacticon to perigalacticon when it crosses the kinematic minor axis, and will consequently appear to have an inward line-of-sight motion. The radius and orientation of the ring suggest that it may arise at the inner 4:1 Lindblad (i.e., ultraharmonic) resonance of the bar. While this resonance will not play an important role in the model we describe in Appendix B.1 and develop in Section 2.4, since the latter assumes a perturbing potential $\Phi_1 \propto \cos(2\phi')$ alone, it is likely significant in real galaxies. Approaching (and beyond) corotation, a realistic barred potential can support additional types of orbits beyond the best-known x_1 and x_2 families. The appearance and disappearance of orbit families can be parametrized by the Jacobi constant E_J– the sole combination of energy and angular momentum which is conserved in a rotating potential– and by the distance from the center y at which an orbit crosses the bar's minor axis. The relation $y(E_J)$ traces an orbit family's *characteristic curve* and can exhibit pronounced discontinuities in resonance regions. At the inner 4:1 Lindblad resonance, in particular, the x_1 family beyond a critical value of E_J transitions into a new 4:1 family whose precise shape (either rectangular or diamondlike) depends on properties of Φ_1 (Contopoulos 1988). We

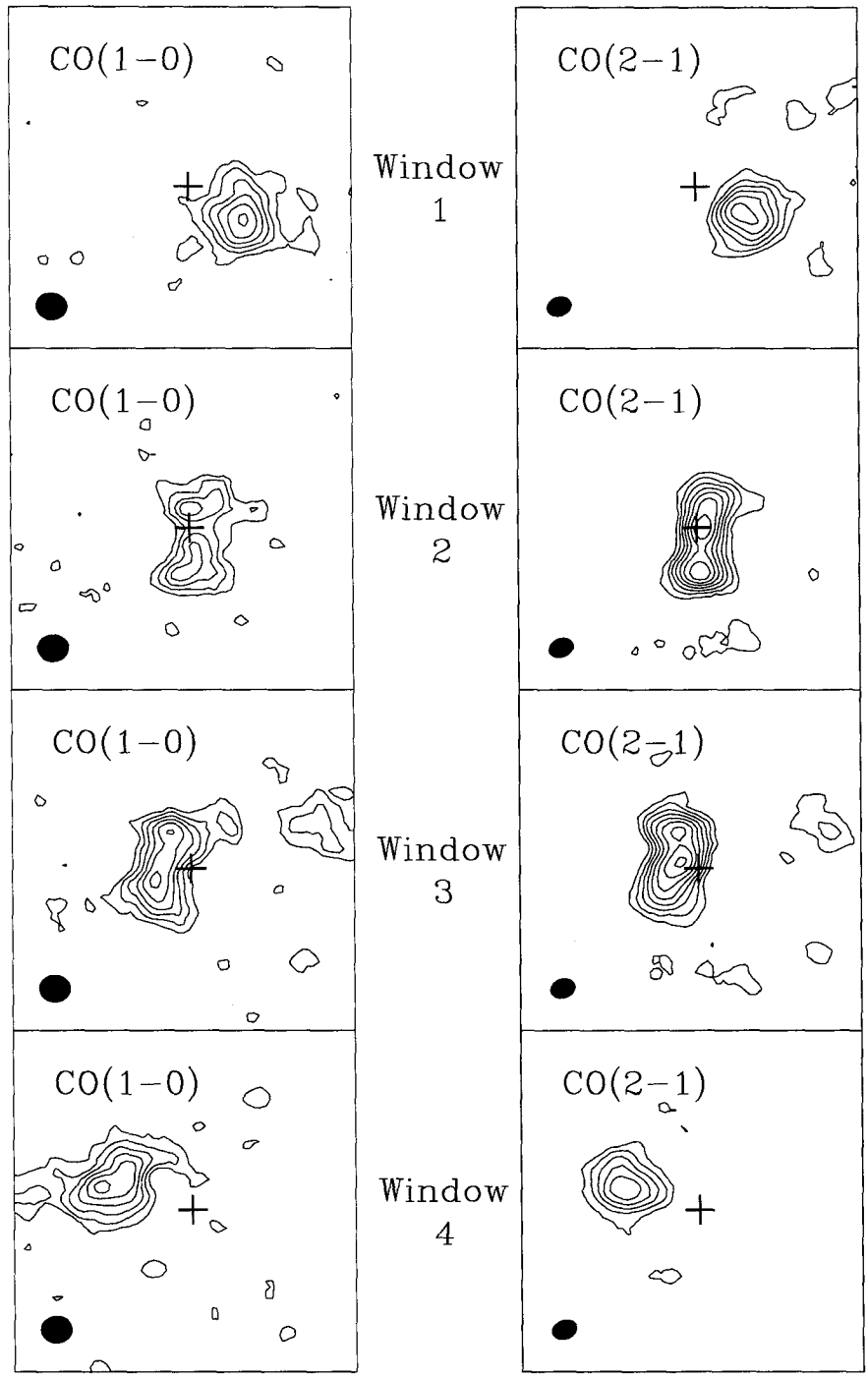

Figure 5.6: Partial moment maps of NGC 5005. We show the inner $8'' \times 8''$ for *both* transitions, over the four velocity windows in which we have continuous coverage of the CO(2–1) line (see Table 5.11). Ellipses show the synthesized beams; crosses mark the position of the radio continuum peak. Contours are multiples of $1.9\,\mathrm{Jy\,bm^{-1}\,km\,s^{-1}}$ for CO(1–0) and $3.7\,\mathrm{Jy\,bm^{-1}\,km\,s^{-1}}$ for CO(2–1).

suspect that orbits in the 4:1 (or more exotic) families are contributing to the stability of the 3 kpc ring.

Figure 5.5 shows a zeroth moment map of the CO(1–0) emission in the nuclear disk of NGC 5005. To produce this map, we recalibrated and reimaged the data according to Section 5.2 and Tables 5.1 and 5.2; we have integrated over $n_{ch} = 68$ velocity channels from 609.7 to 1317.1 km s^{-1}. As a result of adopting a weighting scheme which maximizes angular resolution, we have lost sensitivity to smooth emission with lower surface brightness: the 3 kpc ring is no longer visible, and the northwest stream is only barely detected. When we convolve this map to 23″ and 45″ resolution, we recover only $\sim$ 64% and $\sim$ 37%, respectively, of the emission detected in the single-dish observations of Braine et al. (1993) and Young et al. (1995). Much of the flux we fail to recover in Figure 5.5 does appear in Figure 5.4, however, where the lower resolution and higher sensitivity allow us to recover $\sim$ 94% and $\sim$ 37% of the single-dish fluxes. Figure 5.5 also shows the first moment of the CO(1–0) emission in the nuclear disk. Here we see the characteristic twisting of isovelocity contours which indicates the presence of noncircular or noncoplanar motions. From our detection of noncircular motions on larger scales and the lack of any evidence for small-scale warping, we conclude that the gas in the inner disk is moving on noncircular orbits– possibly in the x_2 family defined relative to the larger bar.

Because our CO(2–1) observations lack complete velocity coverage, computing the zeroth and first moments of our data cube will result in misleading maps. We therefore present (in Figure 5.6) partial zeroth moment maps of the CO(2–1) line, integrated over each of four velocity windows, along with the corresponding partial moment maps of the CO(1–0) line. The emission structures we see in each velocity window are largely consistent for the two lines; even the northwest stream appears at roughly the same position in the partial moment maps just redward of systemic velocity (i.e., in Window 3). We do observe one striking difference between the two transitions, however: while the CO(1–0) emission declines in the center, the CO(2–1) emission rises to a peak. This contrast is most obvious in the two windows on either side of systemic velocity, where a **C**entral peak is much stronger relative to the **N**orth and **S**outh edges of the disk in the CO(2–1) maps than in the CO(1–0) maps. We conclude that NGC 5005 has an excitation gradient in the nucleus, with temperature and/or density increasing as radius decreases. We can characterize this gradient numerically by measuring the intensity ratio at various positions for each of the four velocity windows.

Velocity width (1)	Feature (2)	Quantity (3)	CO(1–0) (4)	CO(2–1) (5)	Units (6)
Full line	Disk emission	peak T_b	8.99 ± 0.25	-	K
		peak I_{CO}	1035 ± 108	-	$K\,km\,s^{-1}$
		F_{CO}	260 ± 14	-	$Jy\,km\,s^{-1}$
		M_{gas}	18.9 ± 1.0		$10^8\,M_\odot$
	NW stream	F_{CO}	23 ± 8	-	$Jy\,km\,s^{-1}$
		M_{gas}	1.7 ± 0.6		$10^8\,M_\odot$
Window 1	Disk emission	F_{CO}	47 ± 4	224 ± 26	$Jy\,km\,s^{-1}$
		M_{gas}	3.4 ± 0.3		$10^8\,M_\odot$
Window 2	N edge	F_{CO}	19 ± 3	-	$Jy\,km\,s^{-1}$
		M_{gas}	1.4 ± 0.2		$10^8\,M_\odot$
	C peak	F_{CO}	9 ± 1	-	$Jy\,km\,s^{-1}$
		M_{gas}	0.7 ± 0.1		$10^8\,M_\odot$
	N+C peak	F_{CO}	-	124 ± 7	$Jy\,km\,s^{-1}$
		M_{gas}	-		$10^8\,M_\odot$
	S edge	F_{CO}	14 ± 2	95 ± 6	$Jy\,km\,s^{-1}$
		M_{gas}	1.0 ± 0.1		$10^8\,M_\odot$
	Disk emission	F_{CO}	44 ± 5	217 ± 11	$Jy\,km\,s^{-1}$
		M_{gas}	3.2 ± 0.3		$10^8\,M_\odot$
Window 3	N edge	F_{CO}	24 ± 2	88 ± 5	$Jy\,km\,s^{-1}$
		M_{gas}	1.8 ± 0.2		$10^8\,M_\odot$
	C peak	F_{CO}	-	63 ± 3	$Jy\,km\,s^{-1}$
		M_{gas}	-		$10^8\,M_\odot$
	S+C peak	F_{CO}	36 ± 3	-	$Jy\,km\,s^{-1}$
		M_{gas}	2.6 ± 0.2		$10^8\,M_\odot$
	Disk emission	F_{CO}	60 ± 5	243 ± 11	$Jy\,km\,s^{-1}$
		M_{gas}	4.4 ± 0.4		$10^8\,M_\odot$
	NW stream	F_{CO}	18 ± 4	40 ± 7	$Jy\,km\,s^{-1}$
		M_{gas}	1.3 ± 0.3		$10^8\,M_\odot$
Window 4	Disk emission	F_{CO}	67 ± 5	174 ± 26	$Jy\,km\,s^{-1}$
		M_{gas}	4.9 ± 0.4		$10^8\,M_\odot$
Sum of windows	Disk emission	F_{CO}	202 ± 12	716 ± 30	$Jy\,km\,s^{-1}$
		M_{gas}	14.7 ± 0.8		$10^8\,M_\odot$

Table 5.10: Parameters of emission in NGC 5005. Notation is as for Table 5.4. Our measurements for the full CO(1–0) line correspond to Figure 5.5; comparable measurements for both lines are made for features which can be isolated in the partial moment maps of Figure 5.6. Central "disk emission" encompasses all features apart from the northwest stream.

Velocities ($\mathrm{km\,s^{-1}}$) (1)	Feature (2)	$T_{b(2-1)}$ (3)	$T_{b(1-0)}$ (4)	R (5)
609.7 - 755.3 (Window 1)	W disk edge	4.41	7.50	0.63 ± 0.17
807.4 - 953.0 (Window 2)	S disk edge	5.07	5.80	0.88 ± 0.17
	N disk edge	4.72	6.45	0.83 ± 0.19
	disk center	4.57	5.39	1.36 ± 0.38
973.8 - 1119.4 (Window 3)	N disk edge	4.66	7.41	0.65 ± 0.08
	S disk edge	5.13	7.59	0.53 ± 0.09
	disk center	4.60	7.43	1.11 ± 0.60
	NW stream	2.96	7.57	0.52 ± 0.12
1171.5 - 1317.1 (Window 4)	E disk edge	5.57	7.50	0.49 ± 0.09
sum of windows	E disk edge	4.41	7.21	0.35 ± 0.08
	W disk edge	5.56	7.38	0.55 ± 0.14
	N disk edge	4.57	5.12	0.66 ± 0.12
	S disk edge	5.07	7.05	0.77 ± 0.15
	disk center	5.13	7.59	1.90 ± 0.68

Table 5.11: Local intensity ratios in NGC 5005. Notation is as for Table 5.5. Uncertainties in peak brightness temperatures are $\pm 1.09\,\mathrm{K}$ for CO(2–1) and $1.34\,\mathrm{K}$ for CO(1–0).

The central CO(2–1) peak is so compact that convolution to the resolution of the CO(1–0) maps renders our measurements of R at the center rather uncertain; however, we conclude with reasonable certainty that $R > 1$. Outside the central CO(2–1) peak and CO(1–0) depression, we infer a mean $R \simeq 0.67$ if we average the six "disk edge" measurements from the individual velocity windows in Table 5.11; we adopt this value for our analysis in Section 5.5.

5.3.5 NGC 5033

For NGC 5033, we have integrated over $n_{ch} = 48$ velocity channels from 621.7 to 1121.1 $\mathrm{km\,s^{-1}}$ to generate the maps in Figure 5.7. Convolution of the zeroth moment maps to a 23″ half-power beamwidth and comparison to the single-dish observations of Braine et al. (1993) implies that we are recovering less than a third as much of the total CO(2–1) emission ($\sim$ 22%) as we are of the total CO(1–0) emission ($\sim$ 75%). As in the case of NGC 3227, we suspect that much of this difference is due to the difference in *uv* sampling between the

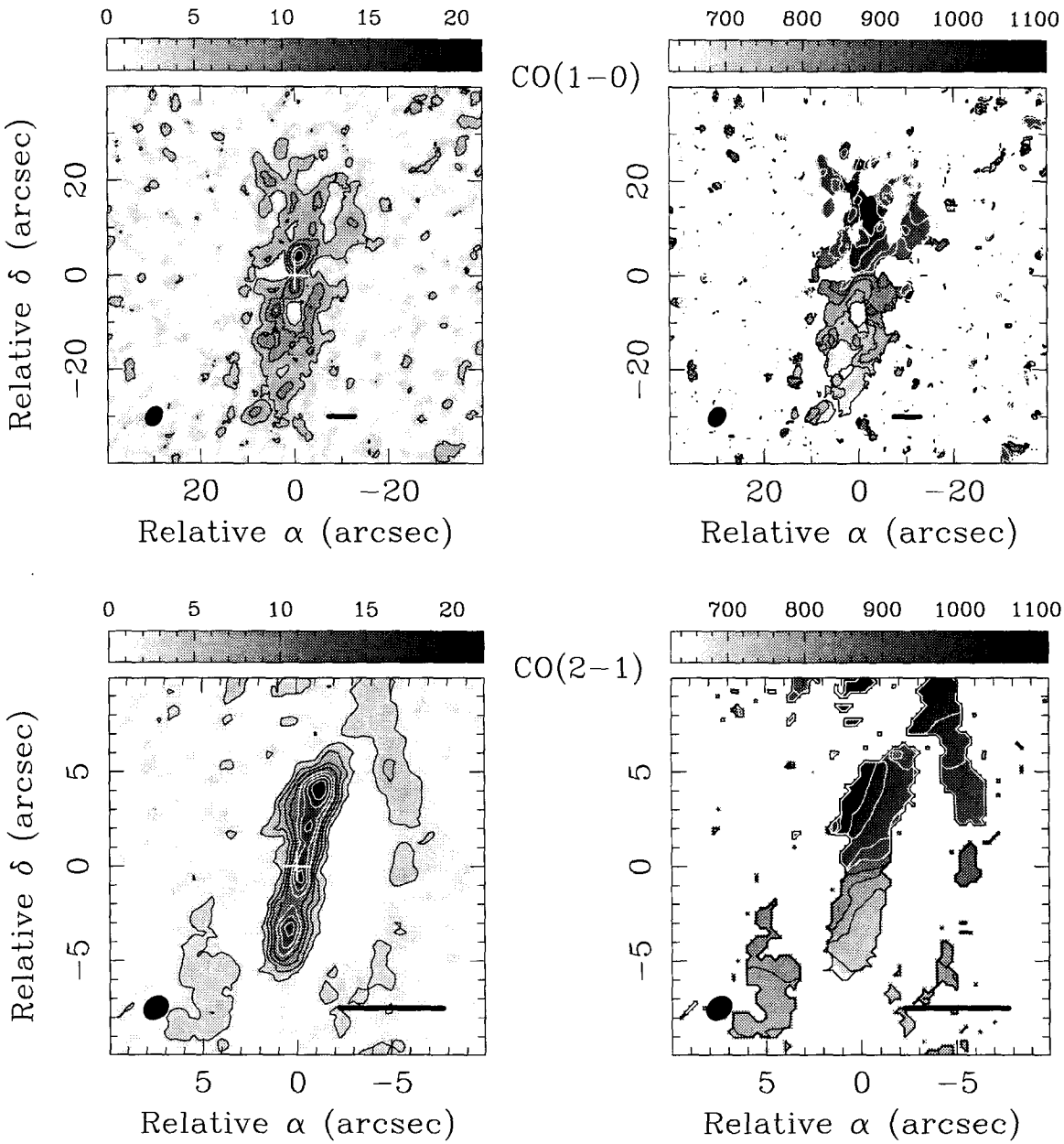

Figure 5.7: Moment maps of NGC 5033. Notation is as in Figure 5.1 (bars are 500 pc at 18.7 Mpc). Contours in the zeroth moment maps are multiples of 3.7 Jy bm^{-1} km s^{-1} for CO(1–0) and 2.4 Jy bm^{-1} km s^{-1} for CO(2–1). Isovelocity contours in both first moment maps run from 650 to 1050 km s^{-1} (heliocentric) in steps of 50 km s^{-1}.

Feature (1)	Quantity (2)	CO(1–0) (3)	CO(2–1) (4)	Units (5)
Central disk	peak T_b	1.21 ± 0.20	3.24 ± 0.27	K
	peak $I_{\rm CO}$	118 ± 14	294 ± 27	$\rm K\,km\,s^{-1}$
	$F_{\rm CO}$	47 ± 6	169 ± 11	$\rm Jy\,km\,s^{-1}$
	M_{gas}	2.6 ± 0.3		$10^8\,\rm M_\odot$
N lobe	$F_{\rm CO}$	26 ± 4	83 ± 6	$\rm Jy\,km\,s^{-1}$
	M_{gas}	1.4 ± 0.2		$10^8\,\rm M_\odot$
S lobe	$F_{\rm CO}$	11 ± 3	46 ± 5	$\rm Jy\,km\,s^{-1}$
	M_{gas}	0.6 ± 0.2		$10^8\,\rm M_\odot$
C peak	$F_{\rm CO}$	-	29 ± 3	$\rm Jy\,km\,s^{-1}$
	M_{gas}	-		$10^8\,\rm M_\odot$
Full galaxy	$F_{\rm CO}$	248 ± 25	329 ± 58	$\rm Jy\,km\,s^{-1}$
	M_{gas}	13.9 ± 1.4		$10^8\,\rm M_\odot$

Table 5.12: Parameters of emission in NGC 5033. Notation is as for Table 5.4. The "central disk" includes the strong north and south lobes, as well as the central peak which is seen (only) in the CO(2–1) map.

two datasets, since the CO(1–0) flux recovery drops sharply to $\sim 12\%$ when we remap the data after truncation at $10\,\rm k\lambda$. We can also convolve our CO(1–0) map to a $45''$ half-power beamwidth and compare the result to the observations of Young et al. (1995). In this case, the interferometer detects only $\sim 34\%$ of the total flux. We attribute the lower flux recovery (relative to the $\sim 75\%$ deduced for a $23''$ beam) to the fact that the galaxy's molecular emission is increasingly smooth on larger angular scales.

In our CO(1–0) zeroth moment map, we see the same wedge-shaped structure as do Kohno et al. (1999); both results improve upon the nondetection of Meixner et al. (1990). The strongest emission within this structure comes from two lobes which lie [slightly west of] north and [slightly east of] south of the position of the radio continuum peak. The north lobe is more than twice as strong as the south lobe in CO(1–0), an indication that (to the extent that use of the Galactic conversion factor is justified) we have detected a significant mass asymmetry with respect to the nucleus. Our CO(1–0) first moment map is largely consistent with regular rotation in a disk; the apparent line of nodes has a position angle near that of the innermost H I annulus ($\simeq 173°$) in the model of Christodoulou et al. (1993). Some divergence from this pattern is evident in the two strong lobes, although our resolution in this transition does not reveal many details.

Velocities ($km\,s^{-1}$) (1)	Feature (2)	$T_{b(2-1)}$ (3)	$T_{b(1-0)}$ (4)	R (5)
621.7 - 746.6	S lobe	0.56	0.77	0.97 ± 0.17
746.6 - 871.4	S lobe	0.62	0.68	1.86 ± 0.37
871.4 - 996.2	N lobe	0.67	0.82	0.96 ± 0.21
996.2 - 1121.1	N lobe	0.70	1.00	1.25 ± 0.34
621.7 - 1121.1	N lobe	0.70	1.00	1.01 ± 0.06
	S lobe (west)	0.58	0.77	1.45 ± 0.11
	S lobe (east)	0.54	0.66	2.06 ± 0.11
	central peak	0.62	0.68	2.42 ± 0.39

Table 5.13: Local intensity ratios in NGC 5033. Notation is as for Table 5.5. Uncertainties in peak brightness temperatures are ± 0.39 K for CO(2–1) and ± 0.23 K for CO(1–0).

Our CO(2–1) moment maps show only a limited amount of emission exterior to the north and south lobes, much of which seems confined to a spiral pattern which trails in the same sense as the galaxy's optical arms on much larger scales. In contrast to its appearance in CO(1–0), the central disk emission is now resolved into an almost linear feature which is *continuous* across the position of the radio continuum peak, and which has a slight eastward protrusion at its northern end. We can identify the CO(2–1) peak at $(+0.5'', -3.5'')$ with the south lobe in the CO(1–0) map, and the sum of the CO(2–1) peak at $(-0.5'', +4'')$ and the adjacent "protrusion" with the north lobe in the CO(1–0) map. The Central CO(2–1) peak, however, corresponds to a position at which our CO(1–0) map is largely devoid of emission; we conclude that (as in NGC 5005) we have detected a pronounced gradient in this galaxy's molecular excitation. In attempting to quantify this gradient, we have found measuring the intensity ratio R to be unusually difficult, since it varies sharply with velocity, and with position relative to our $4.3'' \times 3.4''$ resolution element (see Table 5.2). The precise values we list in Table 5.13 are therefore not entirely self-consistent; they do, however, confirm that the gas of highest temperature and/or density is located closest to the nucleus. For our analysis in Section 5.5, we will adopt $R \simeq 1.01$ (in the north lobe) and $R \simeq 2.06$ (on the eastern side of the south lobe) as representative ratios.

Our CO(2–1) first moment map shows clearly what the CO(1–0) map only suggests– twisted isovelocity contours which are not parallel to the minor axis of the central linear structure, similar (although less dramatic) to the pattern observed in NGC 7479 (see Fig-

ure 2.2). We can infer the presence of noncircular or noncoplanar gas motions in this central structure; we prefer the former explanation for reasons we will explore in Section 5.4.4 below. In either case, our observations clearly prove the value of three-dimensional datasets in describing the nuclear geometry of highly inclined systems. For NGC 5033 in particular, HST imaging by Martini & Pogge (1999) is confounded by the galaxy's inclination and can provide no information on the presence or absence of a nuclear bar.

5.4 Kinematic models

As is clear from the preceding sections, each of our five galaxies shows strong asymmetries in the strength, distribution, and/or kinematics of its molecular emission. Fully realistic models will accurately reproduce these features; for now, however, we are content to derive the approximate parameters of these systems' CO emission by comparing our data cubes to simple axisymmetric models. Our approach is similar to the one laid out in Section 2.4, although our models are somewhat simpler: we now assume not only a flat, axisymmetric emissivity distribution $\sigma(r)$, but also an *unbarred* logarithmic potential. Our comparison of asymmetric data to symmetric models means that we can no longer rely on χ^2_ν to guide us to a "best" set of parameters. Since χ^2 minimization can drive a model to fit strong emission peaks at the expense of weak ones, blind optimization could throw off our results. In certain cases which we note below, we have therefore held a small number of parameters fixed and/or ensured that our results are generally consistent with an analysis of the first moment maps with the AIPS GAL task. In the case of NGC 4438, the CO(1–0) emission has such unusual morphology and kinematics and the CO(2–1) emission is so weak and irregular that converging to even a crude axisymmetric fit is prohibitively difficult. We have therefore restricted our efforts to the four remaining systems.

Tables 5.14 and 5.15 present our estimates of the model parameters; we have attempted to fit our observations in both transitions simultaneously. In general, χ^2_ν for these models is rather high; we are ignoring not only the asymmetric distributions and kinematics of the gas at small radii, but also *any* emission which appears outside $300 - 500\,\mathrm{pc}$. Our decision to fix certain quantities in our models for NGC 4051 and NGC 5033 also means that the parameters in these models do not correspond to minima in χ^2_ν even for our simplistic axisymmetric assumptions. We will discuss individual objects at greater length below, but

Parameter	Units	NGC 3227	NGC 4051	NGC 5005	NGC 5033
(1)	(2)	(3)	(4)	(5)	(6)
$\hat{v}_0$	$\mathrm{km\,s^{-1}}$	1116	721	935	886.5*
i	$^\circ$	140	40*	59	62*
α	$^\circ$	343	125	253	170*
r_p	pc	56	47	378	71
v_p	$\mathrm{km\,s^{-1}}$	295	135	490	196
σ_v	$\mathrm{km\,s^{-1}}$	52	42	66	37
r_{gas}	pc	6	10	14	10
r_{in}	pc	20	22	0	48
$r_{out(1-0)}$	pc	310	300*	550	415
$\bar{\sigma}_{em(1-0)}$	$\mathrm{K\,km\,s^{-1}}$	370	293	391	115
$\eta_{(1-0)}$	-	10	0	0	0
$r_{out(2-1)}$	pc	305	300*	545	520
$\bar{\sigma}_{em(2-1)}$	$\mathrm{K\,km\,s^{-1}}$	281	190	372	70
$\eta_{(2-1)}$	-	38	18	12	15
χ^2_ν	-	96.3	108.6	48.6	110.0
$R(r_{out})$	-	0.76	0.65	0.95	0.61
$R(r_{in})$	-	2.69	12.32	12.37	9.74

Table 5.14: Kinematic model results for the five galaxies. Column (1) lists the model parameters described in Section 2.4, whose units are listed in column (2). The sky coordinates of the dynamical center in each galaxy $(\hat{x}_0, \hat{y}_0)$ are listed in Table 5.15. Starred values were fixed during the fits, for reasons discussed in the text. Velocities are heliocentric in the radio convention. At bottom, we list the reduced chi-square for each model, and the predicted intensity ratios at the outer and inner edges of the disk.

we can make several general observations already. First, in every case the CO(2–1) emission is more strongly centrally peaked than the CO(1–0) emission; in fact, only in NGC 3227 is there evidence that the CO(1–0) surface density is anything other than constant. This trend is consistent with our expectation (and in some cases, as discussed above, clear detection) of higher gas temperature and/or density at smaller radii. Second, the values we infer for the intensity ratio R at the outer and inner edges of the molecular disk– written in terms

Galaxy	Feature	Right ascension (B1950)	Declination (B1950)	Reference(s)
(1)	(2)	(3)	(4)	(5)
NGC 3227	OVRO pointing center	10:20:46.77	+20:07:06.3	
	Radio continuum peak	10:20:46.77	+20:07:06.3	R1,R2,R4
	Peak CO(1–0) intensity	10:20:46.80	+20:07:06.8	
	Peak CO(2–1) intensity	10:20:46.87	+20:07:05.8	
	Dynamical center $(\hat{x}_0, \hat{y}_0)$	10:20:46.76	+20:07:06.6	
NGC 4051	OVRO pointing center	12:00:36.26	+44:48:34.0	
	Radio continuum peak	12:00:36.39	+44:48:34.3	R3,R4
	Peak CO(1–0) intensity	12:00:36.36	+44:48:33.9	
	Peak CO(2–1) intensity	12:00:36.40	+44:48:34.0	
	Dynamical center $(\hat{x}_0, \hat{y}_0)$	12:00:36.36	+44:48:34.7	
NGC 4438	OVRO pointing center	12:25:13.60	+13:17:07.7	
	Radio continuum peak	12:25:13.60	+13:17:07.7	R2
	Peak CO(1–0) intensity	12:25:13.68	+13:17:05.0	
	Peak CO(2–1) intensity	12:25:13.74	+13:17:05.7	
	Dynamical center $(\hat{x}_0, \hat{y}_0)$	-	-	
NGC 5005	OVRO pointing center	13:08:37.70	+37:19:29.0	
	Radio continuum peak	13:08:37.67	+37:19:28.6	R1,R2,R3,R4
	Peak CO(1–0) intensity	13:08:37.74	+37:19:29.0	
	Peak CO(2–1) intensity	-	-	
	Dynamical center $(\hat{x}_0, \hat{y}_0)$	13:08:37.69	+37:19:28.5	
NGC 5033	OVRO pointing center	13:11:09.19	+36:51:30.4	
	Radio continuum peak	13:11:09.19	+36:51:30.4	R2,R4
	Peak CO(1–0) intensity	13:11:09.14	+36:51:34.2	
	Peak CO(2–1) intensity	13:11:09.13	+36:51:34.0	
	Dynamical center $(\hat{x}_0, \hat{y}_0)$	13:11:09.18	+36:31:30.9	

Table 5.15: Coordinates of features in five active nuclei. The pointing center listed for NGC 4051 was used for the CO(2–1) observations (see Section 5.2). Radio continuum positions are arithmetic averages of values taken from R1 = Condon et al. (1990) [1.5″-resolution maps at 20 cm], R2 = van der Hulst et al. (1981) [1″-resolution maps at 6 cm], R3 = Vila et al. (1990) [1″-resolution maps at 6 and 20 cm], and R4 = White et al. (1997) [5.4″-resolution maps at 20 cm from FIRST]. The dynamical center positions are reproduced from Table 5.14.

of the parameters we define in Section 2.4.3 as

$$R(r_{out}) \simeq \frac{\bar{\sigma}_{em(2-1)}}{\bar{\sigma}_{em(1-0)}} \tag{5.1}$$

$$R(r_{in}) = \frac{\bar{\sigma}_{em(2-1)}}{\bar{\sigma}_{em(1-0)}} \times \frac{1+\eta_{(2-1)}}{1+\eta_{(1-0)}} \tag{5.2}$$

uniformly give $R(r_{out}) < 1$ and $R(r_{in}) > 1$. While the extremely high $R(r_{in}) > 4$ seen in three of the models is in part an artifact of our use of an exponential form for emissivity $\sigma(r)$, the results are broadly consistent with the picture that molecular emission is optically thick and thermalized away from the nucleus, but has higher kinetic temperature and lower optical depth close to the center. A third shared feature of the models is the agreement of the estimated velocity dispersions (σ_v) to within a factor of 1.8. Finally, we note that three of the four models discriminate against the presence of gas down to a galactocentric radius $r = 0$. That NGC 5005 is the sole exception to this rule may result from our lack of information about the CO(2–1) emission in a $20.8\,\mathrm{km\,s^{-1}}$ range near systemic velocity.

5.4.1 NGC 3227

We have imposed no *a priori* constraints in deriving our model for NGC 3227, which gives rise to the CO(2–1) position-velocity cuts shown in Figure 5.8. In spite of the pronounced asymmetry in the molecular gas structures, our fit implies an orientation on the sky $(i, \alpha) \simeq (140°, 343°)$ which is reasonably close to the parameters derived by Mundell et al. (1995b) from their H I observations. Figure 5.9 is a schematic representation of how the molecular emission we see relates to this inferred geometry. We are encouraged by the good agreement $r_{out(2-1)} \simeq r_{out(1-0)}$; this suggests that the different uv sampling for the two CO datasets does not translate to different emission structure on the length scales which our model fits. One rather remarkable implication of our model– confirming the independent work of Schinnerer et al. (2000a)– is that the dynamical center lies considerably to the southwest of the molecular gas peak. The fact that $(\hat{x}_0, \hat{y}_0)$ agrees well with the radio continuum peak (see Table 5.15) suggests that this offset corresponds to a true asymmetry in the molecular emissivity and/or mass on opposite sides of the nucleus.

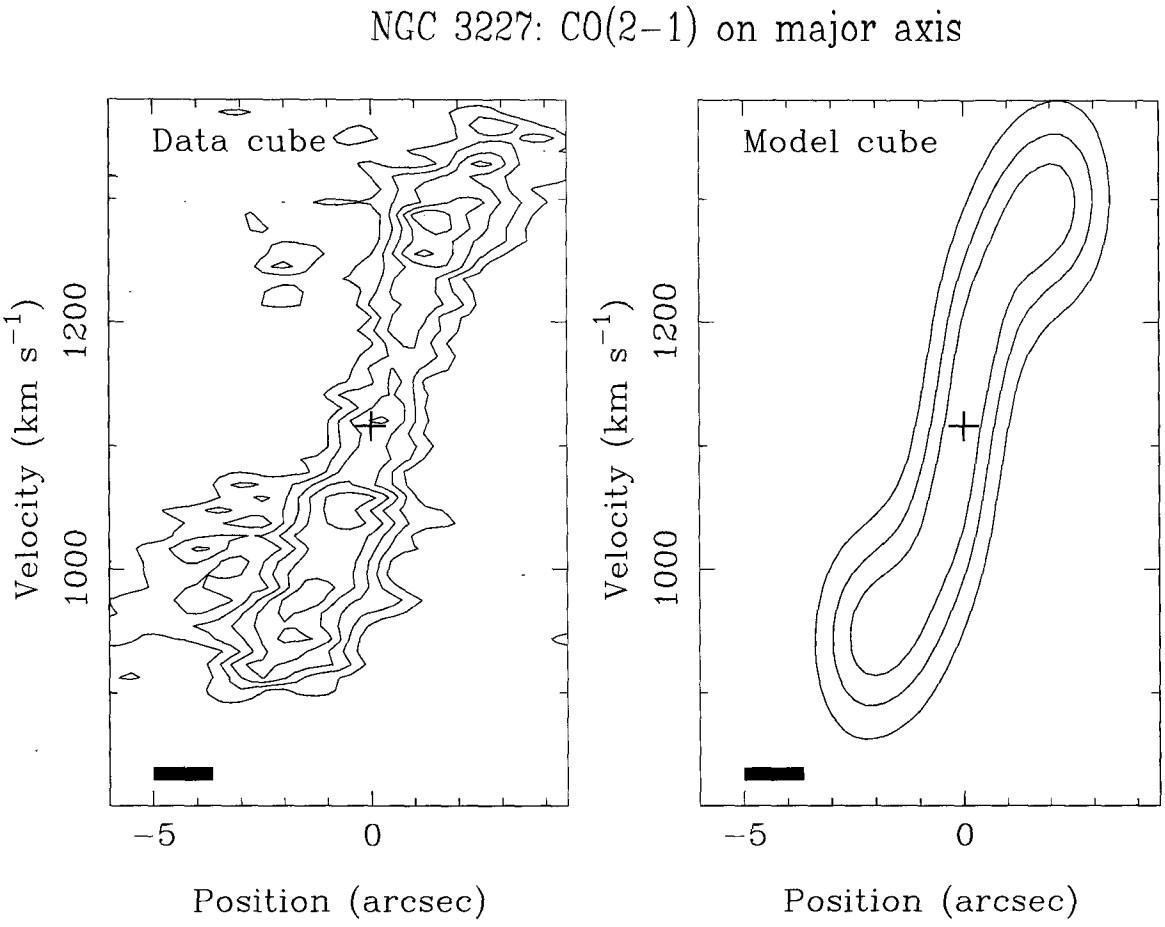

Figure 5.8: Position-velocity diagram for the CO(2–1) line in NGC 3227. A 1″-wide cut was taken at the position angle of the ascending node (see Table 5.14). The cross marks the galaxy's spatial and velocity center; offsets along the spatial axis are relative to this position. The rectangle indicates the spatial and velocity resolutions. Contours are multiples of 42 mJy bm^{-1}.

5.4.2 NGC 4051

Because the inner bar and the CO(1–0) clumps to the north and south clearly do not trace material in circular motion, we have confined our model to the nuclear disk by fixing $i = 40°$ (i.e., matching the inclination of the larger H I disk) and $r_{out(1-0)} = r_{out(2-1)} = 300\,\mathrm{pc}$. With these constraints, we obtain the CO(2–1) position-velocity cuts shown in Figure 5.10. The agreement between the data and model cuts in this plot is good but not excellent; among other problems, the velocity dispersion at large radius which is specified by our model appears to be too large. We attribute this discrepancy to pressure for the model to fit streaming motions elsewhere in the disk, i.e., higher velocities which for an axisymmetric

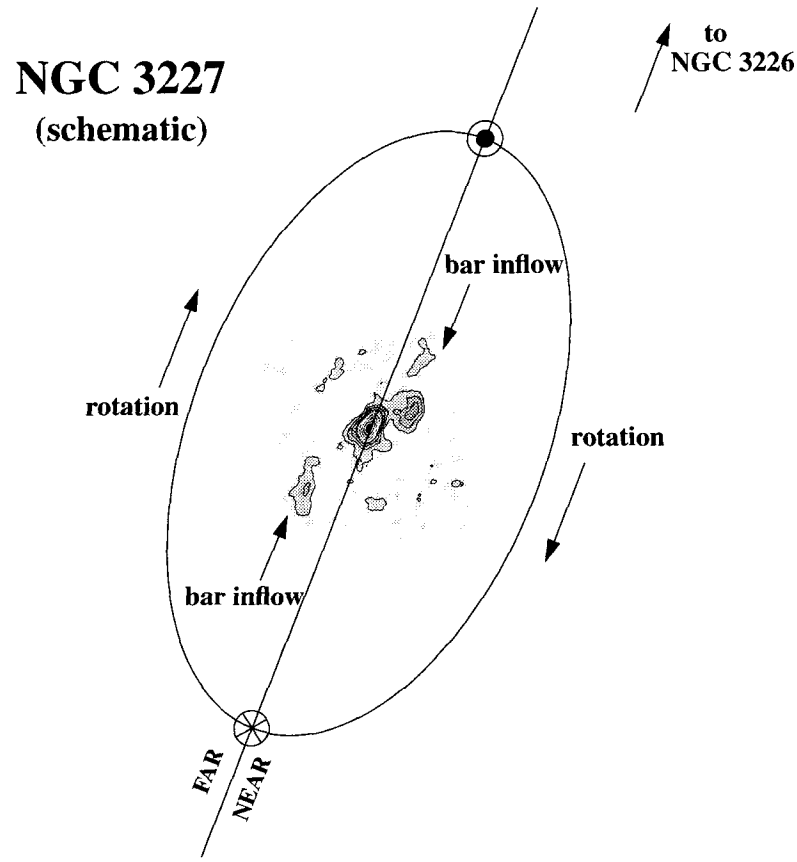

Figure 5.9: Schematic of NGC 3227. The large ellipse is a [not-to-scale] disk projected to the inclination ($i \sim 124°$) and orientation ($\alpha \sim 338°$) inferred from the H I observations of Mundell et al. (1995b). Additional studies (Mulchaey et al. 1997; González Delgado & Pérez 1997) suggest a bar extends nearly parallel to the line of nodes and points towards the companion galaxy NGC 3226. We overlay the CO(1–0) zeroth moment map from Figure 5.1.

potential can only be reached by increasing σ_v. Our model does select a position angle for the ascending node $\alpha = 125°$ which is in good agreement with the value (132°) determined by Liszt & Dickey (1995). In Figure 5.11, we show a schematic view of the geometry we envision for the molecular gas relative to the larger disk. Table 5.15 indicates that the radio continuum peak, the integrated intensity peaks, and the dynamical center are all within a beamwidth of each other; we have no clear evidence of $m = 1$ asymmetry in the gas mass or excitation with respect to the nucleus.

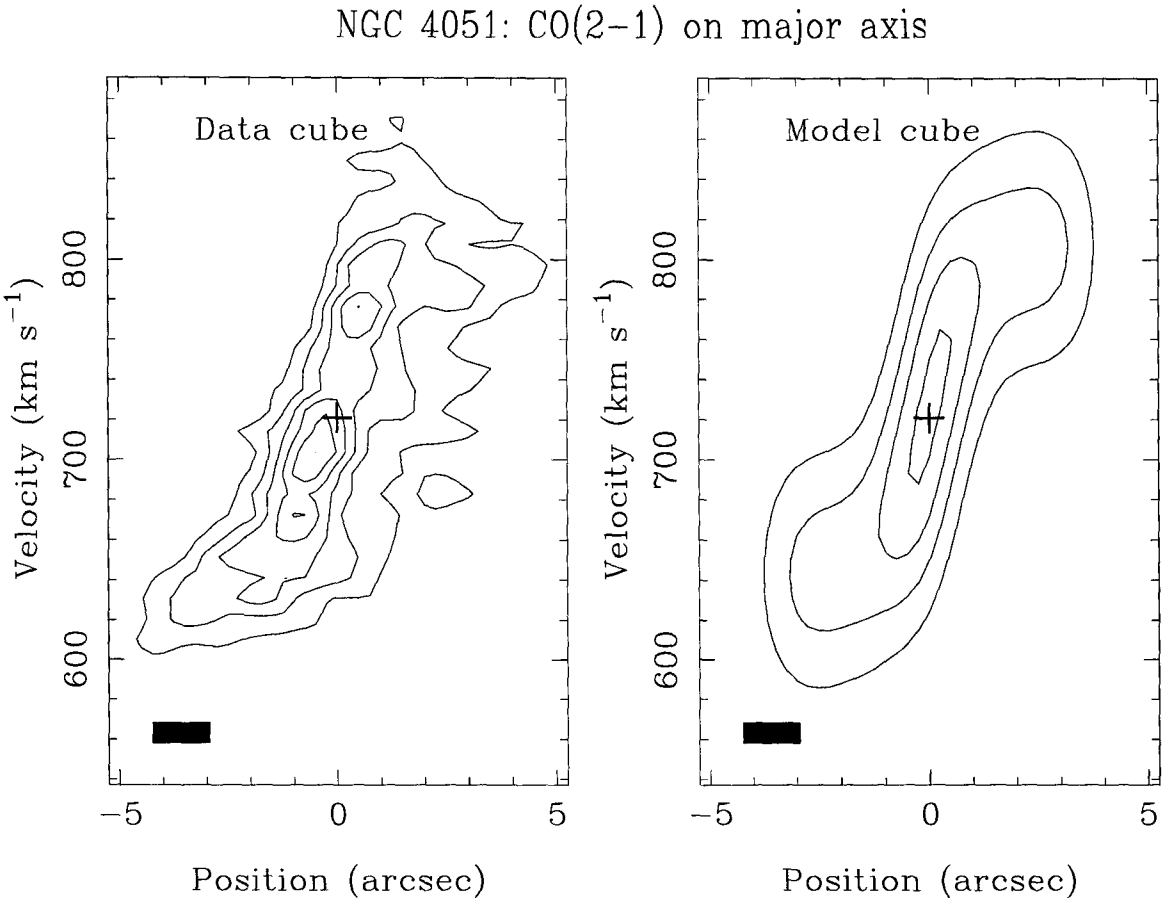

Figure 5.10: Position-velocity diagram for the CO(2–1) line in NGC 4051. Notation is as for Figure 5.8; contours are multiples of 48 mJy bm^{-1}.

5.4.3 NGC 5005

We have imposed no *a priori* constraints in deriving the model for NGC 5005, although we have excluded emission from the northwest stream from our chi-square evaluation of each fit to the nuclear disk. Figure 5.12 shows position-velocity cuts through the CO(2–1) data and model cubes, clearly showing the discontinuity in our velocity coverage. We plot the model emission in the three velocity gaps only for the sake of completeness; these gaps were not included in calculating χ^2_ν. Encouragingly, our estimates of r_{out} from the two CO lines agree well with each other. Our estimates of the geometrical parameters $(i, \alpha) \simeq (59°, 253°)$ agree well with the values $(62°, 245°)$ derived from optical isophote fitting and application of the AIPS GAL task by Sakamoto et al. (2000). Figure 5.13 shows a schematic view of the gas dynamics in NGC 5005, based on this geometry and on the discussion in Section 5.3.4

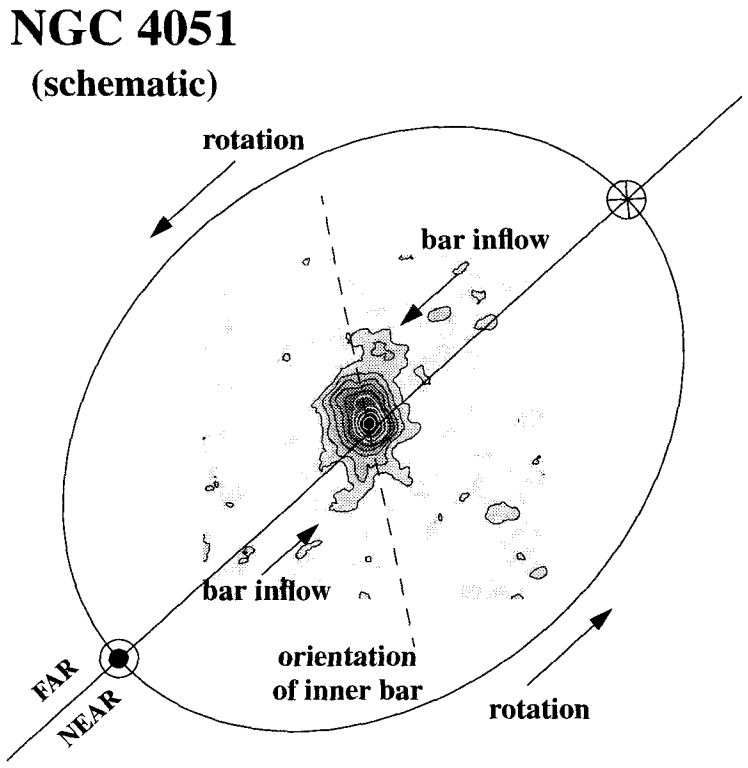

Figure 5.11: Schematic of NGC 4051. The large ellipse is a [not-to-scale] disk projected to the inclination ($i \sim 140°$) and orientation ($\alpha \sim 132°$) inferred from the H I observations of Liszt & Dickey (1995). NIR imaging by Mulchaey et al. (1997) suggests a bar extends nearly parallel to the line of nodes. The elongation of the emission in the (overlaid) CO(1–0) zeroth moment map implies there is an additional inner bar, which feeds the nuclear disk resolved in our CO(2–1) zeroth moment map.

above. Our predicted dynamical center agrees almost perfectly with the position of the radio continuum peak (see Table 5.15). The peak intensity in the CO(1–0) line falls somewhat to the northeast of this location, but inspection of Figure 5.5 suggests that the exact value of this offset is not likely to be significant. Due to our incomplete velocity coverage of the CO(2–1) line, we do not determine a position for its peak intensity.

5.4.4 NGC 5033

Because of the asymmetrically strong emission to the north (and especially to the northeast) of the nucleus in NGC 5033, we have fixed $\hat{v}_0 = 886.5\,\mathrm{km\,s^{-1}}$ (to match the average of fits to

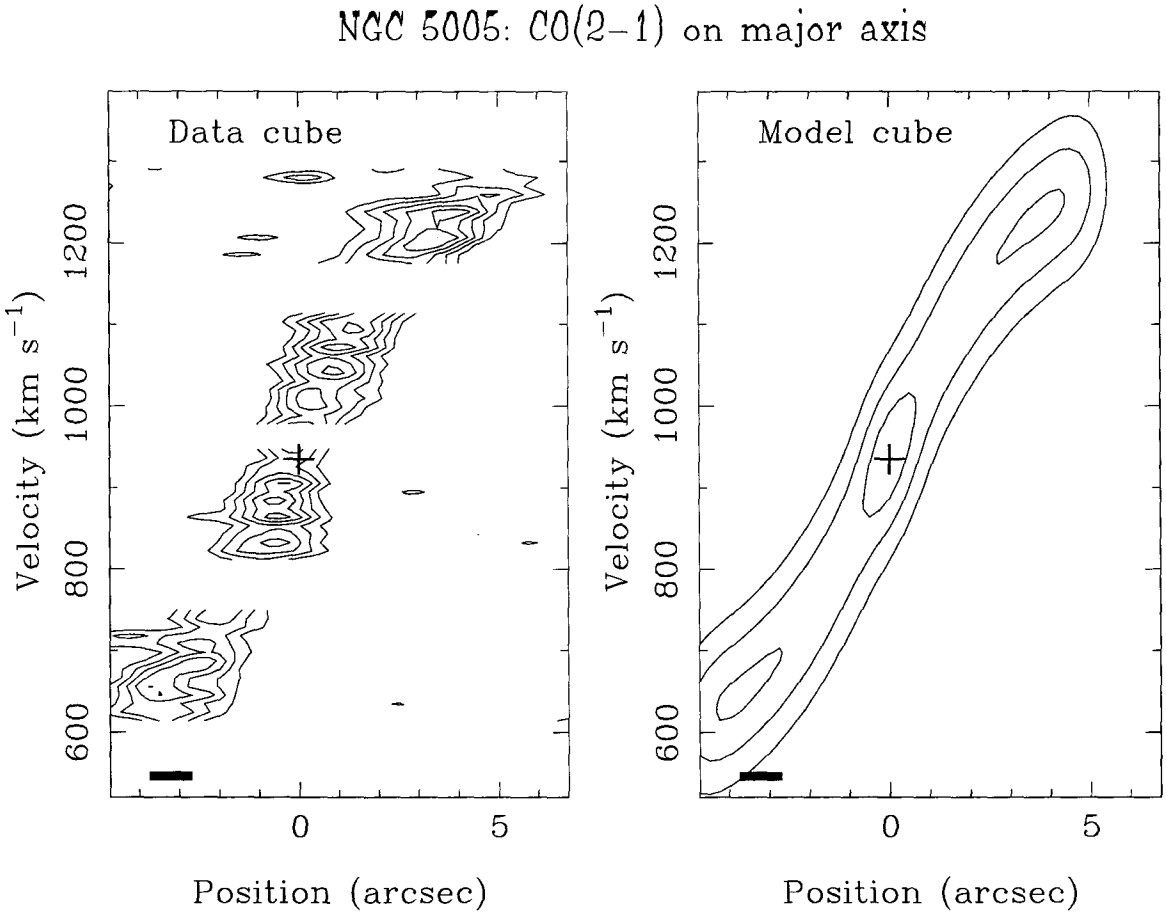

Figure 5.12: Position-velocity diagram for the CO(2–1) line in NGC 5005. Notation is as for Figure 5.8; contours are multiples of 57 mJy bm^{-1}. Note the three gaps in the velocity coverage of our data.

the two first moment maps with the AIPS GAL task), $i = 62°$ (to match the H I observations of Christodoulou et al. (1993)), and $\alpha = 170°$ (to match the visual elongation of the linear CO(2–1) feature). With these constraints, we obtain the parameters listed in Tables 5.14 and 5.15, and the CO(2–1) position-velocity cuts shown in Figure 5.14. The fact that $r_{out(2-1)}$ exceeds $r_{out(1-0)}$ by 25% is a clear indication that an axisymmetric model cannot perfectly describe the asymmetric emission in NGC 5033. On the other hand, the model's dynamical center does fall between the north and south CO(1–0) lobes (in particular, south of the peak gas intensities), and agrees fairly well with the location of the radio continuum peak. Figure 5.15 shows a schematic view of our CO(1–0) map for the disk orientation we have assumed and the dynamical center we have derived.

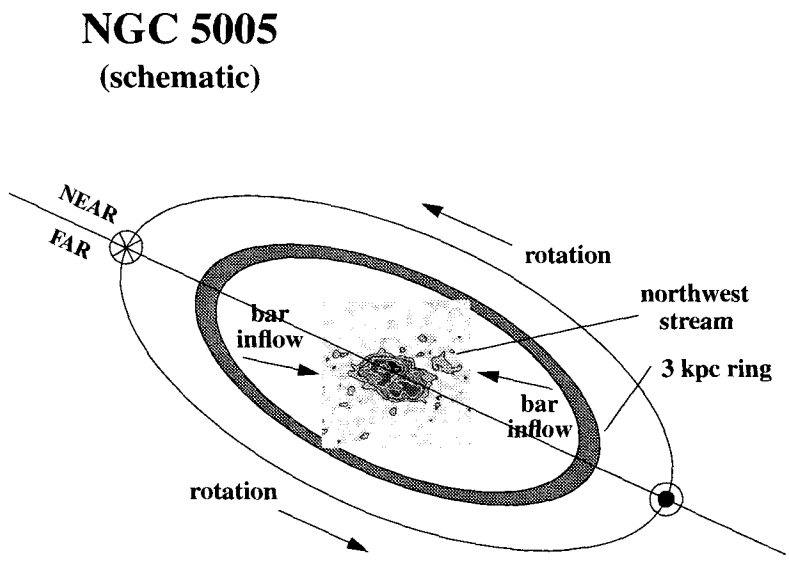

Figure 5.13: Schematic of NGC 5005. The large ellipse is a [not-to-scale] disk projected to the inclination ($i \sim 62°$) and orientation ($\alpha \sim 245°$) derived by Sakamoto et al. (2000). We see the same elongations in the 3 kpc molecular ring (idealized here, but see also Figure 5.5) and the nuclear disk (seen in the overlaid CO(1–0) zeroth moment map). Episodic inflow occurs along a bar running roughly east-west, with the "northwest stream" on the verge of depositing $\sim 2 \times 10^8\,M_\odot$ in the nuclear disk.

Our position-velocity diagrams indicate that an axisymmetric model also fails to provide a good description of the kinematics we observe in NGC 5033. The precise respects in which our model falls short merit some comment. We see from the left-hand panel of Figure 5.14 that the CO(2–1) emission appears to trace *two* distinct kinematic components in the nucleus– an inner feature with approximate spatial and velocity extents $\pm 1''$ and $\pm 145\,\mathrm{km\,s^{-1}}$, and an outer feature extending to $\pm 5''$ and $\pm 230\,\mathrm{km\,s^{-1}}$. This pattern has two natural explanations. First, the inner structure might correspond to gas in circular rotation, but in a nuclear disk with $i > 62°$ so that larger velocities are directed along our line of sight and the rotation law appears steeper. Second, the inner and outer structures might be produced by clouds on two sets of elongated orbits with misaligned major axes. This explanation is analogous to the attribution of large-scale "tilted X" patterns in

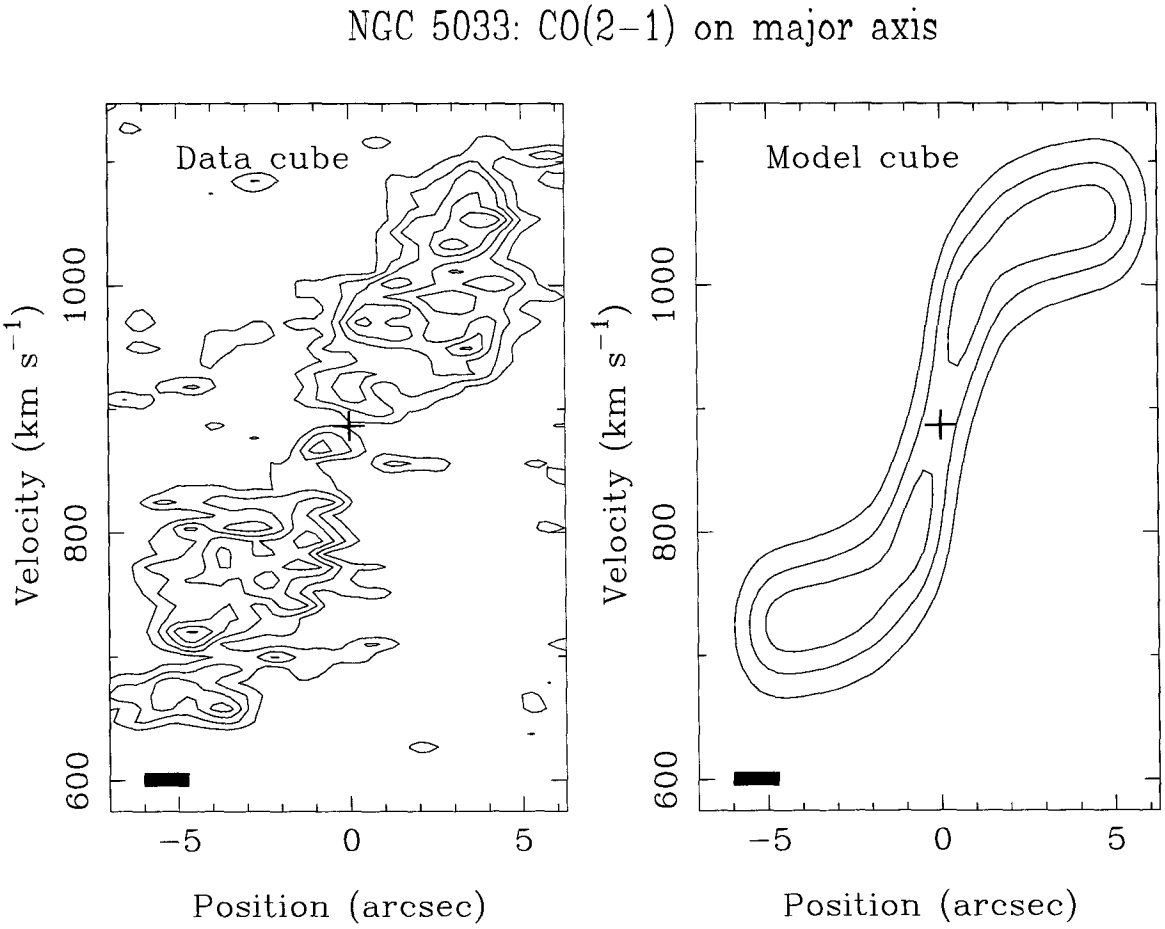

Figure 5.14: Position-velocity diagram for the CO(2–1) line in NGC 5033. Notation is as for Figure 5.8; contours are multiples of 28 mJy bm^{-1}.

position-velocity diagrams to gas on orbits in the x_1 and x_2 families (see Section 2.4.1); we would hesitate to make this precise identification for NGC 5033, however, because we do not know the radii of its dynamical resonances. Choosing between these noncoplanar and noncircular schemes for explaining the galaxy's gas motions will ultimately require more realistic kinematic modelling. At present, we have a slight preference for a nuclear bar over a nuclear warp, since (a) the isovelocity contours at smallest radii are roughly parallel to the minor axis of the galaxy– as is the case for NGC 7479 but not for NGC 1068; (b) the discreteness of the two components in the position-velocity diagram is more plausibly explained by two distinct orbit families than by a continuous warp; (c) we lack any of the evidence for warping we might expect to see at other wavelengths, e.g., a bent jet and/or ionization cone; and (d) this scenario can naturally explain the north and south lobes, as

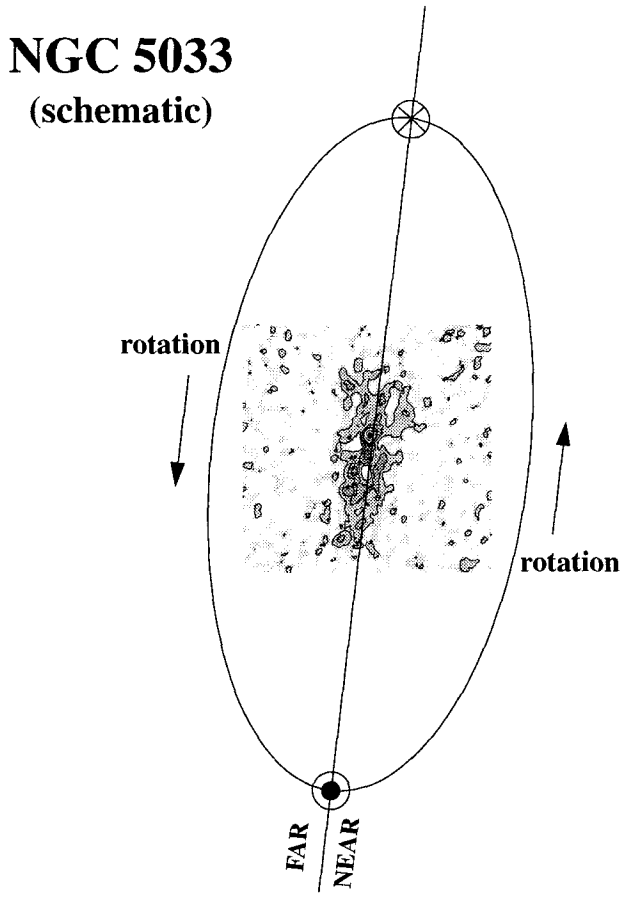

Figure 5.15: Schematic of NGC 5033. The large ellipse is a [not-to-scale] disk projected to the inclination ($i \sim 62°$) and orientation ($\alpha \sim 173°$) of the *inner* H I disk in the study of Christodoulou et al. (1993). A warp in the H I disk is present at radii much larger than the field of view of our (overlaid) CO(1–0) zeroth moment map.

"twin peaks" marking the corotation resonance of a nuclear bar and the inner 2:1 Lindblad resonance of some outer $m = 2$ distortion (see Section 2.4.1).

5.5 Excitation models

We have attempted to characterize the physical conditions in each of the five nuclei by analyzing our measurements (in Tables 5.4 through 5.13) and kinematic model predictions (in Table 5.14) for the assumption of a single "zone" of gas (see Section 3.5). We first estimate the kinetic temperature of the gas in each nucleus by considering dust temperature

Galaxy	$L_{\rm FIR}$ ($10^9\,L_\odot$)	T_d (K)	$< Q >$ ($\times 10^{-3}$)	M_{dust} ($10^6\,M_\odot$)	M_{gas}/M_{dust}
(1)	(2)	(3)	(4)	(5)	(6)
NGC 3227	9.8	34	1.6	1.5	1182
NGC 4051	8.5	34	1.6	1.4	575
NGC 4438	3.4	32	1.3	0.9	1300
NGC 5005	32.1	31	1.3	9.0	239
NGC 5033	19.0	30	1.1	6.6	196

Table 5.16: Dust properties estimated from the IRAS observations reported by Soifer et al. (1989). Column (2) is calculated using Equation 3.7; column (3) is estimated from the $60\,\mu$m/$100\,\mu$m color temperature, assuming emissivity $\propto \nu$; column (4) is the Planck-weighted dust emissivity from Draine & Lee (1984); column (5) is calculated using Equation 3.8 adjusted for the appropriate $< Q >$; and column (6) is the ratio of the total M_{gas} inferred from our CO(1–0) zeroth moment map with M_{dust}.

estimates. IRAS flux densities tabulated by Soifer et al. (1989) yield the estimates of global FIR luminosity, mass-weighted grain temperature, and dust mass which are presented in Table 5.16. As was the case for NGC 2681, the total gas mass we estimate for each system from the CO(1–0) luminosity exceeds the inferred dust mass by more than the canonical gas-to-dust ratio ~ 100. Improving on our analysis of NGC 2681, however, we can (for three of the five galaxies) test our hypothesis that we have underestimated M_{dust} because of our insensitivity to very cold material in the IRAS $60\,\mu$m band. Pérez García et al. (1998) report ISO observations (for $\lambda \leq 200\,\mu$m) of a sample of Seyfert galaxies which includes NGC 3227, NGC 4051, and NGC 5033. A maximum likelihood analysis of spectral energy distributions implies that three distinct thermal components contribute to each galaxy's FIR emission. The authors suggest that "warm" dust is heated by the active nucleus, "cold" dust emission originates in star-forming regions, and "very cold" dust is heated by the interstellar radiation field. In Table 5.17, we present the luminosity and temperature of each component in each galaxy, along with our calculated values for the corresponding dust masses. We find not only that M_{dust} in each system is dominated by the "very cold" component with $T_d \simeq 16 - 18\,$K, but also that the revised estimates for total dust mass imply a gas-to-dust ratio which is *less* than the canonical value. This is a more sensible inconsistency: we would expect the smaller field of view and insensitivity to smooth emission of our CO observations to lead to underestimates of the true global M_{gas}.

Galaxy	$L_{\rm FIR}$ ($10^9\,{\rm L}_\odot$)	T_d (K)	$< Q >$ ($\times 10^{-3}$)	M_{dust} ($\rm M_\odot$)	M_{gas}/M_{dust}
(1)	(2)	(3)	(4)	(5)	(6)
NGC 3227	3.5	136	22.4	1.5×10^2	-
	7.4	45	3.2	1.9×10^5	-
	6.0	16	0.3	1.1×10^8	17
NGC 4051	2.7	151	23.4	7.2×10^1	-
	2.7	47	3.2	5.7×10^5	-
	7.2	18	0.4	5.7×10^7	14
NGC 5033	3.7	151	23.4	9.9×10^1	-
	7.8	40	2.4	4.1×10^5	-
	15.1	18	0.4	1.2×10^8	11

Table 5.17: Dust properties estimated from the ISO observations reported by Pérez García et al. (1998). The authors' maximum likelihood analysis decomposes each galaxy's FIR spectral energy distribution into a sum of three components, whose luminosities and central temperatures are listed in columns (2) and (3). The contents of the remaining columns are obtained as described in Table 5.16.

Although we now have a more consistent account of an active galaxy's dust emission, it remains for us to estimate T_{kin} for its gas. The relatively consistent estimates of M_{gas}/M_{dust} for the three galaxies listed in Table 5.17 suggest that the "very cold" dust emission and the CO emission in our maps may be spatially correlated. We therefore adopt $T_{kin} \simeq 20\,{\rm K}$ as an initial guess, although we note that (as suggested in the preceding sections) material at very small radii may well have higher temperatures. We can now consider the characteristic intensity ratios adopted in Section 5.3 in light of the 20 K LVG model of Goldsmith et al. (1983) which is reproduced in Figure 3.10. The results of our analysis are presented in Table 5.18, where we have assessed thermalization by comparing the minimum $n_{\rm H_2}$ (deduced from the observed R) for each galaxy to the critical densities $n_{crit(1-0)} \simeq 1850\,{\rm cm}^{-3}$ and $n_{crit(2-1)} \simeq 7090\,{\rm cm}^{-3}$ at 20 K. In NGC 3227, NGC 4051, and the north lobe of NGC 5033, the CO(1–0) transition is thermalized by collisions alone but the CO(2–1) transition is not. We suspect that NGC 4438 should probably belong in this category as well, since correcting our suspiciously weak CO(2–1) zeroth moment map upwards would increase our estimates of R and $n_{\rm H_2}$. In the south lobe of NGC 5033, we can seemingly conclude that both transitions are in LTE. As in the case of NGC 2681, however, a high intensity ratio (here ~ 2.06) is a likely signature of higher-temperature material, and our estimates for

Galaxy	$< R >$	$\min(n_{H_2})$ (cm^{-3})	CO(1–0) thermalized?	CO(2–1) thermalized?
(1)	(2)	(3)	(4)	(5)
NGC 3227	0.89	2510	yes	maybe
NGC 4051	0.99	2880	yes	maybe
NGC 4438	0.77	1780	maybe	maybe
NGC 5005	0.67	1584	maybe	maybe
NGC 5033	1.01	2510	yes	maybe
	2.06	15850	yes	yes

Table 5.18: Number density estimates for the nuclear regions. Columns are (1) galaxy; (2) representative intensity ratio R taken from Table 5.5 *et al.* (we list two values for NGC 5033, in which R has unambiguous variations in the inner $r \leq 500$ pc); (3) lower limit for n_{H_2} inferred from the adopted R and the 20 K LVG model of Goldsmith et al. (1983); and (4) and (5) assessments of whether the molecular lines are thermalized. "Yes" means $\min(n_{H_2}) > n_{crit}$ so that $T_{ex} \rightarrow T_{kin}$ due to collisions alone; "maybe" means we may need to rely partly on NLTE photon trapping to thermalize the transition.

n_{crit} are probably too low. In the nucleus of NGC 5005, the number density does not seem adequate to thermalize *either* CO transition collisionally; we will therefore exclude this galaxy from our LTE analysis altogether.

In Table 5.19, we present lower limits on the optical depth τ_v and filling factor $f_a(v)$ at the local peak of the CO(1–0) velocity profile for the three galaxies in which the line is clearly thermalized and for which we have kinematic models. Using Equation 3.13, we estimate the brightness temperature at the peak of the profile from our kinematic model parameters and compare it to $T_{kin} = 20$ K to constrain the product $f_a(v)\,(1 - \exp(-\tau_v))$. Clearly either the optical depth and/or the filling factor is $\ll 1$ for all three systems. Our canonical picture of molecular gas in external galaxies (see Section 3.5.1) leads us to conclude that the CO(1–0) emission we observe comes from discrete, optically thick clouds whose areal filling factor is on the order of $\sim 10\%$. An accurate description of the molecular emission from gas with lower density (e.g., in NGC 5005) or higher temperature (e.g., in the nucleus of NGC 5033) will require a full NLTE version of the analytical approach we develop on Section 3.5.2.

Galaxy	$T_{b(1-0)}(v_{pk})$ (K)	$\min(f_a(v))$	$\min(\tau_v)$
(1)	(2)	(3)	(4)
NGC 3227	2.8	0.17	0.18
NGC 4051	2.8	0.17	0.18
NGC 5033	1.2	0.07	0.08

Table 5.19: Parameters of CO(1–0) emission at velocity peak, for galaxies in which the transition is thermalized to 20 K. Columns are (1) galaxy; (2) brightness temperature at the peak of the velocity profile, estimated from the kinematic model using Equation 3.13; (3) lower limit on areal filling factor at this velocity; and (4) lower limit on optical depth at this velocity.

5.6 Molecular gas and the narrow-line region

Of the galaxies we have discussed in this chapter, two (NGC 3227 and NGC 4051) show wedges of ionized gas in narrow-band images of the [OIII] λ5007 Å emission line. In each case, the wedge has a vertex at the nucleus and is projected against the far side of the galactic disk; [OIII] emission is confined to position angles $\sim 30 \pm 27$ in NGC 3227 (Mundell et al. 1995a) and to $\sim 33 \pm 27.5$ in NGC 4051 (Christopoulou et al. 1997). Such wedges can be produced by the ejection of excited gas from the nucleus, or by the emergence of photons from the nucleus which ionize galactic disk gas; the former scenario describes a narrow-line region (NLR), while the latter defines an extended narrow-line region (ENLR). In NGC 3227, the large linewidth in the wedge ($\sim 450-600\,\mathrm{km\,s^{-1}}$) suggests that the ionized gas originates in the nucleus, although the agreement of the line centroids with the local galactic rotation velocities is consistent with an ENLR scenario (Mundell et al. 1995a). In NGC 4051, the wedge is clearly an NLR: Christopoulou et al. (1997) observe line splitting consistent with outflow and/or entrainment along the surface of a cone.

Radio continuum observations of NGC 4051 at 6 cm (Baum et al. 1993) and 3.6 cm (Kukula et al. 1995) show emission extending northeast from the nucleus with position angle and opening half-angle similar to those of the NLR. At higher resolution, however, Christopoulou et al. (1997) find that the both the radio jet and the [OIII] emission are extended at position angle 73°. Mundell et al. (1995a) detect a similar phenomenon in NGC 3227, in which the radio emission on small scales has position angle $\sim -10°$ (vs. 30°)

on the sky. Such discrepancies can be explained for ENLRs (in other objects) by misalignments between the symmetry axes of an ionization cone and a galaxy's disk. However, this account will only work for NGC 3227 if its spiral arms lead (i.e., if we reverse "near" and "far" in Figure 5.9), and will not work at all for the NLR in NGC 4051. We therefore conclude that the radio jets and ionizing photons in NGC 3227 and NGC 4051 are redirected on their way out of the nucleus. The molecular gas structures detected in our OVRO maps not only are plausible agents of this redirection, but may also exhibit signatures of it. Pringle et al. (1999) combine observations of the Fe Kα line (to obtain the inclination of the inner accretion disk), H I emission (to obtain the inclination of the galactic disk), and radio continuum (to obtain the difference in position angle between the radio jet and the galaxy's major axis on the sky) to derive the angle β between the jet axis of an active nucleus and the rotation axis of its host galaxy. For NGC 4051, they determine $\beta \simeq 23°$; for NGC 3227, we infer $\beta \simeq 53°$ (using their formula but our assumed near/far geometry). We would expect the implied misalignment in NGC 3227 to result in substantial cloud compression and heating where the jet and flux of high-energy photons encounter clouds in the plane of the disk; this effect may account for the asymmetrically strong CO emission we see to the northeast of the nucleus. In contrast, the milder misalignment in NGC 4051 implies that the jet and ionizing photon flux will impinge on the disk at a larger scale height than that of the molecular gas distribution, and will thus have little effect on the emergent CO emission.

5.7 Acknowledgments

We thank Kazushi Sakamoto for an enjoyable collaborative study of NGC 5005 and his permission to use Figure 5.4. We also thank Eva Schinnerer for useful discussions of NGC 3227.

Chapter 6 Summary

We have mapped eight nearby active galaxies at $1''$ resolution in the CO(2–1) transition, and at lower resolution in the CO(1–0) transition. Our observations have allowed us to describe the molecular gas distributions on scales $\sim 100\,\mathrm{pc}$, and in particular the asymmetries which are likely to drive mass transfer. Millimeter interferometry turns out to be remarkably well-suited for the detection of nonaxisymmetric structures at small radius. Table 6.1 contrasts our probable identification of such structures at $r \leq 500\,\mathrm{pc}$ in six of the eight sample galaxies– confirmed in two cases by independent molecular line studies (Schinnerer et al. 2000a, 2000b)– with the routine failure of optical and/or infrared imaging studies to do as well. Our high angular resolution and access to kinematic information are two of the key factors in our success.

Because the nuclei in our sample have steeply rising rotation curves, we can also exploit the high *velocity* resolution of our observations to improve on our [already excellent] spatial resolution. This strategy motivates our simultaneous modelling of the potential (i.e., the velocity field) in which the gas moves and the [emissivity] distribution of the gas in the potential, as described in Section 2.4. Table 6.2 reproduces some of the key parameters from the seven kinematic models presented in previous chapters. The precision with which we can determine these and other model parameters is ultimately limited by large and small-scale nonaxisymmetry which defies easy parametrization, and by our effective velocity resolution. The latter corresponds to the observed velocity dispersion in each galaxy, listed in Table 6.2, since in every case σ_v exceeds our instrumental resolution of $\Delta v_{ch} = 10.4\,\mathrm{km\,s^{-1}}$. Our simultaneous fits of the CO(1–0) and CO(2–1) data cubes for a galaxy have as many as 21 independent parameters, a level of specificity which is merited by the high quality of the data and the sensitivity of our approach to modelling them.

From the predictions of our models and the observed parameters of the CO emission in our maps– some of which we present in Table 6.3– we have been able to reach a number of conclusions about molecular gas in active galaxies, and about their circumnuclear regions in particular:

1. For five of the galaxies in our sample, we can compare our maps to published single-

Galaxy (1)	Component (2)	$r \geq 500\,\mathrm{pc}$ (3)	$r \leq 500\,\mathrm{pc}$ (4)
NGC 1068	stellar	global [optical] oval^S + "outer" [infrared] bar	
	gaseous	clumpy outer bar^S	**warped nuclear disk^S**
NGC 2681	stellar	outer primary bar + outer secondary bar	tertiary bar
	gaseous		
NGC 3227	stellar	outer bar	
	gaseous	**clumpy outer bar^S**	**asymmetric disk^S** + warped nuclear disk^S
NGC 4051	stellar	outer bar (?)	
	gaseous	**clumpy outer bar**	**inner bar (?)**
NGC 4438	stellar		
	gaseous		
NGC 5005	stellar	outer bar	
	gaseous	**clumpy outer bar**	**inner bar (?)**
NGC 5033	stellar		
	gaseous		**asymmetric disk + inner bar**
NGC 7479	stellar	outer bar	
	gaseous	continuous outer bar	**inner bar**

Table 6.1: CO emission as a tracer of nonaxisymmetry. We list clear evidence of asymmetric structures on large ($r \geq 500\,\mathrm{pc}$) and small ($r \leq 500\,\mathrm{pc}$) scales from observations of stars (using broadband imaging) and molecular gas (using millimeter interferometry). Results first obtained in this thesis are boldfaced; recent results (in many cases identical) from the independent work of Schinnerer et al. (2000a, 2000b) are labelled with an "S."

dish observations of both CO lines in the same $23''$ half-power beamwidth. In four of the five– NGC 2861, NGC 3227, NGC 5033, and NGC 7479– we infer that the integrated CO(2–1) to CO(1–0) intensity ratio is higher for the emission we recover in our maps than for the smooth and/or low-surface-brightness emission which the interferometer fails to detect. This pattern is natural if smoothly distributed molecular material has lower temperature and/or density than the massive central gas concentrations which our maps detect. In NGC 1068, smoothly distributed CO emission may come from diffuse gas heated by the galaxy's widespread and vigorous star formation.

2. The emission which is present in our maps tends to be strongly *centrally* concentrated,

Galaxy	Σ_{gas} ($M_\odot\,pc^{-2}$)	r_{out} (pc)	σ_v ($km\,s^{-1}$)	$R(r_{out})$	$R(r_{out}/2)$	χ^2_ν
(1)	(2)	(3)	(4)	(5)	(6)	(7)
NGC 1068	2328	161	47	1.50	1.62	126.3
NGC 2681	2001	151	21	0.96	2.25	75.9
NGC 3227	2419	308	52	0.76	1.01	96.3
NGC 4051	1916	300	42	0.65	0.99	108.6
NGC 5005	2557	548	66	0.95	1.01	48.6
NGC 5033	752	468	37	0.61	0.81	110.0
NGC 7479	6460	350	68	0.96	1.02	134.4
Mean	2633	326	48	0.91	1.24	82.7

Table 6.2: Summary of key parameters from the seven kinematic models of Chapters 2 through 5. Columns are (1) galaxy (2) gas mass surface density, calculated using a Galactic conversion factor as $\Sigma_{gas} = 1.36 \times 4.808 \times \bar{\sigma}_{em(1-0)}$ (3) outer gas radius, taken as the mean of $r_{out(1-0)}$ and $r_{out(2-1)}$ (4) velocity dispersion (5) R at the outer radius, estimated as $\bar{\sigma}_{em(2-1)}/\bar{\sigma}_{em(1-0)}$ (6) R at half the outer radius, estimated as the ratio of the enclosed line luminosities (7) reduced χ^2_ν for a joint fit of the two CO transitions. For NGC 7479 we have adopted the χ^2_ν achieved by Model 3B.

rather than distributed in clumps or along arms in the disk. Table 6.3 indicates that the typical sample galaxy has $\geq 50\%$ of its molecular mass within 500 pc of the nucleus. Surface densities of molecular gas are also high: six of the eight galaxies have Σ_{gas} in the range $1000 - 3500\,M_\odot\,pc^{-2}$ which characterizes starburst nuclei (Jogee 1998), with NGC 5033 falling just below and NGC 7479 well above these limits.

3. Within this central concentration, the CO(2–1) emissivity rises more strongly towards the nucleus than the CO(1–0) emissivity. Although the true emissivity peaks are not likely to be as sharp as implied by our exponential models thereof, the fact that the radial CO(1–0) and CO(2–1) profiles differ systematically for the *same* parametrization implies that the trend is real. Table 6.2 quantifies this statement: in every galaxy, the integrated intensity ratio at the outer edge of the molecular disk is lower than the [cumulative] ratio halfway in. Since only one model (for NGC 3227) shows any evidence for $\eta_{(1-0)} > 0$, we must attribute this pattern to increasing excitation at small radius, rather than to increasing beam filling factor and *mass* surface density.

4. The intensity ratios attained at the outer edges of the molecular structures (see Ta-

Galaxy	Total M_{gas} ($10^8\,M_\odot$)	Nuclear M_{gas} ($10^8\,M_\odot$)	f_{conc}	Peak $T_{b(2-1)}$ (K)	Peak $T_{b(1-0)}$ (K)	Mean R
(1)	(2)	(3)	(4)	(5)	(6)	(7)
NGC 1068	57.1	1.0	0.02	6.72	1.61	1.61
NGC 2681	1.8	1.1	0.61	9.40	2.65	1.85
NGC 3227	17.3	8.8	0.51	4.91	3.30	0.89
NGC 4051	7.7	6.1	0.79	5.92	3.87	0.99
NGC 4438	10.1	6.7	0.66	4.20	1.95	0.77
NGC 5005	40	18.9	0.47	8.94	9.25	0.67
NGC 5033	13.9	2.6	0.19	3.24	1.21	1.54
NGC 7479	37	23	0.62	10.03	1.88	1.06
Mean	23.1	8.5	0.48	6.67	3.21	1.17
Median	15.6	6.4	0.56	6.32	2.30	1.02

Table 6.3: Summary of key observed parameters. Columns are (1) galaxy; (2) total molecular gas mass, calculated from the CO(1–0) luminosity using a Galactic conversion factor; (3) molecular mass in the dominant nuclear structure; (4) degree of gas concentration, i.e., the ratio of columns (2) and (3); (5) peak CO(2–1) brightness temperature observed in the nucleus; (6) peak CO(1–0) brightness temperature observed in the nucleus; (7) typical intensity ratio in the nucleus. Column (2) for NGC 5005 is taken from Sakamoto et al. (2000); column (7) for NGC 5033 is the mean of two values used in Section 5.5.

ble 6.2) are (with the exception of NGC 1068) all less than unity, consistent with a standard paradigm in which optically thick CO emission comes from a population of discrete molecular clouds with low areal filling factor. All exceed the ratio $R \simeq 0.65$ which characterizes Galactic molecular clouds; their mean of 0.91 is nearly identical to the average $R \simeq 0.89$ obtained by Braine et al. (1993) from a single-dish survey of extragalactic spirals.

5. The intensity ratios $R > 1$ predicted and observed in many of the nuclei suggest that at least some of the molecular gas at small radii is warm (with $T_{kin} \geq 60\,K$) and that the emergent CO emission has rather low optical depth. The latter conclusion is hard to reconcile with the persistence of [weakly self-shielding] CO molecules in the vicinity of active nuclei. We argue that at least part of the elevated intensity ratio is due to the external heating of molecular clouds by UV or X-ray photons: in such clouds, the CO(2–1) transition will reach an optical depth of unity in gas with a higher temperature than characterizes the material where the CO(1–0) line

becomes optically thick. We confirm in Section 3.5.3 that an X-ray irradiated cloud can produce optically thick CO lines whose intensity ratio lies in the range 1.2–1.3.

6. The intensity ratios at *all* radii generally require that the molecular hydrogen number density exceed the critical density of the CO(1–0) transition, provided that $T_{kin} \sim 20\,\mathrm{K}$ (roughly half the IRAS 60/100 μm color temperature) is a reasonable estimate. Higher T_{kin} may be inferred by requiring that the relation between path length and velocity width match the expectation for virialized clouds. We suspect that T_{kin} actually spans a range of values, and that in the nucleus high-temperature molecular gas will be spatially correlated with the high-temperature dust components seen in some AGN (Pérez García et al. 1998).

7. In four of the six galaxies known to contain large-scale stellar bars (see Table 6.1), we have detected discrete concentrations of molecular gas whose positions and/or velocities imply they are streaming inward along the bar's leading edge. This detection rate suggests that *episodic* fuelling may characterize many barred galaxies and account for a non-unity duty cycle in nuclear star formation and/or accretion.

8. The prevalence of episodic inflow underlines the surprising continuity of molecular emission along the *full* length of the primary bar in NGC 7479. We attribute the rapid rate of inflow in this system to the fact that we are observing it at an unusual time, part way into its digestion of a satellite galaxy Laine & Heller (1999); the extremely high gas mass surface density we infer (see Table 6.2) is further evidence for this scenario.

9. Within $r \leq 500\,\mathrm{pc}$, we have inferred nonaxisymmetric (i.e., barred) potentials in NGC 4051, NGC 5005, NGC 5033, and NGC 7479. In NGC 4051 and NGC 5005, we do not know the pattern speed of either the primary or the [putative] secondary bar, and our current axisymmetric models do not constrain the orientations of the latter in the plane of the disk. For these two systems, therefore, we cannot yet determine whether the inner structure traces the x_2 orbits associated with the x_1 orbits of the outer structure, or whether the two are truly dynamically decoupled. In NGC 5033, there is no observational evidence for *any* outer bar. In NGC 7479, we measure a pattern speed for the inner structure which is ten times higher than that inferred for

the primary bar, implying that the former is a true secondary bar. This configuration matches the theoretical expectation that the corotation resonance of the secondary bar will coincide with an inner 2:1 Lindblad resonance of the primary bar, although the ratio of pattern speeds we infer is higher than models have thus far achieved (see Section 2.5.2).

10. Within $r \leq 500\,\mathrm{pc}$, we have also detected nonaxisymmetric gas distributions in NGC 1068, NGC 3227, and NGC 5033. In NGC 1068, we conclude that the molecular gas lies in a warped, twisted disk which we view edge-on at small radius and more nearly face-on at its outer edge. We attribute the pronounced excitation gradient from east to west across the nucleus to external cloud heating, which will more strongly affect emission from the directly illuminated surface of the disk which is visible from our viewing angle. In NGC 3227, the enhanced molecular emission to the northeast of the nucleus may be due to the injection of mechanical energy from an impinging radio jet. If the emission asymmetry in this nucleus corresponds to a true mass asymmetry (as we surmise is the case in NGC 5033), we suspect tidal torques exerted by the molecular gas itself may help drive mass inflows.

11. In NGC 1068, NGC 3227, and NGC 4051, the radio jet axis on small scales is not parallel to the axis of radio emission and the ionized gas wedge on large scales. These misalignments suggest that the radio jets and ionizing photons are redirected on their way out of the nucleus. The molecular gas disks, with elongations roughly perpendicular to the large-scale jet and wedge axes, are plausible agents of this redirection. We can make an especially strong case for NGC 1068 in this regard, since the jet and wedge would be aligned due north of the nucleus if they were confined by *either* material at the smallest radii or by material in the plane of the large-scale disk. This scenario does not rule out the existence of obscuring and/or collimating structures on much smaller scales than those we observe.

12. Our models for NGC 1068 and NGC 2681 imply large enclosed masses at small radius. In NGC 1068, our fit includes an effective point mass $\sim 3.0\times10^7\,\mathrm{M}_\odot$ within $r_{in} = 32\,\mathrm{pc}$ of the nucleus, a factor of two larger than the black hole mass estimated from water maser observations by Greenhill & Gwinn (1997). In NGC 2681, a LINER whose claim to a black hole has until now rested solely on its broad Hα emission, we deduce

a mass of $2.0 \times 10^9\,M_\odot$ within 26 pc of the center.

13. In the seven galaxies for which we have kinematic models, the location of the dynamical center agrees better with the position of the radio continuum peak (i.e., the probable site of the putative black hole) than with either of the CO intensity peaks. Since our assumption of a centrally peaked emissivity distribution will tend to bias a model's estimated dynamical center towards a gas peak, we interpret this result as strong evidence that black holes are not substantially offset from their host galaxies' centers.

Appendix A Millimeter interferometry

For readers whose experience is limited to other wavelength regimes, we present here an introduction to the theory and practice of millimeter interferometry. Thompson et al. (1986), Perley et al. (1989), Wohlleben et al. (1991), and Taylor et al. (1999) provide general treatments of aperture synthesis in radio astronomy, but the nontrivial problems caused by the atmosphere at millimeter wavelengths call for special attention to certain key concepts. In Appendix A.1 we discuss the problems of performing aperture synthesis with a small array in this regime, and in Appendices A.2 and A.3 emphasize how to overcome these problems in the course of calibration and imaging. We close with a brief discussion of units and uncertainties in radio maps in Appendix A.4.

A.1 Aperture synthesis

The basic requirement for aperture synthesis (Ryle & Hewish 1960) is a pair of telescopes separated by some baseline vector $\vec{B}$. The product of these telescopes' signals is proportional to a single Fourier component of a source's brightness distribution at the observing wavelength λ– in particular, to a component whose spatial frequency depends on $\vec{B}/\lambda$. As the earth rotates under a source, the effective value of $\vec{B}/\lambda$ (i.e., the *projected baseline*) changes so that the two telescopes can measure many Fourier components of the sky brightness distribution. For $N \geq 2$ telescopes operating as an array, the number of baselines and sampled Fourier components increases as $N(N-1)/2$. Ideally, with enough telescopes and enough observing time, nearly all of a source's Fourier components can be measured, and the original sky brightness distribution (modulo attenuation by the primary beam response of the individual telescopes) can be recovered by Fourier transform, with angular resolution $\sim B_{max}/\lambda$.

Reality intrudes in several ways. First, sampling of the Fourier plane may be far from complete if the number of baselines is relatively small. This problem most severely affects sources near the celestial equator: here the earth's rotation cannot twist any of the baselines under the source, rendering the sampling smooth along the u axis but incomplete along

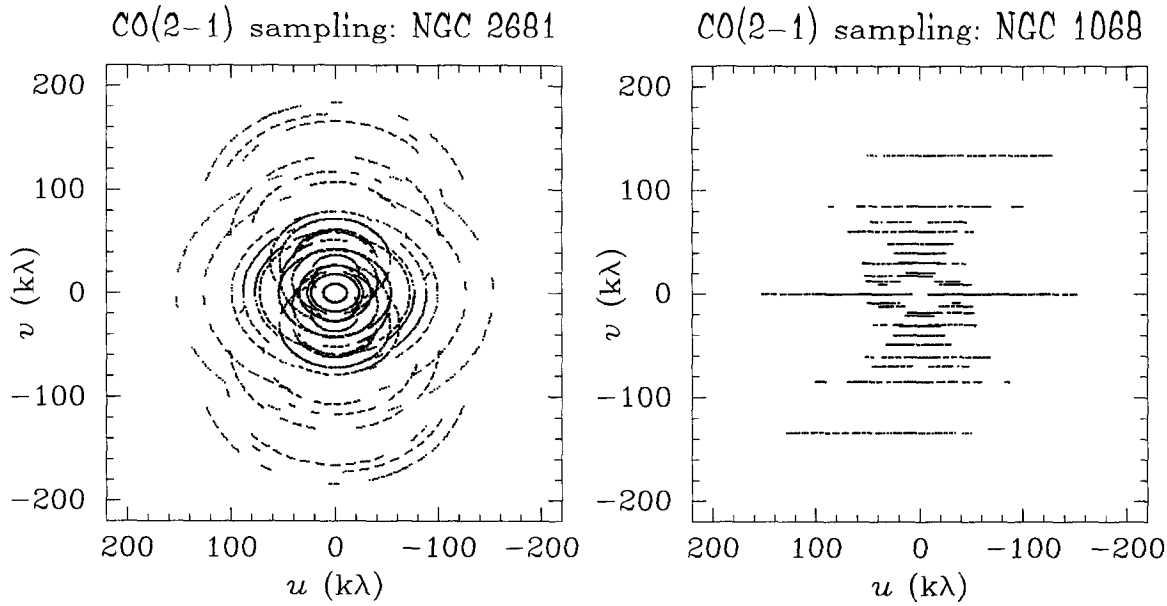

Figure A.1: Array sampling of the Fourier plane. CO(2–1) datasets for NGC 2681 (3069 visibilities) and NGC 1068 (1434 visibilities) are plotted in (u, v) coordinates. The difference in evenness of sampling along the v axis stems not from the difference in dataset size, but from the difference in declination: NGC 2681 has $\delta \simeq +51°$, while NGC 1068 has $\delta \simeq -00°$.

the v axis of the Fourier plane (Figure A.1). Second, sampling with an interferometer is always incomplete at low spatial frequencies: for telescopes with diameter D, projected baselines can never be shorter than D/λ without shadowing. An array therefore behaves as a spatial filter, "resolving out" any emission which is smooth and extended on angular scales larger than $\sim D/\lambda$. Finally, each measurement of a Fourier component (i.e., *visibility*) has attendant noise. At centimeter wavelengths, this arises predominantly in the receivers, but in the millimeter regime it is frequently dominated by atmospheric effects. Fluctuations in pressure-broadened water lines change the index of refraction on short timescales; if these fluctuations also have small spatial scales (less than the length of a baseline), they will degrade incoming planar wavefronts, and cause phase drifts and amplitude decorrelation in the detected signals.

Standard strategies can compensate for each of the above limitations. For a small array, we can improve sampling of the Fourier plane by cycling the telescopes through several different configurations (with nonredundant baselines), and by observing a source over a full range in hour angle (i.e., *track*) in each. Filled-aperture (i.e., single-dish) observations

are sensitive to spatial frequencies $< D/\lambda$, although merging interferometric and single-dish data can give alarmingly different results for different assignments of the visibilities' relative weights. Atmospheric effects in the millimeter regime can be minimized by interleaving integrations on a source with visits to a relatively bright ($\sim 1\,\mathrm{Jy}$) and nearby ($\Delta\theta \leq 20^\circ$) quasar calibrator. To a limited extent (Lay 1997b), source and calibrator will see the same atmospheric structure, whose effects on phase and amplitude (i.e., the complex gain) can then be corrected for the source if they are well-measured as a function of time for its stronger proxy.

A.2 Calibration

The most challenging step in calibrating millimeter array data is the determination of the gain calibrator flux densities at the epochs of observation. Quasars' millimeter strengths can vary on few-week timescales, so a correct combination of data obtained in different array configurations (perhaps months or years apart) requires flux density estimates to be as accurate as possible. The planets Uranus and Neptune have constant brightness temperatures, making them suitable (primary) flux calibrators; however, not all tracks will include observations of planets. Even those which do may observe gain calibrators and planets at different times and/or elevations, leading to systematically different degrees of decorrelation which make unbiased comparisons impossible. At OVRO, tracks without planets can be flux-calibrated using archived observations of secondary flux calibrators– bright ($\geq 4\,\mathrm{Jy}$) quasars observed a few times per week in tracks which also include observations of planets. Since these observations– for unrelated projects– are obtained at various frequencies across the 3 mm and 1 mm bands, we assume that quasar spectra are (on average) flat across each. To surmount the problem of unmatched atmospheric conditions, we can limit our comparisons to only those observations of planets and/or secondary flux calibrators and/or gain calibrators which have similar elevations and coherences in a given track. The uncertainty in the flux scale defined by this stringent approach can be estimated from the dispersions of our multiple (independent) measurements of 3C273 and 1308+326 over a several-week period in 1997: 8% in the 3 mm band and 11% in the 1 mm band. We have adopted more conservative estimates of 10% and 15% uncertainties elsewhere in this thesis.

After flux calibration, we correct the source integrations for gain variations by applying

a fit to the varying phase and amplitude of the gain calibrator. This fit is determined separately for each baseline: although assuming telescope-based gains would allow us to use the relations for closure phase and amplitude, atmospheric decorrelation depends primarily on the lengths and orientations (relative to the wind) of the baselines (Lay 1997a). For passband calibration, we derive a three-channel boxcar fit to the spectrum of the brightest available (secondary) flux calibrator in each track. Subsets of the data for which gain and passband calibrator observations are poor (e.g., highly time-variable) or nonexistent can be deleted at once, but we also inspect the source data themselves in order to eliminate visibilities with anomalously high amplitudes.

A.3 Imaging

Errors which survive (or arise in) calibration of the visibility data are propagated to the image plane by Fourier inversion. Because the sampling pattern within the Fourier plane never produces the regular coverage required by Fast Fourier Transform routines, the visibilities must first be convolved with a smoothing function and resampled on a rectilinear grid of uv cells. Inversion proceeds on these regridded data, with the Fourier component at a particular spatial frequency present in the image according to the amplitude and weight of the corresponding uv grid point. Weights are assigned so as to optimize the response which data with the same uv sampling would produce if we had observed a point source above some noise background. This optimization is realized mathematically as the minimization of a particular L_2 norm, and different weighting schemes correspond to different strengths of the hypothetical point source relative to the noise (Briggs 1995). An extremely strong point source gives *uniform* weights, which are inversely proportional to the numbers of observed visibilities in the uv cells. An extremely weak point source gives *natural* weights, which are inversely proportional to the uncertainties of the observed visibilities in the uv cells. A point source of moderate strength (i.e., *robustness*) can produce a map with slightly higher noise but far better angular resolution than would result from natural weighting.

Inversion must be followed by deconvolution in order to compensate for incomplete uv sampling. This step amounts to a maximum likelihood problem, with the choice of deconvolution algorithm corresponding to a choice of prior. Maximum entropy methods assume that the true sky brightness distribution is maximally smooth; the various versions

of the CLEAN algorithm, in contrast, assume that the sky brightness distribution can be represented as an ensemble of point sources within a finite solid angle. We have made the latter assumption in this work, since the molecular emission from external galaxies at $\sim$ 20 Mpc is compact within our field of view. To deconvolve a given dataset with the CLEAN algorithm, we must specify a flux density threshold for identifying point sources and an area on the sky (the "clean box") in which to identify them. The threshold can be set by measuring the noise in source-free regions of the inverted (but not deconvolved) velocity channels. Clean boxes can be customized for each velocity range; however, such an approach introduces unquantifiable biases in assessing what constitutes deconvolvable "emission" at low levels. We therefore elect to use the same clean box for *all* velocity channels, defined to include all pixels where emission is seen in any single channel.

For millimeter interferometry, atmospheric corruption of the observed visibilities sets the ultimate limit to map quality. Because the atmospheric conditions seen by the source and the gain calibrator will be at least slightly different, calibration will inevitably introduce new errors into a dataset even as it fixes old ones. Miscalibrated visibilities pose special dangers if they happen to be isolated in uv cells at the regridding stage: for weights which depend at any level on the density of sampling within a cell, such bad points can have substantial impact in the image plane. Their manifestation will be flux "scattered" out of the source, which cannot be recovered by any amount of deconvolution. The effects of poor calibration on the apparent morphologies of extended sources– together with the difficulty of correctly normalizing weights and amplitudes for subsets of data acquired at different times– imply that multiple-configuration observations of resolved sources require extremely careful handling.

A.4 Units and uncertainties in radio maps

Because observations of extended sources are calibrated by point-source quasars, each pixel in an interferometric map has specific intensity units $\propto$ Jy bm^{-1}. To determine the total flux density in an extended source, we integrate its brightness over the solid angle it subtends:

$$S_\nu = \int B_\nu \, d\Omega = \frac{2k}{\lambda^2} \int T_b \, d\Omega \tag{A.1}$$

in units of Jy, for brightness temperature T_b. If we have several maps of velocity channels across an emission line, we obtain the total line flux by integrating over velocity:

$$F_{line} = \int S_\nu \, dv = \frac{2k}{\lambda^2} \int T_b \, d\Omega \, dv \tag{A.2}$$

in units of $\mathrm{Jy\,km\,s^{-1}}$. The order of the solid angle and velocity integrals can naturally be reversed. If we first integrate a data cube over velocity, we have an expression for its zeroth *moment* at each pixel:

$$M_0 = \int B_\nu \, dv = \frac{2k}{\lambda^2} \int T_b \, dv \tag{A.3}$$

in units of $\mathrm{Jy\,bm^{-1}\,km\,s^{-1}}$. The integral on the right-hand side is defined as *integrated intensity* I_{line} and has units of $\mathrm{K\,km\,s^{-1}}$. A second integral, over solid angle, would recover the previous expression for line flux F_{line}. Suppose we instead define a new quantity L' as the integral of the integrated intensity over the source's projected area. For source distance d, we find

$$\begin{aligned} L'_{line} &= \int I_{line} \, dA = \int \left(\int T_b \, dv \right) d^2 \, d\Omega = d^2 \int \left(\int T_b \, d\Omega \right) dv \\ &= d^2 \int \frac{\lambda^2}{2k} \, S_\nu \, dv = \frac{\lambda^2}{2k} \, d^2 \, F_{line} \end{aligned} \tag{A.4}$$

in units of $\mathrm{K\,km\,s^{-1}\,pc^2}$.

For millimeter astronomers, the line luminosity in the CO(1–0) transition is extremely significant. Observations of Galactic molecular clouds reveal a proportionality between I_{CO} and the column density of molecular hydrogen $N_{\mathrm{H_2}}$ (see Section 3.5), such that $X = N_{\mathrm{H_2}}/I_{\mathrm{CO}} \simeq 3 \times 10^{20} \, \mathrm{cm^{-2}} \, (\mathrm{K\,km\,s^{-1}})^{-1}$. We can use this fact to estimate the mass of molecular hydrogen in an extended source:

$$M_{\mathrm{H_2}} = \int 2 m_{\mathrm{H}} \, N_{\mathrm{H_2}} \, dA = 2 m_{\mathrm{H}} \int X I_{\mathrm{CO}} \, dA = 2 m_{\mathrm{H}} \, X L'_{\mathrm{CO}} = \frac{\lambda^2 m_{\mathrm{H}} X}{k} \, d^2 \, F_{\mathrm{CO}} \tag{A.5}$$

after substituting our expression for L'. In physical units, we rewrite this relation as

$$M_{\mathrm{H_2}} = 1.180 \times 10^4 \left(\frac{d}{\mathrm{Mpc}} \right)^2 \left(\frac{X}{3 \times 10^{20}} \right) \left(\frac{F_{\mathrm{CO}}}{\mathrm{Jy\,km\,s^{-1}}} \right) \mathrm{M_\odot} \tag{A.6}$$

following Sanders et al. (1991), or more familiarly as

$$M_{\mathrm{H_2}} = 4.808 \left(\frac{X}{3 \times 10^{20}}\right)\left(\frac{L'_{\mathrm{CO}}}{\mathrm{K\,km\,s^{-1}\,pc^2}}\right) \mathrm{M_\odot} \tag{A.7}$$

To account for the helium content of molecular clouds, we multiply $M_{\mathrm{H_2}}$ by a factor of 1.36 to obtain their total gas mass M_{gas}.

As we measure the above quantities in a particular dataset, we can estimate their uncertainties in one of two ways. An *a priori* approach entails multiplying the per-channel rms σ_{ch} by appropriate factors as we perform each integral:

$$\Delta B_\nu = \sigma_{ch} \tag{A.8}$$

$$\Delta M_0 = \sigma_{ch}\,\Delta v_{ch}\,\sqrt{n_{ch}} \tag{A.9}$$

$$\Delta F_{line} = \sigma_{ch}\,\Delta v_{ch}\,\sqrt{n_{ch}}\,\sqrt{n_{bm}} \tag{A.10}$$

where n_{ch} is the number of velocity channels over which we integrate, and n_{bm} is the solid angle over which we integrate in units of synthesized beams. An alternate, more empirical approach exploits the convention– when calculating a data cube's zeroth moment– of ignoring all pixels which take [unphysical negative or insignificant positive] values $\leq k\sigma_{ch}$, where $k > 0$ is some constant of order unity. Such a practice improves a moment map's general appearance, but also gives it an unfortunate positive bias. The bias is on average *identical* if we create a new moment map ignoring all data cube pixels with values $< -k\sigma_{ch}$. We can therefore estimate the uncertainties in our line parameters by measuring each one twice, using the separate moment maps blanked at $\pm k\sigma_{ch}$. This empirical approach is extremely helpful if we must consider highly extended line emission: correction for primary beam attenuation increases the noise away from the map center, thereby causing the *a priori* calculation to underestimate the true uncertainty. A map blanked at $-k\sigma_{ch}$ is also of some intrinsic interest, since better agreement of its rms with the *a priori* estimate of ΔM_0 implies that it gives us a more realistic sense of a dataset's quality.

Appendix B Useful mathematical material

B.1 Epicyclic motion of gas clouds in a barred potential

To describe a weakly barred potential, we separate the axisymmetric and nonaxisymmetric components in a (primed) reference frame which rotates with the bar:

$$\Phi(r', \phi') = \Phi_0(r') + \Phi_1(r', \phi') = \Phi_0(r') + \Phi_b(r') \cos(m\phi') \tag{B.1}$$

for $\Phi_b \ll \Phi_0$ and the standard choice $m = 2$. The equations of motion in a frame rotating counter-clockwise at angular frequency Ω_p are

$$\ddot{r}' - r' (\dot{\phi}')^2 = -\frac{\partial \Phi}{\partial r'} + 2\Omega_p r' \dot{\phi}' + \Omega_p^2 r' \tag{B.2}$$

$$r' \ddot{\phi}' + 2\dot{r}' \dot{\phi}' = -\frac{1}{r'} \frac{\partial \Phi}{\partial \phi'} - 2\Omega_p \dot{r}' \tag{B.3}$$

If we write $r'(t) = r'_0 + r'_1(t) = r_0 + r'_1(t)$ and $\phi'(t) = \phi'_0(t) + \phi'_1(t)$, then the zeroth-order terms in the equations of motion imply that $\phi'_0(t) = (\Omega_0 - \Omega_p)t$ (if we choose $t = 0$ so that $\phi'_0(0) = 0$). For clockwise rotation, Ω_p would enter the equations of motion with opposite sign, implying $\phi'_0(t) = -(\Omega_0 - \Omega_p)t$. The remaining terms give two equations for r'_1 and ϕ'_1:

$$\ddot{r}'_1 + (\kappa_0^2 - 4\Omega_0^2) r'_1 - 2\Omega_0 r_0 \dot{\phi}'_1 = -\left(\frac{d\Phi_b}{dr'}\right)_{r_0} \cos(m\phi'_0) \tag{B.4}$$

$$r_0 \ddot{\phi}'_1 + 2\Omega_0 \dot{r}'_1 = -\left(\frac{m\Phi_b}{r'}\right)_{r_0} \sin(m\phi'_0) \tag{B.5}$$

At this point, we can modify the equations to describe *gas* orbits by introducing dissipative terms for the damping of radial and azimuthal oscillations. Different formulations are recommended by Sanders & Huntley (1976), Goldreich & Tremaine (1981), and Lindblad & Lindblad (1994). Here we will simply add conveniently scaled drag terms, proportional

to the perturbed velocities with $\lambda > 0$ and $\mu > 0$ in frequency units:

$$\ddot{r}'_1 + (\kappa_0^2 - 4\Omega_0^2)\, r'_1 - 2\Omega_0\, r_0\, \dot{\phi}'_1 + m\lambda\, \dot{r}'_1 = -\Big(\frac{d\Phi_b}{dr'}\Big)_{r_0} \cos\left(m\phi'_0\right) \tag{B.6}$$

$$r_0\, \ddot{\phi}'_1 + 2\Omega_0\, \dot{r}'_1 + m\mu\, r_0\, \dot{\phi}'_1 = -\Big(\frac{m\Phi_b}{r'}\Big)_{r_0} \sin\left(m\phi'_0\right) \tag{B.7}$$

Damping will cause phase shifts of the density response relative to the major axis of the perturbing potential. Non-decaying solutions will therefore take the form

$$r'_1(t) = a'(r_0) \cos\Big(m\phi'_0 + \alpha'(r_0)\Big) \tag{B.8}$$

$$r_0\, \phi'_1(t) = -b'(r_0) \sin\Big(m\phi'_0 + \beta'(r_0)\Big) \tag{B.9}$$

Evaluating the equations of motions for these expressions yields four equations, two each for terms proportional to $\sin\left(m\phi'_0\right)$ and $\cos\left(m\phi'_0\right)$, which can be solved for the four quantities $\{a', \alpha', b', \beta'\}$. The solutions can be expressed compactly in terms of

$$X = m^2(\Omega_0 - \Omega_p)^2\Big[m^2\lambda\,\mu + \kappa_0^2 - m^2(\Omega_0 - \Omega_p)^2\Big] \tag{B.10}$$

$$Y = m\,(\Omega_0 - \Omega_p)\Big[m^3\,(\lambda + \mu)\,(\Omega_0 - \Omega_p)^2 - m\mu\,(\kappa_0^2 - 4\Omega_0^2)\Big] \tag{B.11}$$

$$Z = (X^2 + Y^2)^{\frac{1}{2}} \tag{B.12}$$

$$J = -2m\,\Omega_0\,(\Omega_0 - \Omega_p)\Big(\frac{d\Phi_b}{dr'}\Big)_{r_0} - \Big(m^2(\Omega_0 - \Omega_p)^2 - \kappa_0^2 + 4\Omega_0^2\Big)\Big(\frac{m\Phi_b}{r'}\Big)_{r_0} \tag{B.13}$$

$$K = -m^2(\Omega_0 - \Omega_p)^2\Big(\frac{d\Phi_b}{dr'}\Big)_{r_0} - 2m\,\Omega_0\,(\Omega_0 - \Omega_p)\Big(\frac{m\Phi_b}{r'}\Big)_{r_0} \tag{B.14}$$

$$L = m^2\lambda\,(\Omega_0 - \Omega_p)\Big(\frac{m\Phi_b}{r'}\Big)_{r_0} \tag{B.15}$$

$$M = m^2\mu\,(\Omega_0 - \Omega_p)\Big(\frac{d\Phi_b}{dr'}\Big)_{r_0} \tag{B.16}$$

Note that for the logarithmic and modified Plummer potentials used in this work, both Φ_b and its derivative will be negative. Our solutions proceed from

$$a' \sin\alpha' = \frac{1}{Z^2}(-KY + MX) \tag{B.17}$$

$$a' \cos\alpha' = \frac{1}{Z^2}(KX + MY) \tag{B.18}$$

$$b' \sin\beta' = \frac{1}{Z^2}(-JY + LX) \tag{B.19}$$

$$b' \cos\beta' = \frac{1}{Z^2}(JX + LY) \tag{B.20}$$

a' and b' must have signs which agree with those of J and K in the limit that $\lambda = \mu = 0$:

$$a' = \left(\frac{K^2 + M^2}{Z^2}\right)^{\frac{1}{2}} = \frac{K}{Z}\left(1 + (M/K)^2\right)^{\frac{1}{2}} \tag{B.21}$$

$$b' = \left(\frac{J^2 + L^2}{Z^2}\right)^{\frac{1}{2}} = \frac{J}{Z}\left(1 + (L/J)^2\right)^{\frac{1}{2}} \tag{B.22}$$

For the phase shifts, we rewrite

$$\begin{aligned} \alpha' &= \text{Arctan}\left(\frac{-KY + MX}{KX + MY}\right) \\ &= \text{Arctan}\left(\frac{(M/K) - (Y/X)}{1 + (M/K)(Y/X)}\right) \\ &= \text{Arctan}\,(M/K) - \text{Arctan}\,(Y/X) \end{aligned} \tag{B.23}$$

$$\begin{aligned} \beta' &= \text{Arctan}\left(\frac{-JY + LX}{JX + LY}\right) \\ &= \text{Arctan}\left(\frac{(L/J) - (Y/X)}{1 + (L/J)(Y/X)}\right) \\ &= \text{Arctan}\,(L/J) - \text{Arctan}\,(Y/X) \end{aligned} \tag{B.24}$$

Since the ratios M/K and L/J are never singular, ambiguity in the inverse tangents is restricted to Y/X. We need only add $\pm\pi$ to Arctan (Y/X) when X becomes negative at an inner or outer m:1 Lindblad resonance, since the singularity at corotation does not coincide with a change of sign in Y/X. Eliminating Y/X altogether gives us the identity

$$\alpha' + \text{Arctan}\,(L/J) = \beta' + \text{Arctan}\,(M/K) \tag{B.25}$$

These results are equivalent to those of Sakamoto et al. (1999a) for the case $\mu = 0$, to those of Wada (1994) and Byrd et al. (1998) for the case $\mu = b' = 0$, and to those of Binney & Tremaine (1987) for the case $\lambda = \mu = b' = 0$.

Figure B.1 shows the effects on gas motions of introducing $\lambda \neq 0$ and/or $\mu \neq 0$. Although the formulation of the damping terms is somewhat *ad hoc*, the agreement of the shapes and orientations of orbits with those seen in full hydrodynamic models (Lindblad & Lindblad 1994; Wada 1994) is quite good and reassures us that the analytic approach is reasonable.

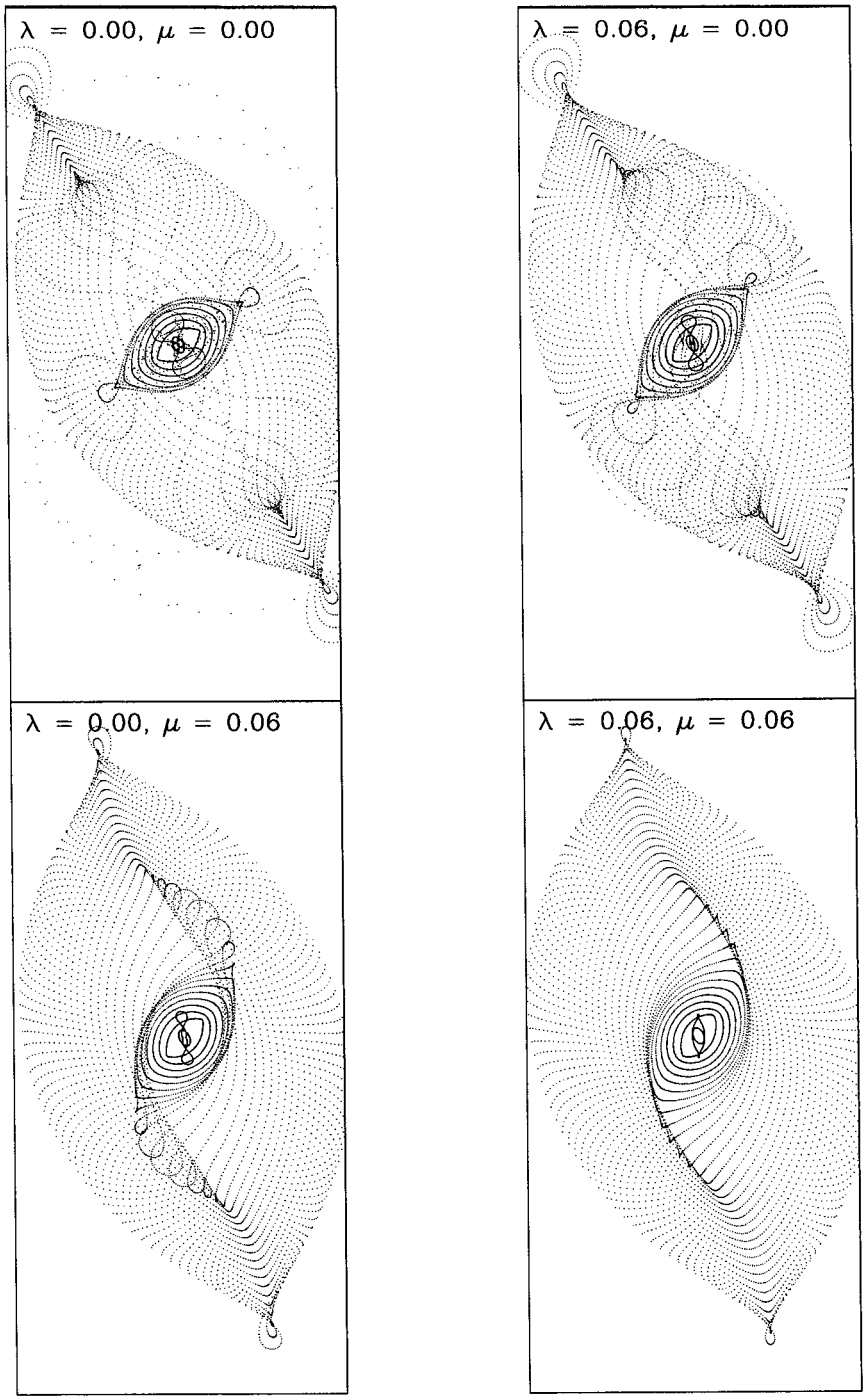

Figure B.1: Gas orbits in a barred potential. Orbits are traced in the rest frame of a clockwise-rotating bar which lies along position angle $\sim 31°$; further parameters are taken from a preliminary version of the model for NGC 7479 in Section 2.4. Nonzero damping terms $\propto \{\lambda, \mu\}$ cause the gas orbits to lead the bar and minimize self-intersection near the (outer) inner 2:1 Lindblad resonance. Near corotation (just outside the radii plotted here), motions become singular for all $\{\lambda, \mu\}$ in any strictly linear treatment.

B.2 Coordinate transformations

In general, we construct model data cubes using circular or elliptical gas rings as building blocks. To calculate the expected line-of-sight velocities for gas clouds in a given ring, we must be able to project the equation for a ring from its natural axes– call them (x, y, z)– into coordinates on the sky $(\hat{x}, \hat{y}, \hat{z})$. We adopt here a scheme for linking the galaxy and sky reference frames which is inspired by (but not identical to) those of Christodoulou et al. (1993) and Herrnstein (1995). We begin with a ring which (a) is centered at $(\hat{x}_0, \hat{y}_0, \hat{z}_0)$; (b) is parallel to the $\hat{x}\hat{y}$ plane; (c) has some preferred axis– suppose for now the major axis of an ellipse– parallel to the $\hat{x}$ axis; and (d) has counter-clockwise (i.e., right-handed) circulation. We then apply a translation and three rotations [through Euler angles in the main convention] to this ring so that it is deprojected to the position and orientation on the sky of the real galaxy. Finally, we invert these transformations to obtain the projection of galaxy coordinates into sky coordinates. Our conventions are as follows:

1. Define right-handed coordinates on the sky $(\hat{x}, \hat{y}, \hat{z})$ such that $-\hat{x} \sim$ right ascension, $+\hat{y} \sim$ declination, and $+\hat{z}$ points towards the observer.

2. Translate the ring so that it is centered at $(0, 0, 0)$ rather than $(\hat{x}_0, \hat{y}_0, \hat{z}_0)$.

3. Define α as the position angle on the sky of the ring's ascending node, i.e., of the blueshifted end of the intersection of the ring plane with the sky plane. α is measured east of north and falls in the range $0 \leq \alpha < 2\pi$.

4. Rotate the ring by $\pi/2+\alpha$ counter-clockwise about $+\hat{z}$, so that the $+\hat{x}$ axis is mapped into a $+\hat{x}'$ axis along the ascending node.

5. Define i as the inclination of the disk with respect to the sky plane. Let $0 \leq i < \pi/2$ correspond to counter-clockwise circulation on the sky and $\pi/2 < i \leq \pi$ to clockwise circulation on the sky.

6. Rotate the ring by i counter-clockwise about $+\hat{x}'$, so that the $+\hat{z}'$ axis is mapped into $+\hat{z}'' = +z$ (the ring's rotation axis in the frame of the galaxy).

7. Define ϕ_0 as the angle in azimuth *in the ring plane* by which the major axis of the elliptical ring leads its ascending node (for the appropriate sense of circularion). We use $\phi_0 = 0$ for a circular ring.

8. Rotate the ring by ϕ_0 counter-clockwise about $+\hat{z}'' = +z$, so that the $+\hat{x}' = +\hat{x}''$ axis is mapped into a $+x$ axis parallel to the major axis of the ellipse in the galaxy. The ring axes are now at (x, y, z).

These operations on the ring can be written in matrix form:

$$\begin{pmatrix} x \\ y \\ z \end{pmatrix} = \begin{pmatrix} \cos\phi_0 & \sin\phi_0 & 0 \\ -\sin\phi_0 & \cos\phi_0 & 0 \\ 0 & 0 & 1 \end{pmatrix} \begin{pmatrix} 1 & 0 & 0 \\ 0 & \cos i & \sin i \\ 0 & -\sin i & \cos i \end{pmatrix} \begin{pmatrix} -\sin\alpha & \cos\alpha & 0 \\ -\cos\alpha & -\sin\alpha & 0 \\ 0 & 0 & 1 \end{pmatrix} \begin{pmatrix} \hat{x} - \hat{x}_0 \\ \hat{y} - \hat{y}_0 \\ \hat{z} - \hat{z}_0 \end{pmatrix} \tag{B.26}$$

yielding three equations for *deprojecting* a point's sky coordinates $(\hat{x}, \hat{y})$ into a galaxy's reference frame:

$$\begin{aligned} x &= -(\hat{x} - \hat{x}_0)(\sin\alpha\cos\phi_0 + \cos\alpha\sin\phi_0\cos i) \\ &\quad +(\hat{y} - \hat{y}_0)(\cos\alpha\cos\phi_0 - \sin\alpha\sin\phi_0\cos i) \\ &\quad +(\hat{z} - \hat{z}_0)(\sin\phi\sin i) \end{aligned} \tag{B.27}$$

$$\begin{aligned} y &= +(\hat{x} - \hat{x}_0)(\sin\alpha\sin\phi_0 - \cos\alpha\cos\phi_0\cos i) \\ &\quad -(\hat{y} - \hat{y}_0)(\cos\alpha\sin\phi_0 + \sin\alpha\cos\phi_0\cos i) \\ &\quad +(\hat{z} - \hat{z}_0)(\cos\phi\sin i) \end{aligned} \tag{B.28}$$

$$\begin{aligned} z &= +(\hat{x} - \hat{x}_0)(\cos\alpha\sin i) \\ &\quad +(\hat{y} - \hat{y}_0)(\sin\alpha\sin i) \\ &\quad +(\hat{z} - \hat{z}_0)(\cos i) \end{aligned} \tag{B.29}$$

These equations cannot generally be solved, because we do not know the $\hat{z}$ coordinate in the sky frame. However, for the special case of a disk which is flat and thin, $z = 0$ and we can rewrite the third equation:

$$\hat{z} - \hat{z}_0 = -\sec i\Big[(\hat{x} - \hat{x}_0)(\cos\alpha\sin i) + (\hat{y} - \hat{y}_0)(\sin\alpha\sin i)\Big] \tag{B.30}$$

Eliminating $\hat{z} - \hat{z}_0$ from the first two equations now gives

$$\begin{aligned} x &= -(\hat{x} - \hat{x}_0)\,(\sin\alpha\cos\phi_0 + \cos\alpha\sin\phi_0\sec i) \\ &\quad +(\hat{y} - \hat{y}_0)\,(\cos\alpha\cos\phi_0 - \sin\alpha\sin\phi_0\sec i) \end{aligned} \tag{B.31}$$

$$\begin{aligned} y &= +(\hat{x} - \hat{x}_0)\,(\sin\alpha\sin\phi_0 - \cos\alpha\cos\phi_0\sec i) \\ &\quad -(\hat{y} - \hat{y}_0)\,(\cos\alpha\sin\phi_0 + \sin\alpha\cos\phi_0\sec i) \end{aligned} \tag{B.32}$$

Cases which are not amenable to deprojection include the following:

1. Flat disks which are thick. Some of the gas will have $z \neq 0$ in the frame of the galaxy.

2. Thin disks which are warped. Gas rings with different radii r have different inclinations i and position angles α, so emission from multiple radii can appear at certain sky positions $(\hat{x}, \hat{y})$.

3. Flat, thin disks which are seen edge-on. Emission from multiple radii will appear at *every* sky position; this corresponds to the singularity in $\sec i$ at $i = \pi/2$.

4. Gas disks in realistic barred potentials. Even if the gas distribution is coplanar, the same $(\hat{x}, \hat{y}, \hat{z})$ position may be the location of nominally intersecting orbits.

If we invert the matrices above, we obtain the *projection* of galaxy coordinates into sky coordinates:

$$\begin{pmatrix} \hat{x} - \hat{x}_0 \\ \hat{y} - \hat{y}_0 \\ \hat{z} - \hat{z}_0 \end{pmatrix} = \begin{pmatrix} -\sin\alpha & -\cos\alpha & 0 \\ \cos\alpha & -\sin\alpha & 0 \\ 0 & 0 & 1 \end{pmatrix} \begin{pmatrix} 1 & 0 & 0 \\ 0 & \cos i & -\sin i \\ 0 & \sin i & \cos i \end{pmatrix} \begin{pmatrix} \cos\phi_0 & -\sin\phi_0 & 0 \\ \sin\phi_0 & \cos\phi_0 & 0 \\ 0 & 0 & 1 \end{pmatrix} \begin{pmatrix} x \\ y \\ z \end{pmatrix} \tag{B.33}$$

equivalent to

$$\begin{aligned}
\hat{x} - \hat{x}_0 &= -x\,(\sin\alpha\cos\phi_0 + \cos\alpha\sin\phi_0\cos i) \\
&\quad +y\,(\sin\alpha\sin\phi_0 - \cos\alpha\cos\phi_0\cos i) \\
&\quad +z\,(\cos\alpha\sin i)
\end{aligned} \tag{B.34}$$

$$\begin{aligned}
\hat{y} - \hat{y}_0 &= +x\,(\cos\alpha\cos\phi_0 - \sin\alpha\sin\phi_0\cos i) \\
&\quad -y\,(\cos\alpha\sin\phi_0 + \sin\alpha\cos\phi_0\cos i) \\
&\quad +z\,(\sin\alpha\sin i)
\end{aligned} \tag{B.35}$$

$$\begin{aligned}
\hat{z} - \hat{z}_0 &= +x\,(\sin\phi_0\sin i) \\
&\quad +y\,(\cos\phi_0\sin i) \\
&\quad +z\,(\cos i)
\end{aligned} \tag{B.36}$$

These are the appropriate equations for constructing a model galaxy whose position and orientation match those of the data.

The motions of gas clouds in a circular disk can be obtained from their positions in the frame of the galaxy: $x = r\cos\phi$ and $y = r\sin\phi$, where $\phi(t) = \Omega_0(r)t > 0$ for counter-clockwise circulation if t is chosen so that $\phi_0(0) = 0$. Differentiating with respect to time yields $v_x = -v_c(r)\sin\phi$ and $v_y = v_c(r)\cos\phi$ for circular velocity $v_c(r) = \Omega_0 r$. Projecting these equations into the sky plane then gives

$$\hat{x} - \hat{x}_0 = -r\cos(\Omega_0 t)\sin\alpha - r\sin(\Omega_0 t)\cos\alpha\cos i \tag{B.37}$$

$$\hat{y} - \hat{y}_0 = +r\cos(\Omega_0 t)\cos\alpha - r\sin(\Omega_0 t)\sin\alpha\cos i \tag{B.38}$$

$$\hat{v}_z = +v_c(r)\cos(\Omega_0 t)\sin i \tag{B.39}$$

for the quantities which we can observe directly. Note that these results are invariant under the mapping $(\Omega_0, i) \rightarrow (-\Omega_0, \pi - i)$; the latter option describes clockwise circulation with near and far sides of the disk reversed. In either case, since the $+\hat{z}$ axis points towards the observer in our choice of sky coordinates, the convention of positive recessional velocities means that the radial (line-of-sight) velocity will be $\hat{v}_r = \hat{v}_0 - \hat{v}_z$.

We can as easily write the equations of motion for gas clouds in a barred potential. The model of Appendix B.1 provides the positions of gas clouds in a (primed) reference

frame which is rotating counter-clockwise with the bar at Ω_p: $x'(t) = r'(t)\cos\phi'(t)$ and $y'(t) = r'(t)\sin\phi'(t)$. We have two options for transforming these equations to a standard inertial $(\hat{x}, \hat{y}, \hat{z})$ frame on the sky. First, we can trace the trajectory of a *single* particle over *many* time steps, by applying a counter-clockwise rotation of $-\Omega_p t$ which sends $\phi'(t) \rightarrow \Omega_0 t + \phi_1'(t)$. After projecting into the sky frame, we obtain

$$\begin{aligned} \hat{x} - \hat{x}_0 &= -r'(t)\cos\Big(\Omega_0 t + \phi_1'(t)\Big)\left[\sin\alpha\cos\phi_0 + \cos\alpha\sin\phi_0\cos i\right] \\ &\quad +r'(t)\sin\Big(\Omega_0 t + \phi_1'(t)\Big)\left[\sin\alpha\sin\phi_0 - \cos\alpha\cos\phi_0\cos i\right] \end{aligned} \tag{B.40}$$

$$\begin{aligned} \hat{y} - \hat{y}_0 &= +r'(t)\cos\Big(\Omega_0 t + \phi_1'(t)\Big)\left[\cos\alpha\cos\phi_0 - \sin\alpha\sin\phi_0\cos i\right] \\ &\quad -r'(t)\sin\Big(\Omega_0 t + \phi_1'(t)\Big)\left[\cos\alpha\sin\phi_0 + \sin\alpha\cos\phi_0\cos i\right] \end{aligned} \tag{B.41}$$

Note that r_1' and ϕ_1' have periods $2\pi/(\Omega_0 - \Omega_p)$ incommensurate with the period of the guiding center $2\pi/\Omega_0$: as expected, orbits in an inertial frame do not close. Of greater relevance, however, is describing the motions of *many* particles (with different phases along the bar) at any *single* moment. We can take equal steps of ϕ_0', calculate r' and ϕ' for each step, and finally evaluate x' and y' (as well as $\hat{x}$, $\hat{y}$, and $\hat{v}_z$) around the circumference of the bar. For a particular value of ϕ_0', then, we have

$$\begin{aligned} \hat{x} - \hat{x}_0 &= -r'(t)\cos\Big(\phi'(t)\Big)\left[\sin\alpha\cos\phi_0 + \cos\alpha\sin\phi_0\cos i\right] \\ &\quad +r'(t)\sin\Big(\phi'(t)\Big)\left[\sin\alpha\sin\phi_0 - \cos\alpha\cos\phi_0\cos i\right] \end{aligned} \tag{B.42}$$

$$\begin{aligned} \hat{y} - \hat{y}_0 &= +r'(t)\cos\Big(\phi'(t)\Big)\left[\cos\alpha\cos\phi_0 - \sin\alpha\sin\phi_0\cos i\right] \\ &\quad -r'(t)\sin\Big(\phi'(t)\Big)\left[\cos\alpha\sin\phi_0 + \sin\alpha\cos\phi_0\cos i\right] \end{aligned} \tag{B.43}$$

To obtain the line-of-sight velocity for this ϕ_0', we first compute the velocity in the bar's rest frame:

$$\begin{aligned} v_x' &= -r'(t)\left(\Omega_0 - \Omega_p - \frac{2b'}{r_0}(\Omega_0 - \Omega_p)\cos\left(2\phi_0' + \beta'\right)\right)\sin\phi'(t) \\ &\quad -2\left(\Omega_0 - \Omega_p\right)a'\sin\Big(2\phi_0' + \alpha'\Big)\cos\phi'(t) \end{aligned} \tag{B.44}$$

$$\begin{aligned} v_y' &= +r'(t)\left(\Omega_0 - \Omega_p - \frac{2b'}{r_0}(\Omega_0 - \Omega_p)\cos\left(2\phi_0' + \beta'\right)\right)\cos\phi'(t) \\ &\quad -2\left(\Omega_0 - \Omega_p\right)a'\sin\Big(2\phi_0' + \alpha'\Big)\sin\phi'(t) \end{aligned} \tag{B.45}$$

Next, using the fact that $v = v' + \vec{\Omega}_p \times \vec{r}'$, we compute the velocity in the inertial frame of the galaxy:

$$\begin{aligned} v_x &= -r'(t)\left(\Omega_0 - \frac{2b'}{r_0}(\Omega_0 - \Omega_p)\cos\left(2\phi_0' + \beta'\right)\right)\sin\phi'(t) \\ &\quad -2\left(\Omega_0 - \Omega_p\right)a'\sin\Big(2\phi_0' + \alpha'\Big)\cos\phi'(t) \end{aligned} \tag{B.46}$$

$$\begin{aligned} v_y &= +r'(t)\left(\Omega_0 - \frac{2b'}{r_0}(\Omega_0 - \Omega_p)\cos\left(2\phi_0' + \beta'\right)\right)\cos\phi'(t) \\ &\quad -2\left(\Omega_0 - \Omega_p\right)a'\sin\Big(2\phi_0' + \alpha'\Big)\sin\phi'(t) \end{aligned} \tag{B.47}$$

Finally, we correct to the sky frame:

$$\begin{aligned} \hat{v}_z &= -\Big[r'(t)\left(\Omega_0 - \frac{2b'}{r_0}(\Omega_0 - \Omega_p)\cos\left(2\phi_0' + \beta'\right)\right)\sin\phi'(t) \\ &\quad +2\left(\Omega_0 - \Omega_p\right)a'\sin\Big(2\phi_0' + \alpha'\Big)\cos\phi'(t)\Big]\sin\phi_0\sin i \\ &\quad +\Big[r'(t)\left(\Omega_0 - \frac{2b'}{r_0}(\Omega_0 - \Omega_p)\cos\left(2\phi_0' + \beta'\right)\right)\cos\phi'(t) \\ &\quad -2\left(\Omega_0 - \Omega_p\right)a'\sin\Big(2\phi_0' + \alpha'\Big)\sin\phi'(t)\Big]\cos\phi_0\sin i \end{aligned} \tag{B.48}$$

B.3 The optical depth of a rotational transition

For use in Section 3.5, we follow Carlstrom (1988) in deriving an expression for the optical depth τ_v in the $J+1 \rightarrow J$ rotational transition of CO at some velocity v. The line's total opacity (in velocity units) is the absorption coefficient α_ν integrated over path length and velocity:

$$\tau = \int \tau_v \, dv = \int\int \alpha_\nu \, dv \, ds \tag{B.49}$$

We can write α_ν in terms of the Einstein coefficients: accounting for stimulated emission,

$$\alpha_\nu = \frac{h\nu}{4\pi}\Big(n_J B_{J\rightarrow J+1} - n_{J+1}B_{J+1\rightarrow J}\Big)\phi(\nu) \tag{B.50}$$

where $\phi(\nu)$ is a line profile with unit integral. For consistency with the velocity integral (which we will shortly drop), we rewrite the line profile in terms of velocity:

$$\int \phi(\nu)d\nu = \int \phi(v)dv = \int \phi(\nu)\frac{\nu}{c}dv \tag{B.51}$$

Using the Einstein relations, we also rewrite $B_{J\to J+1}$ to obtain

$$\tau_v = \int ds\, \frac{hc}{4\pi}\, \phi(v)\, n_{J+1} B_{J+1\to J}\Big(\frac{n_J}{n_{J+1}}\frac{g_{J+1}}{g_J} - 1\Big) \tag{B.52}$$

For level populations described by the excitation temperature T_{ex},

$$n_J = X_{\rm CO}\, n_{\rm H_2}\, Z^{-1}\, g_J \exp\Big[-\frac{E_J}{kT_{ex}}\Big] \tag{B.53}$$

and likewise for n_{J+1}, where $X_{\rm CO}$ is the fractional abundance of CO relative to H_2 and Z is the partition function for T_{ex}. Because $E_J = hB_0J(J+1)$ for the rotational constant B_0, we can write

$$E_{J+1} - E_J = 2hB_0(J+1) \tag{B.54}$$

$$Z(T_{ex}) \simeq \frac{kT_{ex}}{hB_0} \tag{B.55}$$

with the latter approximation valid for large T_{ex}. Finally, for dipole selection rules,

$$\begin{aligned} B_{J+1\to J} &= \frac{c^2}{2h\nu^3}\, A_{J+1\to J} \\ &= \frac{c^2}{2h\nu^3}\,\frac{64\pi^4\nu^3}{3hc^3}\,|\mu_{J+1\to J}|^2 \\ &= \frac{32\pi^4}{3ch^2}\,\mu_0^2\,\frac{J+1}{2J+3} \end{aligned} \tag{B.56}$$

Substituting these values into Equation B.52 now yields

$$\begin{aligned} \tau_v &= \int ds\, \frac{hc}{4\pi}\, \phi(v)\, n_{J+1} B_{J+1\to J}\Big(\frac{n_J}{n_{J+1}}\frac{g_{J+1}}{g_J} - 1\Big) \\ &= \frac{8\pi^3\mu_0^2}{3h}\,\frac{J+1}{2J+3}\, X_{\rm CO}\, n_{\rm H_2}\, Z^{-1}\, g_{J+1} \exp\Big[-\frac{E_{J+1}}{kT_{ex}}\Big]\Big(\frac{n_J}{n_{J+1}}\frac{g_{J+1}}{g_J} - 1\Big)\int ds\,\phi(v) \\ &= \frac{8\pi^3\mu_0^2}{3hZ}\,(J+1)\exp\Big[-\frac{E_{J+1}}{kT_{ex}}\Big]\Big(\exp\Big[\frac{E_{J+1}-E_J}{kT_{ex}}\Big] - 1\Big)\,\Theta(v) \end{aligned} \tag{B.57}$$

where the integral

$$\Theta(v) = \int ds\, n_{\mathrm{H_2}} X_{\mathrm{CO}}\, \phi(v) \sim \mathrm{cm}^{-3}\,\mathrm{s} \tag{B.58}$$

describes the fraction of the CO column density along the line of sight which lies in each velocity range. The total opacity can be obtained trivially:

$$\int \Theta(v)\, dv = N_{\mathrm{CO}} \Rightarrow \tag{B.59}$$

$$\tau \simeq \frac{8\pi^3 B_0 \mu_0^2}{3kT_{ex}} (J+1) \exp\Big[-\frac{(J+1)(J+2)}{Z}\Big] \Big(\exp\Big[\frac{2(J+1)}{Z}\Big] - 1\Big) \times N_{\mathrm{CO}} \tag{B.60}$$

using the high-T_{ex} approximation for Z. In contrast, concisely expressing Θ (and τ_v) alone requires that we assume some relation between path length and velocity. A direct proportionality is the easiest choice; this implies that for homogeneous conditions within a cloud, the identical gas column in each velocity interval will produce a rectagular velocity profile. $\phi(v)$ now becomes the reciprocal of the total linewidth Δv, and $\Delta s/\Delta v = ds/dv$ is a constant. We can thus write

$$\tau_v \simeq \frac{8\pi^3 B_0 \mu_0^2}{3kT_{ex}} (J+1) \exp\Big[-\frac{(J+1)(J+2)}{Z}\Big] \Big(\exp\Big[\frac{2(J+1)}{Z}\Big] - 1\Big) \times n_{\mathrm{H_2}} \times \frac{X_{\mathrm{CO}}}{dv/ds} \tag{B.61}$$

This approach to evaluating $\Theta(v)$ is used in Large Velocity Gradient (LVG) radiative transfer models; indeed, the last two terms in Equation B.61 are precisely the physical parameters used as axes in Figure 3.10.

Bibliography

Aalto, S., Booth, R. S., Black, J. H., & Johansson, L. E. B. 1995, A&A, 300, 369

Aalto, S., Booth, R. S., Black, J. H., Koribalski, B., & Wielebinski, R. 1994, A&A, 286, 365

Aalto, S., Hüttemeister, S., Scoville, N. Z., & Thaddeus, P. 1999, ApJ, 522, 165

Allen, R. J. & Lequeux, J. 1993, ApJL, 410, L15

Anantharamaiah, K. R., Ekers, R. D., Radhakrishnan, V., Cornwell, T. J., and Goss, W. M. 1989, in *Synthesis Imaging in Radio Astronomy*, ed. R. A. Perley, F. R. Schwab, & A. H. Bridle (San Francisco: ASP), 431

Antonucci, R., Hurt, T., & Miller, J. 1994, ApJ, 430, 210

Athanassoula, E. 1992, MNRAS, 259, 345

Athanassoula, E. & Bureau, M. 1999, ApJ, 522, 699

Axford, W. I. 1994, ApJS, 90, 937

Balzano, V. A. 1983, ApJ, 268, 602

Baum, S. A., O'Dea, C. P., Dallacassa, D., de Bruyn, A. G., & Pedlar, A. 1993, ApJ, 419, 553

Binney, J., Gerhard, O. E., Stark, A. A., Bally, J., & Uchida, K. I. 1991, MNRAS, 252, 210

Binney, J. & Tremaine, S. 1987, *Galactic Dynamics* (Princeton: Princeton University Press)

Black, J. H. 1987, in *Astrophysical Processes*, ed. D. J. Hollenbach & H. A. Thronson, Jr. (Dordrecht: Kluwer), 731

Bland-Hawthorn, J., Gallimore, J. F., Tacconi, L. J., Brinks, E., Baum, S. A., Antonucci, R. R. J., & Cecil, G. N. 1997, ApSS, 248, 9

Bloemen, J. B. G. M., Strong, A. W., Blitz, L., Cohen, R. S., Dame, T. M., Grabelsky, D. A., Hermsen, W., Lebrun, F., & Thaddeus, P. 1986, A&A, 154, 25

Bock, J. J., Marsh, K. A., Ressler, M. E., & Werner, M. W. 1998, ApJL, 504, L5

Braine, J., Combes, F., Casoli, F., Dupraz, C., Gérin, M., Klein, U., Wielebinski, R., & Brouillet, N. 1993, A&AS, 97, 887

Briggs, D. S. 1995, Ph.D. thesis

Brinks, E., Skillman, E. D., Terlevich, R. J., & Terlevich, E. 1997, ApSS, 248, 23

Bryant, P. M. & Scoville, N. Z. 1996, ApJ, 457, 678

Bureau, M. & Athanassoula, E. 1999, ApJ, 522, 686

Buta, R. & Combes, F. 1996, Fundamentals of Cosmic Physics, 17, 95

Byrd, G. G., Ousley, D. & Dalla Piazza, C. 1998, MNRAS, 298, 78

Byrd, G. G., Sundelius, B., & Valtonen, M. 1987, A&A, 171, 16

Capetti, A., Macchetto, F. D., & Lattanzi, M. G. 1997, ApJL, 476, L67

Carlstrom, J. E. 1988, Ph.D. thesis

Cecil, G., Bland, J., & Tully, R. B. 1990, ApJ, 355, 70

Christodoulou, D. R., Tohline, J. E., & Steiman-Cameron, T. Y. 1993, ApJ, 416, 74

Christopoulou, P. E., Holloway, A. J., Steffen, W., Mundell, C. G., Thean, A. H. C., Goudis, C. D., Meaburn, J., Pedlar, A. 1997, MNRAS, 284, 385

Combes, F. 1994, in *Mass-Transfer Induced Activity in Galaxies*, ed. I. Shlosman (Cambridge: Cambridge University Press), 170

Combes, F., Dupraz, C., Casoli, F., Pagani, L. 1988, A&A, 203, L9

Condon, J. J., Helou, G., Sanders, D. B., & Soifer, B. T. 1990, ApJS, 73, 359

Contopoulos, G. 1988, A&A, 201, 44

Crawford, M. K., Genzel, R., Townes, C. H., & Watson, D. M. 1985, ApJ, 291, 755

Crosas, M. & Weisheit, J. 1996, ApJ, 465, 659

de Vaucouleurs, G., de Vaucouleurs, A., Corwin, H. G., Buta, R. J., Paturel, G., & Fouqué, P. 1991, *Third Reference Catalogue of Bright Galaxies* (New York: Springer Verlag)

Dickman, R. L., Snell, R. L., & Schloerb, F. P. 1986, ApJ, 309, 326

Downes, D. & Solomon, P. M. 1998, ApJ, 507, 615

Downes, D., Solomon, P. M., & Radford, S. J. E. 1993, ApJL, 414, L13

Draine, B. T. & Lee, H. M. 1984, ApJ, 285, 89

Eckart, A., Downes, D., Genzel, R., Harris, A. I., Jaffe, D. T., & Wild, W. 1990, ApJ, 348, 434

Erwin, P. & Sparke, L. S. 1999, ApJL, 521, L37

Eskridge, P. B. 1999, personal communication

Fernandez, B. R., Holloway, A. J., Meaburn, J., Pedlar, A., & Mundell, C. G. 1999, MNRAS, 305, 319

Ferrarese, L. & Ford, H. C. 1999, ApJ, 515, 583

Ferrarese, L., Ford, H. C., & Jaffe, W. 1996, ApJ, 470, 444

Friedli, D. & Benz, W. 1993, A&A, 268, 65

Friedli, D. & Martinet, L. 1993, A&A, 277, 27

Gallimore, J. F., Baum, S. A., & O'Dea, C. P. 1997, Nature, 388, 852

Gallimore, J. F., Baum, S. A., O'Dea, C. P., & Pedlar, A. 1996, ApJ, 458, 136

García-Burillo, S. & Guélin, M. 1995, A&A, 299, 657

García-Burillo, S., Sempere, M., Combes, F., & Neri, R. 1998, A&A, 333, 864

Gautier, T. N., Hauser, M.G., Beichman, C. A., Low, F. J., Neugebauer, G., Rowan-Robinson, M., Aumann, H. H., Boggess, N., Emerson, J. P., Harris, S., Houck, J. R., Jennings, R. E., & Marsden, P. L. 1984, ApJL, 278, L57

Goldreich, P. & Kwan, J. 1974, ApJ, 189, 441

Goldreich, P. & Tremaine, S. 1981, ApJ, 243, 1062

Goldsmith, P. F., Young, J. S., & Langer, W. D. 1983, ApJS, 51, 203

González Delgado, R. M. & Pérez, E. 1997, MNRAS, 284, 931

Green, S. & Chapman, S. 1978, ApJS, 37, 169

Greenhill, L. J. & Gwinn, C. R. 1997, ApSS, 248, 261

Handa, T., Nakai, N., Sofue, Y., Hayashi, M. & Fujimoto, M. 1990, PASJ, 42, 1

Heckman, T. M. 1999, in *The Most Distant Radio Galaxies*, ed. H. J. A. Rottgering, P. N. Best, & M. D. Lehnert (Dordrecht: Kluwer)

Helfer, T. T. 1999, personal communication

Helfer, T. T. & Blitz, L. 1995, ApJ, 450, 90

Heller, C. H. & Shlosman, I. 1994, ApJ, 424, 84

Heller, C. H. & Shlosman, I. 1996, ApJ, 471, 143

Helou, G., Soifer, B. T., & Rowan-Robinson, M. 1985, ApJL, 298, L7

Hernquist, L. 1989, Nature, 340, 687

Herrnstein, J. R. 1997, Ph.D. thesis

Ho, L. C. 1999, ApJ, 516, 672

Ho, L. C., Filippenko, A. V., & Sargent, W. L. W. 1997a, ApJ, 487, 568

Ho, L. C., Filippenko, A. V., & Sargent, W. L. W. 1997b, ApJ, 487, 591

Ho, L. C., Filippenko, A. V., Sargent, W. L. W., & Peng, C. Y. 1997c, ApJS, 112, 391

Hüttemeister, S., Aalto, S., & Wall, W. 1999, A&A, 346, 45

Hüttemeister, S., Aalto, S., Das, M., & Wall, W. 2000, A&A, in preparation

Jackson, J. M., Paglione, T. A. D., Ishizuki, S., & Rieu, N.-Q. 1993, ApJL, 418, L13

Jogee, S. 1998, Ph.D. thesis

Kaneko, N., Aoki, K., Kosugi, G., Ohtani, H., Yoshida, M., Toyama, K., Satoh, T., Sasaki, M. 1997, AJ, 114, 94

Kaneko, N., Morita, K., Fukui, Y., Sugitani, K., Iwata, T., Nakai, N., Kaifu, N., & Liszt, H. S. 1989, ApJ, 337, 691

Kaneko, N., Morita, K., Fukui, Y., Takahashi, N., Sugitani, K., Nakai, N., & Morita, K.-I. 1992, PASJ, 44, 341

Kaufmann, D. E. & Contopoulos, G. 1996, A&A, 309, 381

Kenney, J. D. P., Rubin, V. C., Planesas, P., & Young, J. S. 1995, ApJ, 438, 135

Kenney, J. D. P., Wilson, C. D., Scoville, N. Z., Devereux, N. A., & Young, J. S. 1992, ApJL, 395, L79

Kenney, J. D. & Young, J. S. 1988, ApJS, 66, 261

Knapen, J. H., Shlosman, I., & Peletier, R. F. 1999, ApJ, in press [astro-ph/9907379]

Kohno, K., Kawabe, R., & Vila-Vilaró, B. 1999, in *The Physics and Chemistry of the Interstellar Medium*, ed. V. Ossenkopf, J. Stutzki, & G. Winnewisser (Aachen: Shaker Verlag), 34

Krabbe, A., Genzel, R., Eckart, A., Najarro, F., Lutz, D., Cameron, M., Kroker, H., Tacconi-Garman, L. E., Thatte, N., Weitzel, L., Drapatz, S., Geballe, T., Sternberg, A., & Kudritzki, R. 1995, ApJL, 447, L95

Krolik, J. H. & Begelman, M. C. 1988, ApJ, 329, 702

Kuijken, K. & Merrifield, M. R. 1995, ApJL, 443, L13

Kukula, M. J., Pedlar, A., Baum, S. A., & O'Dea, C. P. 1995, MNRAS, 276, 1262

Kwan, J. & Sanders, D. B. 1986, ApJ, 309, 783

Laine, S. & Gottesman, S. T. 1998, MNRAS, 297, 1041

Laine, S. & Heller, C. H. 1999, MNRAS, 308, 557

Laine, S., Kenney, J. D. P., Yun, M. S., & Gottesman, S. T. 1999, ApJ, 511, 709

Laine, S., Shlosman, I. & Heller, C. H. 1998, MNRAS, 297, 1052

Lay, O. P. 1997a, A&AS, 122, 535

Lay, O. P. 1997b, A&AS, 122, 547

Leighton, R. B. 1978, *Final Technical Report for National Science Foundation Project AST 73-04708*

Leung, C. M. & Liszt, H. S. 1976, ApJ, 208, 732

Lin, D. N. C., Pringle, J. E., & Rees, M. J. 1988, ApJ, 328, 103

Lindblad, P. O. & Lindblad, P. A. B. 1994, in *Physics of the Gaseous and Stellar Disks of the Galaxy*, ed. I. R. King (San Francisco: ASP), 29

Liszt, H. S. & Dickey, J. M. 1995, AJ, 110, 998

Maciejewski, W. & Sparke, L. S. 1997, ApJL, 484, L117

Maciejewski, W. & Sparke, L. S. 1999, MNRAS, in press [astro-ph/9911281]

Maiolino, R., Risaliti, G., & Salvati, M. 1999, A&A, 341, 35

Maloney, P. M & Black, J. H. 1988, ApJ, 325, 389

Maloney, P. R., Hollenbach, D. J., & Tielens, A. G. G. M. 1996, ApJ, 466, 561

Maoz, D. 1998, Advances in Space Science, 23:5-6, 855

Martin, H. M., Sanders, D. B., & Hills, R. E. 1984, MNRAS, 208, 35

Martini, P. & Pogge, R. W. 1999, AJ, in press [astro-ph/9909032]

Meixner, M., Puchalsky, R., Blitz, L., Wright, M., & Heckman, T. 1990, ApJ, 354, 158

Muhleman, D. O. & Berge, G. L. 1991, Icarus, 92, 263

Mulchaey, J. S., Mushotzky, R. F., & Weaver, K. A. 1992, ApJL, 390, L69

Mulchaey, J. S. & Regan, M. W. 1997, ApJL, 482, L139

Mulchaey, J. S., Regan, M. W., & Kundu, A. 1997, ApJS, 110, 299

Mundell, C. G., Holloway, A. J., Pedlar, A., Meaburn, J., Kukula, M. J., & Axon, D. J. 1995a, MNRAS, 275, 67

Mundell, C. G., Pedlar, A., Axon, D. J., Meaburn, J., & Unger, S. W. 1995b, MNRAS, 277, 641

Mundell, C. G. & Shone, D. L. 1999, MNRAS, 304, 475

Narayan, R., Mahadevan, R., & Quataert, E. 1998, in *The Theory of Black Hole Accretion Discs*, ed. M. A. Abramowicz, G. Bjornsson, & J. E. Pringle (Cambridge: Cambridge University Press), 148

Norman, C. & Scoville, N. 1988, ApJ, 332, 124

Norman, C. A., Sellwood, J. A., & Hasan, H. 1996, ApJ, 462, 114

Odenwald, S. F. & Fazio, G. G. 1984, ApJ, 283, 601

Orton, G. S., Griffin, M. J., Ade, P. A. R., Nolt, I. G., Radostitz, J. V., Robson, E. I., & Gear, W. K. 1986, Icarus, 67, 289

Packham, C., Young, S., Hough, J. H., Axon, D. J., & Bailey, J. A. 1997, MNRAS, 288, 375

Padin, S., Clark, T. S., Ewing, M. S., Finch, R. P., Lawrence, R. P., Navarro, J., Scott, S. L., Scoville, N. Z., Seelinger, C., & Seling, T. V. 1993, IEEE Transactions on Instrumentation and Measurement, 42, 793

Padin, S., Scott, S. L., Woody, D. P., Scoville, N. Z., Seling, T. V., Finch, R. P., Giovanine, C. J., & Lawrence, R. P. 1991, PASP, 103, 461

Park, Y.-S. & Hong, S. S. 1995, A&A, 300, 890

Park, Y.-S. & Hong, S. S. 1998, ApJ, 494, 605

Park, Y.-S., Hong, S. S., & Minh, Y. C. 1996, A&A, 312, 981

Pérez García, A. M., Rodríguez Espinosa, J. R., & Santolaya Rey, A. E. 1998, ApJ, 500, 685

Perley, R. A., Schwab, F. R., & Bridle, A. H. (ed.) 1989, *Synthesis Imaging in Radio Astronomy* (San Francisco: ASP)

Phinney, E. S. 1994, in *Mass-Transfer Induced Activity in Galaxies*, ed. I. Shlosman (Cambridge: Cambridge University Press), 1

Piner, B. G., Stone, J. M., Teuben, P. J. 1995, ApJ, 449, 508

Planesas, P., Gomez-Gonzalez, J., & Martin-Pintado, J. 1989, A&A, 216, 1

Planesas, P., Scoville, N., & Myers, S. T. 1991, ApJ, 369, 364

Pogge, R. W. 1988, ApJ, 328, 519

Polk, K. S., Knapp, G. R., Stark, A. A., & Wilson, R. W. 1988, ApJ, 332, 432

Press, W. H., Teukolsky, S. A., Vetterling, W. T., & Flannery, B. P. 1992, *Numerical Recipes in FORTRAN 77: Second Edition* (Cambridge: Cambridge University Press)

Pringle, J. E. 1996, MNRAS, 281, 357

Pringle, J. E., Antonucci, R. R. J., Clarke, C. J., Kinney, A. L., Schmitt, H. R., & Ulvestad, J. S. 1999, ApJL, 526, L9

Quillen, A. C., Frogel, J. A., Kenney, J. D. P., Pogge, R. W., & DePoy, D. L. 1995, ApJ, 441, 549

Regan, M. W., Sheth, K., & Vogel, S. N. 1999, ApJ, 526, 97

Ryle, M. & Hewish, A. 1960, MNRAS, 120, 220

Sakamoto, K., Baker, A. J., & Scoville, N. Z. 2000, ApJ, 530, in press [astro-ph/9910021]

Sakamoto, K., Okumura, S. K., Ishizuki, S., & Scoville, N. Z. 1999a, ApJS, 124, 403

Sakamoto, K., Okumura, S. K., Ishizuki, S., & Scoville, N. Z. 1999b, ApJ, 525, 691

Sanders, D. B., Phinney, E. S., Neugebauer, G., Soifer, B. T., & Matthews, K. 1989, ApJ, 347, 29

Sanders, D. B., Scoville, N. Z., & Soifer, B. T. 1991, ApJ, 370, 158

Sanders, D. B., Scoville, N. Z., & Solomon, P. M. 1985, ApJ, 289, 373

Sanders, D. B., Solomon, P. M., & Scoville, N. Z. 1984, ApJ, 276, 182

Sanders, R. H. 1977, ApJ, 217, 916

Sanders, R. H. & Huntley, J. M. 1976, ApJ, 209, 53

Schinke, R., Engel, V., Buck, U., Meyer, H., & Diercksen, G. H. F. 1985, ApJ, 299, 939

Schinnerer, E., Eckart, A., & Tacconi, L. J. 1999, ApJL, 524, 5

Schinnerer, E., Eckart, A., & Tacconi, L. J. 2000a, ApJ, in press [astro-ph/9911487]

Schinnerer, E., Eckart, A., Tacconi, L. J., Genzel, R., & Downes, D. 2000b, ApJ, in press [astro-ph/9911488]

Scott, S. L. & Finch, R. P. 1992, in *Observing at a Distance*, ed. D. T. Emerson & R. G. Clowes (London: World Scientific Publishing), 93

Scoville, N. Z., Carlstrom, J. E., Chandler, C. J., Phillips, J. A., Scott, S. L., Tilanus, R. P. J., & Wang, Z. 1993, PASP, 105, 1482

Scoville, N. Z. & Good, J. C. 1989, ApJ, 339, 149

Scoville, N. Z. & Solomon, P. M. 1974, ApJL, 187, L67

Scoville, N. Z., Yun, M. S., & Bryant, P. M. 1997, ApJ, 484, 702

Sellwood, J. A. & Wilkinson, A. 1993, Reports on Progress in Physics, 56, 173

Sempere, M. J., Combes, F. & Casoli, F. 1995, A&A, 299, 371

Shepherd, M. C. 1997, in *Astronomical Data Analysis Software and Systems VI*, eds. G. Hunt & H. E. Payne (San Francisco: ASP), 77

Shlosman, I., Frank, J., & Begelman, M. C. 1989, Nature, 338, 45

Shu, F. S. 1991, *The Physics of Astrophysics: Radiation* (Mill Valley: University Science Books)

Soifer, B. T., Boehmer, L., Neugebauer, G., & Sanders, D. B. 1989, AJ, 98, 766

Soifer, B. T., Sanders, D. B., Neugebauer, G., Danielson, G. E., Lonsdale, C. J., Madore, B. F., & Person, S. E. 1986, ApJL, 303, L41

Solomon, P. M. & Barrett, J. W. 1991, in *Dynamics of Galaxies and Their Molecular Cloud Distributions*, ed. F. Combes & F. Casoli (Dordrecht: Kluwer), 1991

Solomon, P. M., Downes, D., & Radford, S. J. E. 1992, ApJL, 387, L55

Solomon, P. M., Downes, D., Radford, S. J. E., & Barrett, J. W. 1997, ApJ, 478, 144

Solomon, P. M., Rivolo, A. R., Barrett, J., & Yahil, A. 1987, ApJ, 319, 730

Tacconi, L. J., Gallimore, J. F., Genzel, R., Schinnerer, E., & Downes, D. 1997, ApSS, 248, 59

Tacconi, L. J., Genzel, R., Blietz, M., Cameron, M., Harris, A. I., & Madden, S. 1994, ApJL, 426, L77

Tauber, J. A. & Goldsmith, P. F. 1990, ApJL, 356, L63

Taylor, G. B., Carilli, C. L., & Perley, R. A. (ed.) 1999, *Synthesis Imaging in Radio Astronomy II* (San Francisco: ASP)

Thompson, A. R., Moran, J. M., & Swenson, G. W. 1986, *Interferometry and Synthesis in Radio Astronomy* (New York: Wiley)

Tremaine, S. & Weinberg, M. D. 1984, ApJL, 282, L5

Tully, R. B. 1988, *Nearby Galaxies Catalog* (Cambridge: Cambridge University Press)

Turner, J. L., Martin, R. N., & Ho, P. T. P. 1990, ApJ, 351, 418

Unger, S. W., Lewis, J. R., Pedlar, A., & Axon, D. J. 1992, MNRAS, 258, 371

van der Hulst, J. M., Crane, P. C., & Keel, W. C. 1981, AJ, 86, 1175

van der Marel, R. P. 1998, in *Galaxy Interactions at Low and High Redshift*, ed. D. B. Sanders & J. Barnes (Dordrecht: Kluwer), 333

van der Marel, R. P. & van den Bosch, F. C. 1998, AJ, 116, 2220

Vila, M. B., Pedlar, A., Davies, R. D., Hummel, E., & Axon, D. J. 1990, MNRAS, 242, 379

Wada, K. 1994, PASJ, 46, 165

Wada, K. & Habe, A. 1995, MNRAS, 277, 43

Wall, W. F., Jaffe, D. T., Bash, F. N., Israel, F. P., Maloney, P. R., & Baas, F. 1993, ApJ, 414, 98

Wandel, A. 1999, ApJL, 519, L39

Wandel, A., Peterson, B. M., & Malkan, M. A. 1999, ApJ, 526, 579

White, R. L., Becker, R. H., Helfand, D. J., & Gregg, M. D. 1997, ApJ, 475, 479

Wilson, A. S. & Tsvetanov, Z. I. 1994, AJ, 107, 1227

Wilson, A. S. & Ulvestad, J. 1982, ApJ, 263, 576

Wohlleben, R., Mattes, H., & Krichbaum, T. 1991, *Interferometry in Radioastronomy and Radar Techniques* (Dordrecht: Kluwer)

Young, J. S. & Scoville, N. Z. 1984, ApJ, 287, 153

Young, J. S. & Scoville, N. Z. 1991, ARAA, 29, 581

Young, J. S., Xie, S., Tacconi, L., Knezek, P., Viscuso, P., Tacconi-Garman, L., Scoville, N., Schneider, S., Schloerb, F. P., Lord, S., Lesser, A., Kenney, J., Huang, Y.-L., Devereux, N., Claussen, M., Case, J., Carpenter, J., Berry, M., & Allen, L. 1995, ApJS, 98, 219